CRANFIELD UNIVERSITY

Tracey ROBERTS

The Structure and Stability of High Temperature Intermetallic Phases for Application within Coating Systems

SCHOOL OF APPLIED SCIENCES

PhD THESIS

SCHOOL OF APPLIED SCIENCES

PhD THESIS

Academic Year 2009-2010

Tracey ROBERTS

The Structure and Stability of High Temperature Intermetallic Phases for Application within Coating Systems

Supervisor: **Prof. J. R. Nicholls**

November 2009

Abstract

The reduction of noise and emissions is becoming increasingly important in civil aircraft jet engines as well as requirements for reduced fuel consumption and improved efficiency. This has resulted in the drive towards increasing turbine entry temperatures and the development of thermal barrier coatings (TBCs). Due to the effectiveness of the platinum-modified nickel aluminides currently used as bond coat layers for Ni-based superalloy TBCs, higher temperature ruthenium-containing bond coat layers are being examined as a possible low cost alternative to platinum.

Rolls Royce have a patented process, whereby precious metal layers directly react with single crystal substrate alloys to form an aluminium containing surface coating. The aluminium is sourced from the single crystal alloy and the coating so formed has a $\gamma + \gamma'$ structure, but contains other intermetallic phases due to the reaction between the coating and the single crystal substrate. This bond coat layer acts as a diffusion barrier, which limits interdiffusion between the coating and the substrate.

The aim of this research was to examine the stability of various phases within platinum and ruthenium-containing multilayer systems formed during the above reaction process and to determine the most stable intermetallics for inclusion in future coating systems. Foil samples were manufactured using multilayer sputter coating methods and the exothermic formation of these phases was examined using differential scanning calorimetry. The identification of the phases formed was carried out using X-ray diffraction.

It was found that the interdiffusion between the initial multi-layers had been incomplete during the samples heat treatment, and so more intermetallic phases formed in some samples than aimed for. Hence, from the large number of samples studied it was shown that, as a result of kinetic factors, the reaction onset (or trigger) temperature was not related to the

enthalpy of the intermetallic phases formed or the sample compositions within a target phase field.

For the β-phase (NiAl) type intermetallic systems, the samples that produced the highest enthalpy values (i.e. the most stable intermetallic compounds) were those with the nominal compositions (in atomic %) of; ‘47Ni53Al’, ‘48Ni6Pt46Al’ and ‘51Ni7Ru42Al’.

For the γ′-phase (Ni_3Al) type intermetallic systems, the highest enthalpy values were from samples with nominal compositions of ‘60Ni16Pt24Al’ and ‘74Ni5Ru24Al’.

Acknowledgements

I would like to thank the following people:

My supervisor, Prof. John Nicholls for his helpful advice, guidance and encouragement throughout the project.

Jitka MacAdam for her useful advice during coffee time and the students in the PhD office for providing a distraction and an enjoyable working environment.

My parents, Andy and Barbara Anderson, for all their support and their belief that I could do this.

Finally, I would like to thank my sons, Chris and Peter, for their patience, love and support.

List of Contents

Notation

Al	Aluminium
Ag	Silver
APS	Air plasma spraying
at.%	Concentration in atomic percentage
B	Boron
bcc	Body centred cubic
C	Carbon
Co	Cobalt
Cr	Chromium
CT	Chisel Toughness
CTE	Coefficient of Thermal Expansion
Cu	Copper
CVD	Chemical Vapour Deposition
DBTT	Ductile to Brittle Transition Temperature
DC	Direct Current
DS	Directionally Solidified
DSC	Differential Scanning Calorimeter
DTA	Differential Thermal Analysis
EB	Electron Beam
EDX	Energy Dispersive X-Ray Analysis
EHF	Effective Heat of Formation
fcc	Face centred cubic
Fe	Iron
FIB	Focused Ion Beam
FOD	Foreign Object Damage
H	Enthalpy
Hf	Hafnium
HVOF	High Velocity Oxy Fuel spraying
k	Parabolic Rate Constant
LMIS	Liquid Metal Ion Source
LPPS	Low Pressure Plasma Spraying
Mo	Molybdenum
Nb	Niobium
Ni	Nickel
O	Oxygen
ODS	Oxide Dispersion Strengthened
Pd	Palladium
PSZ	Partially Stabilised Zirconia
Pt	Platinum
PVD	Physical Vapour Deposition
RF	Radio Frequency
Rh	Rhodium
Ru	Ruthenium
SC	Single Crystal
SEM	Scanning Electron Microscope
Ta	Tantalum
TBC	Thermal Barrier Coating
TET	Turbine Entry Temperature
TGO	Thermally Grown Oxide
Ti	Titanium
Tm	Melting Temperature
VPS	Vacuum Plasma Spraying
W	Tungsten
XRD	X-Ray Diffraction
Y	Yttrium
YSZ	Yttria Stabilised Zirconia
Zn	Zinc

List of Figures

List of Tables

1.0 Introduction

Gas turbines are used in a wide variety of applications including aircraft propulsion, marine propulsion and electric power generation. The high temperature components of such engines experience very high stresses at elevated temperatures in severely corrosive gas environments and are required to retain their mechanical and surface properties for thousands of operating hours. Early in the developmental history of gas turbines, temperature levels were limited by the strength of superalloys which meant that loss of surface integrity was not a limiting problem.

The reduction of noise and emissions is becoming increasingly important in civil aircraft jet engines as well as requirements for reduced fuel consumption and improved efficiency. The use of cooling air has allowed higher gas operating temperatures which has had a powerful effect on the performance of the gas turbine engine. In order to improve efficiency further it is necessary to decrease the amount of air used for cooling. According to Meetham [(1)], an increase of 150°C in turbine entry temperature (TET), combined with the elimination of internal air cooling of turbine components, can result in an improvement of around 6% in aero-engine thermal efficiency.

Intensive materials development programmes have produced alloys with steadily increasing strength, allowing an increase in operating temperatures and greater fuel efficiency. This has resulted in decreased chromium contents, which has in turn led to a decrease in the corrosion and oxidation resistance of these alloys. In the middle 1960s, coatings were introduced in order to protect the surfaces from degradation.

The first applications of such coatings were in aircraft engines. This was followed in the early 1970s by increased use of coatings in ground-based and marine engines.[(2)] Simple metallic coatings were unable to keep up with the increases in operational temperatures and

since the 1980s, the use of thermal barrier coatings (TBCs) has become standard in order to meet the increasing TETs and to provide protection against surface attack.

A typical TBC system consists of a surface coating of 6-8 wt.% Y_2O_3 partially stabilised ZrO_2 (YSZ) for thermal insulation and a bond coat which not only provides oxidation and corrosion resistance but also bonds the surface coating to the underlying material. According to Srinivisan [3], a 300μm YSZ TBC will decrease the metal temperature by 167°C and they have primarily been used to increase component life. The coating system must be carefully selected in order to meet the increased TET and component life requirements. YSZ has adequate strain tolerance for current applications, but the continued drive for increased performance means that advanced turbine systems call for developments in bond coat optimisation, improved YSZ deposition and manufacturing processes and the use of alternative ceramics.

This thesis examines novel bond coat developments for thermal barrier coatings. Particularly, Rolls Royce have a patented process, whereby precious metal layers are diffused and directly react with single crystal substrate alloys to form an aluminium containing surface coating. The aluminium is sourced from the single crystal alloy and the coating formed has a $\gamma + \gamma'$ structure, but contains other intermetallic phases due to the reaction between the coating and the single crystal substrate.

This thesis aims to examine the stability of various phases formed in the above reaction process and to determine the most stable intermetallics for inclusion in future coating systems.

Literature Review

2.0 Turbine Materials

2.1 Introduction

The aircraft gas turbine engine consists of three main sections:

i) the compressor section,
ii) the combustion section,
iii) the turbine section.

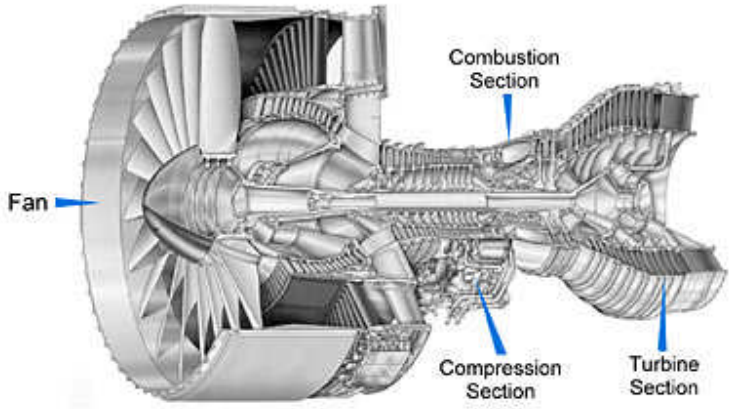

Figure 1 Cutaway Drawing of a Commercial Turbofan Engine[(4)]

The compressor draws in air and compresses it. The compressed air then enters the combustion section at a pressure of 30 to 35 atmospheres and a temperature of 550˚C to 625˚C. In the combustion section fuel is injected into the compressed air stream and ignited. Hot combustion gases are then forced into the turbine section which contains stator vanes and rotor blades. The combustion gases flow through the stationary stator vanes and turn the rotor blades and turbine which in turn rotates the compressor. The hot, high pressure gas then exits the engine through the propelling nozzle, providing the thrust.[(4)]

Additional thrust is provided by the fan, which is rotated by mechanical work generated by the turbine. In the latest high performance engines more thrust is provided by the fan than by the hot gas exiting the turbine. At high thrust, efficient gas turbine operation is achieved by a high compression ratio and high turbine entry temperature (TET). Despite the severe environmental conditions experienced by high-pressure turbine blades, TETs have more than doubled since the Whittle engine of the 1940s, and modern TETs can reach greater than 1500˚C.[5,6] Shi estimates that future turbine TETs may even be as high as 1760˚C (see Table 1).[7]

Service year	Compressor exit temperature (˚C)	Turbine entry temperature (˚C)
1955	379	771
1965	427	938
1975	593	1343
1995	693	1427
2008	>700	>1500
2015	766	1760

Table 1 Representative gas turbine temperatures as a function of time

The high-pressure turbine blade operates under the most aggressive conditions of temperature and stress of any component in the engine. The blade is not only exposed to high temperatures and direct stress, but also to rapid temperature transients at various points in the flight cycle. The hot gases surrounding the blade are highly oxidising, may contain contaminants which lead to hot corrosion, and can also contain erosive particles.[8]

Turbine blade components must have a property mix comprising of: improved corrosion resistance, creep strength and fatigue resistance.[6] This is the reason that more than 50% of

the weight of modern aircraft gas turbine engines comes from superalloys. Superalloys represent a class of metallic materials that display an excellent combination of long term strength at temperatures greater than 650°C and high resistance to corrosion and erosion.[9]

2.2 Superalloys

The term 'superalloy' was first introduced shortly after World War II in order to describe a group of alloys developed for high performance use at high temperatures, in applications such as turbosuperchargers and aircraft turbine engines.[10] According to Sims and Hagel [11], the term 'superalloy' is defined: ' Superalloys are alloys based on Group VIIIA base elements developed for elevated temperature service, which demonstrate combined mechanical strength and surface stability'.

Superalloys can be divided into three major classes, depending on the prime alloying element: Fe-base, Ni-base and Co-base alloys. The Ni-based superalloys are widely used within the high temperature stages of aircraft turbine engines and are utilised within the high-pressure compressor, the combustor, the turbine stages and the exhaust outlet. This is due to their unique ability to withstand high stresses and remain stable after long-term exposure to temperatures in excess of 85% of their melting temperature (T_m).[12]

2.2.1 Nickel-based Superalloys

Nickel-based superalloys are usually either solid solution strengthened or precipitation strengthened. Solid solution strengthened alloys (e.g. Hastelloy X) are used for applications requiring moderate strength. Precipitation strengthened alloys are used in the most demanding applications, such as hot sections of gas turbine engines. Precipitates strengthen the alloy by impeding the movement of dislocations and, therefore, deformation under load.

Most wrought Ni-based superalloys contain 10-20% chromium, up to 8% aluminium and titanium, 10-20% cobalt and small amounts of beryllium, zirconium and carbon and commonly added are molybdenum, tungsten, tantalum, hafnium and niobium. Later, cast alloys saw a reduction in chromium to include increased refractory metals. Most recently, single crystal alloys have seen the chromium level reduced even further, down to approximately 6wt%, and the addition of rhenium, ruthenium, iridium, tantalum and titanium. Some of the common solid solution strengthened and precipitation strengthened nickel-based alloys are listed in Table 2. Single crystal superalloy compositions are listed in Table 3 (p.12).

Alloy	Composition (%) Cr	Ni	Co	Mo	W	Nb	Ti	Al	Fe	C	Other
Ni-base solid-solution strengthened alloys											
Hastelloy C	16.5	56.0	-	17.0	4.5	-	-	-	6.0	0.15 max	-
Hastelloy X	22.0	49.0	1.5max	9.0	0.6	-	-	2.0	15.8	0.15	-
Inconel 600	15.5	76.0	-	-	-	-	-	-	8.0	0.08	0.25max Cu
Nimonic 75	19.5	75.0	-	-	-	-	0.4	0.15	2.5	0.12	0.25max Cu
Inconel 625	21.5	61.0	-	9.0	-	3.6	0.2	0.2	2.5	0.05	-
Ni-base precipitation-strengthening alloys											
Inconel 718	19.0	52.5	-	3.0	-	5.1	0.9	0.5	18.5	0.08 max	0.15max Cu
MAR-M 246	9.0	59.2	10.0	2.5	10.0	-	1.5	5.5	-	-	1.5 Ta, 0.01 B, 0.05 Zr
Nimonic 95	19.5	53.5	18.0	-	-	-	2.9	2.0	5.0 max	0.15 max	+B, +Zr
Nimonic 105	11.0	56.0	20.0	5.0	-	-	1.5	5.0	2.0 max	0.30 max	+B, +Zr
René 80	14.0	60.0	9.5	4.0	4.0	-	5.0	3.0	-	0.17	0.015 B, 0.03 Zr
René 100	9.5	61.0	15.0	3.0	-	-	4.2	5.5	1.0 max	0.16	0.015 B, 0.06 Zr, 1.0V
Udimet 630	17.0	50.0	-	3.0	3.0	6.5	1.0	0.7	18.0	0.04	0.004 B
Udimet 710	18.0	55.0	14.8	3.0	1.5	-	5.0	2.5	-	0.07	0.01 B
Waspaloy	19.5	57.0	13.5	4.3	-	-	3.0	1.4	2.0 max	0.07	0.006 B, 0.09 Zr

Table 2 Some superalloy compositions [10]

In broad terms, the elemental additions in Ni-base superalloys can be categorised as being:

i**) γ formers** -	Group V, VI and VII elements such as Co, Cr, Mo, W and Fe that tend to partition to the gamma matrix.
ii) **γ′ formers** -	Group III, IV, and V elements that tend to partition to the gamma prime precipitate. These include Al, Ti, Nb, Ta and Hf.
iii) **Carbide formers -**	The main carbide formers are Cr, Mo, W, Nb, Ta, Hf and Ti.
iv) **Grain boundary elements** -	Elements that segregate to the grain boundaries. The main grain boundary elements are B, C and Zr.

The continuous γ matrix is a face-centred-cubic (fcc) nickel-based austenitic phase that usually contains a high percentage of solid-solution elements such as Co, Cr, Mo, W, Hf, Ti and Re. The principal strengthening phase is the gamma prime (**γ′**) $Ni_3(Al,Ti)$ intermetallic compound. It is a coherently precipitating phase with an ordered fcc structure. The two phases have similar lattice parameters, which combined with their chemical compatibility, allows the γ′ to precipitate homogeneously throughout the γ matrix and have long-term stability. The strength of the alloy increases as the volume fraction of γ′ increases. The lowest volume fraction amounts (generally less than about 25 vol %) of γ′ are found in the first-generation nickel-based superalloys**.** The γ′ is often spheroidal in lower volume fraction alloys, but often cuboidal in higher volume fraction (≥ 35 vol %) nickel-base superalloys. In some alloys, niobium is used along with lesser amounts of aluminium and titanium, to form the metastable intermetallic Ni_3Nb phase. This phase has a body-centred tetragonal structure and is sometimes known as gamma double prime (γ′′).[13] The latest second and third generation single crystal alloys contain about 3 wt% and 6 wt% of rhenium respectively.

Carbides are also an important constituent of wrought and polycrystalline cast superalloys. When carbon is added at levels of 0.05 - 0.2%, it combines with reactive and refractory elements such as titanium, tantalum, niobium and hafnium to form the carbides TiC, TaC, NbC or HfC. During heat treatment and service these form lower carbides such as $M_{23}C_6$ and M_6C (where M designates 1 or more type of metal atom) on the grain boundaries, strengthening these boundaries. These common carbides all have fcc crystal structures. The addition of grain boundary elements such as boron, zirconium and hafnium can, within limits, achieve significant improvements in mechanical properties for these wrought alloys. The presence of these elements may modify the initial grain boundary carbides or tie-up deleterious elements such as lead and sulphur.

Figure 2 shows some of the microstructures that can be found in nickel-base superalloys.

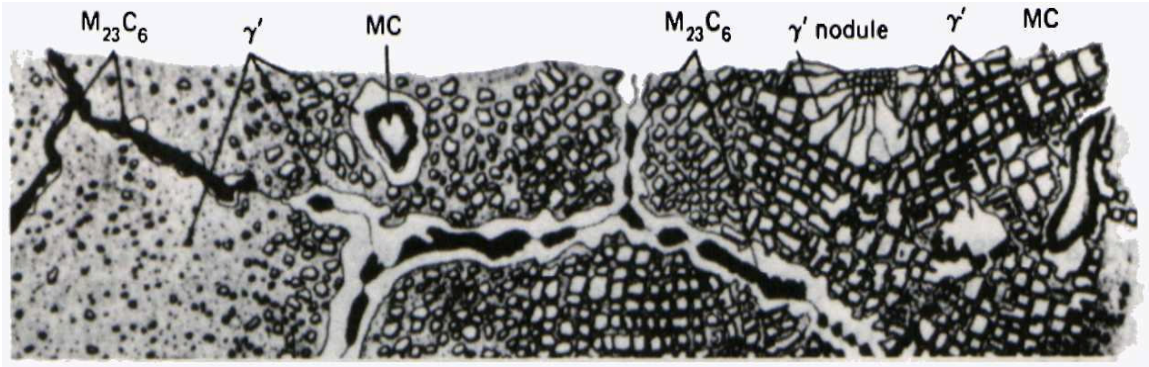

Figure 2 Schematic microstructure of nickel superalloys [9]

The elemental additions that may be present in nickel superalloys are summarised in Figure 3. The height of the major alloying element blocks gives an indication of the amount that may be present and their main functions are also indicated.[14] Trace elements can have a large influence on properties and behaviour. Beneficial trace elements are indicated by cross-hatching, while detrimental trace elements are horizontally shaded.

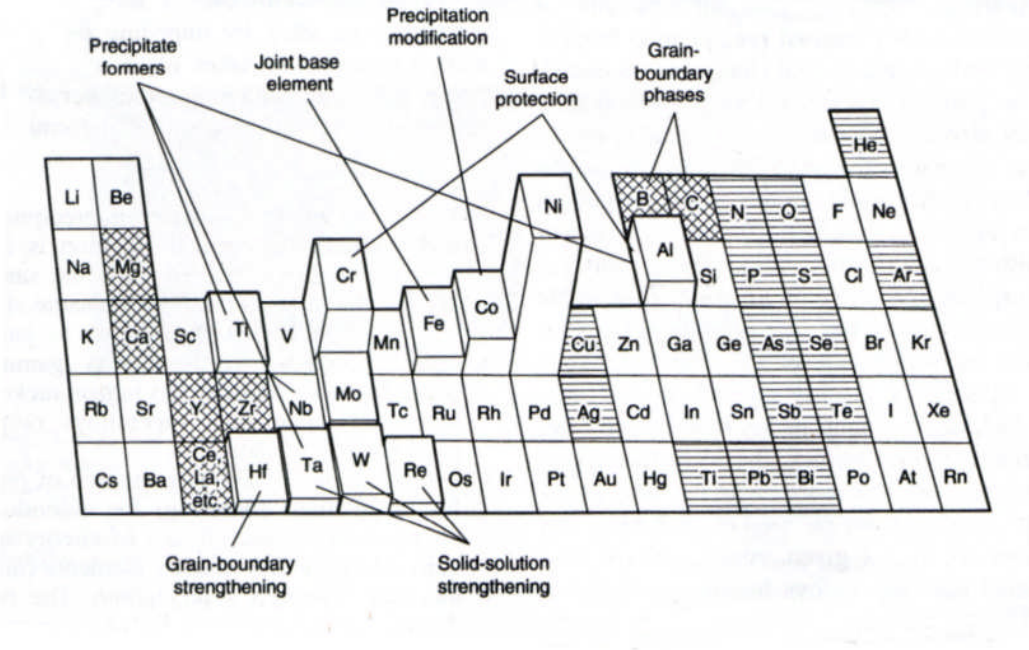

Figure 3 Summary of elemental additions in nickel superalloys[14]

2.3 Superalloy Processing and the Development of Cast and Single Crystal Superalloys

First, there were wrought superalloys and turbine blades in the 1940s, these were die-forged. They were limited in alloying additions, in order to increase the creep strength. Alloy contents greater than those of Nimonic 115 resulted in serious forging problems. This means that wrought alloys have moderate elevated temperature strength and are only used for temperatures up to ~ 650°C.[9]

Cast alloys were developed with higher elevated temperature strength due to increased aluminium and titanium content raising the γ' volume fraction and reduced chromium or increased cobalt contents raising the solvus temperature. The reactivity of Al and Ti caused

problems in air melting and casting and in the late 1950s the development of vacuum melting and casting techniques made the manufacture of blades by casting possible in the strongest superalloys.

In the 1960s internal cooling was introduced and since then air-cooling has played a large part in allowing increased turbine operating temperatures.

In the mid 1960s oxide dispersion strengthened (ODS) alloys were introduced. The first commercially available ODS alloy was TD Nickel (nickel with 2% thoria oxide). This had poor oxidation resistance, which was remedied by the addition of 20% Cr to produce TD Nichrome. These TD materials were produced by selective hydrogen reduction processes. Mixing of thoria sols with nickel-containing solutions ensured good dispersion and the subsequent reduction of the metallic oxides after drying produced fine composite Ni-ThO_2 powder which was compacted and extruded and rolled to develop strength. It was impossible to process the γ' forming Al and Ti in this way, as their oxides are not reduced by hydrogen. Mechanical alloying was developed to provide this capability. [10, 15]

Mechanical alloying is a dry, high-energy ball milling process. Particles of elemental or pre-alloyed powder are continually welded together and broken up until a homogeneous mixture of constituent powder particles and dispersoid is produced. ODS superalloys usually contain 1% of uniformly dispersed oxide particles such yttrium oxide (Y_2O_3). The dispersion-strengthened powders can be consolidated by extrusion or by hot isostatic pressing followed by mechanical processing to produce the final product. Since the process allows elements such as Ti and Al to be included in the base composition, the alloy can be strengthened by γ' hardening at intermediate temperatures and dispersion hardening at high temperatures.[16, 17]

The first cast turbine blades were produced as equiaxed castings with relatively fine grains, but during the 1960s, directionally solidified (DS) castings were introduced by Pratt and

Whitney. In DS processing columnar grains are formed parallel to the growth axis. Liquid metal is poured into a mould containing a water-cooled bottom plate. The metal starts to solidify at the bottom of the mould, after which the mould is slowly withdrawn from the furnace, allowing the metal inside to directionally solidify from the bottom to the top. Since creep failures in conventionally cast blades initiate at grain boundaries that are normal to the major direct stress, aligning the grains from blade root to tip eliminates transverse grain boundaries, which in turn increases the creep life of the blade, raises the rupture strength capability and improves the thermal fatigue resistance.

In the 1970s, DS technology was extended by an elegant but relatively simple process, and alloy composition was modified, to produce single crystal (SC) castings. The major process modification is the introduction of either a geometric constriction device, which eliminates all but one of the grains or a seed crystal, which nucleates one grain of a similar crystal orientation to the seed. The elimination of all grain boundaries in SC castings means that grain boundary strengthening elements such as C, B, Zr and Hf could be eliminated, which results in a reduction of elements that depress the melting point of the material. The higher melting point allows the solution heat treatment temperature to be increased, leading to a more even distribution of the γ' precipitate and, therefore, increasing alloy strength and maximum operating temperature. In some modern alloys the volume fraction of the γ' precipitate is around 70%. [13, 15, 18]

Table 3 shows the composition of some ODS, DS and SC nickel superalloys.

Alloy	Composition (%) Ni	Cr	Co	Mo	W	Nb	Ti	Al	C	Other
Oxide dispersion strengthened Ni-base superalloys										
MA 754	Bal	20	-	-	-	-	0.5	0.3	0.05	0.6 Y_2O_3
MA 6000	Bal	15	-	2	4	-	2.5	4.5	0.05	0.15 Zr, 2 Ta, 0.01 B, 1.1 Y_2O_3
Directionally solidified Ni-base superalloys										
MAR-M 002	Bal	8	10	-	10	-	1.5	5.5	0.15	0.03 Zr, 2.6 Ta, 1.5 Hf, 0.02 B
MAR-M 200	Bal	9	10	-	12.5	1	2	5	-	0.05 Zr, 2 Hf, 0.01 B
MAR-M 246	Bal	9	10	2.5	10	-	1.5	5.5	-	0.05 Zr, 1.5 Ta, 0.01 B
MAR-M 247	Bal	8.3	10	0.7	10	-	1.0	5.5	0.15	0.05 Zr, 3.0 Ta, 1.5 Hf, 0.02 B
First generation single crystal Ni-base superalloys										
René N4	Bal	9	8	2	6	0.5	4.2	3.7	-	4.0 Ta
SRR 99	Bal	8.5	5	-	9.5	-	2.2	5.5	-	2.8 Ta
CMSX-2	Bal	8	4.6	0.6	7.9	-	0.9	5.6	-	5.8 Ta
CMSX-3	Bal	8	4.6	0.6	8	-	1	5.6	-	6.0 Ta, 0.1 Hf
CMSX-6	Bal	10	5	3	-	-	4.7	4.8	-	2.0 Ta, 0.1 Hf
Second generation single crystal Ni-base superalloys										
René N5	Bal	7	8	2	5	-	-		-	7.0 Ta, 0.2 Hf, 3.0 Re
CMSX-4	Bal	6.5	9	0.6	6	-	1	5.6	-	6.5 Ta, 0.1 Hf, 3.0 Re
PWA1484	Bal	5	10	2	6	-	-	5.6	-	9.0 Ta, 0.1 Hf, 3.0 Re
Third generation single crystal Ni-base superalloys										
René N6	Bal	4.2	12.5	1.4	6	-	-	5.75	0.05	7.2 Ta, 0.15 Hf, 5.4 Re, 0.004 B, 0.01 Y
CMSX-10	Bal	2	3	0.4	5	0.1	0.2	5.7	-	8.0 Ta, 0.03 Hf, 6.0 Re
TMS-75	Bal	3	12	2	6	-	-	6	-	6.0 Ta, 0.1 Hf, 5.0 Re
TMS-80	Bal	2.9	11.6	1.9	5.8	-	-	5.8	-	5.8 Ta, 0.1 Hf, 4.9 Re, 3.0 Ir

Table 3 Chemical composition of Ni-base superalloys [9, 19, 20, 21]

2.4 Surface Degradation and the Need for Coatings

During operational use, turbine blades are exposed to high non-uniform temperatures, thermal cycling and a high velocity gas stream that may be oxidising, corrosive, erosive or even locally reducing. An optimum balance of mechanical properties and microstructural stability is achieved by reducing the chromium content of the base material at the expense of oxidation and corrosion resistance. It has been well recognised since 1978, that the life-limiting factor of hot component parts is surface degradation.[22, 23]

The two main environmental effects that are of concern in the case of aircraft turbine blades are;

i) Oxidation
ii) Hot Corrosion

These are briefly described here and are discussed further in later chapters.

2.4.1 Oxidation

Superalloys generally react with oxygen, which is the primary environmental factor affecting service life. At temperatures up to 870°C, general uniform oxidation is not considered to be a problem. With increasing temperatures, however, commercial nickel superalloys are attacked by oxygen at progressively higher rates.

Oxidation resistance is a function of the superalloy chromium and aluminium content, although at temperatures of less than 980°C it is dominated by the chromium content, since Cr_2O_3 forms the predominant protective scale. At temperatures greater than 980°C, aluminium content becomes a more important factor in oxidation resistance, since Al_2O_3 forms the predominant protective scale. Cr and Al can interact in order to provide

protection against oxidation, since the higher the Cr content, the less Al is needed to form an Al_2O_3 layer and this interaction will be discussed in a later chapter. However, the Al and Cr content of many superalloys, especially the latest single crystal alloys, is not sufficient to provide long-term protection and thus the use of protective coatings is necessary to provide a satisfactory service life. [10, 24]

2.4.2 Hot Corrosion

At moderate temperatures (<870°C), the influence of selective fluxing agents may accelerate oxidation in superalloys. One of the best known of these accelerated oxidation processes is hot corrosion, which is sometimes known as sulphidation. [10] There are two types of hot corrosion, low temperature (600-850°C) and high temperature (750-950°C). [25] Hot corrosion can be triggered by sulphur in fuel or impurities, such as salt, in the environment. The main method for minimising attack due to hot corrosion is a high Cr content (≥ 20 wt.%) in the base alloy, but this is incompatible with high temperature strength and microstructural stability. Therefore, again coatings are used to prevent surface degradation of superalloys for elevated temperature use. [10, 24]

Coating requirements to resist high temperature oxidation and hot corrosion are discussed in a later chapter.

3.0 Coating Systems

3.1 Introduction

Aircraft gas turbines are exposed to a wide range of thermal and mechanical loading during their service lifetime, in addition to a highly oxidising atmosphere which may contain contaminants such as chlorides, sulphates or erosive particles.

Since the increase in mechanical properties of turbine materials has been achieved at the expense of corrosion resistance, it is now generally accepted practice to coat high temperature components in order to protect them from the service environment. The two main reasons for the application of surface coatings are: (i) to maintain the surface finish; and (ii) to ensure that the component achieves its design lifetime.

The bulk material of turbine blades is developed to achieve maximum high temperature strength whilst the surface coating provides maximum protection from the service environment. The properties required by a surface coating system for turbine blade applications are listed in Table 4.[26, 27]

Property	Requirements
Corrosion and oxidation resistance	- Initial rapid formation of a continuous thin uniform, adherent protective oxide film. - Slow subsequent rate of scale growth. - Highly stable and adherent scale. - Acceptable oxidation/corrosion rate.
Erosion resistance	- Ductile and adherent oxide scale. - Moderate coating ductility.
Coating and alloy interfacial stability	- Low rates of diffusion across interface. - Minimum compositional changes, particularly with reference to brittle phase formation.
Coating adhesion	- Similar/matched coating and substrate properties. - Clean substrate-coating interface.
Mechanical properties	- Ability to withstand all strain-temp. cycles encountered by the component during service. - Appropriate coating ductility. - Minimum effects on substrate properties.
Aerodynamic properties	- Best possible surface finish. - Acceptable thickness and uniformity on aerofoil. - Minimum loss of surface smoothness during service.
Coating process	- Ability to coat complex shapes. - Optimised for composition, structure, thickness, thickness distribution and uniformity. - Cost effectiveness.

Table 4 Property requirements of coating systems for gas turbine blade applications [26, 27]

The coating systems currently in use in gas turbine blade applications can be divided into three generic groups[25, 26, 27]:

1) Diffusion coatings. Coatings formed by diffusing one or more elements into the surface of the metal to be protected. Application processes include pack cementation and gas-phase processes such as chemical vapour deposition.

2) Overlay coatings. Coatings of specific composition applied as an 'add-on' to the surface to be protected by plasma spray or physical vapour deposition. Typical overlay coatings are of the MCrAlY type, where M is usually nickel or cobalt.

3) Thermal Barrier Coatings. Insulating ceramic coatings typically applied over a metallic bond coat. Applied by plasma spray or physical vapour deposition processes.

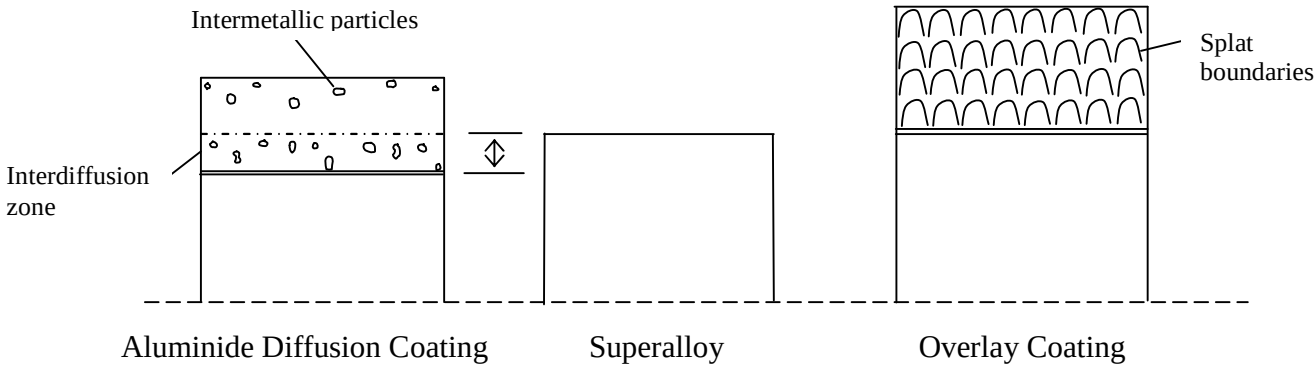

Figure 4 Sketch of diffusion and overlay coatings (adapted from ref. 31)

3.2 Diffusion coatings

Diffusion coatings can be applied to components using a variety of techniques based on chemical vapour deposition (CVD). The techniques include pack cementation, slurry cementation and various forms of gas phase coating.[32] They involve the surface enrichment of an alloy with aluminium, silicon or chromium to form aluminised, siliconised or chromised surfaces.[28]

The most widely used diffusion coatings, since their introduction in the mid-1950s, have been the aluminide coatings (nickel aluminide, cobalt aluminide and platinum aluminide). They are still used extensively for protecting turbine blades for aero, marine and industrial applications.[33]

3.2.1 Diffusion Aluminide Coatings

In 1952, the first aluminising of nickel-based turbine blades was carried out at Allison and Curtiss Wright using a hot-dip process. In 1963, Pratt and Whitney then introduced a slurry-fusion process for aluminising nickel-base blades. In the slurry process, the part is sprayed with a suspension of aluminium or aluminium alloy and is subjected to a high temperature treatment to produce melting and interdiffusion of the substrate and the deposit.[10, 30]

Since about 1970 most blade coatings have been carried out using pack cementation but nowadays vapour phase aluminising has become more prominent. The superalloy components to be coated are cleaned and masked and placed in a retort or reaction chamber. They are then immersed in a pack containing aluminium or pre-alloyed powder known as the donor alloy, a halide energiser (NH_4Cl) for example, that transports the aluminium from the pack to the component to be coated and an inert oxide diluent such as alumina (Al_2O_3) to prevent the pack sintering. The retort is heated to the required process

temperature under an inert gas or hydrogen atmosphere to prevent oxidation from occurring. [10, 34, 35, 36]

Diffusion aluminide coatings are classified as either 'inward' or outward' types. An inward coating (also known as the 'high activity' process) is produced at temperatures between 760°C and 980°C, when the aluminium activity is high with respect to nickel. The aluminium then diffuses inward faster than the nickel can diffuse outward through the Ni_2Al_3 layer that initially forms at the surface. A subsequent heat treatment then leads to the formation of NiAl. An outward coating ('low activity' process) is produced at temperatures above 1000°C, when the aluminium activity is low with respect to nickel. The NiAl phase is directly produced by an outward diffusion of nickel from the substrate. [31, 37]

Conventional base metal aluminide coatings offer limited protection at temperatures greater than 1100°C or under severe hot corrosion conditions. Therefore, modified aluminide coatings were developed in the early 1970s for improved hot corrosion and oxidation resistance.

3.2.2 Modified Aluminide Coatings

Several techniques have been developed for improving aluminide coatings by changing their compositions [31]:

1) co-deposition of elements from the pack
2) pre-treatment of the superalloy (e.g. chromising) prior to aluminising
3) deposition of a metallic layer (e.g. platinum) prior to aluminising

One of the most significant modified aluminide coatings has been platinum aluminide. The platinum is electroplated as a thin layer (up to 10μm), followed by an aluminising treatment during which the platinum and aluminium interdiffuse with the substrate and each other. [24, 36] Precious metals also used in modified aluminide coatings include palladium and rhodium. Other alloying additions include chromium, silicon, tantalum, hafnium, zirconium and the rare earth elements such as yttrium. [28]

3.3 Overlay Coatings

The main limitation of the diffusion type coatings is that they are tied to the substrate composition. This can lead to the inclusion of substrate elements, which are detrimental to hot corrosion and oxidation resistance, in the coating. They are also limited to thicknesses from a few microns to 1.5mm. [38] Overlay coatings are 'add-on' layers that are applied to the substrate surface and do not rely on reaction with the substrate for their formation, although a small amount of interdiffusion usually occurs during service. They were introduced in the mid-1970s to allow greater flexibility in the design of coating compositions tailored to a wide variety of applications. Typified by the M-Cr-Al-Y series, where M is nickel, cobalt, iron or a combination of these, a wide range of oxidation and hot corrosion properties can be balanced with good ductility of the coating. [24, 27]

Recent coatings are based on the more complex M-Cr-Al-X system, where M is Ni, Co, or Fe, as before, and X is an active element such as yttrium, silicon, tantalum or hafnium. The active element improves the adherence of the oxide scale and can reduce oxidation rates, while the M, Cr and Al system gives a good balance between corrosion resistance and coating ductility and improves resistance to thermal fatigue cracking.

Overlay coatings can be applied by a range of methods, including:

- Plasma spraying
- High velocity oxy fuel (HVOF) spraying
- Electron beam physical vapour deposition (EB-PVD)
- Sputtering

The first three of these methods are routinely used for overlay coatings. EB-PVD was the earliest production method and involved the melting and evaporating of a coating material source bar with a focused electron beam in an evacuated chamber. [39] However, the high costs involved in setting up an EB PVD plant led to the plasma spraying of a pre-alloyed powder becoming an accepted method of production. Sputtered overlay coatings of good quality can be achieved and are widely used in coating development programmes, but this method is not yet used on a commercial scale. [10, 27, 39]

3.3.1 Plasma Spraying

Plasma sprayed overlay coatings are applied by injecting a pre-alloyed powder into a plasma jet and transferring the molten droplets to the unheated surface of the substrate, where they impact and solidify. Plasma spraying has the advantage of being able to deposit metals, ceramics or a combination of both, to produce homogeneous coatings with fine, equiaxed grains. This method can be carried out in an ambient atmosphere (APS), but better quality coatings are produced using argon shrouded plasma spraying or an inert gas shroud at reduced pressure. This is known as low-pressure plasma spraying (LPPS) or vacuum plasma spraying (VPS), depending on the absolute base pressure achieved.

High rates of deposition can be achieved with plasma spraying but it is limited to line-of-sight applications. Only surfaces directly exposed to the flow of material from the plasma torch can be coated with acceptable uniformity. This leads to the use of complex robotic manipulations in order for complete coverage to be achieved. Torches have also been designed to spray large internal cavities such as combustor cans. [10, 27, 39]

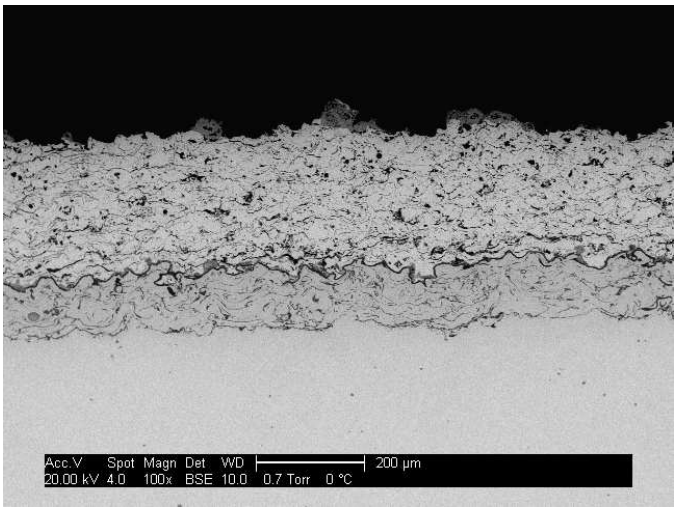

Figure 5 Micrograph of an air plasma sprayed thermal barrier coating system consisting of an APS MCrAlY bond coat with an APS YSZ top coat (courtesy of Peter Smith)

3.3.2 High Velocity Oxy Fuel Spraying (HVOF)

HVOF spraying uses higher pressures and flow rates than conventional flame spraying and can be used to deposit low porosity metal, ceramic and polymer coatings up to 2mm thick. In the HVOF process, powder is introduced into a chamber in which a gas flame, fuelled by gases, such as propylene, hydrogen or acetylene, or liquids, such as kerosene, is constantly burning under high pressure. The exhaust gas exits through an expansion nozzle which produces a high velocity gas stream. The powder particles are heated in this gas stream and

transferred to the surface of the component, forming a dense coating (compared to plasma and arc spraying) with high bond strength.[40, 41]

3.3.3 Electron Beam Physical Vapour Deposition (EB PVD)

Commercial EB PVD coatings are produced in a vacuum environment. Components are cleaned and introduced into the chamber where they are pre-heated to between 800 and 1100°C. An electron beam (100-200kW) evaporates the target material to form a vapour cloud and the components are rotated in the evaporant cloud. During deposition the substrate is held at temperature by a combination of melt pool radiation and an oversource heater. The use of pre-heat and substrate heating during deposition leads to an adherent coating.

EB PVD is a line-of-sight process and so component rotation is used in order to achieve uniform surface coverage. This results in an as-deposited columnar grain structure with unbounded interfaces known as 'leader defects'. Shot peening, using glass beads, followed by heat treatment results in the complete closure of these leaders and also removes chemical masking materials and coating overspray. [26, 42]

In 1969, Movchan and Demchishin developed a structure zone model to describe the microstructure of thermally evaporated coatings (Figure 6a). [43] This diagram shows schematically how the substrate temperature, T, relative to the melting temperature, Tm, of the coating affects the coating morphology. Thornton adapted this diagram for magnetron sputtered coatings and added in a third axis describing the sputtering gas pressure (Figure 6b). [44]

In zone 1, the coatings develop at low substrate temperatures and are porous with a tapered, columnar structure. At intermediate temperatures, zone 2, increased surface diffusion

results in columnar grains with dense grain boundaries. At higher temperatures, zone 3, bulk diffusion becomes important and the film consists of equiaxed grains with a diameter that increases with substrate temperature. In addition to these three zones, Thornton identified a transition zone, zone T, between zones 1 and 2 consisting of dense, poorly defined fibrous grains. [45, 46]

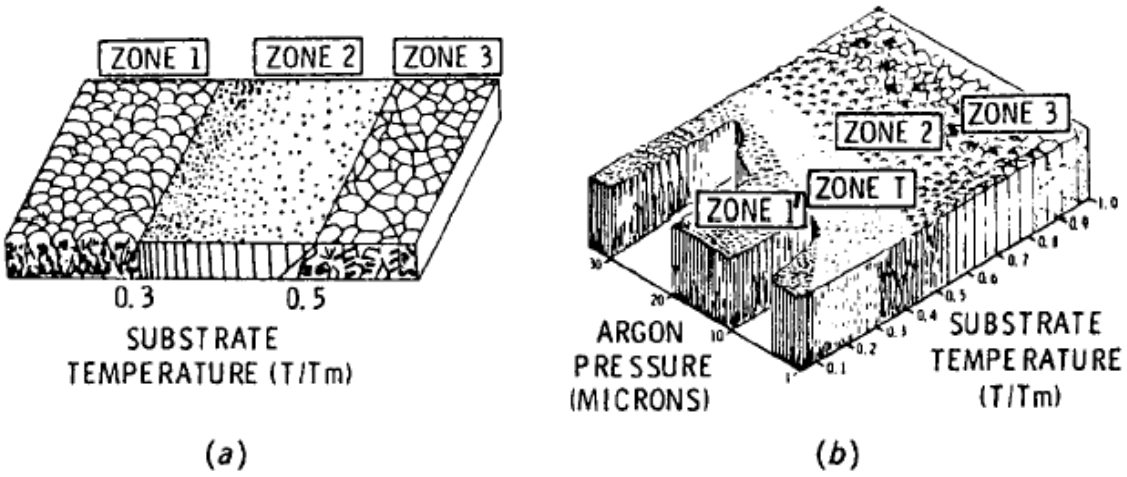

Figure 6 Structural zone models for coating growth proposed by a) Movchan and Demchishin[43]; b) Thornton[44]

3.4 Thermal Barrier Coatings (TBCs)

Thermal barrier coatings (TBCs) are duplex coating systems comprising of an oxidation resistant metallic inner layer or 'bond coat' and an insulating ceramic outer layer or 'top coat'.

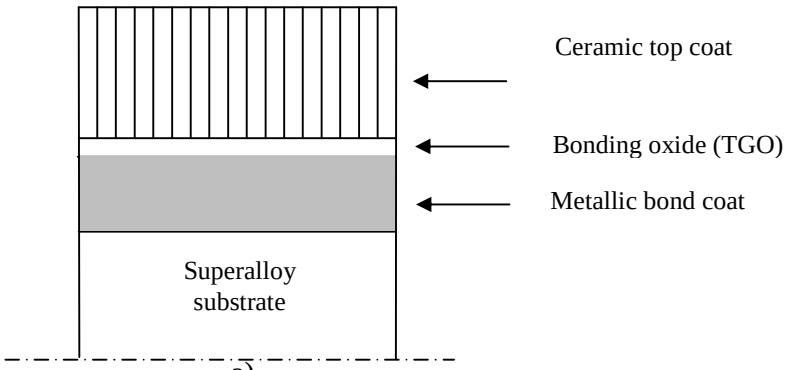

a)

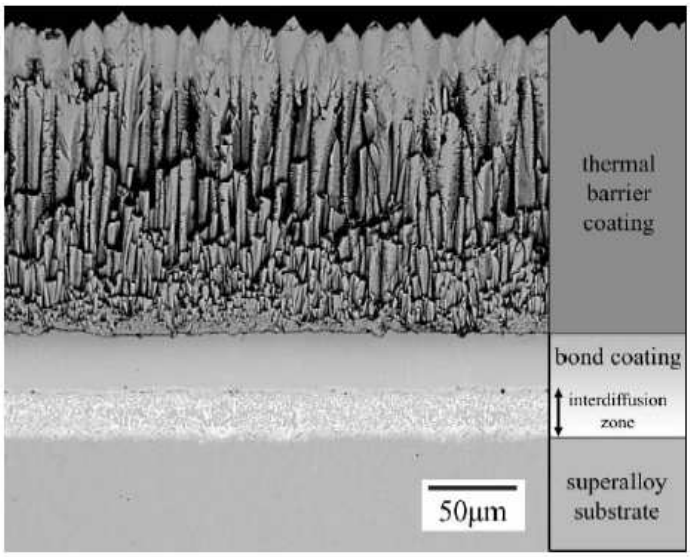

b)

Figure 7 a) Schematic of TBC; b) BSE image of a conventional EB-PVD TBC structure[47]

The function of the top coat is to form a thermal barrier to insulate the cooled substrate from the high temperature gas stream. A temperature gradient of 170°C can be produced through a 300μm thick YSZ TBC.[3] The top coat, whilst being an excellent barrier to heat, is often porous and does not protect the surface of the substrate from oxidation or high temperature corrosion, apart from the fact that it may provide protection from corrosion by limiting salt deposition. The metallic bond coat layer is used to bond the ceramic top coat to the substrate as well as providing oxidation and corrosion resistance. The oxidation resistance of these bond coat systems is based on their ability to form a protective external oxide scale, primarily consisting of α-Al_2O_3, known as a thermally grown oxide (TGO). The Al_2O_3 scale forms along the bond coat/top coat interface and appears to form a chemical bond between the ceramic top coat and the metallic bond coat. The thermo-mechanical stability of the interfacial Al_2O_3 scale is most often the life-limiting factor of current EB-PVD TBC systems.[48]

As well as the obvious requirements of refractory properties and low thermal conductivity, TBCs must have strain tolerance, i.e. high resistance to spalling under thermal cycling. Strain tolerance is not a property of the ceramic thermal barrier alone but of the complete system, since the stresses that drive spalling are mainly the result of the mismatch in coefficient of thermal expansion between the substrate, the top coat and the TGO.[49]

Typical TBC systems consist of a nickel-base superalloy substrate, coated with a M-Cr-Al-Y or diffusion aluminide (NiAl, NiPtAl) bond coat, upon which an alumina TGO layer has formed during the deposition of an yttria-stabilised zirconia (YSZ) TBC. $\gamma + \gamma'$ based diffusion coatings may also be used as bond coats. The TBC can be deposited by air plasma spraying (APS) or EB-PVD. The EB-PVD coatings are used for the most demanding applications in aero-engines, such as leading edges of airfoils.[50]

3.4.1 TBC Top Coat

Two ceramic top coats are widely used; EB-PVD and air plasma spray (APS). The microstructure of the EB PVD ceramic top coat is fundamentally different from that of the plasma sprayed ceramic. Plasma spraying results in the deposition of platelet-shaped particles surrounded by microcracks and with a porosity of 10-20%. The bonding mechanism of these coatings is mainly mechanical and the laminar structure contains disc-like voids that occur between the splats, parallel to the plane of the coating, which promote superior insulating efficiency and enhanced durability, over a more dense microstructure.[51, 52]

The EB PVD-deposited ceramic top coat has a columnar structure. The segmented nature of the individual columns prevents the build-up of any tensile stresses and matches the coefficient of thermal expansion (CTE) differences between the ceramic outer layer and the base material.[53] Industrial turbine manufacturers have reported longer lives for APS systems,[54] but in severe thermal gradients EB PVD coatings have a longer life, especially for parts in the high-pressure stage of the turbine where the stresses due to thermal shock are the highest[55]. Besides having a higher cycle life, EB PVD TBCs also have other features that make them more desirable for high pressure turbine use in aero-gas turbines compared to plasma sprayed TBCs. The surface finish is smoother, the bonding method is chemical rather than mechanical resulting in better adhesive strength and the columnar structure offers better resistance to erosion failure. However, plasma sprayed TBCs do have some advantage over EB PVD TBCs, lower thermal conductivity, greater flexibility allowing larger components to be coated and lower costs.[53]

Zirconia (ZrO_2) based coatings are most commonly used for the ceramic top coat because of their low thermal conductivities and their relatively high CTEs (for a ceramic), which reduce the detrimental interfacial stresses between the top coat and bond coat. ZrO_2 is polymorphic and the resulting volume changes from monoclinic to tetragonal (1100°C) and tetragonal to cubic (2370°C) phase transformations preclude its use as a TBC. The high

temperature cubic phase can be stabilised by the addition of sufficient amounts of yttria (Y_2O_3), magnesia (MgO), calcium oxide (CaO) and cerium oxide (CeO_2). At lower concentrations, partial stabilisation occurs and all three phases can be retained on cooling. The resulting ceramic is known as partially stabilised zirconia (PSZ) and is a superior TBC compared with a fully stabilised zirconia coating, with better thermal shock resistance and a lower CTE. Zirconia partially stabilised with yttria (8 wt.%) is used as the TBC material of choice because of its superior mechanical stability under thermal cycling conditions.[51]

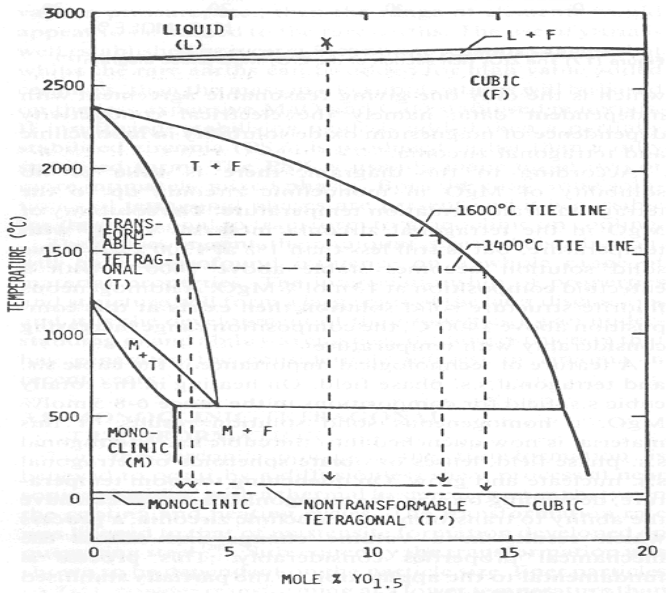

Figure 8 Zirconia-yttria phase diagram[56]

3.4.2 TBC Bond Coat

The bond coat is an important part of the TBC system, not only must it protect the substrate from oxidation and corrosion, but must also provide sufficient bonding to ensure that the ceramic top coat adheres to the substrate. Today, most bond coats are based either on M-Cr-Al-Y type overlay coatings or on diffusion aluminides or platinum-modified aluminides (NiAl, NiPtAl). Rolls-Royce has proposed alternative systems using a platinum diffused

γ+γ′ bond coat.[57, 58, 59] The oxidation resistance of these intermetallic bond coats is based on their ability to form and maintain a protective, external alumina scale (TGO) at the bond coat-top coat interface. This TGO is usually a few microns thick and acts as a 'glue' which bonds the ceramic layer to the metal substrate. Formation and growth of the alumina scale is considered to be a major life limiting factor in TBC performance [48, 60] and will be reviewed in more detail later in the chapter on oxidation.

Early M-Cr-Al-Y bond coats were air plasma sprayed onto the substrate. However, LPPS, VPS or HVOF are used where possible to prevent bond coat oxidation. With the development of EB PVD TBCs, there has been a return to applying M-Cr-Al-Y bond coats using EB PVD.

The Al_2O_3 layer can be produced on the bond coat surface by different methods, but surface oxidation of aluminium from the bond coat alloy or intermetallic in a vacuum chamber prior to ceramic layer deposition, at the residual gas pressure of up to 10 torr, is most commonly used.[61]

3.4.3 Intermetallics

Intermetallics are compounds that are not mixtures and whose crystal structures are different from those of the constituent metals. Intermetallics form because the strength of bonding between the respective unlike atoms is larger than that between like atoms.[62] Intermetallics form particular crystal structures with ordered atom distributions where atoms are preferentially surrounded by unlike atoms (Figure 9).

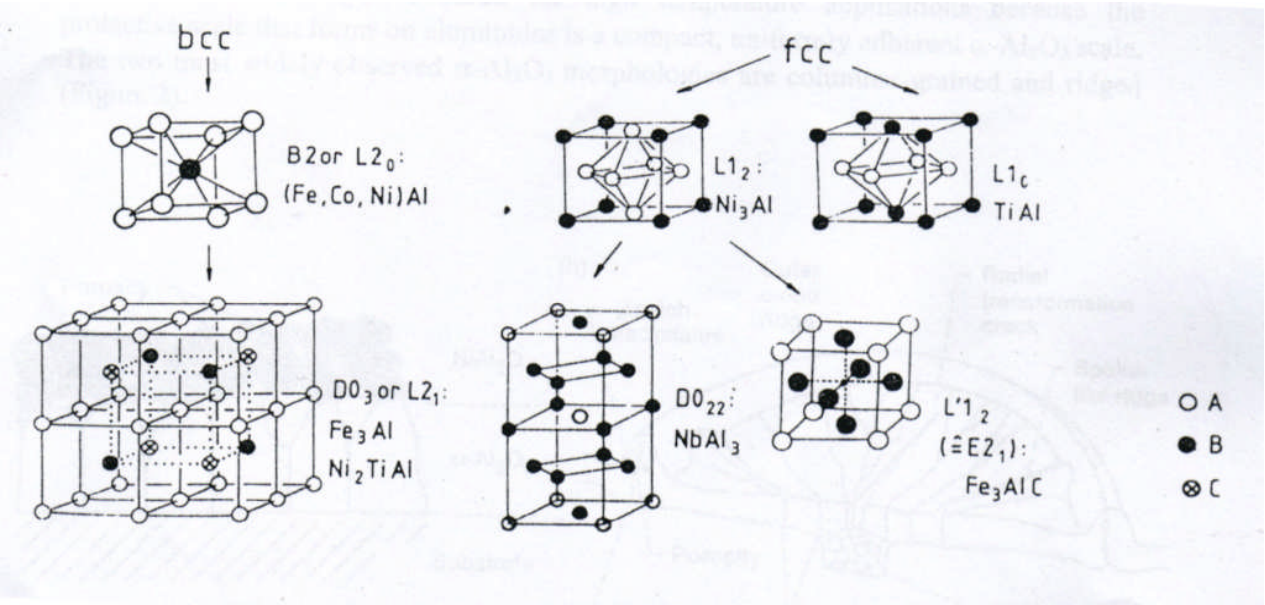

Figure 9 Some simple intermetallic structures [62]

The crystal structure of an intermetallic compound is determined by the strength and character of bonding in the crystal, which depends on the particular electronic configuration and the relative atomic sizes.

Intermetallics for any application should be corrosion resistant and for high temperature use this means oxidation resistance. Intermetallic compounds are generally perceived to be a class of materials that offer very stable microstructures owing to a generally large exothermic heat of formation, which is reflected in their relatively high melting temperatures. [63]

3.4.3.1 Aluminides [64]

A protective oxide scale consisting of a continuous external oxide layer on an intermetallic substrate has the following requirements:

- High thermodynamic stability
- Slow growth rate
- Adherence to the intermetallic substrate
- Easily formed and re-formed (in case of mechanical damage or oxide scale spallation).

Aluminides are strongly favoured for high temperature applications because the protective scale that forms on aluminides is a compact, uniformly adherent α-Al_2O_3 scale. The two most widely observed α-Al_2O_3 morphologies are columnar-grained and ridged (Figure 10).

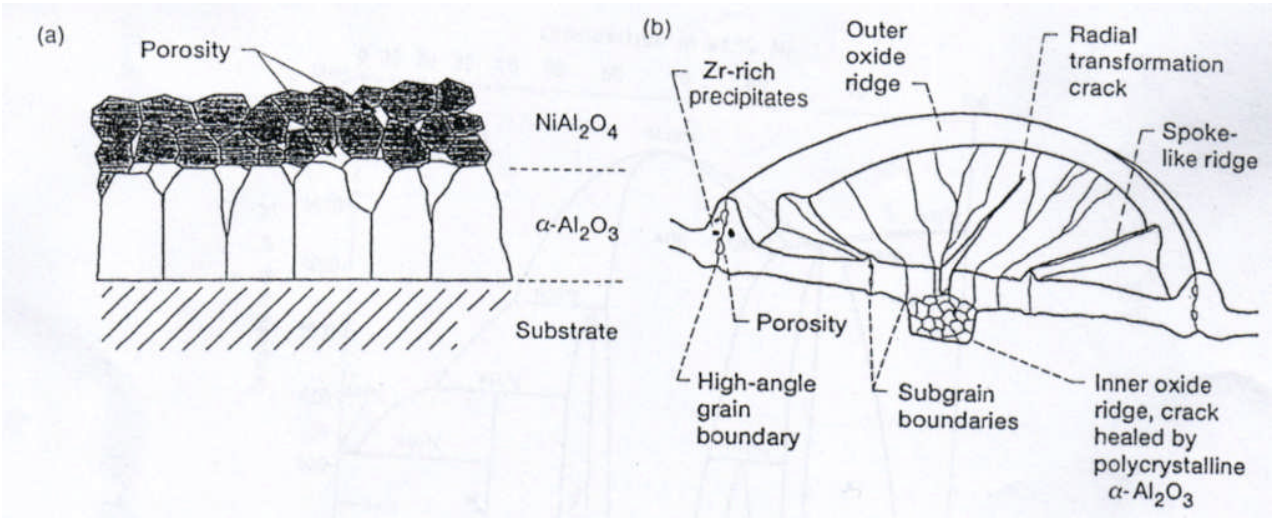

Figure 10 Protective oxide scale morphologies that form on aluminide intermetallics[64]:
a) columnar morphology; b) ridged morphology

The columnar-grained morphology consists of large, randomly oriented α-Al_2O_3 grains, and forms as a result of nucleation of α-Al_2O_3 beneath a transient oxide scale. The ridged morphology consists of flat α-Al_2O_3 radial subgrains, often arranged in a pie-shaped fashion with ridges forming at high-angle grain boundaries where the pie-shaped grains intersect.

The two high temperature intermetallics of interest in the Ni-Al system are NiAl and Ni_3Al.

3.4.3.2 NiAl [65]

NiAl has been studied extensively for over three decades. The attractive characteristics of NiAl include a high melting temperature, low density, metal-like properties above a modest ductile-to-brittle transition temperature (DBTT) and low raw materials cost. It can be processed relatively easily by conventional melting, powder and metal-forming techniques.

NiAl is the best known of the intermetallics with a cubic B2 structure (Figure 9). As can be seen from the phase diagram in Figure 11, the stability range of NiAl varies with temperature but has a minimum Ni content of 41.5 at.% (at ~1100°C) and a maximum Ni content of 65 at.% (at ~1380°C) and melts at about 1640°C for the stoichiometric composition with 50 at.% Al.

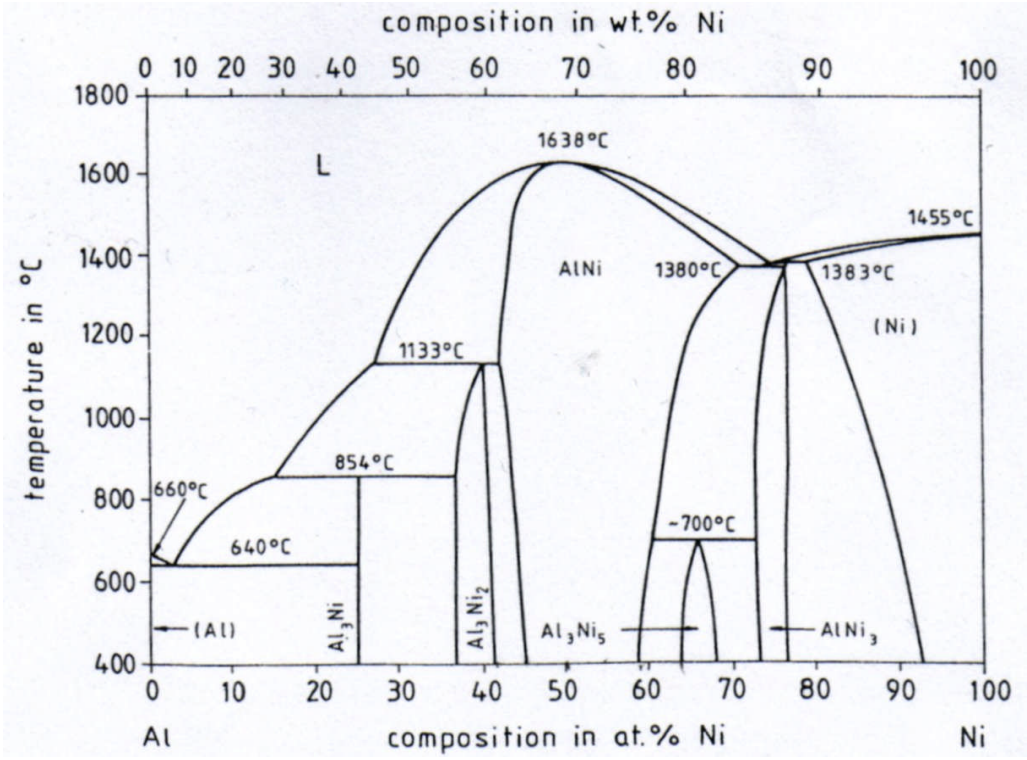

Figure 11 The Ni-Al binary phase diagram

This melting temperature is nearly 300°C higher than those of conventional Ni-based superalloys and is also higher than the melting temperatures of the constituent elements, indicating a strong bonding between Ni and Al and a corresponding high phase stability with a strong tendency for atomic ordering [(62)]. Nonstoichiometric compositions have a reduced melting temperature, but still maintain an advantage over current airfoil materials. NiAl with a stoichiometric composition is strongly ordered, even above 0.65 Tm (where Tm is the melting temperature in K). Deviations from stoichiometry result in constitutional disorder, with excess Ni atoms on Al sites on the Ni-rich side of the stoichiometric composition and vacancies in the Ni sub lattice on the Al-rich side [(66)].

The density of non-stoichiometric NiAl ranges from 5.35 g cm^{-3} at the Al-rich boundary of the NiAl phase to 6.50 g cm^{-3} at the Ni-rich boundary. The density of binary NiAl at the stoichiometric composition is 5.85 g cm^{-3} and is roughly two-thirds that of conventional Ni-

based superalloys, which provides one of the major benefits of NiAl as an aerospace material.

NiAl forms the basis of a family of high temperature, oxidation resistant and corrosion resistant alloys that have been used as coatings on Ni-based and Co-based superalloys in gas turbine engines for over 30 years. Binary NiAl readily forms a continuous protective layer of alumina over a range of temperatures and compositions. The Al content is sufficiently high and the Al diffusion rate is sufficiently fast in NiAl at all temperatures to form stable Al_2O_3 scales at the surface and prevent internal oxidation in the bulk of the material.

The coefficient of thermal expansion (CTE) is important for coating applications as a mismatch between the substrate and coating can create thermal stresses and lead to spallation. The CTE of NiAl is comparable to that of typical Ni-based superalloys and is 15.1 x 10^{-6} K^{-1} from 820°C to 1560°C for stoichiometric NiAl. Deviations from stoichiometry and minor alloying additions have little effect on the CTE.

3.4.3.3 Ni_3Al

Ni_3Al is the best known and most studied intermetallic because it has been used as a strengthening phase in the superalloys for a long time. It is the first intermetallic compound formed as aluminium is added to nickel and has an $L1_2$ ordered crystal structure below 1395°C (Figure 8). Its unit cell contains four atoms, with three nickel atoms occupying face-centred positions and with one aluminium atom at corner positions. [67]

Ni_3Al has a homogeneous phase field of only about 3% around its stoichiometric composition (73.8 at.% Ni to 76.6 at.% Ni). It melts at about 1383°C for the stoichiometric composition with 25 at.% Al.

The density of Ni_3Al is 7.50 g cm^{-3} which is only slightly lower than that of the superalloys (7.9 g cm^{-3} to 9.1 g cm^{-3}). It can dissolve further elements, in particular other transition metals, and various investigators have studied ternary Ni-Al based phase diagrams [68, 69, 70, 71]. According to the results of specific site occupancy studies, Ni sites are occupied by Co, Pd, Pt, Cu or Sc, and Al sites are occupied by Ti, Zr, Hf, V, Nb, Ta, Mo, W, Zn, Ga, Si or Sn. However, Cr, Mn, or Fe occupy both sites with slight preference for the Al sites, depending on the composition.

3.4.3.4 Platinum-Modified Aluminides

Aluminides suffer from attack by impurities in the combustion gases caused by engines running on low grade fuels or operating in harsh environments.[72] It is generally agreed that platinum aluminides outperform conventional aluminides,[73] due to improved oxidation resistance and a greater resistance to Type I hot corrosion. This improved performance is due to the interaction between the platinum and aluminium producing a number of important effects.[74, 75] The affinity of aluminium for platinum creates an aluminium reservoir in the outer portion of the coating and the platinum promotes the selective oxidation of aluminium due to the fact that; i) no platinum oxide is formed at the coatings operational temperature and ii) aluminium is very mobile in the platinum-rich phases.

The B2 phase is an ordered cubic AB phase such that A atoms are situated on the corners and B atoms at the centre of the unit cell (Figure 8). The enhanced stability of the platinum-modified coating is attributed in the literature [76, 77, 78] to different evolution

mechanisms: the formation of $PtAl_2$ reduces the diffusivity of nickel and/or aluminium in the outer layer, chromium remains in solution and increases the aluminium activity near the surface and the refractory transition elements (Mo, V, W) are impeded from reaching the outer layer and degrading its oxidation resistance. An additional beneficial effect derives from the ability of platinum to reduce oxide spallation by enhancing the adherence of the oxide scales.[79]

3.4.3.5 γ-γ′ Bondcoats

A new class of platinum aluminide bond coat has been developed recently[57]. It is primarily comprised of Pt-modified γ-Ni + γ′- Ni_3Al formed by diffusion. The advantages of these 2-phase coatings are reported [80, 81] to be:

- Excellent oxidation resistance
- Elimination of surface rumpling
- Reduced coating thickness
- Reduced fabrication costs
- Reduction or elimination of Al interdiffusion into the substrate
- Higher solubility for beneficial reactive elements such as Hf
- Improved phase stability

Although there has been a limited amount of research published on γ-γ′ coatings, the main concerns are related to their long-term high temperature oxidation behaviour and their sensitivity to substrate composition.

Gleeson et al, [82] found that NiAlPtHf cast alloys with a γ-γ′ microstructure formed an adherent α-Al_2O_3 layer with reduced rumpling during thermal cycling. The research team also found [83] that the oxidation resistance of Pt + Hf modified γ-γ′ alloys improves with increasing Pt content.

A simple γ-γ′ coating has been produced [84] by electroplating a Ni-based superalloy with a 7μm Pt layer followed by a diffusion treatment. However, Haynes [81] found that increasing the initial electroplated Pt layer thickness to 12μm appeared to improve the oxidation behaviour. Interdiffusion studies carried out on Pt-modified γ-γ′ coated superalloys [85] found that the system exhibited outward diffusion of Al from the substrate, containing 13-19 at% Al, to the coating containing 22 at% Al, if the Pt content of the coating was > 15 at%.

Zhao et al tested a Pt-enriched γ-γ′ bond coat [86] and found that TBCs with a higher Pt content exhibited a significantly longer isothermal life than those with a lower Pt content. This was because higher Pt inhibited impurities such as S, C and refractory elements segregating to the TGO/bond coat interface. In another study [87] they found that γ-Ni formed underneath the TGO of a Pt-enriched γ-Ni + γ′-Ni_3Al bond coat as a result of Al depletion. X-ray diffraction investigations indicated that a $NiAl_2O_4$ spinel phase formed at the TGO/bond coat interface after prolonged oxidation. It was proposed that the formation of spinel occurred when local cracks were present at the interface and the underlying bond coat was Al-depleted. When spinel forms the interface toughness is compromised due to its brittleness and also, the volume increase associated with spinel formation generates a large tensile stress which could be responsible for crack initiation and eventual failure of the TBC. [87]

3.4.3.6 Ruthenium Additions

Ruthenium is one of four elements (Ru, Re, W, Ir) that increase the liquidus temperature of nickel and is currently being investigated as an alloying addition to bulk Ni-base single crystal superalloys for improvement of high temperature capabilities.[88, 89, 90] In addition, due to the effectiveness of the (Ni, Pt)Al materials presently used as bond coat (BC) layers for Ni-base superalloy thermal barrier coatings (TBC), higher temperature RuAl-containing BC layers are being examined as a possible improvement in temperature capability and as a lower cost alternative to platinum.[91] Like the Pt-modified NiAl bond coat layer, RuAl is a B2-based system, also stable over a range of compositions, but with a melting point over 400°C higher than stoichiometric NiAl.

Tryon et al [92] found that RuAl exhibited relatively low coefficients of thermal expansion (CTE) in the range of 5.5 x 10^{-6}/K to 11x10^{-6}/K for temperatures between 400K and 1773K. Therefore, the CTE of RuAl is substantially lower than those of other B2 intermetallics including FeAl, CoAl, NiAl and (Ni/Pt)Al and is closer in value to alumina and zirconia (Figure 12). Matching the CTE of the BC and the TGO could reduce the thermal stresses that develop between the layers of the composite TBC during thermal cycling and having a BC with a CTE closer to that of the superalloy substrate should minimise the total accumulated strain within the composite coating. In addition, the physical properties of RuAl offer several other potential advantages over the Pt-modified NiAl BCs. RuAl exhibits characteristics of better intrinsic deformability than NiAl at low temperatures. It also has a greater number of slip systems than NiAl and is reported to have high toughness and compressional ductility. Further alloying of RuAl may lead to a further enhancement of its properties.

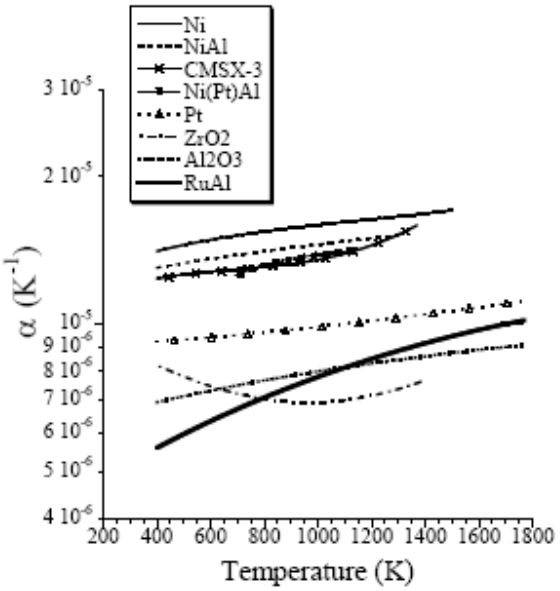

Figure 12 Thermal expansion coefficients of materials used in thermal barrier coatings as a function of temperature [92]

The oxidation of RuAl-based components has only recently been investigated and there has been some disagreement, in the literature, as to whether Ru is detrimental to oxidation resistance, or whether RuAl has good enough oxidation resistance to be considered for bond coat layers.[93, 94] The oxidation of binary RuAl has been shown to produce a layered reaction product of α-Al_2O_3 and δ-Ru. The δ-Ru layer contained in this structure forms a volatile oxide at high temperatures causing catastrophic spallation. However, recently Cao et al,[95] found that Pt additions to near stoichiometric RuAl improved the oxidation resistance of this B2 compound. P. Bellina et al,[94] found that the presence of Ru in bond coats seems to be deleterious to oxidation resistance, with the formation of $RuO_{3(g)}$ leading to an undesirable porous alumina. Although PtAl and RuAl with ceramic top coat both failed after ~100h oxidation at 1100˚C, the spallation of scales was more prevalent in the case of Ru-containing alloys. This was explained based on the increased thermal stresses during cooling to room temperature.

According to I.M. Wolff, [96] the use of RuAl in high temperature environments is restricted by its oxidation resistance. RuAl is found to be reasonably oxidation resistant up to at least 900˚C, but the formation of volatile oxides seriously limits its resistance at higher temperatures. At 1100˚C, rapid initial mass gain is followed by spalling, while at 1300˚C, severe internal oxidation occurs. However, the addition of boron initially extends the resistance to oxidation and yields a relatively limited deviation in mass, before giving way at high temperatures to catastrophic and uniform internal oxidation.

Furnace testing of sputtered Pt/Ru coated CMSX-4 was carried out at King Fahd University,[97] (KFU) under Rolls Royce funding. In contrast to Bellina et al, they found that the presence of Ru was beneficial to the oxidation resistance of bond coats.

Sample	Pt thickness (µm)	Ru thickness (µm)	Diffusion conditions	Sputtering sequence
RR 102	10	5	1 hour at 1150°C	Ru on substrate, Pt on Ru
RR 103	10	5	1 hour at 1150°C	Pt on substrate, Ru on Pt

Table 5 Processing details for Pt/Ru coated samples

Table 6 compares the time to spallation of these samples with those achieved with the γ-γ′ bond coat [98].

Sample	Time to spallation of TBC (hours)	
	1150°C	1200°C
RR 102	48, 48, 96, 96, 96	5 @ 24
RR 103	336, 360, 432, 432, 480	144, 144, 144, 168, >168
γ-γ′ bond coat	264, 288, 288, 288, 504, 504	

Table 6 Time to spallation for Pt/Ru coatings compared to γ-γ′ bond coat

The time to spallation of the Pt/Ru coatings was dependent on the sputtering sequence. The samples produced by applying Ru and then Pt (RR102) were inferior to both the γ-γ′ bond coat and the Pt under Ru (RR103). The lifetime of the sample produced by applying Pt and then Ru had a better average time to spallation than the γ-γ′ bond coat. Although, this was not as good as the time to spall for the MCrAlY CN122 + Pt, which was greater than 1000 hours at 1150°C, but was better than the time to spall for the PtAl bond coat RT22LT, which had an average time to spall of ~180 hours at 1150°C [88].

R.L. Fleischer et al,[99] carried out oxidation tests on alloyed RuAl at 1100˚C (Figure 13) and a few tests at 1350˚C (Table 7). Values of the parabolic rate constant, *k*, of about 10^{-10} $g^2/cm^4/s$, corresponding to an oxidation depth of less than 25μm/100h, were identified as potentially useful alloys. Four of the alloys tested qualified and only at 1100˚C. Of the four, the least rapid oxidation occurred for the alloy with the lowest toughness – $Al_{44.5}Ru_{50.5}Cr_5$. The best combinations of low oxidation and high toughness are $Al_{47}Ru_{53}$ and $Al_{48}Ru_{51}Y$. At 1350˚C, the lowest oxidation rate is for $Al_{43}Ru_{52}Sc_5$ with a good chisel toughness of 2+. This has only marginally unacceptable oxidation at 1350˚C, suggesting that it would become potentially useful at a lower temperature.

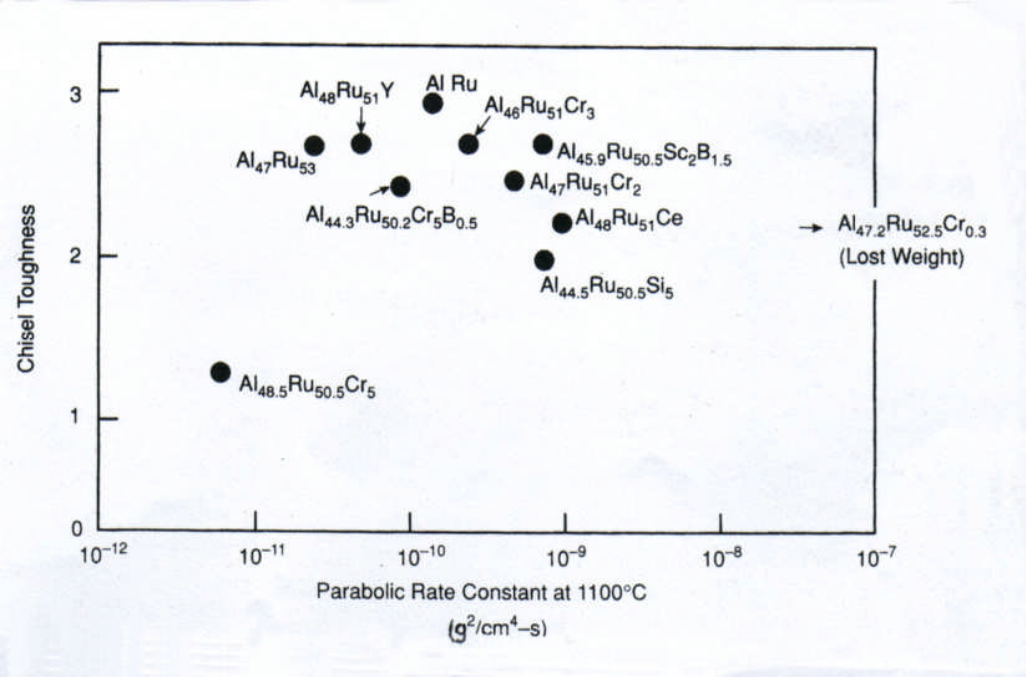

Figure 13 Parabolic rate constants (*k*) at 1100˚C for initial oxidation of various alloys vs. the chisel toughness (CT). Desirable CT's are >2; desirable *k*'s are $\leq 10^{-10}$ $g^2/cm^4/s$.

Alloy	*k* (10^{-8} $g^2/cm^4/s$)
AlRu + 0.5% B	11.0
$Al_{47}Ru_{53}$ + 0.5% B	9.7
$Al_{48.5}Ru_{52}Sc_2$	2.5
$Al_{46}Ru_{52}Sc_2$	0.18
$Al_{43}Ru_{52}Sc_5$	0.076

Table 7 Parabolic initial oxidation rates of AlRu alloys at 1350˚C

Other precious metals are also being investigated as alternatives to platinum. One major competitor is palladium due to it having similar properties to platinum and the fact that it does not form a brittle $PtAl_2$ type phase, which can cause premature spalling. As yet, no engine manufacturer has replaced platinum with palladium, possibly due to the fact that

during field investigations with Pd-modified aluminides the coatings showed very poor high temperature resistance. This was thought to be due to hydrogen absorption during its application leading to hydrogen embrittlement and blister-like surface defects.[100]

Rhodium additions were found to increase the lifetime of coating systems and behaved as well as a platinum aluminide coating under hot corrosion conditions. They also improved the durability of the coating due to the superior stability of the β-type phase.[101] Iridium was reported to have low oxidation rates and a low oxygen diffusivity compared to other refractory metals. When compared with platinum aluminides, iridium-based coatings were found to be relatively thin, promoted alumina-based scale growth and formed effective barriers against outward diffusion of damaging elements, such as hafnium. However, the adherence of the oxide and the stability of the coating were found to be lower than those shown by a platinum aluminide coating. [101]

Coatings containing rhodium, ruthenium or iridium additions were recently deposited at Cranfield using DC magnetron sputtering. The ruthenium additions were found to improve the adherence of the oxide scale and reduce the interdiffusion of harmful elements between the substrate and the oxide scale (TGO). Iridium additions were also found to be a promising candidate to replace some of the platinum.

3.5 Oxidation and Oxidation Mechanisms

The term oxidation refers to the reaction of oxygen with metals to form oxides. In oxygen containing atmospheres, most pure metals and alloys will form very thin, protective oxide films, which protect the underlying metal from further oxidation at low temperatures. However, at elevated temperatures a thicker oxide scale is formed. The growth of this scale is controlled by thermodynamic and kinetic factors as well as gas composition and temperature.

Some metals and alloys are more resistant to oxidation than others and the mechanism and rate of oxidation is influenced by a wide range of factors including: composition, pressure, temperature and surface finish.[102]

3.5.1 Thermodynamics of Oxidation

A simple oxidation reaction between a pure metal (M) and oxygen (O) is given by:

$$M_{(s)} + O_{2\,(g)} \longrightarrow MO_{2\,(s)}$$

The oxidation of alloys or intermetallics is more complex, but whether or not a reaction will occur is governed by the 2nd Law of Thermodynamics.[103] For high temperature oxidation reactions at constant temperature and pressure this can be expressed in terms of the Gibbs Free Energy:

$$\Delta G = \Delta H - T\Delta S$$

where ΔG is the Gibbs Free Energy change, ΔH is the enthalpy change, T is the absolute temperature and ΔS is the entropy change.

For the oxidation reaction to proceed ΔG must be negative. If $\Delta G = 0$, then the system is in a state of equilibrium.

Oxide	- ΔG ˚ (kJ/mol of oxide)
Cu_2O	145
PbO	188
NiO	215
FeO	255 (at 227°C)
ZnO	319
SiO_2	824
Cr_2O_3	986
Al_2O_3	1578

Table 8 Standard Free Energy of Formation of some oxides at 300K and 1 atm[104]

An Ellingham diagram can be used to establish whether or not a corrosion product is likely to form under certain conditions. The standard free energy of formation (ΔG° kJ/mol) is plotted against temperature. This allows the relative stabilities of various oxides, sulphides, nitrides and carbides to be compared. (Figure 14)

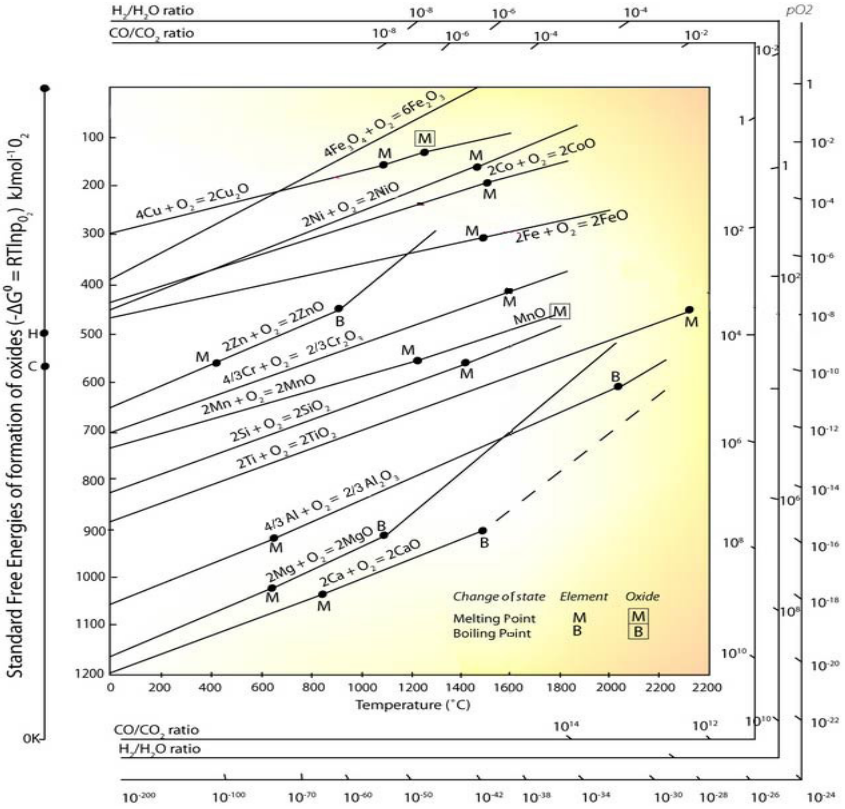

Figure 14 An example of an Ellingham diagram [105]

For complex systems it is possible for several oxides to form. The lower the position of the line on the Ellingham diagram (the more negative the free energy value), the greater the stability of the oxide and the more likely it is to form.

3.5.2 Oxidation Kinetics

Ellingham diagrams are useful for determining whether or not oxide formation is possible under certain conditions, however, they do not give any indication of how rapidly the reaction will occur. Oxidation reaction rates vary depending on various factors including temperature, pressure and surface finish and can be characterised as linear, parabolic, logarithmic or a combination of these.

Linear oxidation is usually observed in metals that form a porous scale, which does not behave as a diffusion barrier between the metal and its environment. The linear rate law is the simplest equation that was found to represent experimental data in terms of weight increase (Δm) and time (t):

$$\Delta m = k_1.t \qquad \text{where } k_1 \text{ is a constant}$$

At high temperatures, oxide films grow parabolically. The parabolic rate law represents a straight line when $(\Delta m)^2$ is plotted against time:

$$(\Delta m)^2 = k_p.t$$

If the line does not intersect the zero point of the axes then the more general form of the parabolic equation can be used:

$$(\Delta m)^2 = k_p.t + c \qquad \text{where } k_p \text{ and } c \text{ are constants}$$

At temperatures below 400ºC, many metals oxidise rapidly at first and then the reaction rate slows. This behaviour can be represented by the logarithmic or inverse logarithmic rate laws. The general logarithmic rate law can be written as:

$$\Delta m = k_e.\log(a.t + t_o) \qquad \text{where a, } k_e \text{ and } t_o \text{ are constants}$$

The inverse logarithmic rate law can be written as:

$$\frac{1}{\Delta m} = b - k_i.\log.t \qquad \text{where b and } k_i \text{ are constants}$$

It is common for a metal or alloy to start off oxidising parabolically and to then continue linearly. This combination of laws is known as paralinear oxidation.

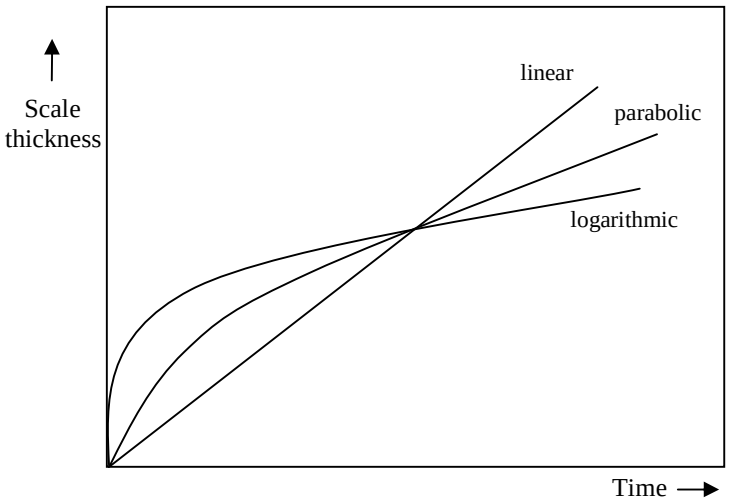

Figure 15 Schematic representations of the rate laws for oxide scale formation [106]

3.5.3 Oxidation Mechanisms

When a metal oxidises, a thin film forms on its surface. As the film thickens, the metal surface becomes separated from the oxidising environment and oxidation can only continue by the transport of reactants through the oxide layer. This can happen either by metal ions from the substrate passing through the oxide layer to react with the atmosphere at the surface (outward diffusion) or by oxygen ions from the atmosphere passing through the oxide layer and reacting with the substrate at the oxide-metal boundary (inward diffusion).[107,108]

Ion movement through an oxide film usually occurs by solid state diffusion, which depends on imperfections in the oxide. It is well known that some kind of defect structure exists in most solids at a temperature above absolute zero. When the crystal lattice of the solid has atoms missing or atoms are displaced from their normal lattice positions it is known as an imperfect solid. This type of defect is called a point defect. Khanna [108] lists the main types of point defect in an oxide as:

- Vacancies – a metal ion or oxygen anion missing from the crystal lattice;
- Interstitials – the displacement of metal ions or oxygen anions from their lattice position;
- Impurities – cations substituted by foreign cations or anions substituted by foreign anions.

The transport of species through the oxide is described by different mechanisms depending on its point defect structure.

In the 1930s, Wagner [109] presented his theory of oxidation in order to explain the mechanism by which oxide growth occurs. The theory applies to compact, perfectly adherent scales and the transport of ions or electrons across the scale is assumed to be the rate determining process.

According to Wagner, metal ions and oxide ions will migrate across the oxide scale in opposite directions and because the ions carry a charge, this creates an electric field across the scale. This will result in the migration of electrons across the scale from the metal to the atmosphere. The migration rates of cations, anions and electrons are balanced and therefore no net charge occurs across the oxide layer. This process is illustrated schematically in Figure 16.

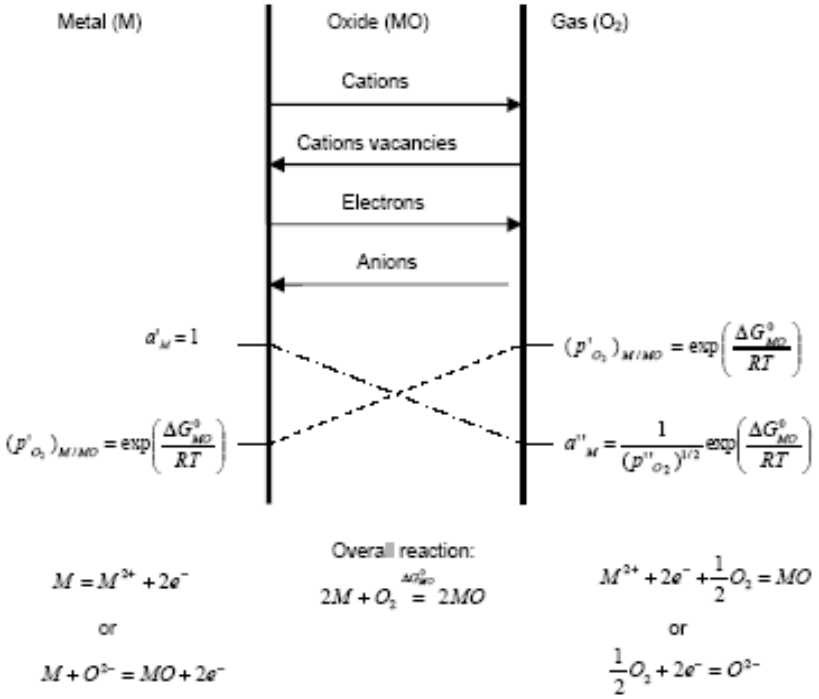

Figure 16 Schematic diagram of oxide scale formation according to Wagner's model [(103)]

3.5.4 Alloy Oxidation

The oxidation of alloys involves many of the same factors as the oxidation of pure metals, however, it is usually more complex. Selective oxidation of certain metals or ions will occur at the surface layer. Initially, all oxides that are thermodynamically stable will form. However, because the metals in the alloy form different oxides with different free energies of formation some will be more stable than others. Several oxide layers may be formed, including ternary and higher oxides and a degree of solid solubility may exist between the oxides.[14, 103]

3.5.3.1 Oxidation of NiAl

The principal oxides that may form on superalloys are those related to the base metals and to chromium and aluminium[14]:

- Chromic oxide (Cr_2O_3)
- Aluminium oxide (Al_2O_3)
- Nickel oxide (NiO)
- Cobalt oxide (CoO)
- Spinel ($NiO.Cr_2O_3$)
- Titanium oxide (TiO_2)

One oxide is, however, likely to be dominant and while NiO and other oxides may form initially at surface locations, only one oxide will spread across the whole surface. The dominant oxide in current Ni-based superalloys is Al_2O_3 or Cr_2O_3, depending on composition and temperature.

The early stage oxidation of β-NiAl, known as transient oxidation, may result in the formation of several transitional oxide phases. These phases include the metastable γ-

Al_2O_3, δ-Al_2O_3 and θ-Al_2O_3. At temperatures above 1000ºC they will be irreversibly transformed into the stable form of alumina, α-Al_2O_3, and a continuous oxide film will form on the surface and continue to grow.[110]

The transition of metastable alumina phases to α-Al_2O_3 will result in a slow growing oxide scale with a ridged morphology (Figure 10) for β-NiAl or a columnar morphology for γ′-Ni_3Al. [103] In the binary NiAl system, the minimum concentration of aluminium at which alumina is the dominant oxide is ~ 35 at%, however, this can be reduced by the addition of certain alloying elements. For example, with the addition of 5 at% Cr, the activity of the Al increases, which helps alumina formation and the minimum concentration of Al is reduced to 12 at%.[14]

3.6 Failure of TBCs

There are a number of degradation modes that can limit the life of a TBC. These include:[50, 53, 111]

- Crack coalescence within the ceramic layer for plasma sprayed TBCs during thermal cycling leading to spalling of part of the coating.
- Crack propagation along the interface between the TBC and the bond coat for EB PVD coatings resulting in spalling of the entire TBC.
- Sintering of the TBC at the outer surface where the temperature is highest leading to crack propagation and spalling of the coating.
- Particle erosion causing continued wear of the coating and, in the case of large particles, propagating cracks in the coatings and along the top coat-bond coat interface.
- Oxidation of the bond coat resulting in growth of the alumina layer causing an increase in strain within the ceramic.

- Thermal fatigue cracking within the TGO driven by the differences in CTE of the ceramic layer, the metallic bond coat and the substrate alloy leading to spalling.

It can be seen from this that the mechanisms of failure are both complex and interactive and that the primary failure mode for TBCs is spallation, typically on cooling from operational temperatures. Some of the major failure categories for thermal barrier systems are shown schematically in Figure 17.

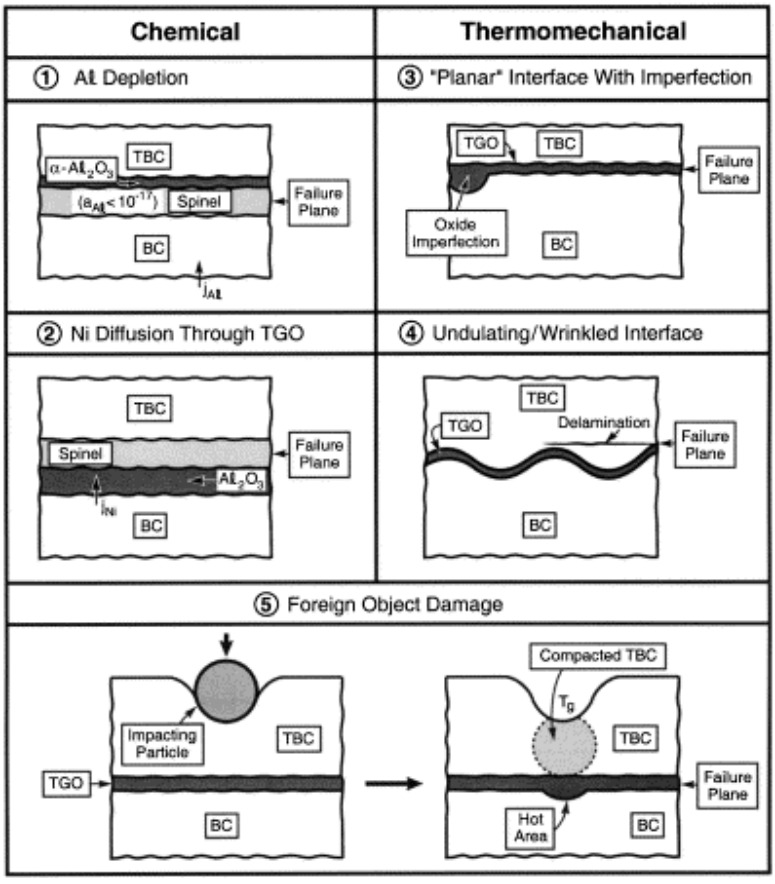

Figure 17 Five of the major failure categories for TBC systems [(112)]

3.6.1 Spallation

Failure of thermal barrier coatings usually refers to spalling, whereby sections of the ceramic top coat separate from the bond coat in a single layer. Spalling can occur as a result of cracks growing; a) at the top coat-TGO interface, b) at the TGO-bond coat interface, c) in the TGO (alumina), d) within the TBC, etc. The growth of these cracks is driven by stresses caused by oxidation of the bond coat and cyclic thermal expansion mismatch (thermal fatigue) or in other locations. Interaction between oxidation and thermal fatigue results in a more rapid deterioration of the coating than predicted from the sum of the damage from these degradation modes acting separately.[52, 113]

Several factors are important with regard to cracking within the top coat or along the top coat-bond coat interface. These include: [50]

- The stress state of the yttria-stabilised zirconia (YSZ) layer.
- The microstructure of the bond coat.
- The thickness of the TGO.
- The stress state in the TGO.
- The fracture resistance of the bond coat-TGO interface.

In the case of EB PVD TBCs, it is believed that spallation occurs at the TGO-bond coat interface or in the alumina layer. It may also sometimes occur at the ceramic-TGO interface for PtAl bond coats. Spallation of alumina scales has been related to accumulation of trace impurities, particularly sulphur, at the bond coat-TGO interface or to the build-up of residual stress in the alumina layer. This residual stress is the sum of growth stresses and thermal stresses minus any stress relaxation that has occurred by plastic deformation of the alloy and/or oxide. [50, 114]

For the plasma sprayed system spallation is generally through cohesive failure within the ceramic layer in the vicinity of the TGO. APS coated systems therefore frequently show

'white failure' whereby significant parts of the ceramic remain adherent to the bond coat after spallation. [114, 115]

3.6.2 Bond Coat Oxidation

TBC life can be affected by a number of factors, however, in the absence of mechanical damage, bond coat oxidation has long been accepted as being one of the major factors controlling TBC life. Oxidation occurs by the diffusion of oxygen through the porous yttria-stabilised zirconia top coat. Even if the top coat was dense, oxygen would still diffuse through it during service, since zirconia is an ionic conductor.[116, 117] The main parameters governing bond coat oxidation induced TBC failure include: the critical thickness of the alumina (around 6-7μm)[118, 119] , defect formation in the TGO and the TGO-bond coat interface[120] and stresses in the scale originating mainly from the thermal expansion mismatch between the bond coat and the oxide scale.[117] Upon cooling from operating temperatures, the TGO develops large in-plane compressive stresses due to thermal expansion mismatch with the substrate. Imperfections in the TGO localise the misfit stress and cause a release of strain energy leading to the nucleation of small cracks and separations. These cracks extend and converge with neighbouring cracks leading to layer separation, which will eventually result in large scale buckling or edge delamination. [121]

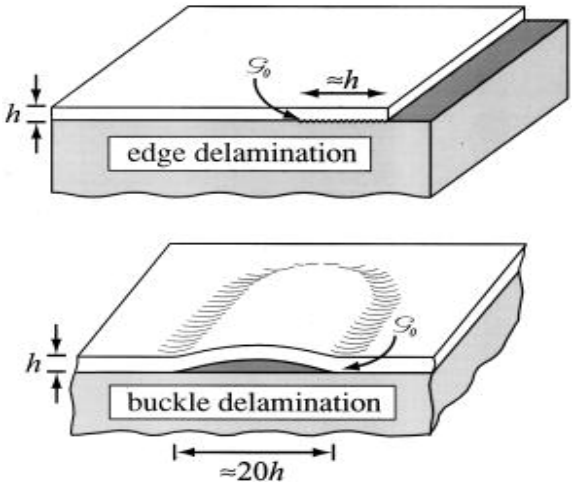

Figure 18 Schematic showing an edge delamination and a buckle delamination[122]

The stress generation depends on the bond coat composition and the phase transformations occurring in the bond coat following temperature changes and during temperature changes, stresses are also caused by differences in thermal expansion coefficients. Other factors affecting the growth of the alumina layer at high temperature include oxidation growth stresses, diffusion of elements and formation cavities. In (Ni, Pt)Al bond coats, one of the major features of oxidation behaviour caused by thermal cycling is the formation of regular, long undulations known as rumpling. [123] This is driven by misfit strains between the substrate and the bond coat caused by thermal expansion, phase transformations and inter-diffusion induced swelling.[124] Another feature is a localised penetration of the TGO into the bond coat in the presence of a ceramic top coat, which is known as ratcheting. According to Evans et al, ratcheting occurs by out-of-plane displacement of thin films on ductile substrates when they are compressed by mismatch stresses and in some cases these undulations increase in amplitude with thermal cycling.[112] The sites at which ratcheting occurs are determined by at least two factors[112, 125] – initial imperfections at the TGO-bond coat interface induce stresses greater than the cyclic yield strength of the bond coat and some of the grains adjacent to the TGO are highly susceptible to plastic straining normal to the interface.

While bond coat oxidation is an important degradation mechanism, it is not the only important parameter for the bond coat. Some bond coat compositions with poorer oxidation resistance may result in a longer top coat life. High chromium (35 wt%), low aluminium (< 6 wt%) Ni-Cr-Al-Y bond coats show significantly better top coat life than Ni-Cr-Al-Y compositions used for overlay coatings (15-22 wt% Cr and > 6 wt% Al), even though the oxidation resistance of the high chromium coating is not as good as that of the overlay coating. Reasons proposed for this suggest that bond coat modulus, CTE, strength and compositional effects on adhesion may be important factors in TBC life. [52, 115, 126]

3.6.3 Hot Corrosion

TBC bond coats can be susceptible to degradation by hot corrosion, especially during elevated temperature service in marine atmospheres. The ceramic top coat can also be attacked by molten salts; this is known as CMAS (calcium-magnesium-aluminium-silicate), but occurs at much higher temperatures than hot corrosion. Hot corrosion can lead to much higher damage rates than in gaseous oxidation and the formation of non-protective oxide scales.

Hot corrosion in gas turbines is a result of a corrosive salt deposit, usually sodium sulphate, which fluxes the protective oxide scale. Sulphur is produced by the fuel burning process and it reacts with sodium (from the sea) which is ingested in the engine intake air.

$$2NaCl + SO_2 + \tfrac{1}{2} O_2 \longrightarrow Na_2SO_4 + HCl$$

Two types of hot corrosion have been identified. High temperature (Type I) hot corrosion is observed in the temperature range 800-950°C when the condensed salt film is liquid. Low temperature (Type II) hot corrosion occurs well below the melting point of Na_2SO_4, in the temperature range 650-800°C. A low melting point eutectic salt deposit may form locally through interaction between Na_2SO_4 and $NiSO_4$ or $CoSO_4$, the latter forming from reaction of NiO or CoO with SO_3. In type I hot corrosion, internal sulphides are formed leading to a depletion of the reactive components such as chromium, resulting in accelerated oxidation. Type II hot corrosion is characterised by uniform pitting corrosion attack, with a thin sulphide layer formed at the pit/alloy interface.

The corrosion process can be separated into two stages - the initiation stage and the propagation stage. In the initiation stage, the corrosion rate is relatively low as the oxide scale is gradually broken down. Once the initiation stage is complete and the oxide scale can no longer be repaired, then the propagation stage results in rapid attack and consumption of the substrate. [24, 34, 127]

3.6.4 Erosion

Aero gas turbines operate in environments where the ingestion of solid particles is inevitable, leading to impact with rotating airfoil components and subsequent erosion damage.[128] In commercial and military aircraft some of the mechanisms that cause solid particle ingestion to the engines are vortices generated during take-off and landing, sand storms, volcanic ash and thrust reverser efflux, which blows sand, ice and dust into the engines.[129] Particles can also be generated within the engine, such as carbon formed during the combustion process, and may also contribute to erosion damage. [128]

Degradation may primarily be caused by erosion, corrosion or oxidation, or by the complex interaction of these processes.[130] Erosion damage to turbine TBCs results in the progressive removal of the ceramic top coat, leading to loss in aerodynamic efficiency and an increase in heat transfer to the component. This can result in much higher rates of corrosion, oxidation and erosion damage to the underlying bond coat and substrate.[131] The rate of TBC erosion depends on particle size and velocity, impact angle, temperature and corrosion/oxidation conditions. [132]

There are three major types of damage mechanism that have currently been identified in EB PVD TBCs :[133]

- Mode I erosion – when small, low energy engine-generated particles impact the TBC resulting in near surface (top 20µm) cracking.

- Mode II compaction damage – column compaction, but not fracture, occurs due to the surface impact.

- Mode III foreign object damage (FOD) – large particles at low velocity or smaller, high velocity particles cause significant deformation of the coating with gross plastic deformation of the columns and often shear band formation and cracking within the TBC, adjacent to the TGO/ceramic interface.

4.0 Experimental Procedure

4.1 Introduction

Experimental procedures were targeted at the manufacture and analysis of intermetallic compounds in the Ni-Al, Ni-Pt-Al and Ni-Ru-Al systems. Intermetallic compounds were produced by sputtering pure metal layers onto foil substrates and then heat treating them in a Differential Scanning Calorimeter (DSC). The thicknesses of the metallic layers were measured between manufacture and heat treatment by optical microscopy and Focused Ion Beam (FIB) analysis.

The samples that evolved the most heat during reaction in the DSC were then analysed using X-ray Diffraction (XRD) and Energy Dispersive X-ray Analysis (EDX) in a Scanning Electron Microscope.

4.2 Coating Deposition

NiAl was produced by sputtering nickel onto both sides of a 10μm thick, commercially pure aluminium foil in a single target coater, CVC2. (Ni, Pt)Al was produced by sputtering a nickel layer onto each side of the aluminium foil and then sputtering platinum on top of the nickel layers in the Nordiko coater. (Ni, Ru)Al was produced by sputtering a nickel layer onto each side of the aluminium foil and then sputtering ruthenium on top of the nickel layers in the multi-target CVCI coater. In all coating systems, the foil was clamped between two stainless steel masks as shown in Figure 19, in order to produce sixteen samples 15mm x 15mm during each deposition. The foil and masks were then cleaned using isopropyl alcohol before coating.

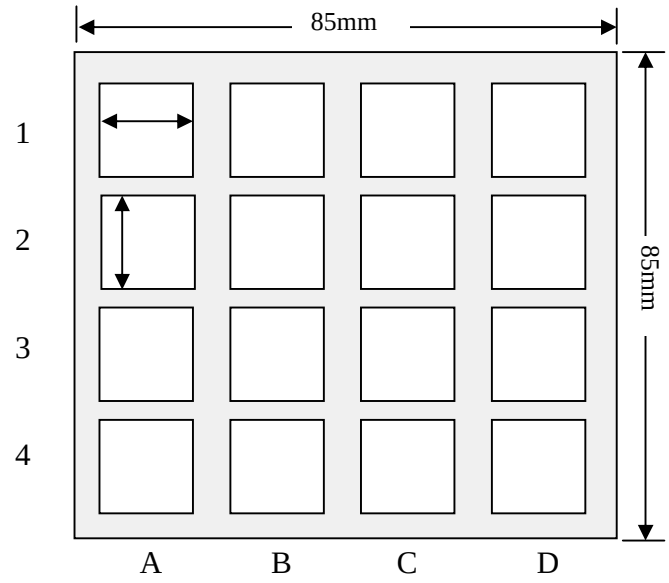

Figure 19 Schematic of the masks used to clamp foils for sputter coating

Ni_3Al was produced by sputtering aluminium onto both sides of a 10μm thick, pure nickel foil in a multi-target coater, CVCI. $(Ni, Pt)_3Al$ and $(Ni, Ru)_3Al$ were produced by sputtering an aluminium layer onto each side of the nickel foil and then sputtering platinum or ruthenium on top of the aluminium layers in the CVCI coater.

Prior to deposition, sputter cleaning of the target was carried out in order to remove oxidation and contaminants from the surface. This was followed by deposition rate calibration runs. Glass microscope slides were used as substrates for the rate runs because their smooth surfaces allow coating thicknesses to be measured accurately. Since the rate of deposition is not uniform throughout the deposition chamber of the coater, three slides were used to map the variations in deposition rates. High temperature resistant adhesive tape was used to mask part of the slides in order to allow step measurements to be taken.

The steps were measured using a precision measuring instrument called a Dektak ST. Measurements are made electronically by moving the sample beneath a diamond-tipped stylus. As the sample moves, the stylus moves over its surface. Surface variations cause

vertical movement of the stylus, creating electrical signals, which are processed and converted into thickness measurements.

Once the deposition rates had been found, the foil samples were loaded onto the worktable in the deposition chamber of the coater. A roughing pump was used to evacuate the chamber to a pressure of 10^{-1} mbar and then a diffusion pump was used to further evacuate the chamber to a pressure of 10^{-6} mbar. Argon was then introduced into the chamber. The argon passes through a 'getter' furnace containing titanium turnings in order to remove oxygen prior to reaching the chamber. The diffusion pump was then throttled in order to increase the chamber pressure from 10^{-6} mbar to the working pressure of 10^{-2} mbar.

A potential was then applied between the worktable and the facing target in order to ionise the inert gas. Argon atoms were accelerated towards the target surface, dislodging atoms of the target material during high energy impact. The dislodged atoms were then deposited onto the foil samples.

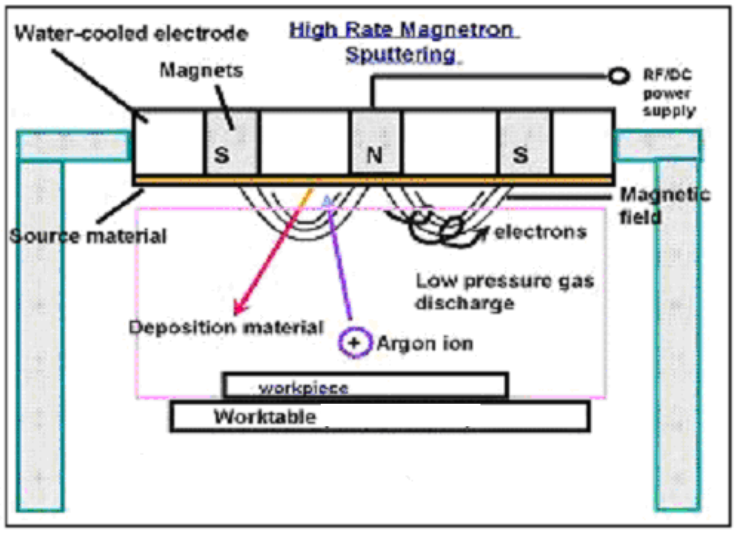

Figure 20 Sectional view through coater vacuum chamber[134]

The required layers were deposited on both sides of the foil leading to the formation of multi-layer coatings without a substrate (Figure 21) for thermal analysis.

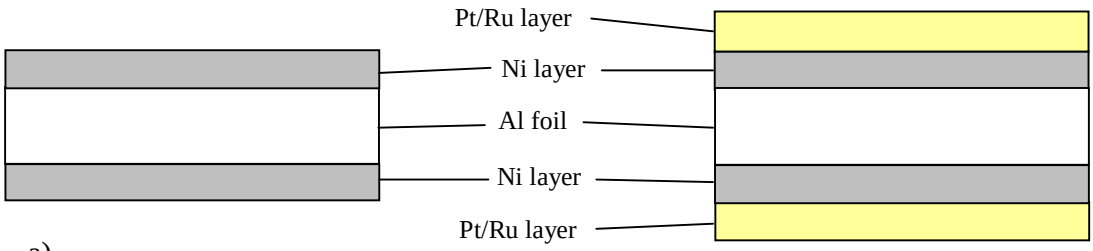

a)

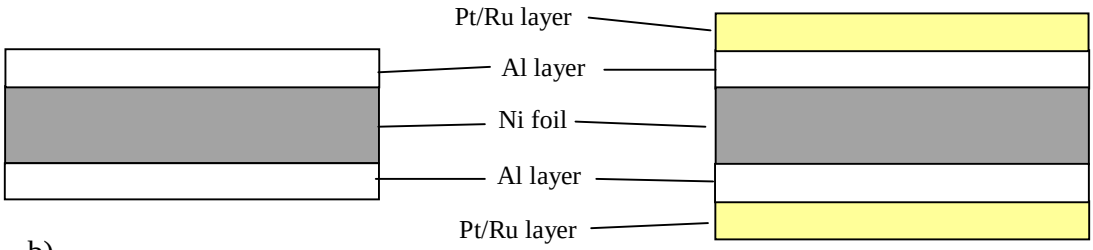

b)

Figure 21 Schematic of a) the aluminium foil coated with nickel and platinum or ruthenium to produce NiAl or (Ni, Pt/Ru)Al, b) the nickel foil coated with aluminium and platinum or ruthenium to produce Ni_3Al or $(Ni, Pt/Ru)_3Al$

Layers of the correct thickness to produce an initial stoichiometry of NiAl were deposited. Since the composition of NiAl on the Ni-Al binary phase diagram (Figure 11) ranges from 35 at.% Al to 65 at.% Al, layers of the correct thickness to produce 45Ni/55Al and 55Ni/45Al were also deposited in order to observe how the variation in composition affects the onset temperature of the reaction during thermal analysis.

(Ni,Pt)Al and (Ni,Ru)Al samples were produced by sputtering a nickel layer onto aluminium foil and then depositing a platinum or ruthenium layer on top of the nickel layer in the multi-target coater CVCI. This was then repeated on the reverse side of the foil. The aim was to produce 5 layer coatings nominally of 45Ni/5Pt/50Al, 40Ni/10Pt/50Al, 35Ni/15Pt/50Al , 30Ni/20Pt/50Al, 45Ni/5Ru/50Al, 40Ni/10Ru/50Al and 35Ni/15Ru/50Al.

Ni_3Al, $(Ni,Pt)_3Al$ and $(Ni,Ru)_3Al$ samples were produced by sputtering an aluminium layer onto nickel foil and then depositing a platinum or ruthenium layer on top of the nickel layer in the multi-target coater CVCI. This was then repeated on the reverse side of the foil. The aim was to produce a 3 layer coating of initial stoichiometry 75Ni/25Al and 5 layer coatings nominally of 50Ni/25Pt/25Al, 55Ni/20Pt/25Al, 60Ni/15Pt/25Al, 65Ni/10Pt/25Al and 70Ni/5Pt/25Al plus 60Ni/15Ru/25Al, 65Ni/10Ru/25Al and 70Ni/5Ru/25Al.

The nickel layers were deposited onto aluminium foil by RF sputtering at a power of 350W. The aluminium layers were deposited onto nickel foil by RF sputtering at a power of 200W.

The platinum and ruthenium layers were deposited onto the nickel or aluminium layers by DC sputtering. For the platinum the applied potential varied between 450 and 480V at a current of 0.65-0.7A, for the ruthenium the potential varied between 350 and 390V at a current of 0.77-0.85A.

4.3 Thickness Ratio Calculation

The stoichiometry of the desired compound is controlled by the thickness ratio of the component materials, assuming that there is no interaction between the coating and the substrate.

For example, a Ni_xAl_y layer containing *n* moles will consist of *n.x* moles Ni and *n.y* moles Al.

The number of moles can be connected to the coating volume:

$$\boldsymbol{m = mol \times M = \rho \times V}$$

where, *m* = mass (g), *mol* = no. of moles, *M* = atomic weight (g/mol), ρ = density (g/cm^3), *V* = volume (cm^3).

The total thickness e of each layer can be related to volume*:*

$$\boldsymbol{V = S \times e}$$

where, *S* = area (cm^2).

Therefore,

$$\boldsymbol{e = \frac{M}{S \times \rho} \times mol}$$

For the Ni and Al layers needed to make Ni_xAl_y ,

$$\frac{e_{Al}}{e_{Ni}} = \frac{y}{x} \times \frac{M_{Al}}{M_{Ni}} \times \frac{\rho_{Ni}}{\rho_{Al}}$$

x and *y* depend on the compound
i.e. For $NiAl_3$, *x* = 1, *y* = 3

	Aluminium	Nickel	Platinum	Ruthenium
Density (g/cm^3)	2.7	8.9	21.45	12.2
Atomic weight (g/mol)	26.9815	58.693	195.078	101.07

Table 9 Atomic weights and densities for Al, Ni, Pt and Ru

Phase	Ni_3Al	NiAl	Ni_2Al_3	Ni_3Al_2
Thickness ratio (Al/Ni)	0.505	1.515	2.273	1.0102
e_{Ni} (mm)	0.01	0.01	0.01	0.01
e_{Al} (mm)	0.00505	0.0015	0.0227	0.0101

Table 10 Thickness values calculated for nickel aluminides

Phase	NiAl	(45Ni, 5Pt)50Al		(40Ni,10Pt)50Al		(35Ni, 15Pt)50Al		(30Ni, 20Pt)50Al	
		Ni_9Al_{10}	$PtAl_{10}$	Ni_4Al_5	$PtAl_5$	Ni_7Al_{10}	Pt_3Al_{10}	Ni_3Al_5	Pt_2Al_5
Thickness ratio (Al/Ni,Pt)	1.515	1.6837	10.988	1.894	5.494	2.1648	3.663	2.526	2.747
e_{Al} (mm)	0.01	0.01		0.01		0.01		0.01	
e_{Ni} (mm)	0.0066	0.00594		0.00528		0.00462		0.00396	
e_{Pt} (mm)			0.00091		0.00182		0.00273		0.00364

(Total thickness of target material removed: Ni = 26.4 μm, Pt = 9.1 μm)

Table 11 Thickness values calculated for the deposition of nickel and platinum onto aluminium foil

Phase	NiAl	(45Ni, 5Pt)50Al		(40Ni,10Pt)50Al		(35Ni, 15Pt)50Al		(30Ni, 20Pt)50Al	
		Ni_9Pt	Ni_9Al_{10}	Ni_4Pt	Ni_4Al_5	Ni_7Pt_3	Ni_7Al_{10}	Ni_3Pt_2	Ni_3Al_5
Thickness ratio (Ni/Al,Pt)	1.515	1.6837	10.988	1.894	5.494	2.1648	3.663	2.526	2.747
e_{Ni} (mm)	0.01	0.01		0.01		0.01		0.01	
e_{Pt} (mm)		0.00153		0.00345		0.00591		0.00919	
e_{Al} (mm)	0.01515	0.01684		0.01894		0.02165		0.02526	

(Total thickness of target material removed: Al = 97.84 μm, Pt = 20.08 μm)

Table 12 Thickness values calculated for the deposition of aluminium and platinum onto nickel foil

Phase	NiAl	(45Ni, 5Ru)50Al	(40Ni, 10Ru)50Al	(35Ni, 15Ru)50Al
e_{Al} (mm)	0.01	0.01	0.01	0.01
e_{Ni} (mm)	0.0066	0.00594	0.00528	0.00462
e_{Ru} (mm)	0.01515	0.00083	0.00166	0.00249

Table 13 Thickness values calculated for the deposition of nickel and ruthenium onto aluminium foil

It was decided that platinum/ruthenium and nickel should be coated onto aluminium foil in order to produce NiAl and (Ni, Pt/Ru)Al since this uses less target material than using nickel foil. It can also be seen that less target material is used when platinum and aluminium are plated onto nickel foil to produce Ni_3Al and $(Ni, Pt/Ru)_3Al$ rather than onto aluminium foil.

Phase	Ni_3Al	(70Ni, 5Pt)25Al	(65Ni, 10Pt)25Al	(60Ni, 15Pt)25Al	(55Ni, 20Pt)25Al	(50Ni, 25Pt)25Al
e_{Ni} (mm)	0.01	0.01	0.01	0.01	0.01	0.01
e_{Al} (mm)	0.00505	0.00541	0.00583	0.00631	0.00689	0.00758
e_{Pt} (mm)		0.000985	0.00212	0.00345	0.00501	0.0069

Table 14 Thickness values calculated for the deposition of aluminium and platinum onto nickel foil

Phase	Ni_3Al	(70Ni, 5Ru)25Al	(65Ni, 10Ru)25Al	(60Ni, 15Ru)25Al
e_{Ni} (mm)	0.01	0.01	0.01	0.01
e_{Al} (mm)	0.00505	0.00541	0.00583	0.00631
e_{Ru} (mm)		0.000897	0.00193	0.00314

Table 15 Thickness values calculated for the deposition of aluminium and ruthenium onto nickel foil

4.4 Thickness Measurements

Thickness measurements and density measurements were carried out on all samples prior to differential scanning calorimeter (DSC) analysis, in order that the atomic percentage of each element could be calculated. The thickness measurements were performed using optical microscopy or focused ion beam analysis. The densities of the sputtered layers were measured by weighing a known volume of multilayer sample, subtracting the weight of the foil and then using this value to calculate the density with an accuracy of +/- 4 g/cm^3.

4.4.1 Optical Methods

Initial thickness measurements were carried out by layering sections of the as-coated foil samples between sheets of copper, mounting them in cross-section in bakelite followed by grinding and polishing. The cross-sections were then measured on the optical microscope. However, this proved unsatisfactory as the foil was only 10μm thick and the coatings were even thinner, which meant that the optical system was not accurate, especially since it was very difficult to ensure that the edge of the foil was mounted perfectly upright. It was impossible to distinguish the outer layers in the 5 layer coating system.

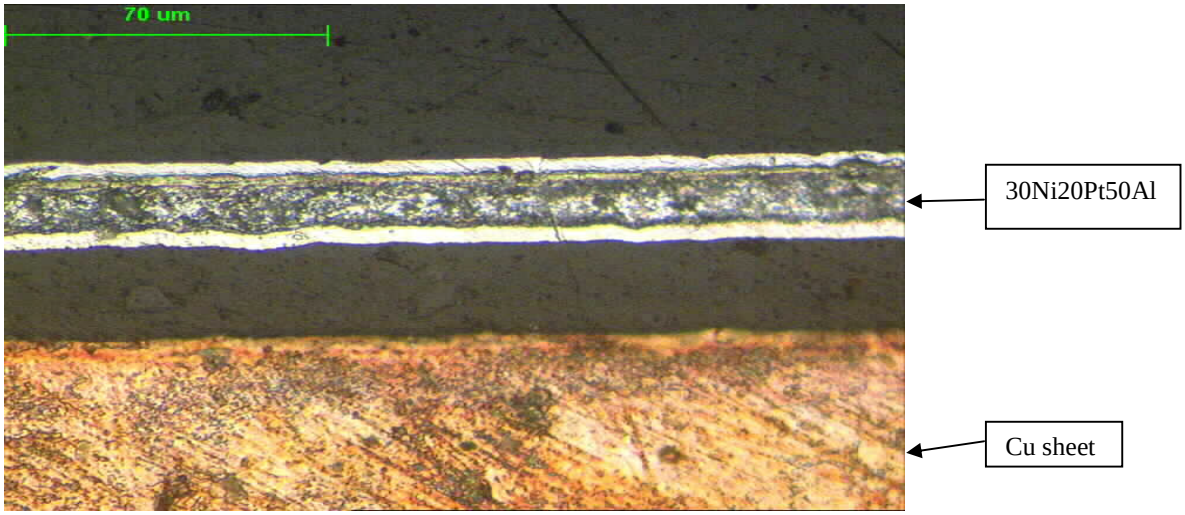

Figure 22 5 layer sample of nominal composition 30Ni20Pt50Al (Cu strip at base of photo)

4.4.2 Focused Ion Beam (FIB)

In order to obtain more accurate thickness measurements the Cranfield Focused Ion Beam system was used. This consisted of an FEI Strata 200xP FIB with a fine gallium beam used for milling, patterning and imaging in precise locations with 15-20nm resolution.

The Focused Ion Beam system (FIB) is similar to a Scanning Electron Microscope (SEM), except that a beam of excited gallium ions (Ga^{+}) replaces the conventional electron beam. The ion beam is generated using a liquid-metal ion source (LMIS) and a strong electric field is applied causing the emission of positively charged particles from a liquid gallium cone formed at the tip of a tungsten rod. (Figure 23)

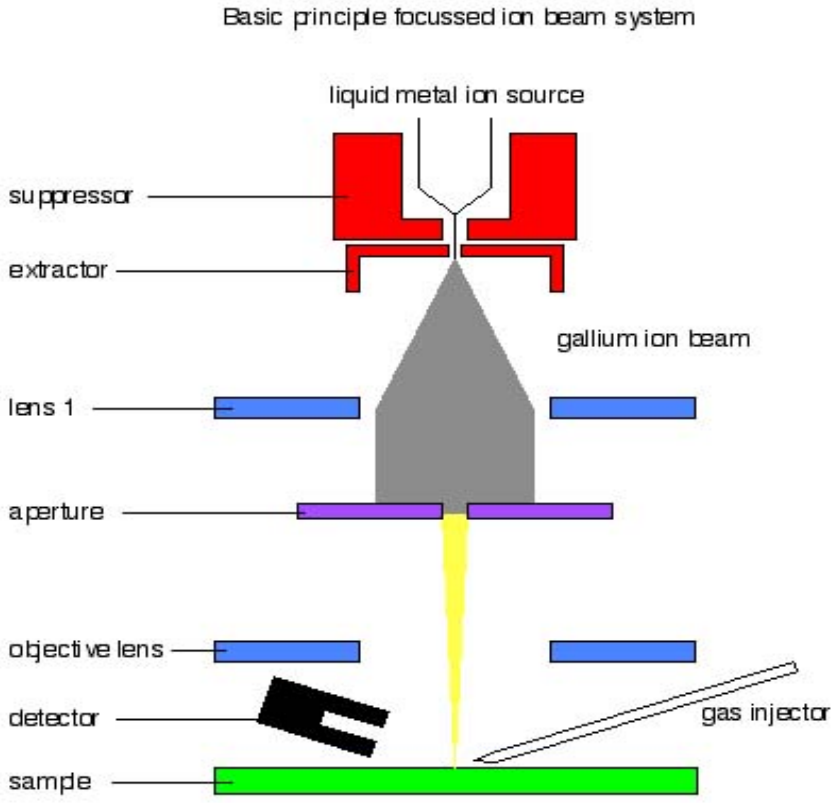

Figure 23 Schematic diagram illustrating the basic principle of a focused ion beam system.[135]

The beam energy is typically 30keV with a beam current in the range of 1 to 20nA. The best image resolution that can be obtained is 15 to 20nm.[135]

Ion beams were used to remove material from the coated foil samples, in order to measure the thickness of the multilayers. This involved milling a crater through the sample and imaging the front wall of the crater after tilting the image by 45˚. The craters were 15-20μm wide and were milled in several steps to create a 'stair-case' shape using a strong beam current (11500pA). The final milling of the wall was performed using scan lines of a lower beam current (1000pA), so that a flat, steep face was obtained. (Figure 24)

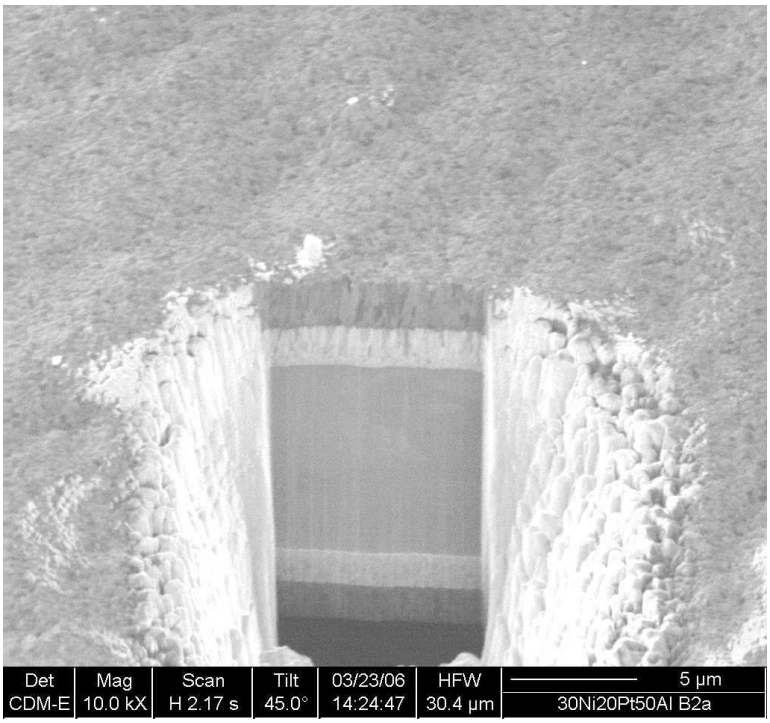

Figure 24 FIB image of nominal composition 30Ni/20Pt/50Al sample B2 - 5 layer system of nickel and platinum coated onto both sides of aluminium foil.

4.5 Differential Scanning Calorimeter (DSC)

The calorimetry was carried out in order to assess the transformation temperature of the intermetallic coatings using Setaram Setsys Evolution 16/18 apparatus with Setsoft 2000 software.

Thermal analysis is defined as the measurement of changes in chemical or physical properties of a sample, as a function of temperature or time, in a controlled atmosphere. Thermal analysis is used as an analytical tool to measure the physical and reactive properties of substances based on temperature:

- Thermal decomposition of solids and liquids
- Solid-solid and solid-gas chemical reactions
- Material specification, purity and identification
- Inorganic solid material adsorption
- Phase transitions

4.5.1 DTA/DSC Apparatus

DTA (differential thermal analysis) and DSC (differential scanning calorimeter) analysis remain the basic techniques for the thermal characterisation of materials at high temperature. The SETSYS Evolution uses a DTA/DSC rod hooked to the balance for simultaneous DTA and DSC measurements. The DTA device is more adapted to qualitative measurements, such as determination of the transition temperature, and the DSC device to quantitative measurements of heat flow.

The DTA/DSC rod consists of a machined metallic plate containing two housings for the measurement and reference crucibles, with a temperature control thermocouple in the central section of the plate (Figure 25). A four wire ceramic shaft receives the various thermocouples for measurement, reference and temperature control. The thermocouple

wires are made from Pt/PtRh10% which can be used over a temperature range of -50 to 1600ºC.

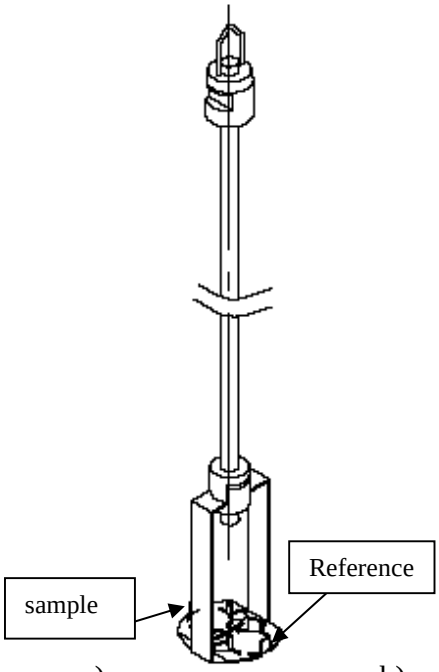

a)

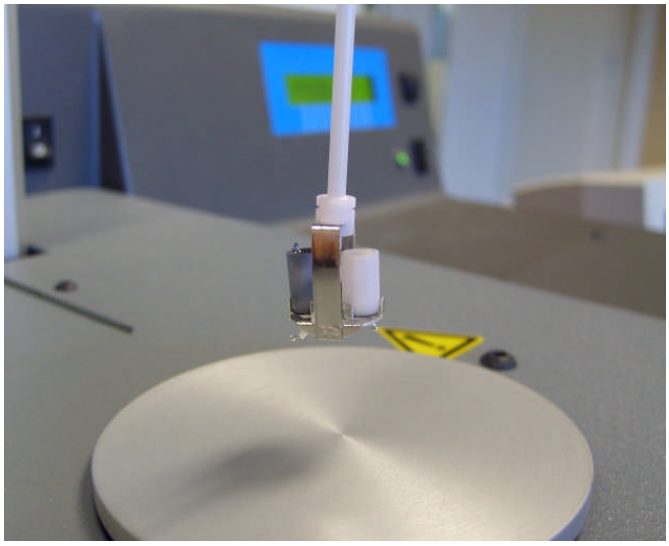

b)

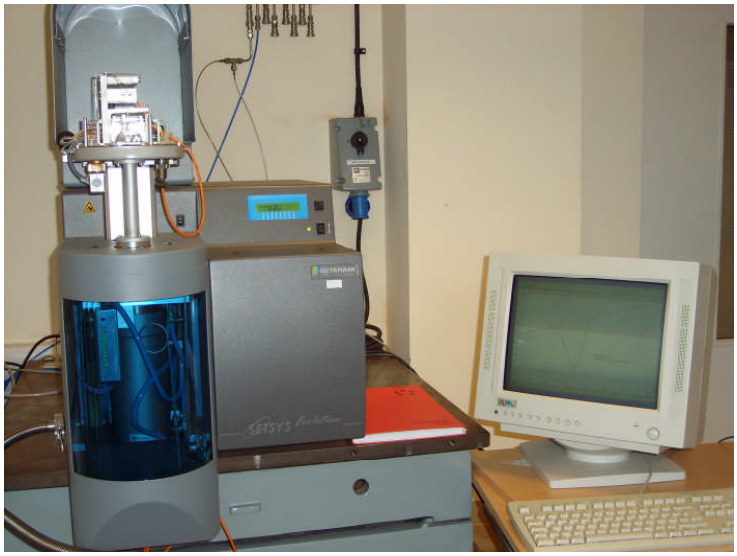

c)

Figure 25 a) Schematic of the DSC/DTA plate rod b) Photograph of the Setaram SETSYS Evolution with the alumina crucibles loaded, c) Setaram SETSYS Evolution

The differential thermocouple is connected to both the reference and sample holders and displays data as a differential temperature curve as a function of time or temperature. An endothermic reaction slows the heating rate because this reaction absorbs heat, leading to a negative heatflow (μV) between the sample and the reference. An exothermic reaction increases the heating rate because it gives out heat, leading to a positive heatflow.

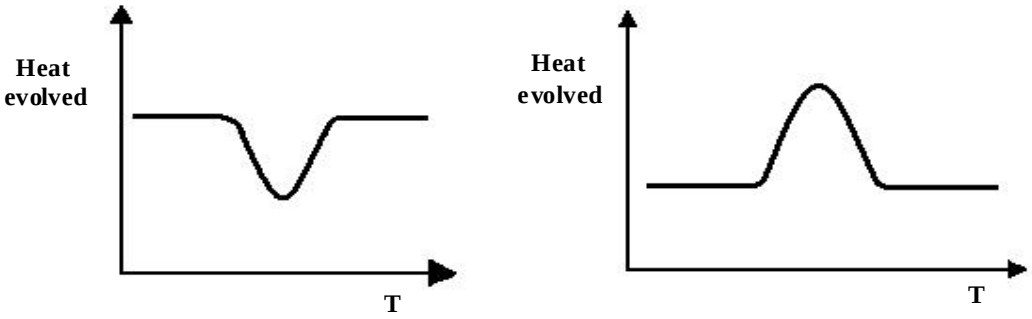

ENDOTHERMIC **EXOTHERMIC**

Figure 26 Endothermic and exothermic reaction curves

Prior to experimental use the DTA/DSC requires temperature calibration.

4.5.2 Temperature Calibration

DSC temperature calibration is carried out using pure materials of known melting temperature, such as zinc and aluminium, within the range of temperature to be used in subsequent experiments. The calibration materials were chosen, weighed and loaded into an alumina crucible which was placed onto the sample side of the DSC/DTA plate. An empty alumina crucible was placed on the reference side. The temperature was set to equilibrate to 100°C below the onset of the literature melting temperature of the chosen material, under an argon atmosphere in order to prevent oxidation. The material was then heated at the same heating rate as used in subsequent experiments, to 50°C above the literature melting temperature. The results were then analysed and compared to the literature values. These results were then sent to the instrument to update the calibration file.

99.999% pure zinc, aluminium and silver were used for the calibrations as these covered the temperature range required for the experiments.

Calibration Material	Melting Point (°C)	Standard Heat (J/g)
Zinc	419.6	107.4
Aluminium	660.3	401
Silver	961.8	104.8

Table 16 Thermal data for pure metals used for DSC calibration

The Al calibration curve can be seen in Figure 27. The melting point is taken as the onset point for temperature calibration purposes.

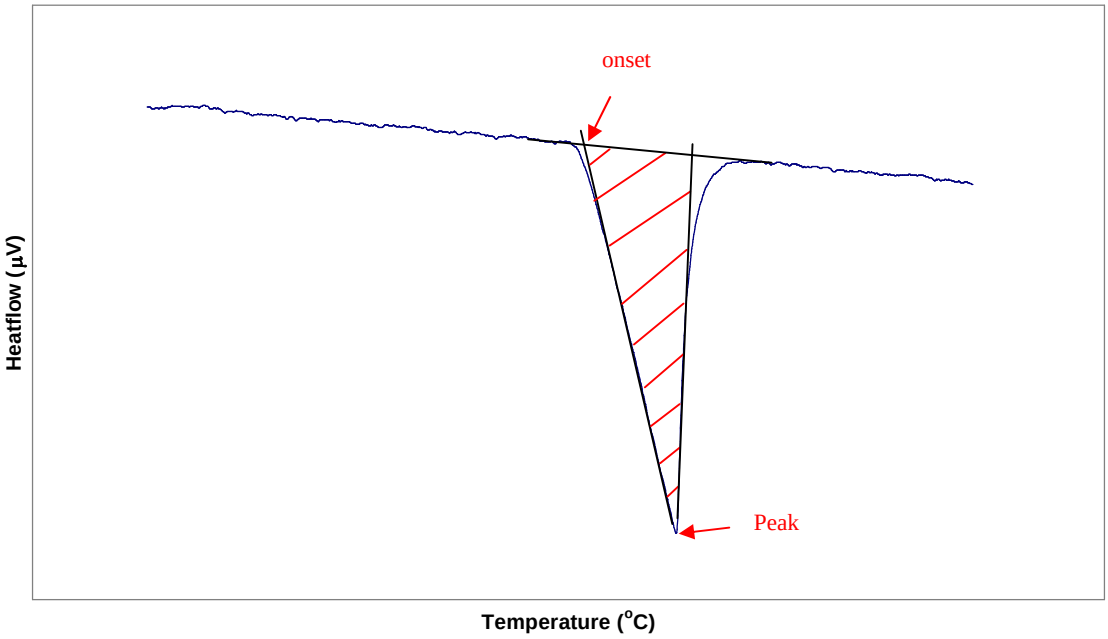

Figure 27 Diagram showing the onset temperature (melting point of pure metals), peak temperature and enthalpy (calculated from the shaded area under the curve) from a DSC graph

4.5.3 DSC Energy Calibration

The DTA is primarily a qualitative technique but by using the calibration standards to calibrate the DTA transducer, the coefficient of calibration, K, can be determined and the electrical signal, S (µV.s), can be transformed into an enthalpy value, H (J/g).

The coefficient of calibration varies with the following parameters:

- Sample shape and mass
- Temperature
- Properties of the crucible
- Properties of the transducer
- Properties and flow-rate of the sweeping gas
- Heating rate

It is, therefore, important that once the calibration has been carried out, the parameters are kept the same for all of the experimental tests.

The area under the curve in Figure 27 gives the heatflow for the sample (in μV.s). This value is calculated by the computer attached to the DSC using the Setsoft2000 software.

If the sample's transformation takes place within a limited temperature range, then a single point of calibration can be used by choosing the standard with a melting point closest to the transformation onset temperature.

Let **H** be the fusion heat content of the metal standard **(J/g)**
Let **S** be the area of the fusion peak **(μV.s)**
Let **m** be the mass of the standard analyzed **(g)**

The coefficient of calibration **K** at the standard's melting temperature is given by:

$$\mathbf{K = \frac{S}{mH}} \qquad \mathbf{(\mu V/W)}$$

For any experimental peak area, **A** (μV.s/mg), the enthalpy of transformation, **Q,** is given by:

$$\mathbf{Q = \frac{A}{K} \times 1000} \qquad \mathbf{(J/g)}$$

The accuracy of K can be improved by plotting a variation curve of calibration coefficient against the standards' measured melting temperature (T_{eim}).

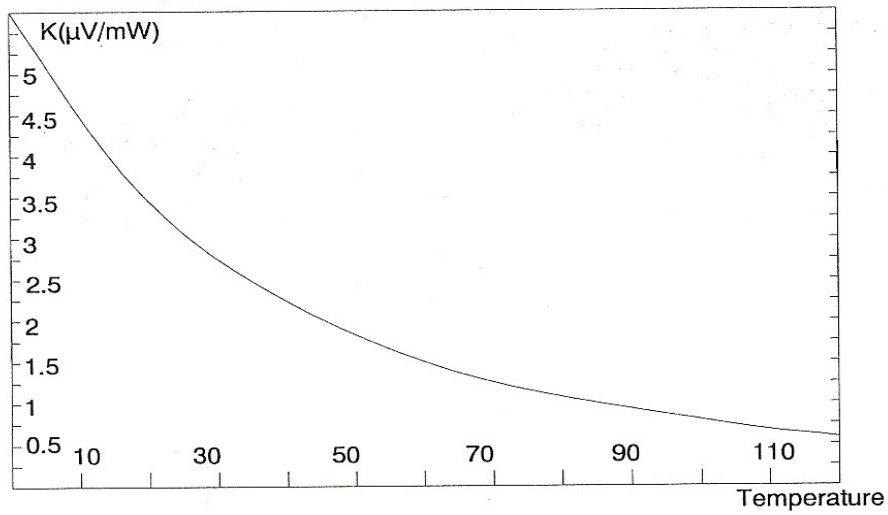

a)

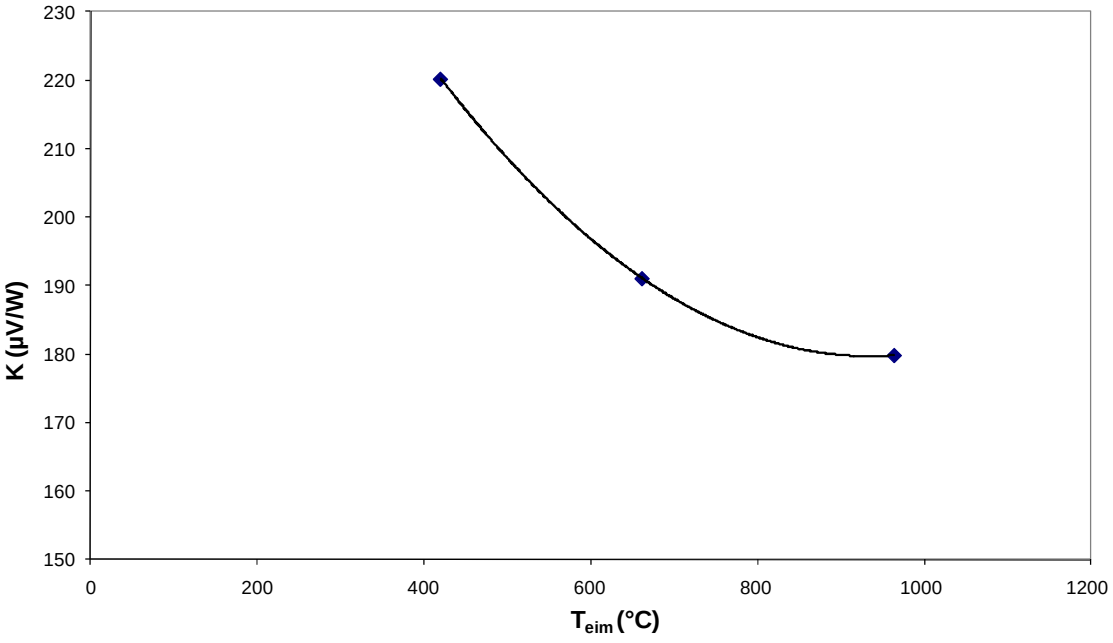

b)

Figure 28 a) Example of the DSC calibration curve shown in the Setaram operational manual; b) Experimental DSC Calibration curve for Zn, Al and Ag standards

As a general rule, since the DTA is designed for qualitative measurements the accuracy of quantitative heat measurement is of the order of 10%.

4.5.4 As-Coated Aluminium Foil Analysis

During B. Saint-Ramond's [136] DTA analysis of platinum aluminides, it was found that relatively thick substrates absorb the heat of the reaction and distort the DTA results. In order to prevent this from happening, thin aluminium foil was used as one layer of the coating and coated each side with nickel to form a three layer coating system with no substrate. The coatings were weighed and loaded into an alumina crucible which was placed onto the sample side of the plate. An empty alumina crucible was placed on the reference side of the plate.

The reaction temperature for NiAl was expected to be found between 550°C and 700°C, so the first run was performed between 450°C and 800°C to ensure that the correct temperature range was covered. The subsequent runs were carried out between 500ºC and 720ºC. The following conditions were used:

Type of Coating	Sample Weight (mg)	Temperature Range (°C)	Heating Rate (°C/min)	Atmosphere
3 layer coating, Ni Al Ni	3.2 – 4.6	500-700	5	Argon
5 layer coating, Pt Ni Al Ni Pt	3 .4– 4.8	500-700	5	Argon
5 layer coating, Ru Ni Al Ni Ru	3.6 – 4.2	520-720	5	Argon

Table 17 DSC conditions used for the NiAl, (Ni, Pt)Al and (Ni, Ru)Al analysis

4.5.5 As-Coated Nickel Foil Analysis

The reaction temperature for Ni_3Al was expected to be found at a similar value to the NiAl, therefore, the first run was performed between 450ºC and 800ºC to ensure that the correct temperature range was covered. The subsequent runs were carried out between 500ºC and 720ºC. The following conditions were used:

Type of Coating	Sample Weight (mg)	Temperature Range (°C)	Heating Rate (°C/min)	Atmosphere
3 layer coating, Al Ni Al	3.9 – 4.2	500-700	5	Argon
5 layer coating, Pt Al Ni Al Pt	3.9 – 4.4	500-700	5	Argon
5 layer coating, Ru Al Ni Al Ru	3.6 – 4.2	520-720	5	Argon

Table 18 DSC conditions used for the Ni_3Al, $(Ni, Pt)_3Al$ and $(Ni, Ru)_3Al$ analysis

4.6 X-Ray Diffraction (XRD)

X-ray diffraction was carried out on all of the reacted coatings following DSC analysis, in order to identify the intermetallic compounds formed.

X-ray diffraction (XRD) is a versatile, non-destructive analytical technique which makes use of the interaction between X-rays and matter, especially crystalline matter, or phases, present in powdered or solid samples. X-rays are part of the electromagnetic spectrum and are generated when high velocity electrons impinge on a solid. In an X-ray tube, the electrons usually originate from a glowing wire under high vacuum, the cathode. They are then directed by a high voltage towards the target, the anode, and impact at high velocity. X-rays are produced at the point of impact and the X-rays consist of a continuous spectrum on which sharp maxima are superimposed that are characteristic of the target material. Filters allow the transmission of monochromatised radiation.

X-ray diffraction means the coherent scattering by the electrons of the atoms in the crystal lattice. A diffracted beam is only produced where certain geometrical conditions are satisfied. This condition is explained by the Bragg equation.[137]

$$n\lambda = 2d\sin\theta$$

When a monochromatic X-ray beam with wavelength **λ** is incident on lattice planes in a crystal at an angle **θ**, diffraction only occurs when the distance travelled by the rays reflected from successive planes differs by a complete number **n** of wavelengths. By varying the angle θ, the Bragg's Law conditions are satisfied by different **d**-spacings in polycrystalline materials (Figure 29a).

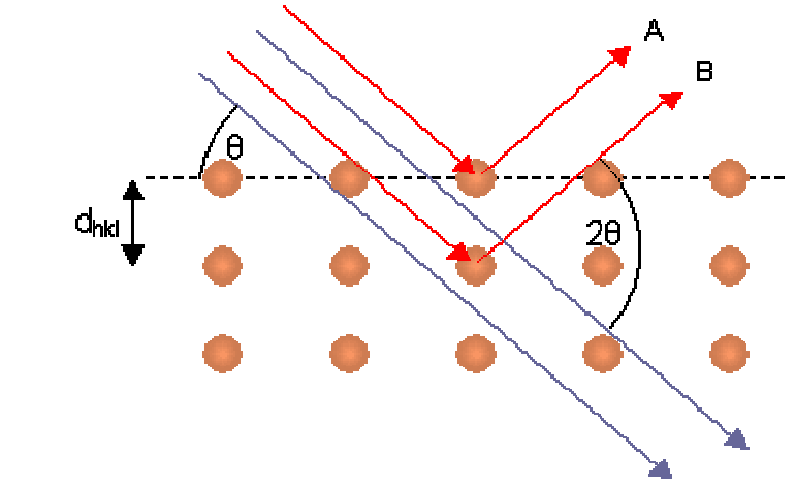

a)

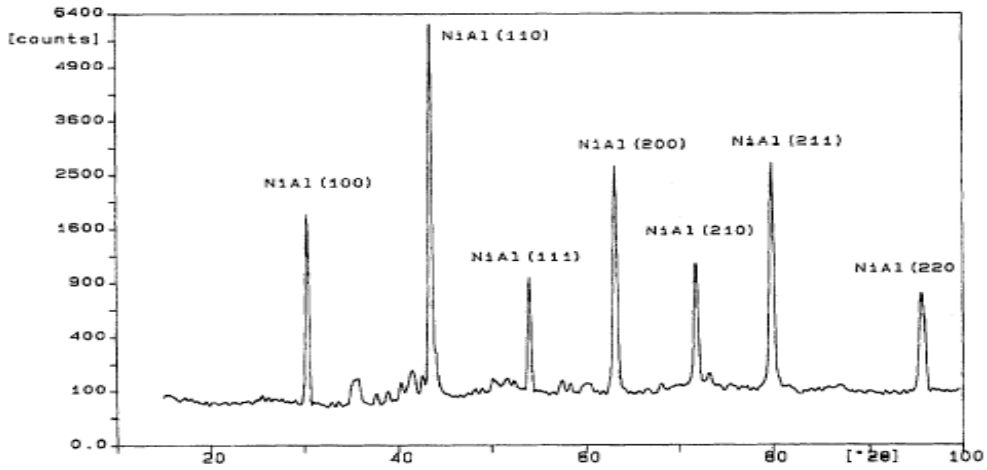

b)

Figure 29 a) Bragg reflection geometry [137]; b) XRD trace for Ni-Al.[138]

Plotting the angular positions and intensities of the resultant diffraction peaks produces a pattern that is characteristic of the sample.

Phase identification is essentially a comparative process whereby an X-ray pattern from an unknown substance is compared to a database containing reference patterns for thousands of elements and compounds.

The XRD work was carried out using a Siemens D5005 X-Ray Diffractometer with the DIFFRAC^{plus} X-ray diffraction software. The samples were analysed using X-rays generated from a copper target at 40kV and 30mA, in the 2θ range 20 to 90 degrees.

Table 19, Table 20, Table 21 and Table 22 give 2θ values for some of the common nickel aluminides, platinum aluminides, ruthenium aluminides and aluminium oxides.

Element or compound	Characteristic peaks
Ni	44.5 51.8 76.4 92.9 98.4
Al	38.5 44.7 65.1 78.2 82.4 99.1
$NiAl_3$	25.7 26.6 28.2 30.2 34.6 41.1 42.7 43.8 48.5 49 51.2 52.9 53.2 54 55.3 56.9 58.2 61.7
Ni_2Al_3	18.1 25.3 31.2 44.7 45.1 48.6 51.8 55.6 62.6 65.35 82.6 83.6
NiAl	31 44.4 55 64.5 73.3 81.6 98
Ni_5Al_3	26.5 33.9 43.5 48.7 54.5 56.3 71.4 76.2 87.6 96
Ni_3Al	24.7 35.2 43.6 50.7 63.6 75.1 91.3 96.7

Table 19 X-Ray diffraction peaks for nickel and aluminium (from software database)

Element or compound	Characteristic peaks
Pt	39.8 46.2 67.5 81.3 85.7
Pt_6Al_{21}	23.7 30.2 41.5 44.7 45.9
Pt_8Al_{21}	19.4 22.2 25.6 26 26.1 27.4 29.4 29.6 32.6 35.5 38.2 39.2 41.8 43 43.2 44.2 45.1 45.2 45.5 45.6 46.2 47.5 47.8 49.9 52 52.8 53.6 53.8 63.5 71.8 72.2 73 73.8 74.8
$PtAl_2$	26.1 30.2 43.3 51 53.6 62.8 69.1 71.5 79.2 85.1
Pt_2Al_3 [1]	24.4 25.5 30 43 53.2 61.5 88
PtAl	25.9 31.9 37 41.5 45.6 56.8 60 72.5
Pt_5Al_3 [2]	23.5 30 32.5 40.5 47.9 53.8 63
Pt_2Al	23.2 25.2 27.4 32.6 40.4 40.7 46.3 47.9 65.7 68.3 71.6 79.7 81.8 89.7

Table 20 X-Ray diffraction peaks for platinum and aluminium (from software database)

[1] Experimental values for Pt_2Al_3 taken from experimental values in reference 136
[2] Experimental values for Pt_5Al_3 taken from experimental values in reference 136

Element or compound	Characteristic peaks
Ru	38.4 43.2 44 58.3 69.4 78.4 84.7 86
$RuAl_6$	18 19.8 20.6 23.8 26.9 27.2 31.1 36.4 39.9 40.2 40.8 41.8 43.1 43.8 44.4 47.8 49.2 55.4 56.9 60.5 62.7 65.5
$RuAl_2$	24.1 30.2 36.4 37.8 40.1 41 43.5 44.5 45.2 45.8 50.1 57.8 61.6 62.2 62.7 63.2 64.6 66.7 67.3 68.8 70.2 78.3
Ru_2Al_3	12.4 24.9 29.7 34.6 41.4 43.1 48.9
RuAl	30.3 43.3 53.8 63 71.5 79.6

Table 21 X-Ray diffraction peaks for ruthenium and aluminium (from software database)

Element or compound	Characteristic peaks
δ-Al_2O_3	32.4 37 39.2 45.1 46.3 61 67.4
γ-Al_2O_3	33.2 37.3 39.5 41.4 45.8 46.6 60.1 67.4 85.1
σ-Al_2O_3	19.3 31.8 37.5 56.8 60.6 66.6
α-Al_2O_3	25.6 35.2 37.8 43.4 52.5 57.5 61.3 66.5 68.2 76.9 77.2 89
θ-Al_2O_3	16.3 19.6 31.5 32.8 35 36.8 38.9 39.9 44.9 47.6 50.7 60 62.4 64.1 67.5
η-Al_2O_3	19.3 31.9 37.4 39.7 46 66.8 85

Table 22 X-Ray diffraction peaks for aluminium oxides (from software database)

4.7 Energy Dispersive X-Ray Analysis (EDX)

EDX was carried out on a selection of the samples following DSC testing. Energy Dispersive X-ray (EDX) analysis is used for qualitative and quantitative element analysis. It is also sometimes referred to as EDS or EDAX analysis. The EDX analysis system works as an integrated feature of a scanning electron microscope (SEM), and cannot operate on its own. It is based on the spectral analysis of the characteristic X-ray radiation emitted from the sample atoms upon irradiation by the focused electron beam of the SEM. The Cranfield system consists of EDX equipment fitted on a FEI XL30 SFEG-SEM connected to a computer with Oxford Instruments INCA analysis software.

The incident beam electrons excite electrons from lower energy levels, prompting their ejection and resulting in the formation of electron holes within the atom's electronic structure. Electrons from an outer, higher-energy shell then fill the holes, and the excess energy of those electrons is released in the form of X-ray photons. The release of these X-rays creates spectral lines that are unique to individual elements. In this way the X-ray emission data can be analyzed to characterize the sample in question.

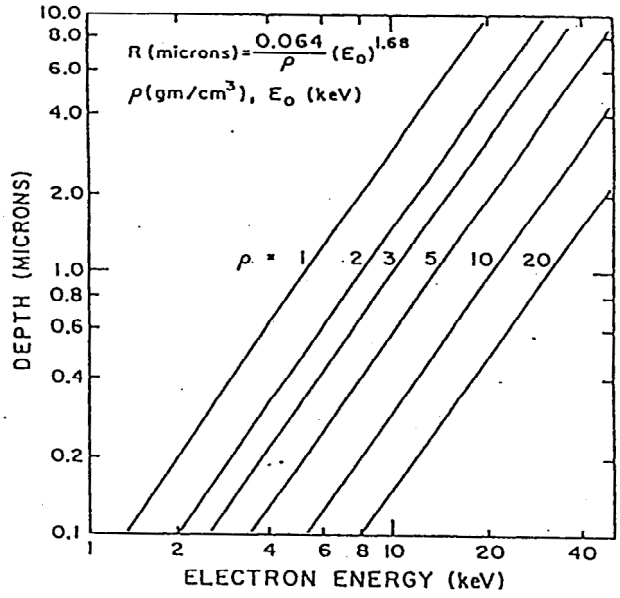

a)

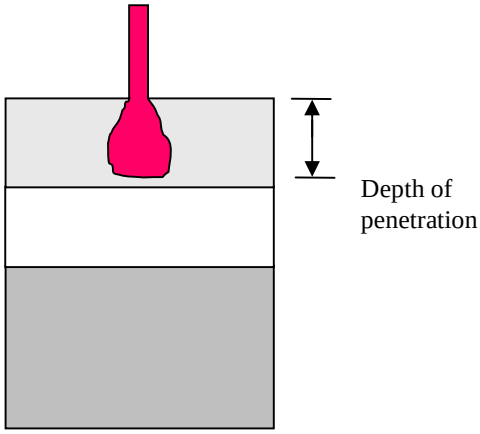

b)

Figure 30 a) Electron energy range with incident electron energy for different density materials [(139)]; b) Schematic showing depth of penetration of the electron beam

Figure 30a) shows the depth of penetration of the electron beam, which is linked to the density of the sample analysed. For a fully dense Pt outer layer, the penetration depth for a 20kV electron beam is ~ 0.5µm, for Ru ~0.8µm, for Ni ~1.1µm and for Al ~3.6µm.

The results given by EDX are an average of the elements present in the area tested. As Figure 30b) shows, if the multilayers have not completely diffused into each other and outwards to the outer layer of the sample to form a homogeneous coating, then only the outer layer is analysed. Therefore, the EDX is used to complement the XRD results.

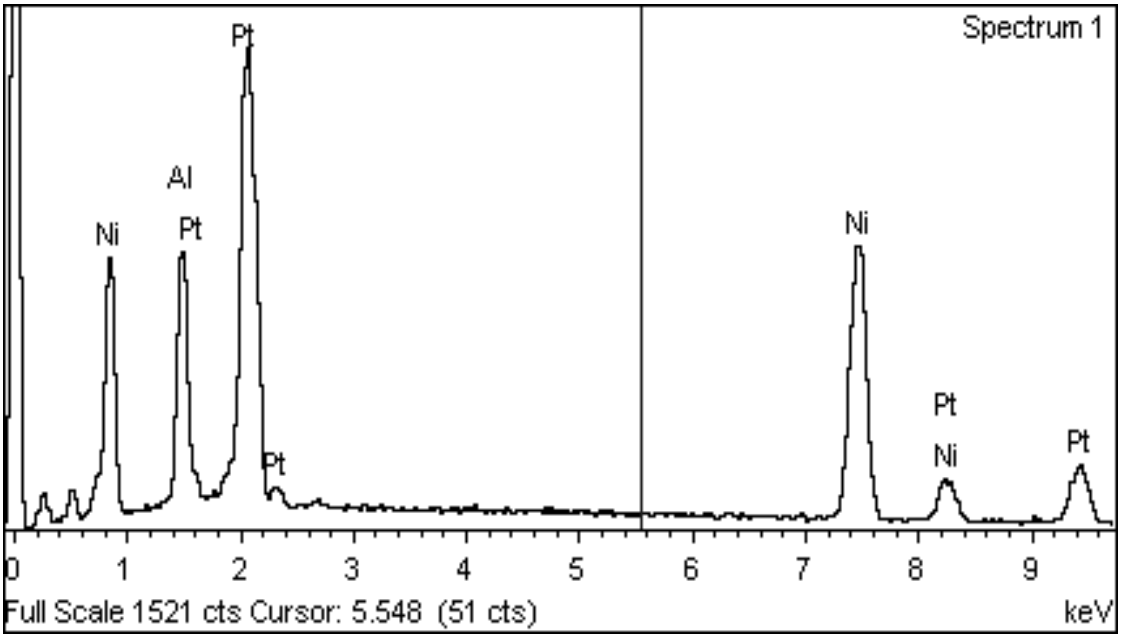

Figure 31 Example of a NiPtAl EDX linescan (generated during the course of this thesis).

The output of an EDX analysis is an EDX spectrum (Figure 31). The EDX spectrum is just a plot of how frequently an X-ray is received for each energy level. An EDX spectrum normally displays peaks corresponding to the energy levels for which the most X-rays had been received. The higher a peak in a spectrum, the more concentrated the element is in the specimen.

5.0 Results

5.1 Introduction

Thickness measurements were performed on the coated foil samples, in order to calculate their as-deposited nominal compositions. The results were plotted on the NiPtAl and NiRuAl ternary diagrams and a selection of the samples that fell within the β and γ′ phases were reacted in the Differential Scanning Calorimeter (DSC). The samples with the largest enthalpy values were then analysed using X-ray Diffraction (XRD) and Energy Dispersive X-ray (EDX) analysis in order to identify the phases produced.

5.2 Coating Characterisation

The deposition rate was not constant over the whole surface of the grid holding the foil. Each of the 16 samples obtained from each coating run has a slightly different composition, which means that it was possible to produce a range of compositions from one coating run.

The aim of the first deposition run was to produce a 3 layer system with NiAl stoichiometry by sputtering the required thickness of Ni onto a 10μm thick aluminium foil. Due to the large range of composition for binary NiAl, samples of nominal compositions 45Ni/55Al 50Ni/50Al and 55Ni/45Al were produced.

5.2.1 Optical Thickness Measurements

The thickness measurements obtained using the optical microscope are recorded in Table 23.

Since the densities of the sputtered coatings are less than those of the target materials (Figure 6), the compositions produced were calculated using the measured density value (section 4.4) for nickel of 8.6 g/cm^3.

Nominal Composition	Sample No.	Expected Ni thickness (μm)	Measured Ni thickness (μm)	Calculated compositions (at.%)
50Ni/50Al	A4	6.6	4.8	41Ni/59Al
	B2		6.5	49 Ni/51Al
	B3		6.0	47Ni/53Al
	C1		6.6	49Ni/51Al
	C2		6.2	48Ni/52Al
	C3		6.1	47Ni/53Al
45Ni/55Al	A2	5.4	6.0	47Ni/53Al
	B1		5.9	46.5Ni/53.5Al
	C4		5.0	42Ni/58Al
	D2		4.8	41Ni/59Al
	D3		5.0	42Ni/58Al
55Ni/45Al	B1	8.1	6.8	50Ni/50Al
	C1		7.3	52Ni/48Al
	D2		7.0	50.5Ni/49.5Al

Table 23 Thicknesses measured using the optical microscope (and resulting composition if all material present interdiffuses)

These samples were measured in cross-section using the optical microscope. However, this proved unsatisfactory as the coated foil was only ~20μm thick in total (Figure 22). This meant that the optical measurements were not accurate enough, especially since it was very difficult to ensure that the edge of the foil was mounted at a 90º angle. It was also impossible to distinguish the outer layers in the 5 layer coating systems.

5.2.2 FIB Thickness Measurements

FIB measurements were performed on several samples from each coating run in order to determine the exact atomic percentage of each element and to ensure that the correct number of layers could be observed. The measurement was taken in the centre of each sample. The results are shown in the tables below (after corrections for the tilt angle effects of the FIB).

5.2.2.1 β-NiAl

Nominal composition	Sample No.	Expected Ni thickness (μm)	Measured Ni thickness (μm)	Calculated compositions (at.%)
50Ni/50Al	A1	6.6	7.0	50.5Ni/49.5Al
	A2		7.7	53Ni/47Al
	A3		6.4	**48.5Ni/51.5Al**
	C4		6.8	**50Ni/50Al**
	D1		6.6	**49Ni/51Al**
	D2		7.4	**52Ni/48Al**
45Ni/55Al	A3	5.4	5.0	**42.5Ni/57.5Al**
	B2		5.6	**45Ni/55Al**
	B3		5.4	**44Ni/56Al**
	C2		6.1	**47Ni/53Al**
55Ni/45Al	A3	8.1	8.1	**54Ni/46Al**
	B2		10.2	60Ni/40Al
	B3		9.6	**58.5Ni/41.5Al**
	C2		9.8	59Ni/41Al
	C3		9.7	58.5Ni/41.5Al

Table 24 Thicknesses measured using the FIB system for β-NiAl (and resulting composition if all material present interdiffuses)

The samples in bold were chosen for DSC testing in order to give the stoichiometric composition of NiAl (50Ni/50Al) as well as a wide range of off-stoichiometric compositions within the β-NiAl region of the binary diagram (Figure 11) ranging from 43 atomic % Ni to 59 atomic % Ni.

Nominal composition	Sample No.	Expected Ni thickness (μm)	Measured Ni thickness (μm)	Expected Pt thickness (μm)	Measured Pt thickness (μm)	Calculated compositions (at.%)
45Ni/5Pt/50Al	B1	5.94	4.0	0.91	0.7	35Ni/5Pt/60Al
	B2		7.5		1.4	49.5Ni/6.5Pt/45Al
	C2		7.1		1.3	**48Ni/6Pt/46Al**
	C3		7.8		1.6	**49Ni/8Pt/43Al**
40Ni/10Pt/50Al	B2	5.28	6.1	1.82	2.5	41Ni/13Pt/46Al
	B3		5.8		2.4	**40Ni/12Pt/48Al**
35Ni/15Pt/50Al	B1	4.62	5.0	2.73	2.2	37.5Ni/11.5Pt/51Al
	B2		6.1		2.7	**41Ni/13Pt/46Al**
	B3		6.0		3.0	**40Ni/14.5Pt/45.5Al**
	C2		6.2		3.3	**40Ni/16Pt/44Al**
30Ni/20Pt/50Al	B2	3.96	4.2	3.64	4.4	30Ni/22Pt/48Al
	C1		3.7		3.8	**29Ni/20Pt/51Al**
	C2		4.1		4.2	**29Ni/22Pt/49Al**

Table 25 Thicknesses measured using the FIB system for β-NiAl with Pt additions (and resulting composition if all material present interdiffuses)

The measured densities for the sputtered Ni and Pt layers were 8.6 g/cm^3 and 20.8 g/cm^3 respectively. The samples in bold were chosen for DSC testing in order to have a range of Pt concentrations within the β-phase of the ternary nickel-platinum-aluminium ternary diagram (Figure 32).

Nominal composition	Sample No.	Expected Ni thickness (μm)	Measured Ni thickness (μm)	Expected Ru thickness (μm)	Measured Ru thickness (μm)	Calculated compositions (at.%)
45Ni/5Ru/50Al	A1	5.94	2.3	0.83	0.8	23Ni/7Ru/70Al
	B2		7.5		1.0	**50Ni/5Ru/45Al**
	B3		8.1		1.5	**51Ni/7Ru/42Al**
	C2		7.9		1.3	50Ni/7Ru/43Al
40Ni/10Ru/50Al	A1	5.28	2.7	1.66	1.0	26Ni/8Ru/66Al
	B2		7.4		1.6	**48Ni/8Ru/44Al**
	B3		6.7		2.2	**44Ni/11Ru/45Al**
	C2		7.4		1.8	48Ni/9Ru/43Al
35Ni/15Ru/50Al	A1	4.62	1.3	2.49	0.8	16Ni/7Ru/77Al
	B2		5.0		2.5	**36Ni/14Ru/50Al**
	B3		6.7		3.7	**40Ni/18Ru/42Al**
	C2		5.5		2.6	**38Ni/14Ru/48Al**

Table 26 Thicknesses measured using the FIB system for β-NiAl with Ru additions (and resulting composition if all material present interdiffuses)

The measured densities for the sputtered Ni and Ru layers were 8.6 g/cm^3 and 11.7 g/cm^3 respectively. The samples in bold were chosen for DSC testing in order to have a range of Ru concentrations within the β-phase of the ternary nickel-ruthenium-aluminium ternary diagram (Figure 33). Some of the samples fell outside this region and some samples had the same concentration of platinum and would only have repeated those results.

5.2.2.2 γ′-Ni_3Al

The samples in bold in the tables below were selected for further testing in the DSC, XRD and EDX.

Nominal composition	Sample No.	Expected Al thickness (μm)	Measured Al thickness (μm)	Calculated compositions (at.%)
75Ni/25Al (coated on one side)	B3	5.05	5.2	**77.5Ni/22.5Al**
	C3		5.3	**77Ni/23Al**
75Ni/25Al (coated both sides)	B2	5.05	3.4	84Ni/16Al
	C2		4.6	**79Ni/21Al**

Table 27 Thicknesses measured using the FIB system for γ′-Ni_3Al (and resulting composition if all material present interdiffuses)

The measured density of the sputtered Al layers was 2.3 g/cm^3. Two of the samples were coated on one side only in order to compare them with the other two samples coated on both sides. During DSC testing of these samples it was found that the samples coated on one side tended to have a problem with layers peeling. This was due to the fact that the layers were thicker, 5μm rather than 2.5μm. Therefore, sample C3 (74Ni/26Al) gave no DSC results and B3 (74.5Ni/25.5Al) gave only one result out of three samples. Sample C2 (77Ni/23Al) produced the usual three results during DSC.

The range of composition for γ′-Ni_3Al can be seen in Figure 11 to be much narrower than the range for β-NiAl. Therefore, there are fewer samples within this phase and sample B2 (85Ni/16Al) is too Ni-rich.

Nominal composition	Sample No.	Expected Al thickness (μm)	Measured Al thickness (μm)	Expected Pt thickness (μm)	Measured Pt thickness (μm)	Calculated compositions (at.%)
70Ni/5Pt/25Al	A1	5.41	4.7	0.99	0.7	**76Ni/4Pt/20Al**
	A4		6.9		1.6	67Ni/7Pt/26Al
	B3		9.2		1.5	61Ni/7Pt/32Al
	C3		9.3		1.3	62Ni/6Pt/32Al
	D1		4.6		1.3	**73Ni/7Pt/20Al**
	D4		7.1		1.0	67Ni/5Pt/28Al
60Ni/15Pt/25Al	A1	6.31	6.1	3.45	1.7	68Ni/8Pt/24Al
	A4		8.6		3.2	58Ni/13Pt/29Al
	B2		10.3		3.1	56Ni/12Pt/32Al
	C2		10.8		3.5	55Ni/13Pt/33Al
	D1		5.9		1.8	**68Ni/9Pt/23Al**
	D4		9.5		1.6	61Ni/6Pt/33Al
55Ni/20Pt/25Al	A1	6.89	6.1	5.01	2.1	**67Ni/10Pt/23Al**
	A4		10.0		4.6	52Ni/17Pt/29Al
	B3		12.4		5.3	48Ni/18Pt/34Al
	C3		12.0		5.7	48Ni/19Pt/33Al
50Ni/25Pt/25Al	A1	7.58	6.7	6.9	2.7	**64Ni/12Pt/24Al**
	A4		9.8		5.4	52Ni/20Pt/28Al
	B2		12.1		6.6	47Ni/21Pt/32Al
	C1		8.5		4.4	56Ni/17Pt/27Al
	C2		11.6		6.5	47Ni/22Pt/31Al
	D1		6.8		3.8	**60Ni/16Pt/24Al**

Table 28 Thicknesses measured using the FIB system for γ′-Ni_3Al with Pt additions (and resulting composition if all material present interdiffuses)

The compositions of the samples were calculated using the measured density values for Al and Pt of 2.3 g/cm^3 and 20.8 g/cm^3 respectively. As can be seen in the above table and in the ternary diagram in Figure 32, there were several samples with similar calculated compositions produced (assuming total interdiffusion). Therefore, only one sample at each concentration was selected for further testing in the DSC. At higher concentrations of Pt (>16 at.%), the concentration of Al was too high causing these samples to fall outside the γ′ phase.

Nominal composition	Sample No.	Expected Al thickness (μm)	Measured Al thickness (μm)	Expected Ru thickness (μm)	Measured Ru thickness (μm)	Calculated composition (at.%)
75Ni/5Ru/20Al	A1	5.41	3.7	0.9	0.8	**78Ni/5Ru/17Al**
	B1		5.0		0.9	**74Ni/5Ru/21Al**
	B2		7.1		0.9	67Ni/5Ru/28Al
	C2		7.2		1.0	67Ni/5Ru/28Al
70Ni/5Ru/25Al	A1	5.41	4.2	0.9	0.9	**77Ni/5Ru/18Al**
	B1		5.1		1.0	**73Ni/6Ru/21Al**
	B2		7.9		0.9	66Ni/5Ru/29Al
	C2		8.3		0.9	65Ni/5Ru/30Al
65Ni/10Ru/25Al	B3	5.83	2.4	1.93	2.6	76Ni/15Ru/10Al
	C2		2.2		1.5	80Ni/10Ru/10Al
	C3		2.1		2.2	78Ni/13Ru/9Al
	C4		2.0		2.5	77Ni/14Ru/9Al
60Ni/15Ru/25Al	B2	6.31	4.4	3.14	2.1	71Ni/11Ru/18Al
	C1		3.3		1.5	77Ni/9Ru/14Al
	C4		3.7		3.8	67Ni/19Ru/14Al
	D4		2.5		3.0	73Ni/17Ru/10Al

Table 29 Thicknesses measured using the FIB system for γ′-Ni_3Al with Ru additions (and resulting composition if all material present interdiffuses)

The compositions of the samples were calculated using the measured density values for Al and Ru of 2.3 g/cm^3 and 11.7 g/cm^3 respectively. As can be seen in the table above and in the ternary diagram (Figure 33), there were several samples with similar calculated compositions produced (assuming total interdiffusion). Also, the γ′ region of the nickel-ruthenium-aluminium ternary diagram is very small meaning that all of the samples fell outside of this region. The four samples (in bold) that were closest to the composition within the γ′ region were chosen for further testing, since the ternary diagram was produced

using computer generated results and if it was modelled experimentally, like the nickel-platinum-aluminium ternary diagram by Gleeson et al [(140)], it is possible that the γ'-Ni_3Al region would increase in size.

The atomic percentages indicated by the thickness measurements performed on the FIB and assuming total interdiffusion can be seen on the ternary diagrams in Figure 32 and Figure 33. The green dots indicate the samples that were reacted in the DSC.

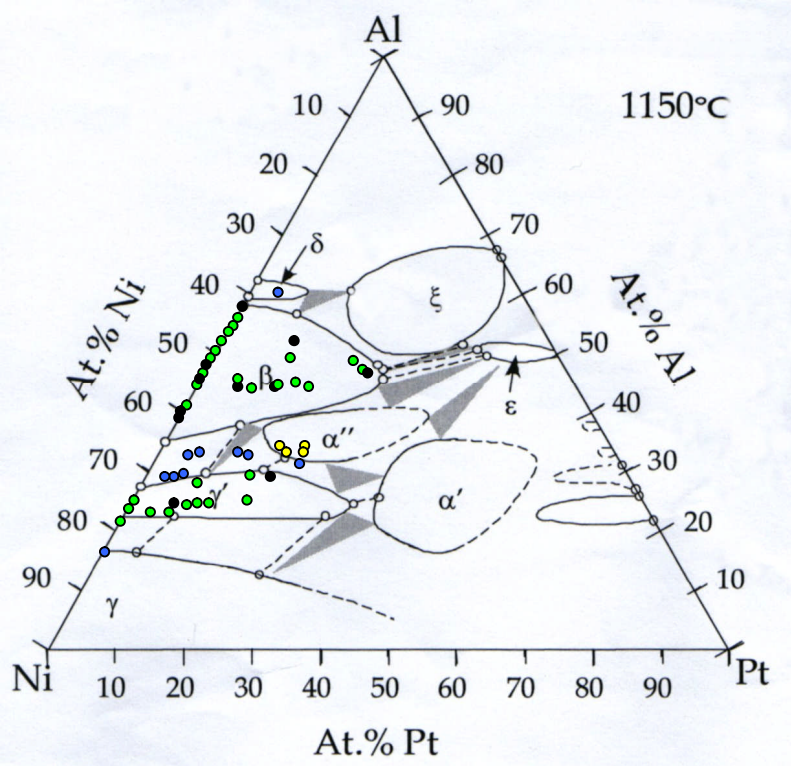

Figure 32 NiPtAl ternary diagram showing the concentrations of the sputtered multilayers.[(140)]

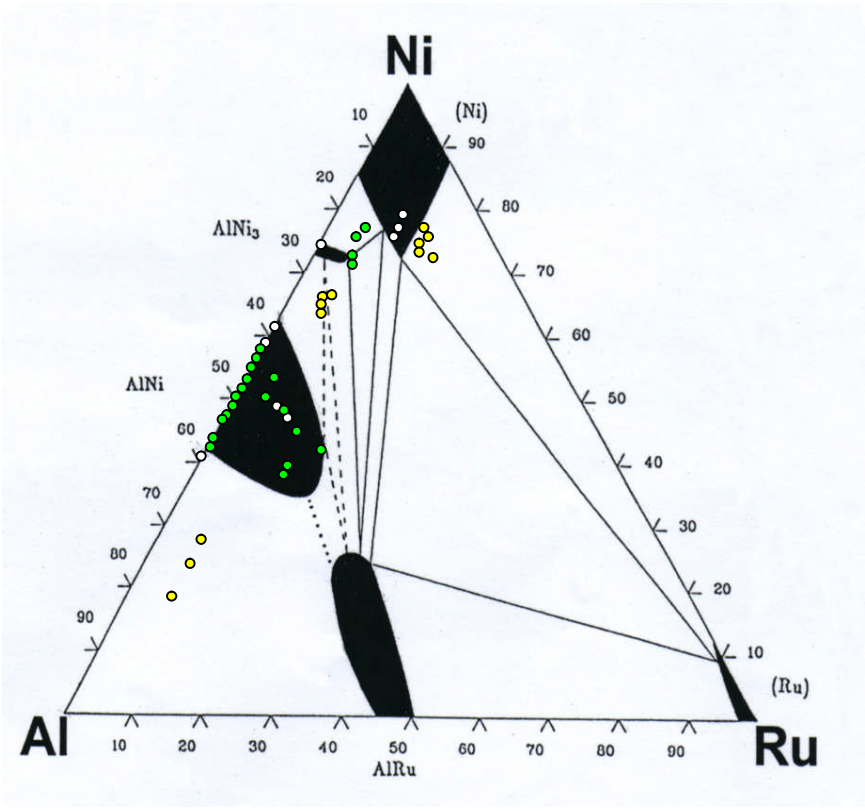

Figure 33 NiRuAl ternary diagram showing the concentrations of the sputtered multilayers.[141]

5.3 DSC Results

5.3.1 Al Calibration

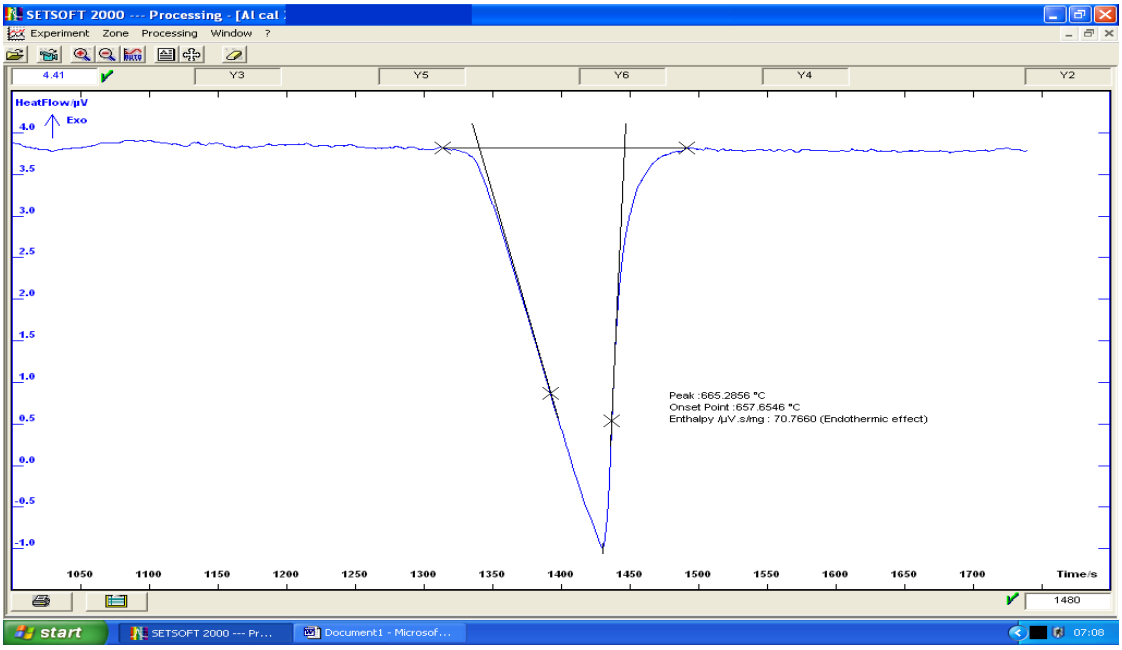

a)

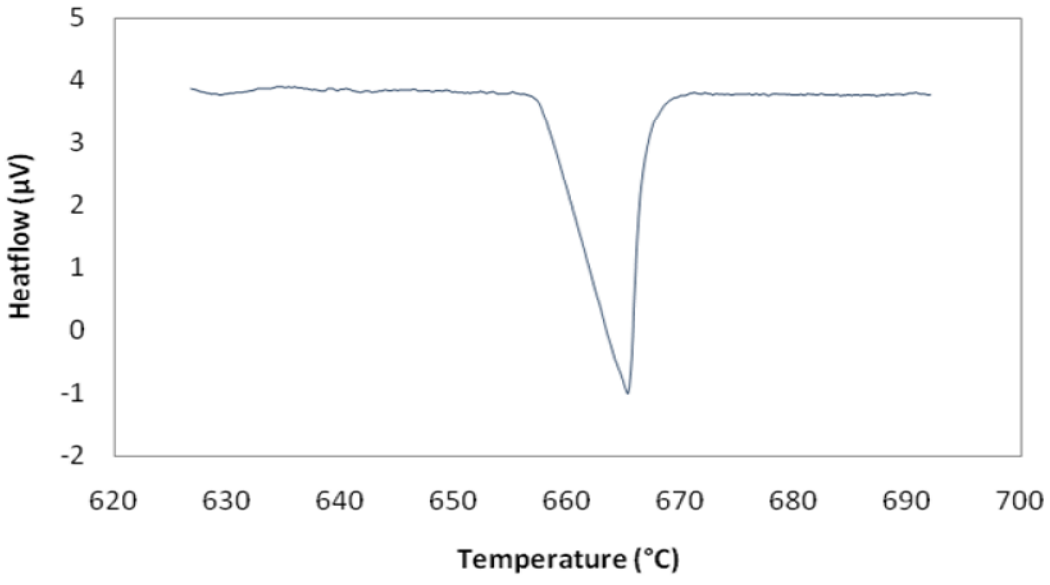

b)

Figure 34 DSC graph showing Al calibration curve; a) Screenshot from DSC showing Setsoft software, b) Graph produced from downloaded DSC data

Calibration runs were carried out before each batch of testing. Typical values are given in the tables below.

Zinc calibration standard	Theoretical value	Measured value
Melting point (ºC)	419.6	419.9
Enthalpy	107.4 (J/g)	23.87 (µV.s/mg)
Calibration coefficient K		222.26 (µV/W)

Table 30 DSC values obtained using the zinc calibration standard

Aluminium calibration standard	Theoretical value	Measured value
Melting point (ºC)	660.3	661.34
Enthalpy	401(J/g)	70.77 (µV.s/mg)
Calibration coefficient K		176.48 (µV/W)

Table 31 DSC values obtained using the aluminium calibration standard

Silver calibration standard	Theoretical value	Measured value
Melting point (ºC)	961.8	964.28
Enthalpy	104.8 (J/g)	15.52 (µV.s/mg)
Calibration coefficient K		148.07 (µV/W)

Table 32 DSC values obtained using the silver calibration standard

The melting point data was used to calculate the correction values for the DSC furnace thermocouples and the enthalpy value was fed into the calculation on page 74 in order to calculate the calibration coefficient, K. The K value was then used to convert the tested enthalpy values from μV.s/mg to a more recognised value.

The enthalpy values in μV.s/mg obtained using the Setsoft2000 software were compared with data obtained by calculating the area under the reaction peak for some of the samples. These results were within +/- 16 μV.s/mg or +/- 8 kJ/mol of each other.

5.3.2 β-NiAl

3 samples were tested in the DSC for each composition. A selection of the graphs produced is shown below. The labels used for all samples refer to the calculated average nominal compositions of the samples in at.%.

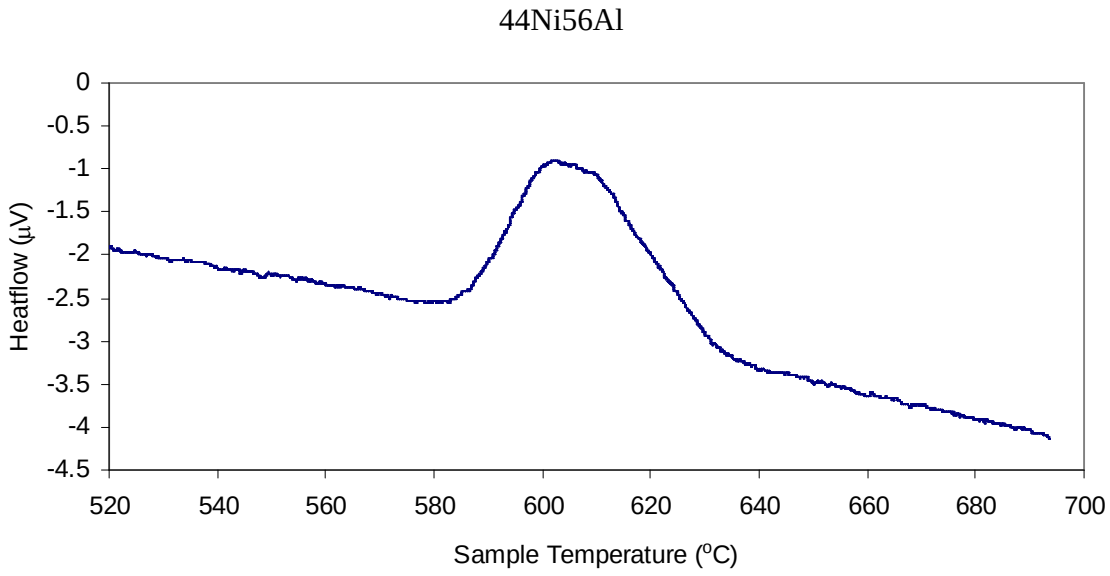

Figure 35 DSC graph from a single '44Ni56Al' sample reaction (exothermic)

47Ni53Al

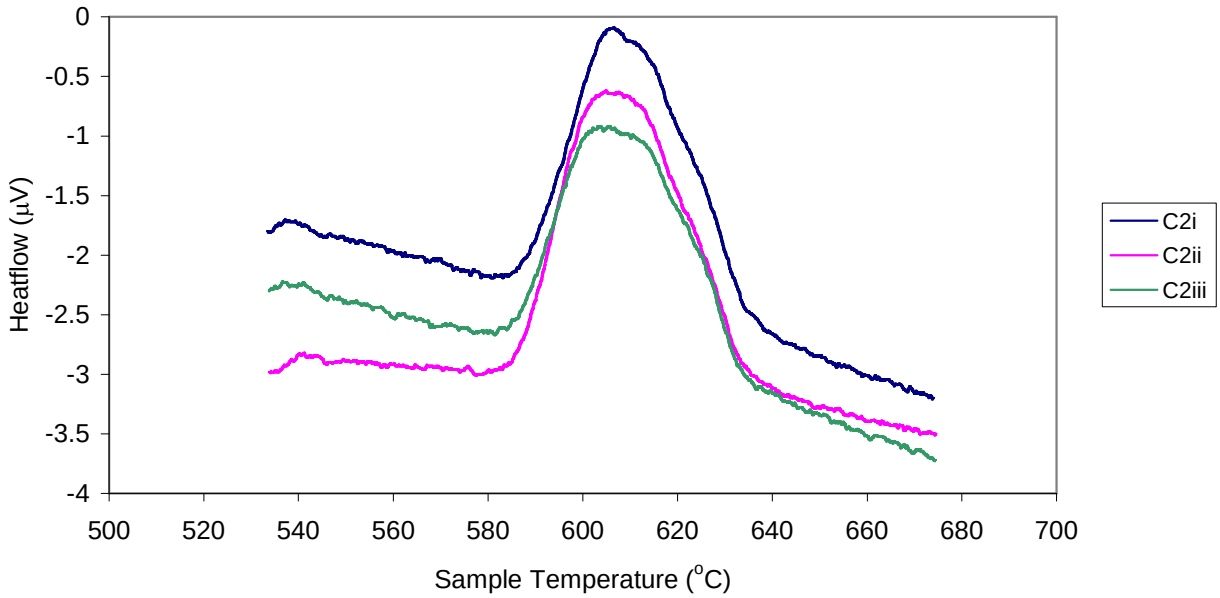

Figure 36 DSC graph showing '47Ni53Al' sample reaction curves

49Ni51Al

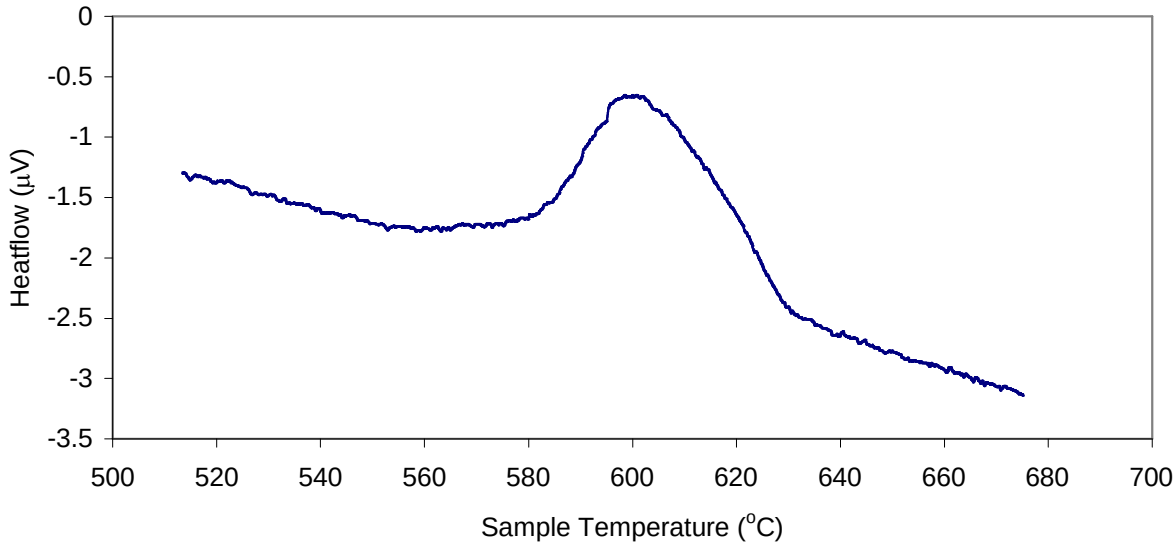

Figure 37 DSC graph showing a '49Ni51Al' sample reaction curve

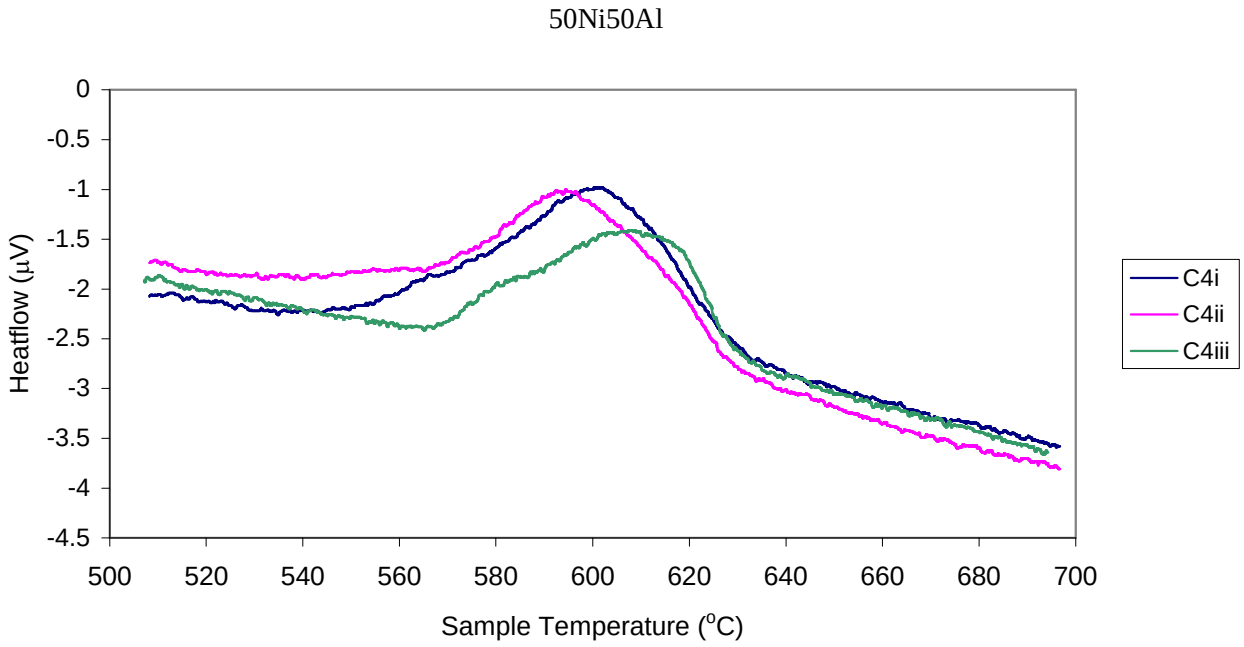

Figure 38 DSC graph showing '50Ni50Al' sample reaction curves

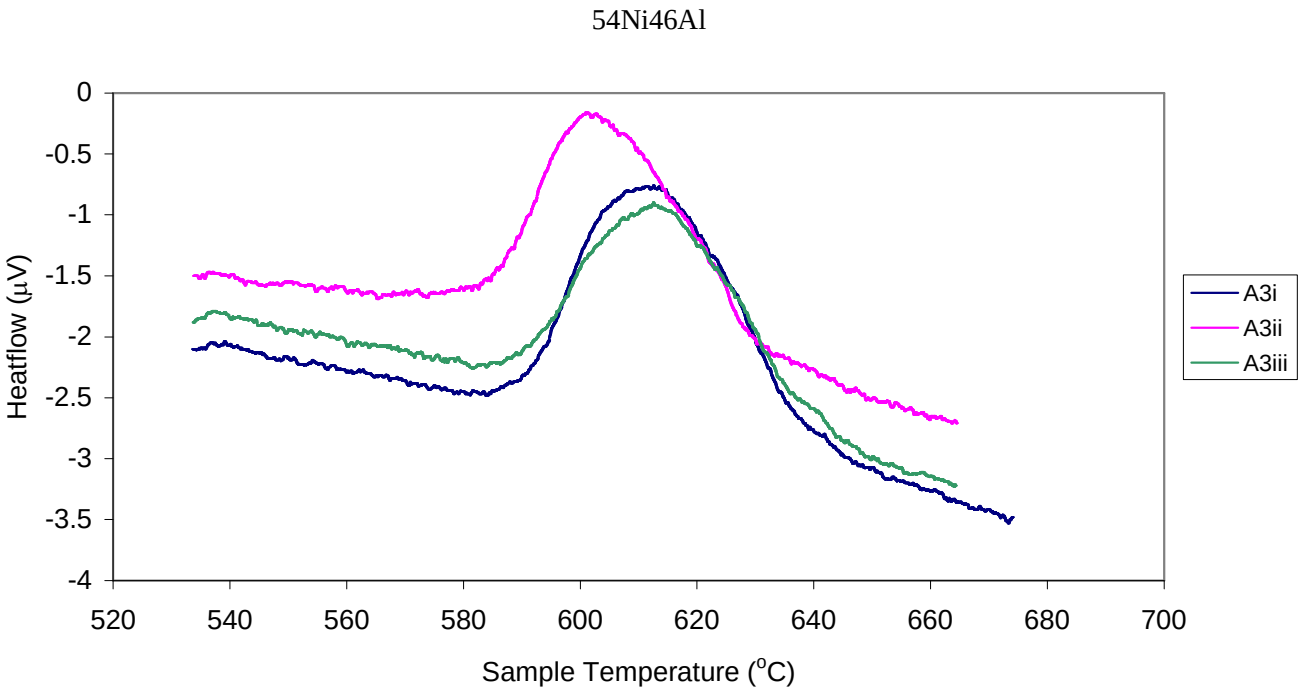

Figure 39 DSC graph showing '54Ni46Al' sample reaction curves

The samples all produced exothermic reactions. The 44% Ni and 47% Ni samples both have a small peak to the right hand side of the reaction peak with not much scatter between the three samples. The 50% Ni sample has a wider reaction peak with a similar depth. C4iii shows a small peak to the left hand side of the reaction peak. 50% Ni and 54% Ni both have more scatter between the three samples than the other NiAl compositions.

The data obtained from the β-NiAl DSC reaction curves in the following table:

Calculated average nominal compositions (at.%)	Onset Temperature (°C) (output from DSC)	Enthalpy (kJ/mol) (output from DSC)
42.5Ni57.5Al	588.6 +/- 1.1	-74.8 +/- 3.3
44Ni56Al	589.8 +/- 1.1	-67.2 +/- 2.0
45Ni55Al	588.0 +/- 0.5	-76.0 +/-1.1
47Ni53Al	589.7 +/- 2.0	-81.8 +/- 3.9
48.5Ni51.5Al	570.8 +/- 0.8	-65.7 +/-2.8
49Ni51Al	585.5 +/- 4.9	-67.5 +/- 2.1
50Ni50Al	576.9 +/-3.2	-71.3 +/- 12
52Ni48Al	578.7 +/- 2.5	-58.1 +/- 14.9
54Ni46Al	591.8 +/- 2.9	-61.3 +/- 10.1
58.5Ni41.5Al	591.1 +/- 2.0	-48.0 +/- 9.6

Table 33 DSC data for β-NiAl (average values from 3 samples +/- std dev.). Automated calculations output from the DSC

The complete set of data obtained from the β-NiAl DSC reaction curves can be found in Appendix 1.

5.3.3 (Ni, Pt)Al

3 samples were tested in the DSC for each composition. A selection of the graphs produced is shown below. The labels used for all samples refer to the calculated average nominal compositions of the samples in at.%.

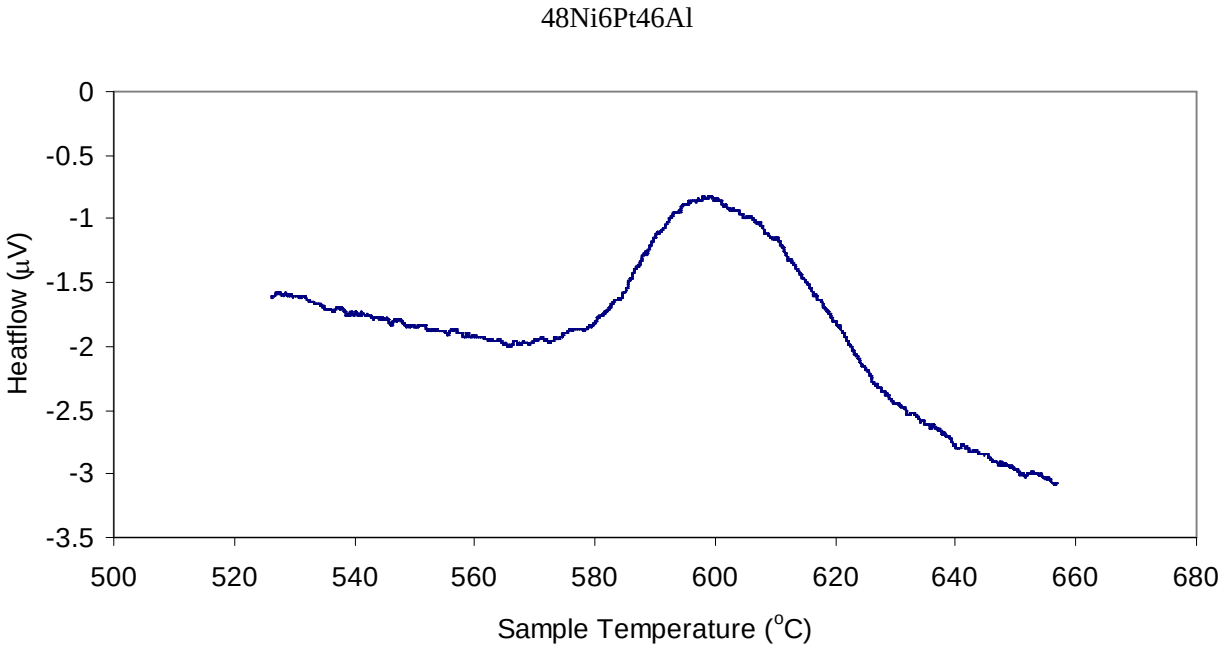

Figure 40 DSC graph showing '48Ni6Pt46Al' reaction curve

41Ni13Pt46Al

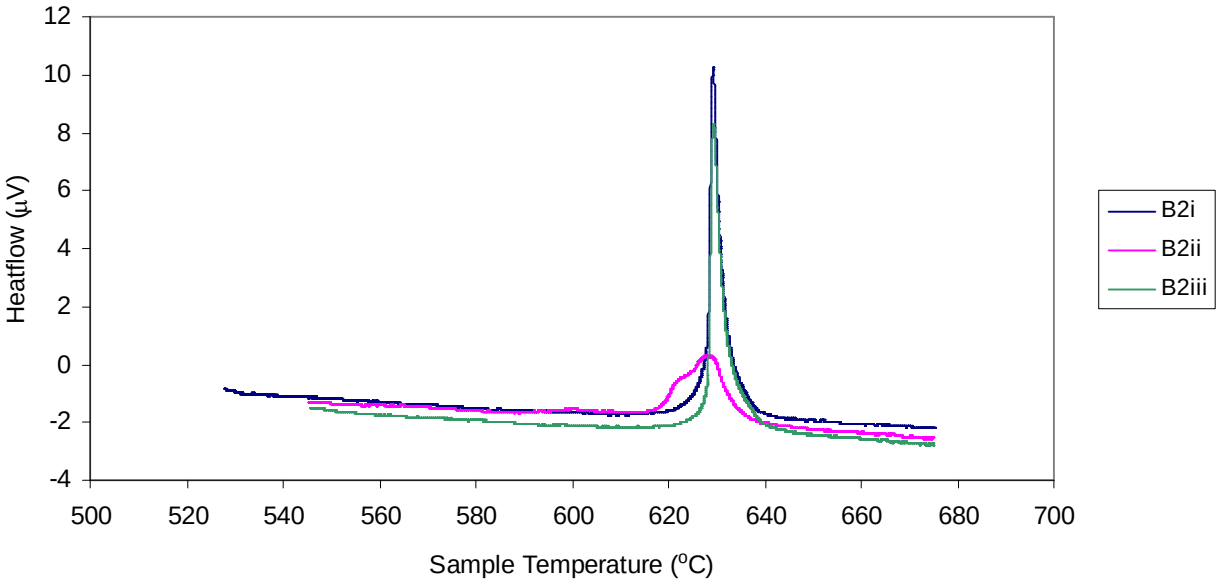

Figure 41 DSC graphs showing '41Ni13Pt46Al' reaction curves

40Ni16Pt44Al

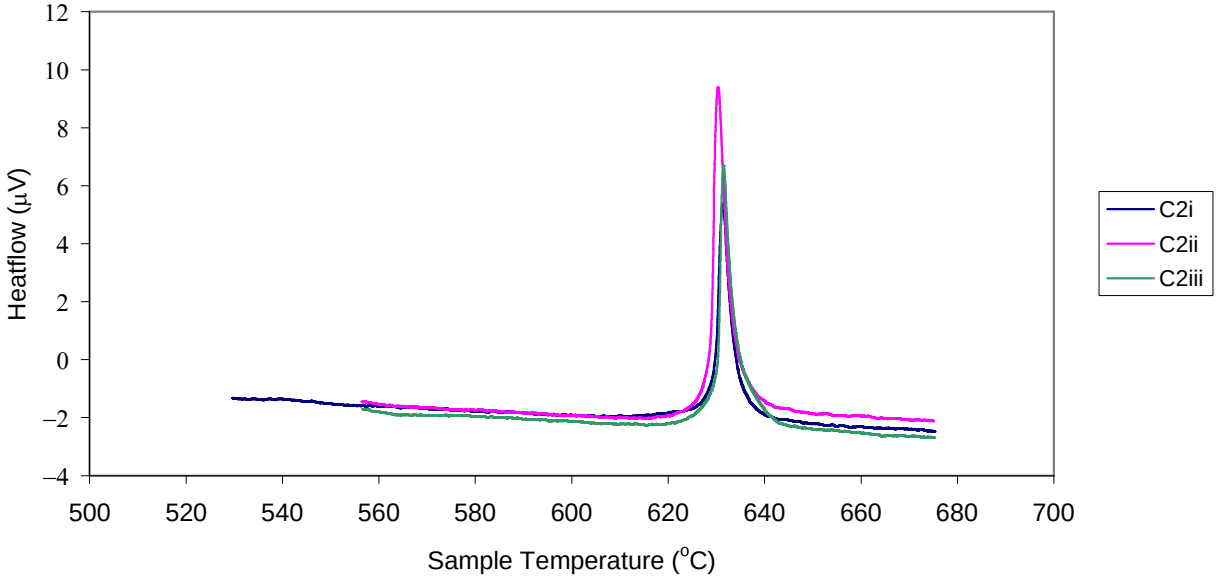

Figure 42 DSC graphs showing '40Ni16Pt44Al' reaction curves

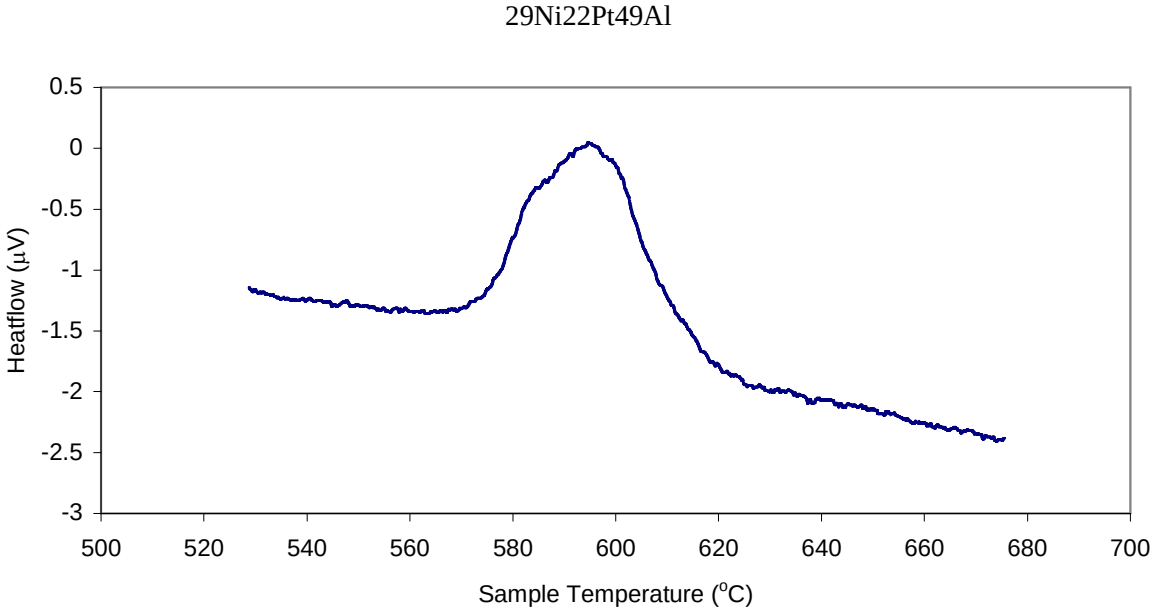

Figure 43 DSC graph showing '29Ni22Pt49'Al reaction curve

As can be seen from the DSC graphs above, the samples containing 13% Pt and 16% Pt have sharper reaction peaks. The 14.5% Pt sample also has this sharper peak. This has led to a higher reaction temperature, but similar enthalpy values. The 13% Pt graph shows that two of the samples had this sharp peak, whereas one of the samples (B2ii) had a wider peak. This sample had a lower onset temperature (618ºC), a lower enthalpy value (52.47 kJ/mol) but a similar peak temperature (628ºC) to the other two (onset temp. 628ºC and 628ºC, enthalpy 64 kJ/mol and 66.5 kJ/mol, peak temp. 629ºC and 629ºC).

The data obtained from the (Ni, Pt)Al DSC reaction curves is summarised below:

Calculated average nominal compositions (at.%)	Onset Temperature (°C) (output from DSC)	Enthalpy (kJ/mol) (output from DSC)
48Ni6Pt46Al	584.7 +/- 1.9	-79.2 +/- 10.2
49Ni8Pt43Al	573.5 +/- 2.9	-66.4 +/- 5.2
40Ni12Pt48Al	587.2 +/- 1.4	-62.0 +/- 10.4
41Ni13Pt46Al	624.9 +/- 5.6	-60.1 +/- 7.4
40Ni14.5Pt45.5Al	629.0 +/- 0.4	-70.2 +/- 5.5
40Ni16Pt44Al	629.6 +/- 0.6	-69.1 +/- 10.1
29Ni20Pt51Al	580.4 +/- 3.6	-66.6 +/- 6.8
29Ni22Pt49Al	577.5 +/- 1.7	-77.1 +/- 3.9

Table 34 DSC data for β-NiAl with Pt additions (average values from 3 samples +/- std dev). Automated calculations output from the DSC

The complete data set can be found in Appendix 1.

5.3.4 (Ni, Ru)Al

3 samples were tested in the DSC for each composition. A selection of the graphs produced is shown below. The labels used for all samples refer to the calculated average nominal compositions of the samples in at.%.

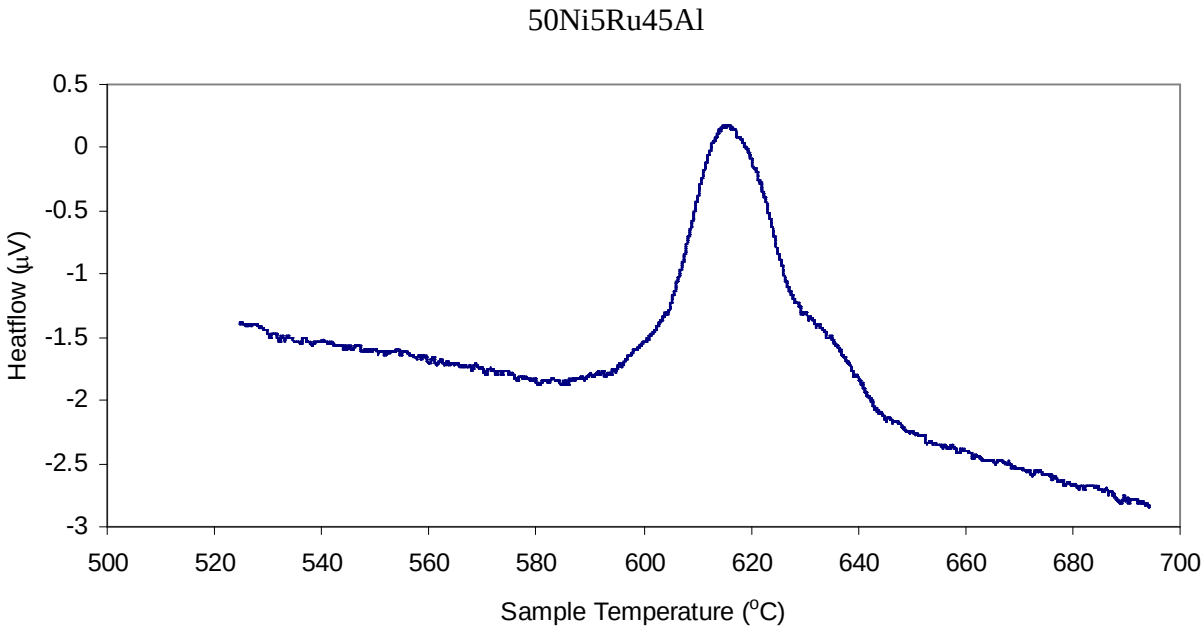

Figure 44 DSC graph showing '50Ni5Ru45Al' reaction curve

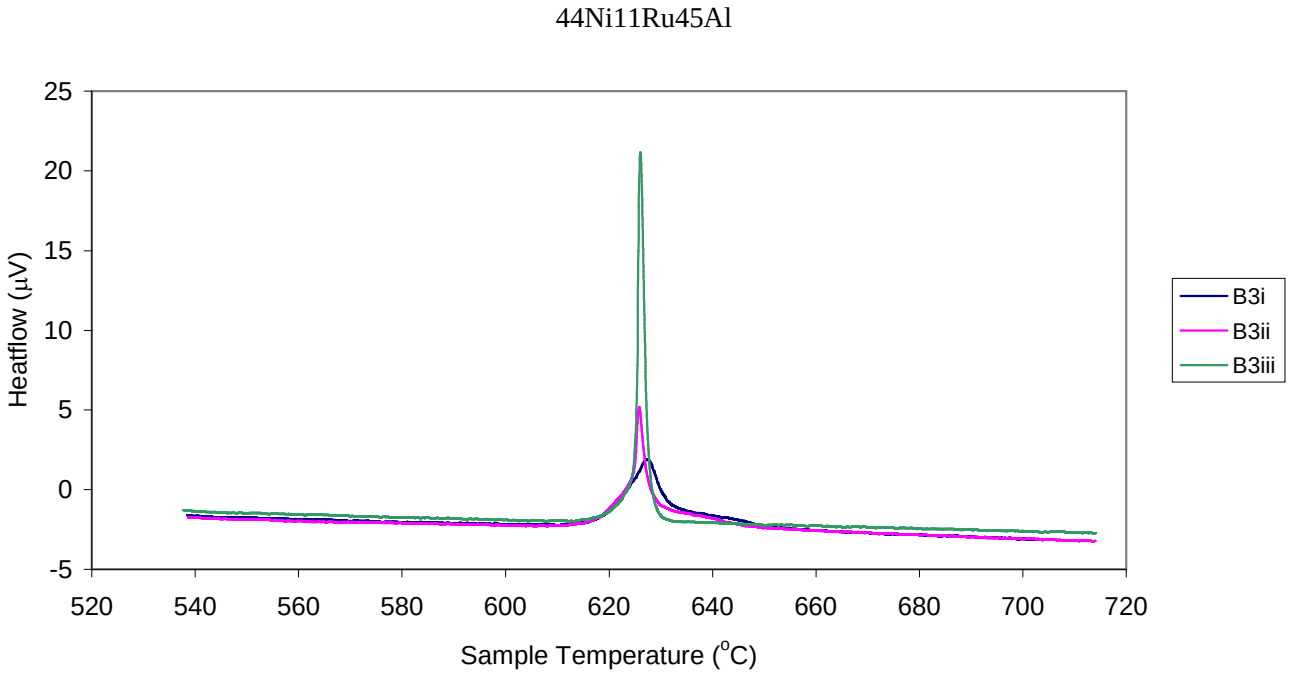

Figure 45 DSC graphs showing '44Ni11Ru45Al' reaction curves

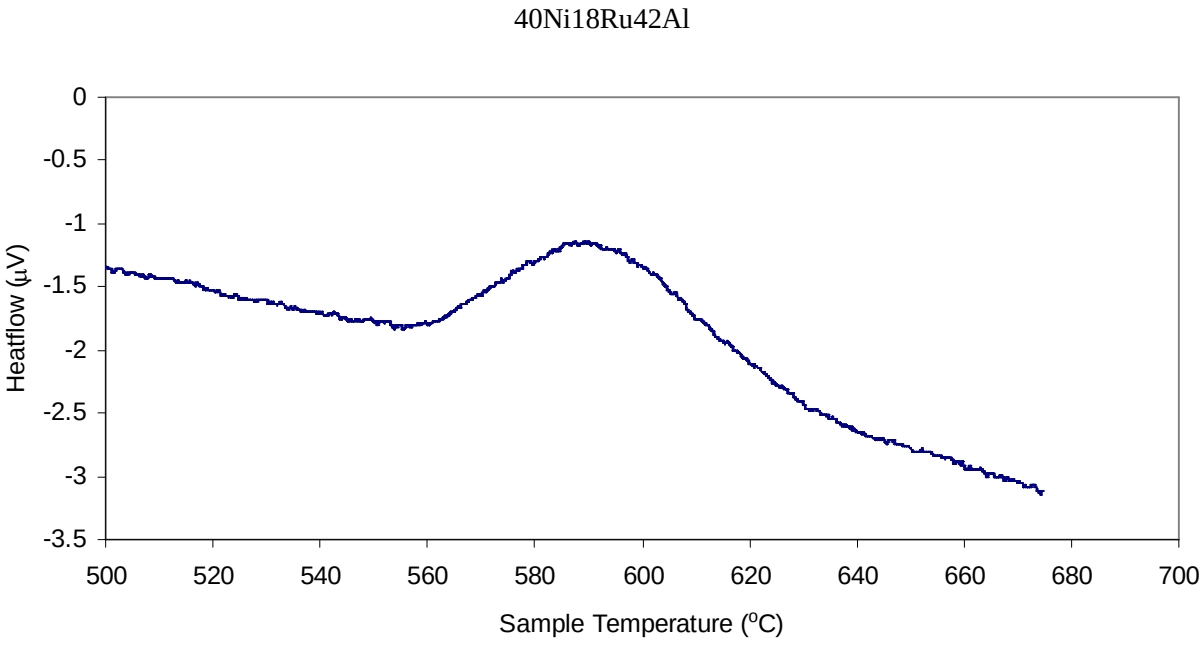

Figure 46 DSC graph showing '40Ni18Ru42Al' reaction curve

As can be seen from Figure 44, the sample containing 5% Ru, had a small peak to the right hand side of the main reaction peak. The reaction peaks for 7% Ru and 8% Ru samples also had this small peak. The 11% Ru B3iii sample had a sharp peak the same as the 13-16% Pt samples, whilst the B3i and B3ii samples had shallower peaks. The 18% Ru sample had a wide, shallow reaction peak.

The data obtained from the (Ni, Ru)Al DSC reaction curves is summarised below:

Calculated average nominal compositions (at.%)	Onset Temperature (°C) (output from DSC)	Enthalpy (kJ/mol) (output from DSC)
50Ni5Ru45Al	607.4 +/-4.9	-77.1 +/-15.1
51Ni7Ru42Al	602.8 +/- 2.0	-81.4 +/- 1.4
48Ni8Ru44Al	611.1 +/- 5.0	-78.2 +/- 4.9
44Ni11Ru45Al	623.4 +/- 1.9	-77.6 +/- 5.7
36Ni14Ru50Al	588.8 +/- 2.3	-64.3 +/- 1.8
38Ni14Ru48Al	584.2 +/-19.1	-75.1 +/- 4.2
40Ni18Ru42Al	566.6 +/- 14.4	-77.9 +/- 6.5

Table 35 DSC data for β-NiAl with Ru additions (average values from 3 samples +/- std dev). Automated calculations output from the DSC

The complete data set can be found in Appendix 1.

5.3.5 γ′-Ni_3Al

3 samples were tested in the DSC for the sample with aluminium coated onto both sides of the nickel foil, 79Ni21Al. However, due to a problem with the layers peeling during heating, the samples with aluminium coated onto only one side of the nickel foil, 77.5Ni22.5Al and 79Ni21Al had only one result and no results respectively. An example of the graphs produced is shown below. The labels used for all samples refer to the calculated average nominal compositions of the samples in at.%.

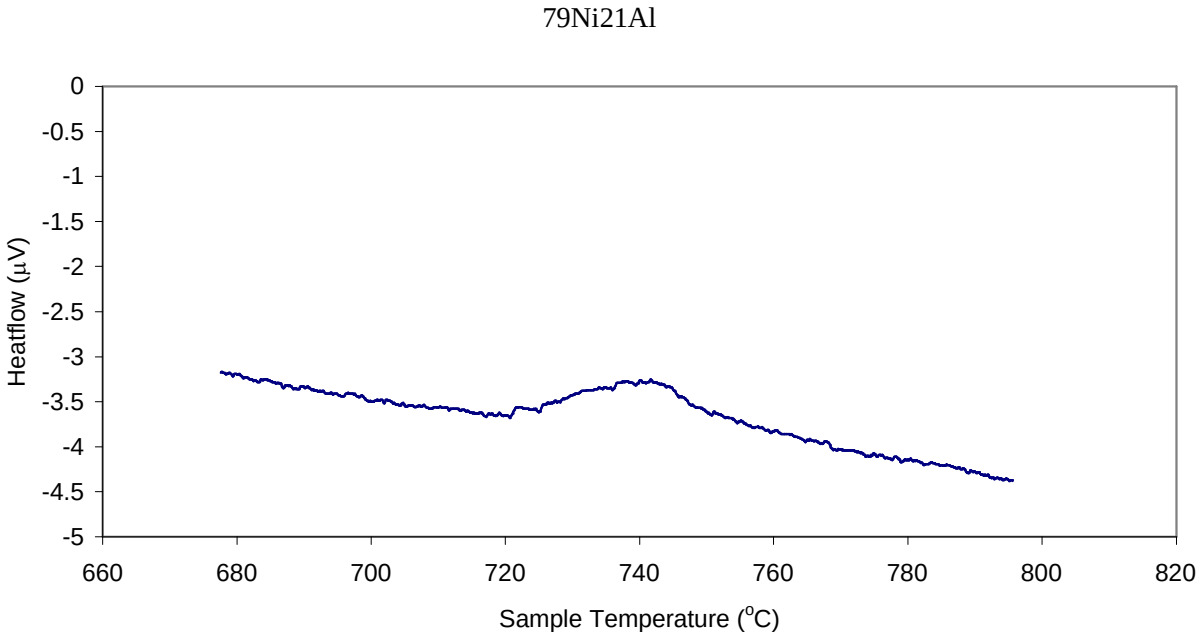

Figure 47 DSC graph showing '79Ni21Al' reaction curve

As can be seen in the graph above, the Ni_3Al samples produced very shallow reaction peaks when compared to those of the NiAl samples as would be expected. It is possible that there was some peeling between the layers, however, the amount of heat evolved during reaction was in the expected range.

The data obtained from the Ni_3Al DSC reaction curves is summarised below:

Calculated average nominal compositions (at.%)	Onset Temperature (°C) (output from DSC)	Enthalpy (kJ/mol) (output from DSC)
77.5Ni22.5Al	702.1	-59.0
79Ni21Al	715.4 +/- 9.2	-67.0 +/- 12.2

Table 36 DSC data for γ′-Ni_3Al (average values). Automated calculations output from the DSC

The complete set of data obtained from the γ′-Ni_3Al DSC reaction curves can be found in Appendix 2.

5.3.6 $(Ni, Pt)_3Al$

3 samples were tested in the DSC for each composition apart from 76Ni4Pt20Al and 68Ni9Pt23Al for which only 2 samples were tested, due to the peeling of layers during sample preparation. A selection of the graphs produced is shown below. The labels used for all samples refer to the calculated average nominal compositions of the samples in at.%.

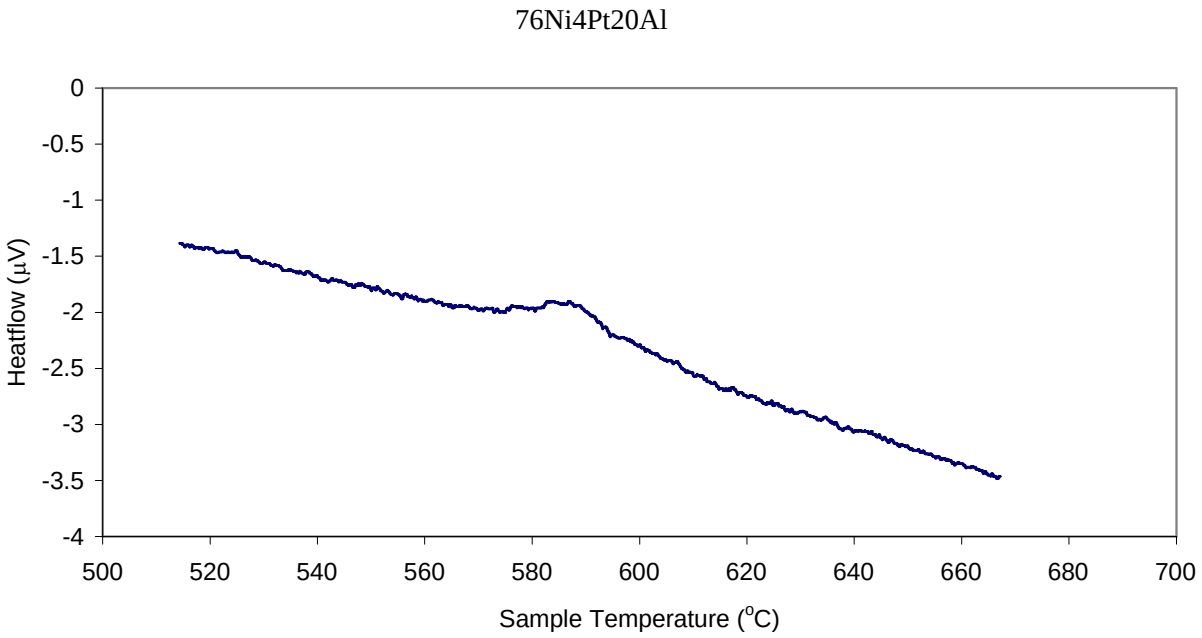

Figure 48 DSC graph showing '76Ni4Pt20Al' reaction curve

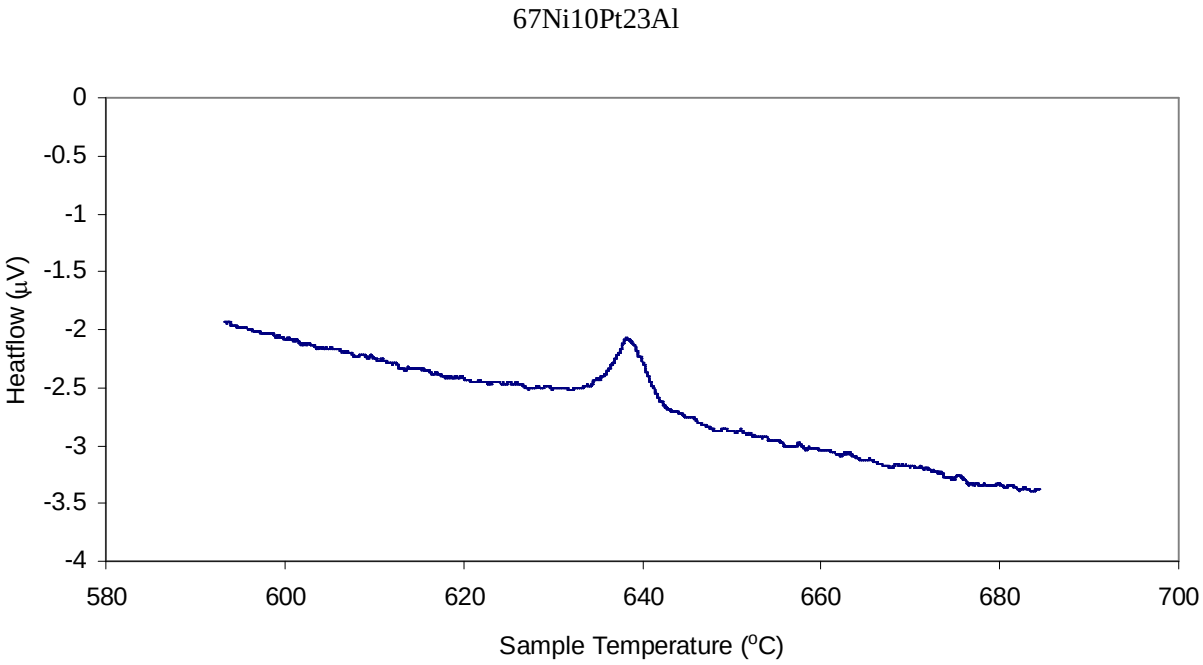

Figure 49 DSC graph showing '67Ni10Pt23Al' reaction curve

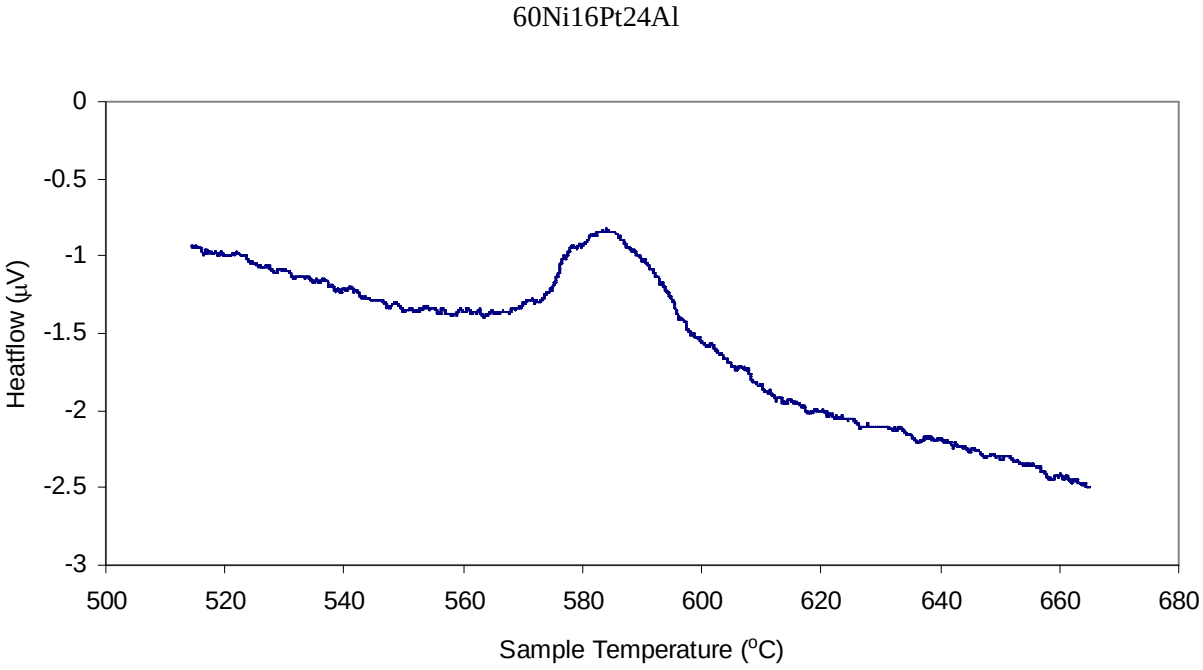

Figure 50 DSC graph showing '60Ni16Pt24Al' reaction curve

The above graphs show very shallow reaction peaks. While (Ni, Pt)$_3$Al is expected to have a shallower reaction curve than (Ni, Pt)Al, these peaks are much shallower than anticipated with a low enthalpy value, indicating that there was possibly some peeling between the layers. The exception is the 16% Pt sample which has the clearest and deepest reaction peak. There are no results for the 68Ni8Pt24Al samples as the layers all peeled during sample preparation.

The data obtained from the (Ni, Pt)$_3$Al DSC reaction curves is summarised below:

Calculated average nominal compositions (at.%)	Onset Temperature (°C) (output from DSC)	Enthalpy (kJ/mol) (output from DSC)
76Ni4Pt20Al	572.6 +/- 2.1	-14.7 +/- 5.5
73Ni7Pt20Al	569.4 +/- 11.4	-27.3 +/- 8.6
68Ni9Pt23Al	638.7 +/- 1.0	-12.1 +/- 1.6
67Ni10Pt23Al	627.8 +/- 11.7	-13.2 +/- 0.7
64Ni12Pt24Al	611.7 +/- 19.7	-12.5 +/- 0.8
60Ni16Pt24Al	567.6 +/- 5.3	-53.3 +/- 16.9

Table 37 DSC data for γ′-Ni$_3$Al with Pt additions (average values +/- std dev). Automated calculations output from the DSC

The complete data set can be found in Appendix 2.

5.3.7 $(Ni, Ru)_3Al$

3 samples were tested in the DSC for each composition. A selection of the graphs produced is shown below. The labels used for all samples refer to the calculated average nominal compositions of the samples in at.%.

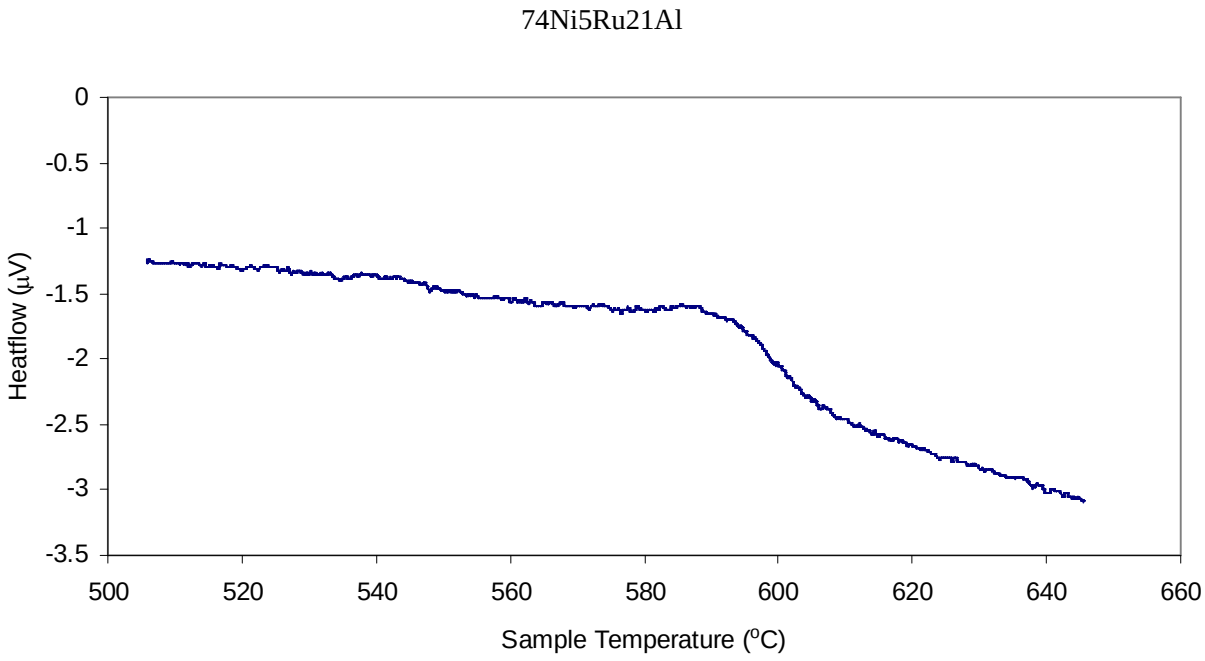

Figure 51 DSC graph showing '74Ni5Ru21Al' reaction curve

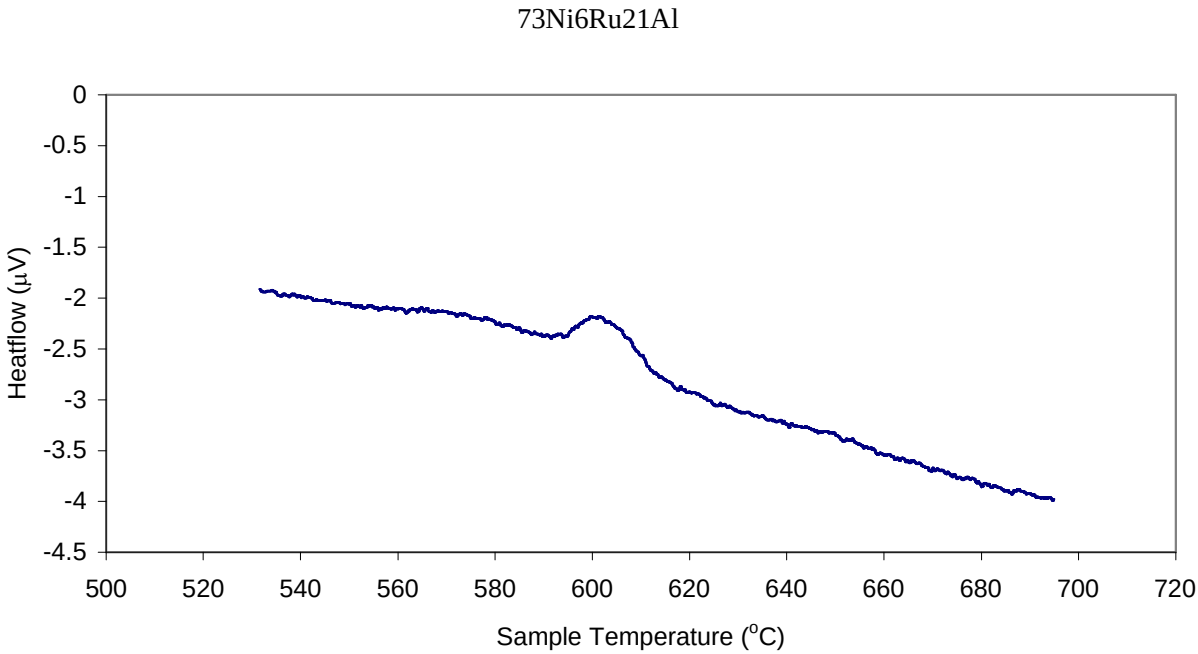

Figure 52 DSC graph showing '73Ni6Ru21Al' reaction curve

The above graphs show very shallow reaction peaks but the amount of heat evolved during reaction was in the expected range.

The data obtained from the $(Ni, Ru)_3Al$ DSC reaction curves is summarised below:

Calculated average nominal compositions (at.%)	Onset Temperature (°C) (output from DSC)	Enthalpy (kJ/mol) (output from DSC)
74Ni5Ru21Al	558.3 +/- 16	-51.4 +/- 26.7
77Ni5Ru18Al	594.8 +/- 0.4	-44.3 +/- 0.8
78Ni5Ru17Al	545.1 +/- 2.4	-46.1 +/- 4.7
73Ni6Ru21Al	587.4 +/- 10.2	-38.8 +/-3.3

Table 38 DSC data for γ'-Ni_3Al with Ru additions (average values +/- std dev). Automated calculations output from the DSC

The complete data set can be found in Appendix 2.

5.4 XRD Results

X-ray diffraction was carried out on the reacted coatings following DSC analysis, in order to identify the intermetallic compounds formed. Below are the XRD traces for the uncoated Al foil (Figure 53) and the uncoated Ni foil (Figure 54).

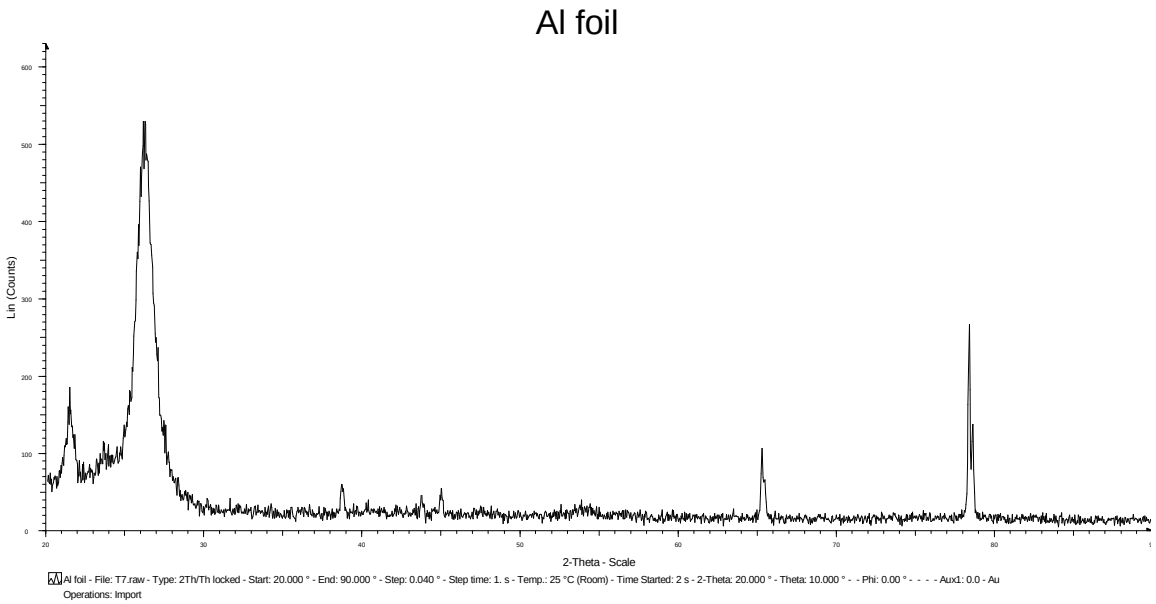

Figure 53 XRD trace for Al foil

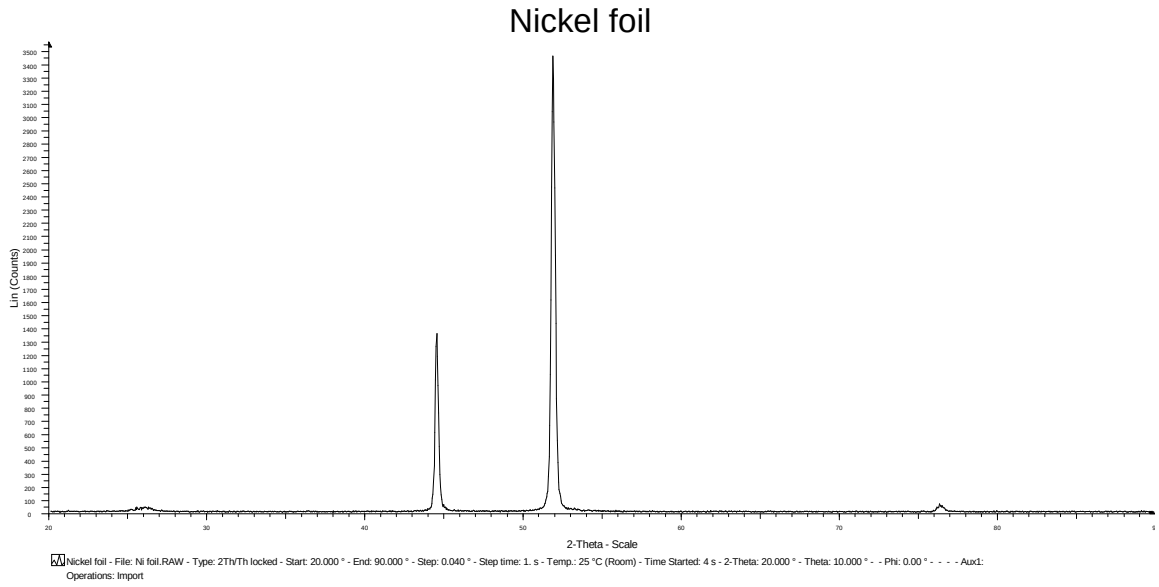

Figure 54 XRD trace for Ni foil

5.4.1 β-NiAl

All of the NiAl samples were found to have produced peaks for NiAl and Ni_2Al_3. Figure 55, Figure 56 and Figure 57 show the XRD traces for samples with nominal compositions of '45Ni55Al', '50Ni50Al' and '58.5Ni41.5Al'. A summary of the compounds detected during XRD can be seen in Table 39.

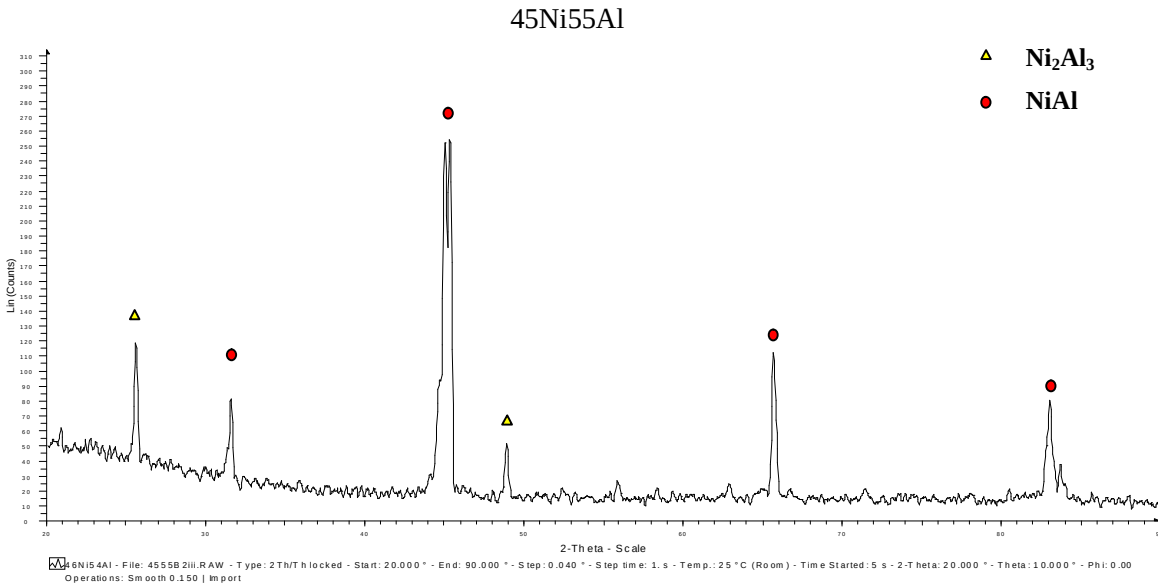

Figure 55 XRD trace for ‘45Ni55’Al

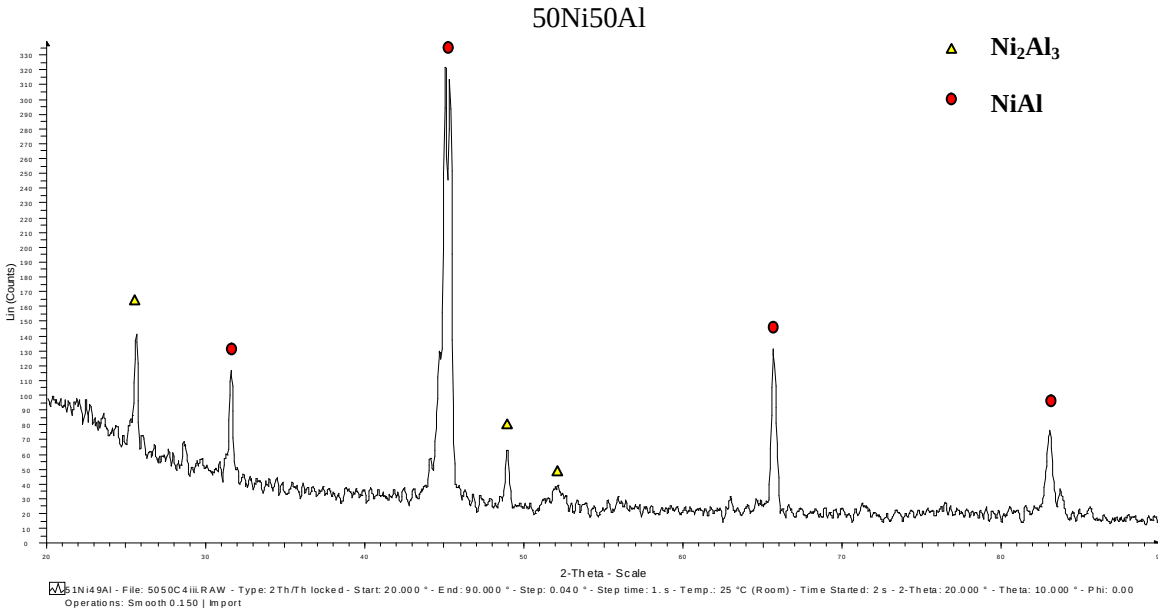

Figure 56 XRD trace for ‘50Ni50’Al

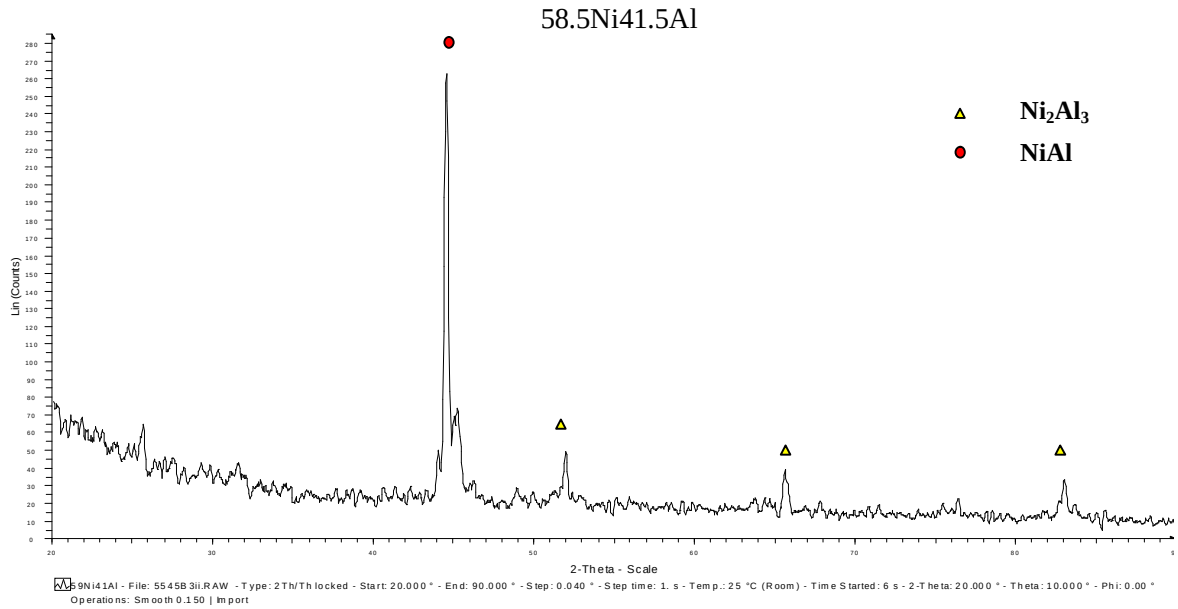

Figure 57 XRD trace for '58.5Ni41.5Al'

Calculated average nominal compositions (at.%)	Compounds detected by XRD
42.5Ni57.5Al	Ni_2Al_3, **NiAl**
44Ni56Al	Ni_2Al_3, **NiAl**
45Ni55Al	Ni_2Al_3, **NiAl**
47Ni53Al	Ni_2Al_3, **NiAl**
48.5Ni51.5Al	Ni_2Al_3, **NiAl**
49Ni51Al	Ni_2Al_3, **NiAl**
50Ni50Al	Ni_2Al_3, **NiAl**
52Ni48Al	Ni_2Al_3, **NiAl**
54Ni46Al	Ni_2Al_3, **NiAl**
58.5Ni41.5Al	Ni_2Al_3, NiAl

Table 39 Compounds detected in β-NiAl samples following DSC reaction

5.4.2 β-NiAl with Pt Additions

Figure 58, Figure 59, Figure 60 and Figure 61 show the XRD traces for samples with nominal compositions of '48Ni6Pt46Al', '41Ni13Pt46Al', '40Ni16Pt44Al' and '29Ni22Pt49Al'. A summary of the compounds detected during XRD can be seen in Table 40.

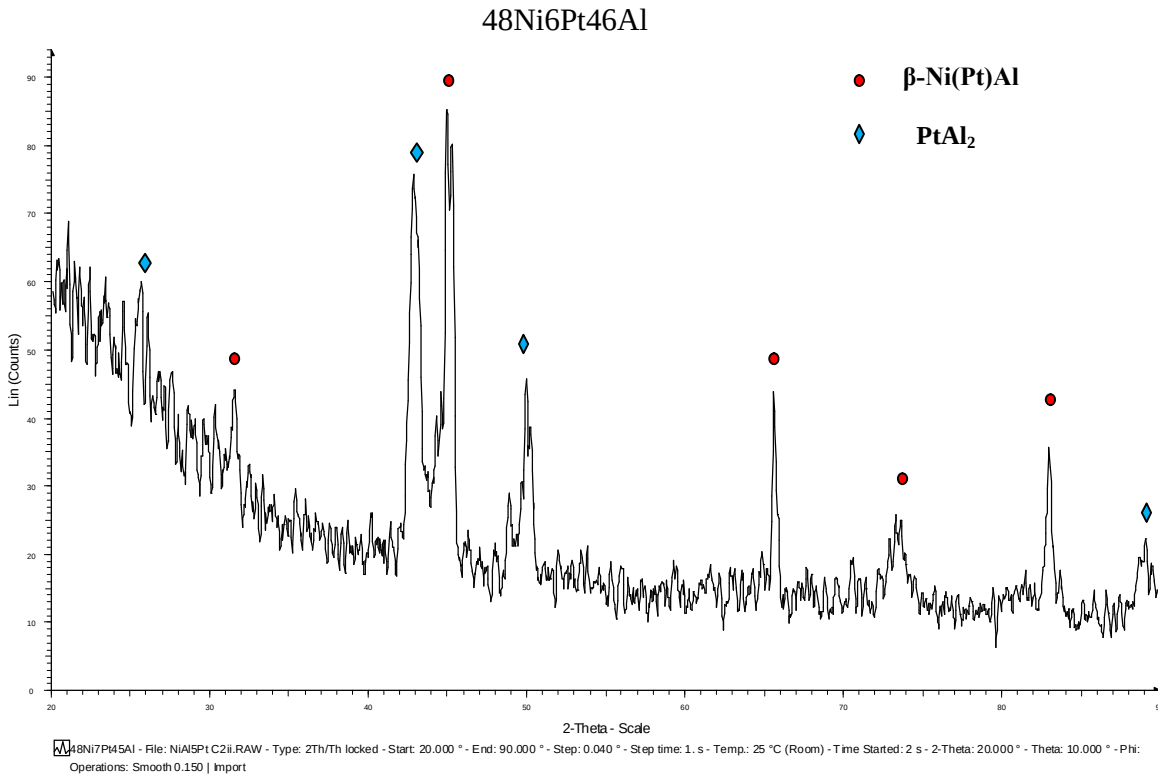

Figure 58 XRD trace for '48Ni6Pt46Al'

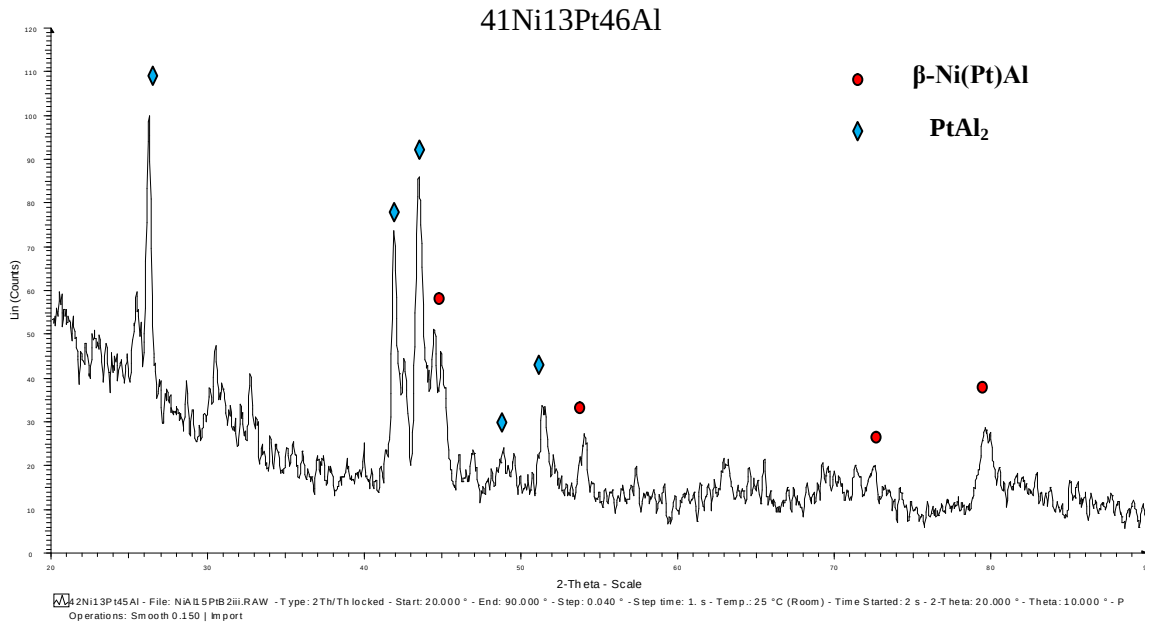

Figure 59 XRD trace for '40Ni12Pt48Al'

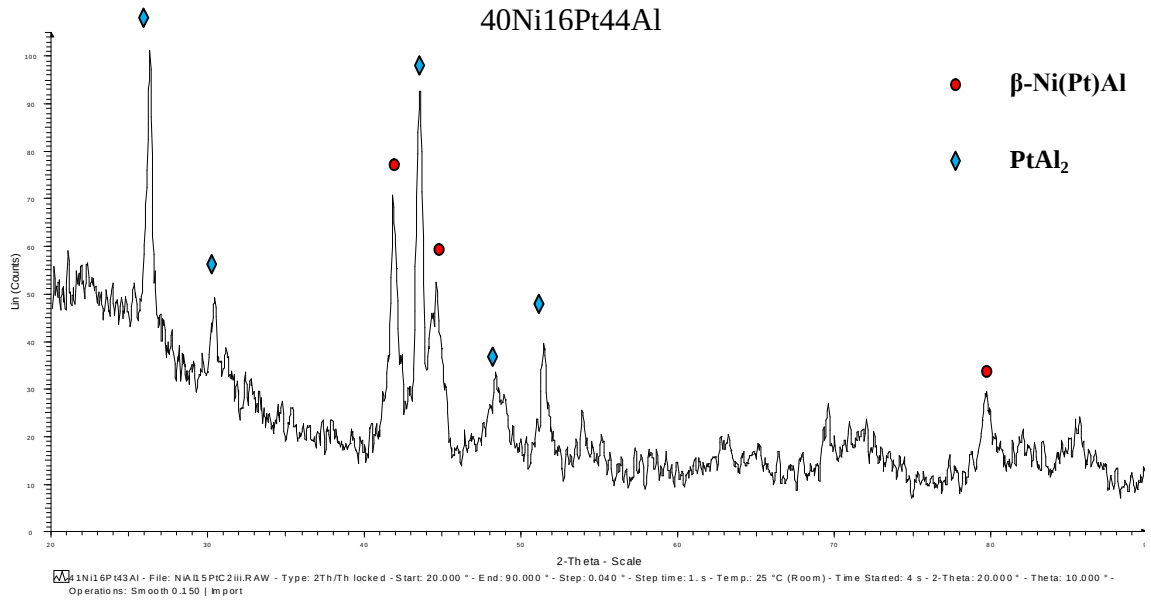

Figure 60 XRD trace for '40Ni16Pt44Al'

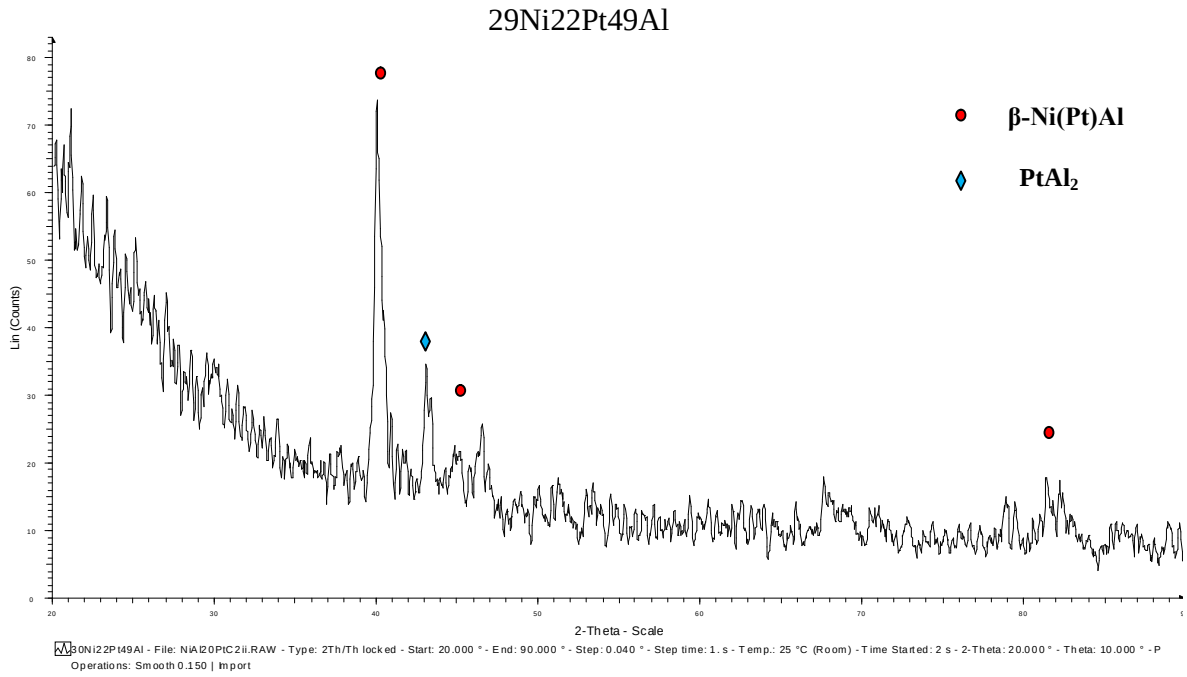

Figure 61 XRD trace for '29Ni22Pt49Al'

Calculated average nominal compositions (at.%)	Compounds detected by XRD
48Ni6Pt46Al	Ni(Pt)Al, $PtAl_2$
49Ni8Pt43Al	Ni(Pt)Al, $PtAl_2$
40Ni12Pt48Al	Ni(Pt)Al, $PtAl_2$
41Ni13Pt46Al	Ni(Pt)Al, $PtAl_2$
40Ni14.5Pt45.5Al	Ni(Pt)Al, $PtAl_2$
40Ni16Pt44Al	Ni(Pt)Al, $PtAl_2$
29Ni20Pt51Al	Ni(Pt)Al, $PtAl_2$
29Ni22Pt49Al	Ni(Pt)Al, $PtAl_2$

Table 40 Compounds detected in β-NiAl with Pt addition following DSC reaction

5.4.3 β-NiAl with Ru Additions

Figure 62, Figure 63, Figure 64 and Figure 65 show the XRD traces for samples with nominal compositions of '51Ni7Ru42Al', '44Ni11Ru45Al', '38Ni14Ru48Al' and '40Ni18Ru42Al'. A summary of the compounds detected during XRD can be seen in Table 41.

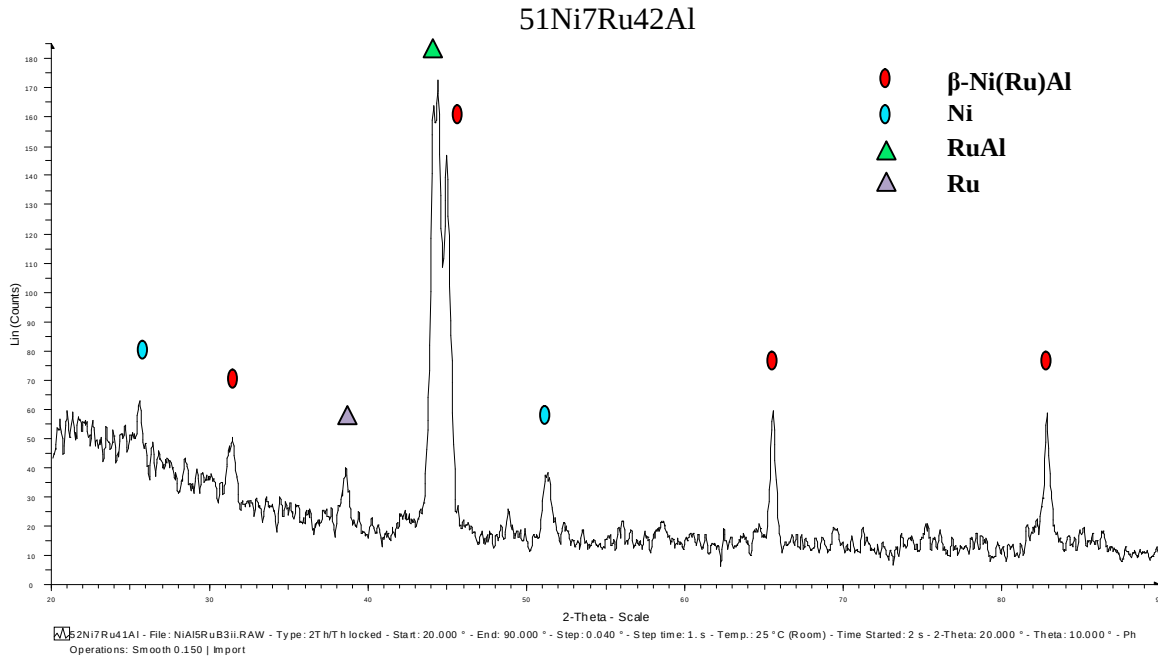

Figure 62 XRD trace for '51Ni7Ru42Al'

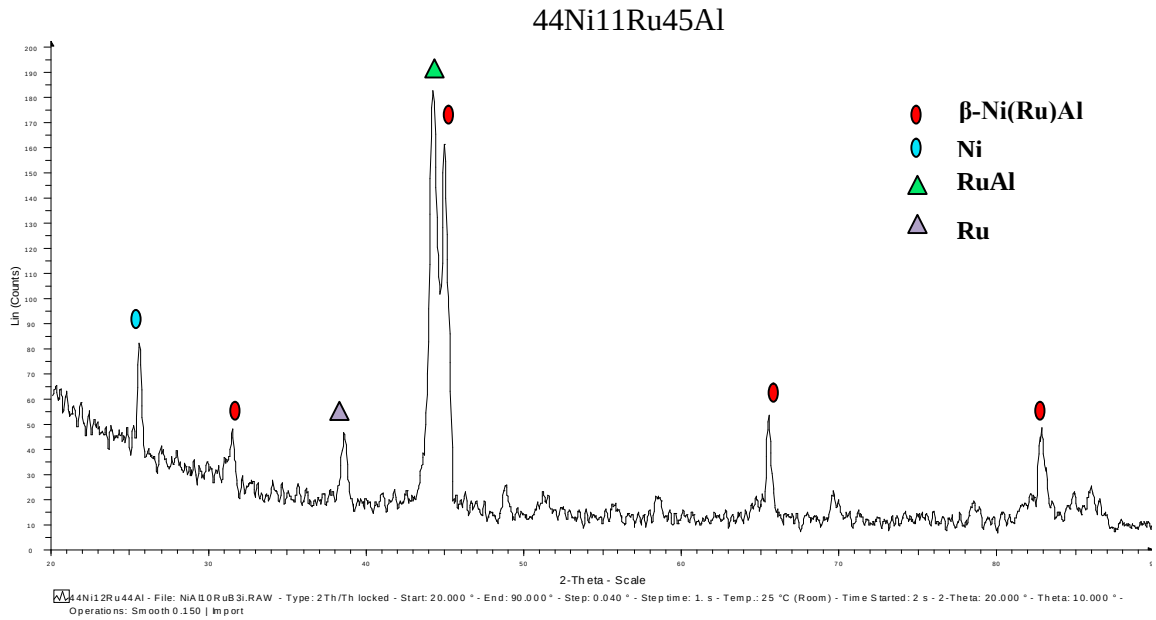

Figure 63 XRD trace for '44Ni11Ru45Al'

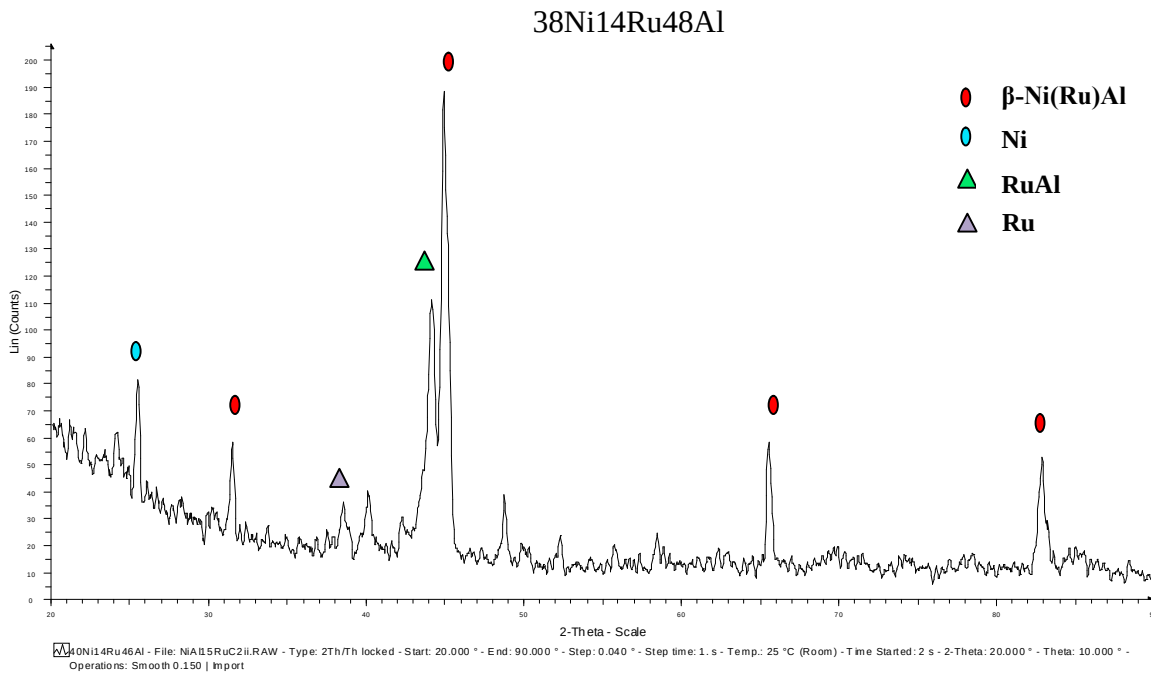

Figure 64 XRD trace for '38Ni14Ru48Al'

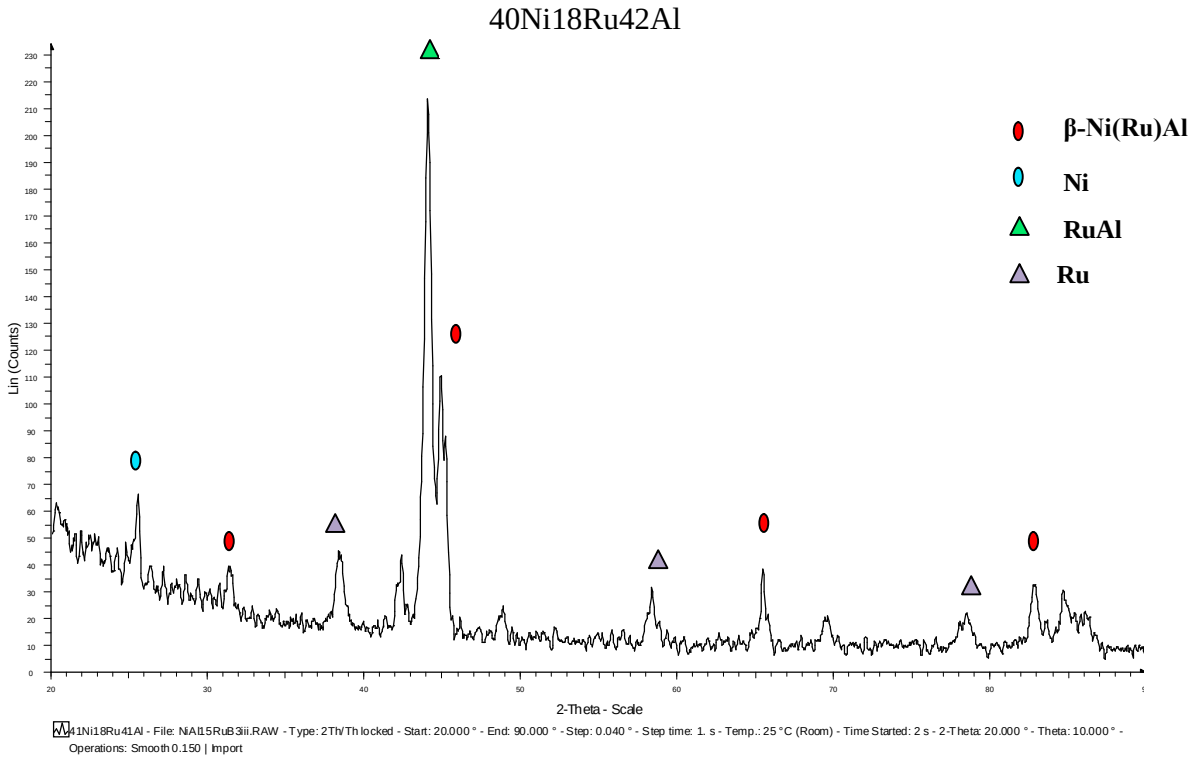

Figure 65 XRD trace for '41Ni18Ru41Al'

Calculated average nominal compositions (at.%)	Compounds detected by XRD
50Ni5Ru45Al	Ni(Ru)Al, Ni, RuAl, Ru
51Ni7Ru42Al	Ni(Ru)Al, Ni, RuAl, Ru
48Ni8Ru44Al	Ni(Ru)Al, Ni, RuAl, Ru
44Ni11Ru45Al	Ni(Ru)Al, Ni, RuAl, Ru
36Ni14Ru50Al	Ni(Ru)Al, Ni, RuAl, Ru
48Ni14Ru48Al	Ni(Ru)Al, Ni, RuAl, Ru
40Ni18Ru42Al	Ni(Ru)Al, Ni, RuAl, Ru

Table 41 Compounds detected in β-NiAl with Ru addition following DSC reaction

5.4.4 γ′-Ni_3Al

The XRD traces for samples with nominal compositions of '77.5Ni22.5Al' and '79Ni21Al' can be seen in Figure 66 and Figure 67. A summary of the compounds detected during XRD can be seen in Table 42.

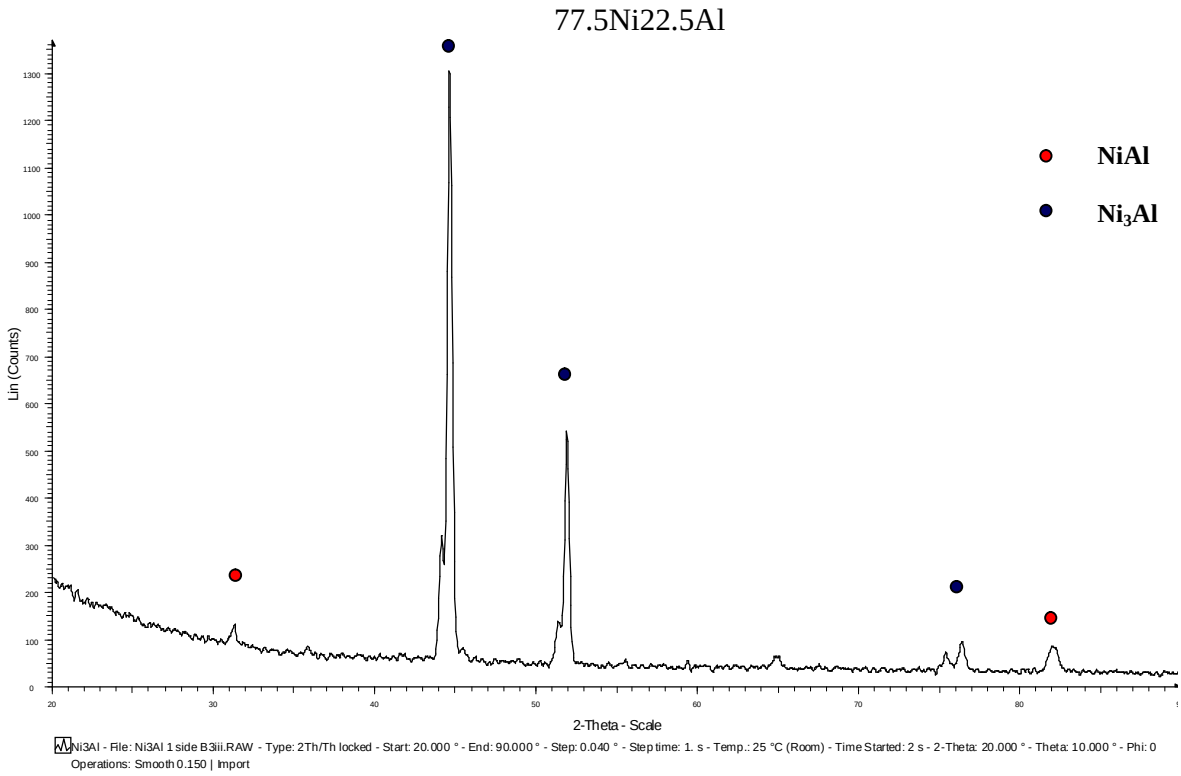

Figure 66 XRD trace for '77.5Ni22.5Al'

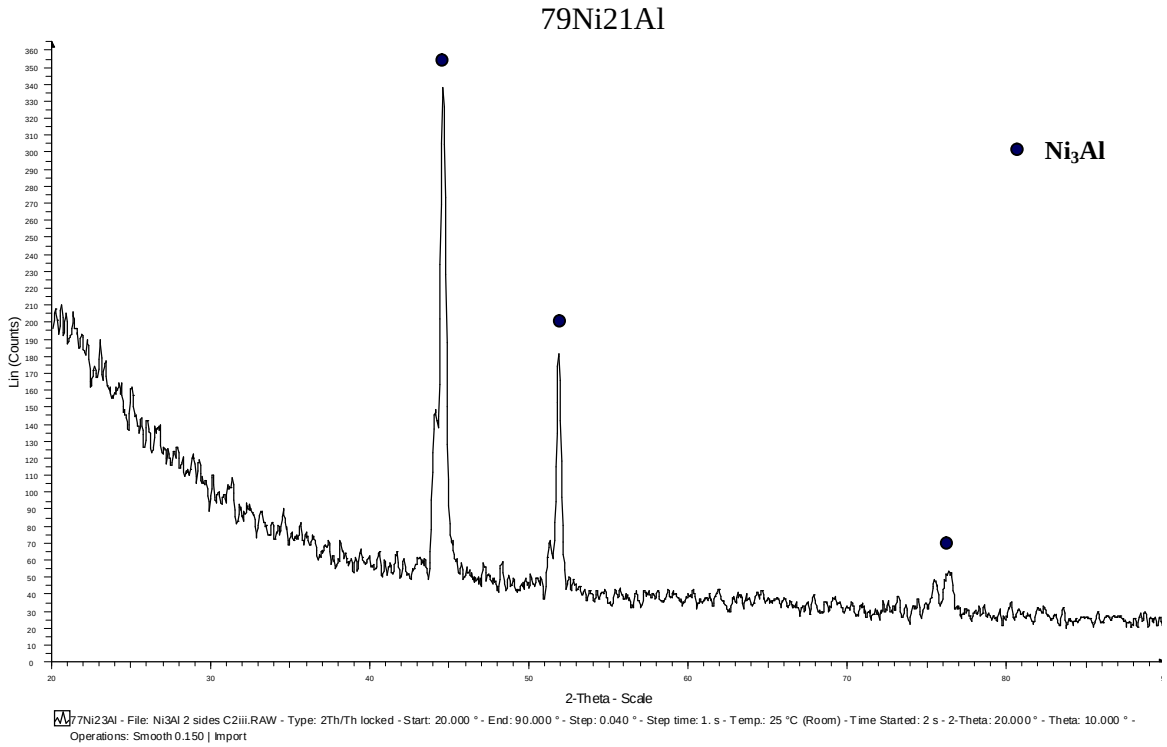

Figure 67 XRD trace for '79Ni21Al'

Calculated average nominal compositions (at.%)	Compounds detected by XRD
77.5Ni22.5Al	**Ni_3Al**, NiAl
79Ni21Al	**Ni_3Al**

Table 42 Compounds detected in γ′-Ni_3Al following DSC reaction

5.4.5 γ′-Ni_3Al with Pt Additions

XRD traces for samples with nominal compositions of ‘76Ni4Pt20Al’, ‘68Ni9Pt23Al’, ‘64Ni12Pt24Al’ and ‘60Ni16Pt24Al’ can be seen in Figure 68, Figure 69, Figure 70 and Figure 71. A summary of the compounds detected during XRD can be seen in Table 43.

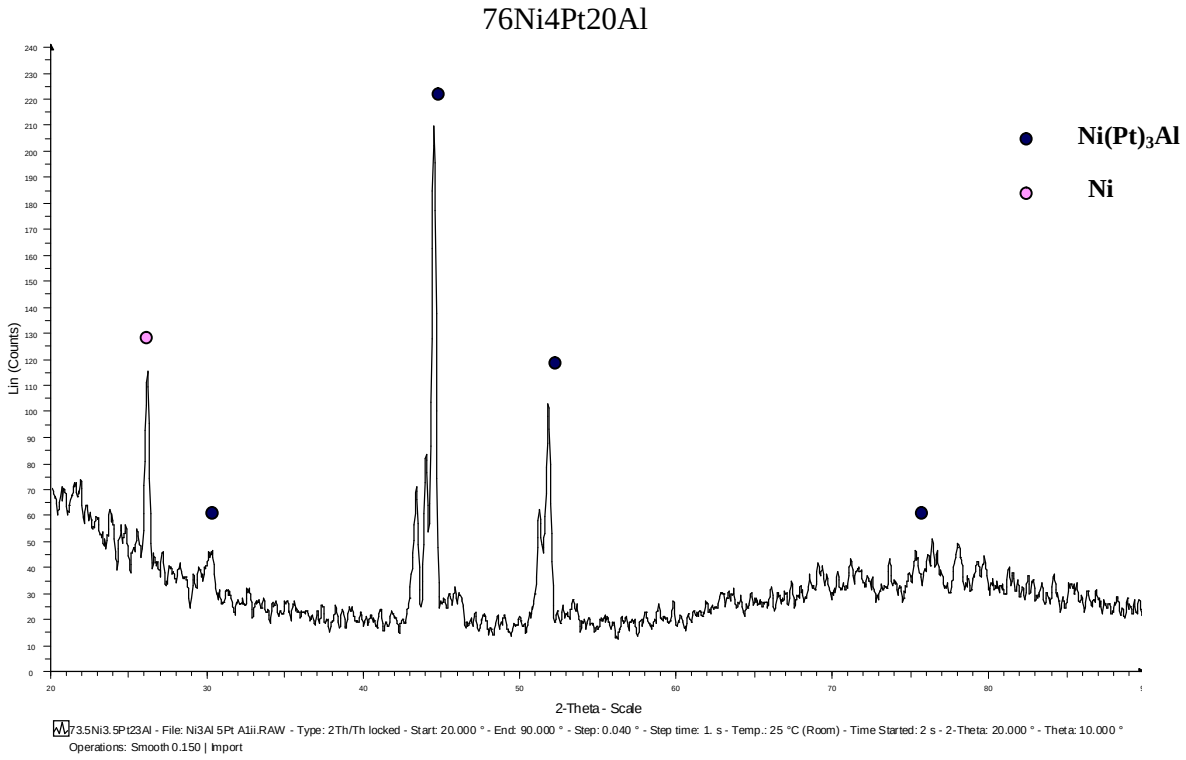

Figure 68 XRD trace for ‘76Ni4Pt20Al’

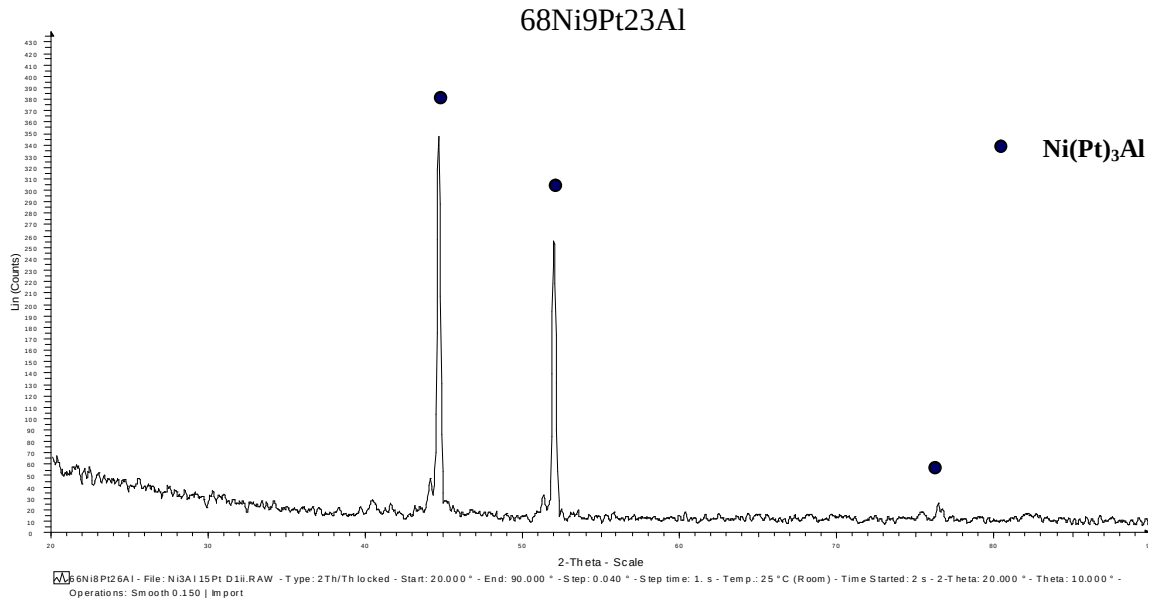

Figure 69 XRD trace for '68Ni9Pt23Al'

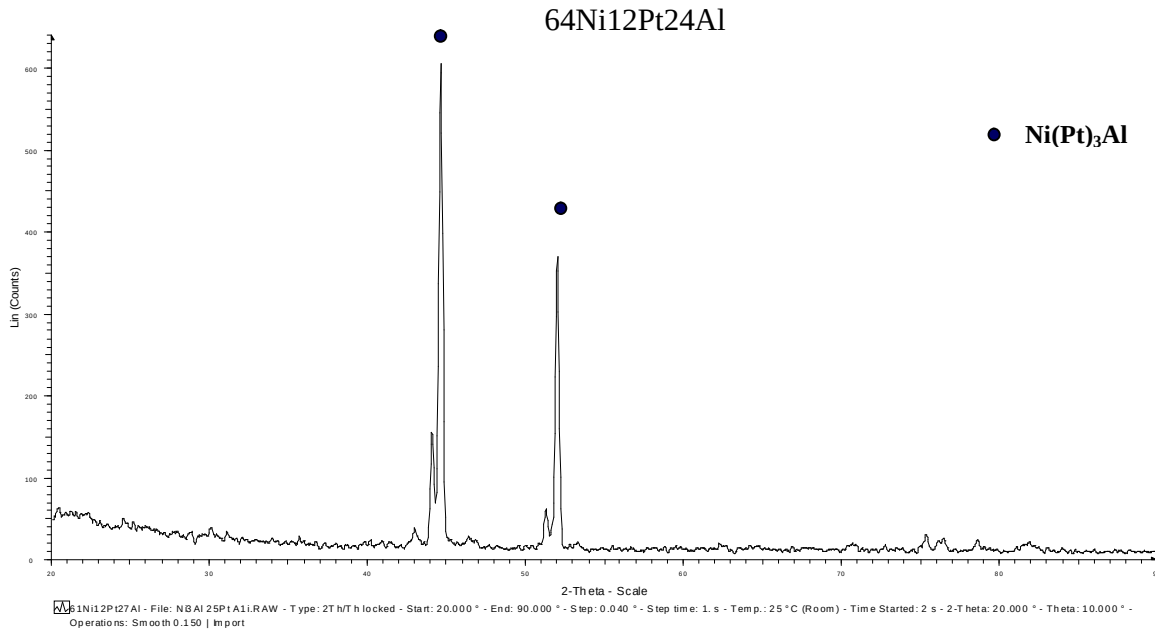

Figure 70 XRD trace for '64Ni12Pt24Al'

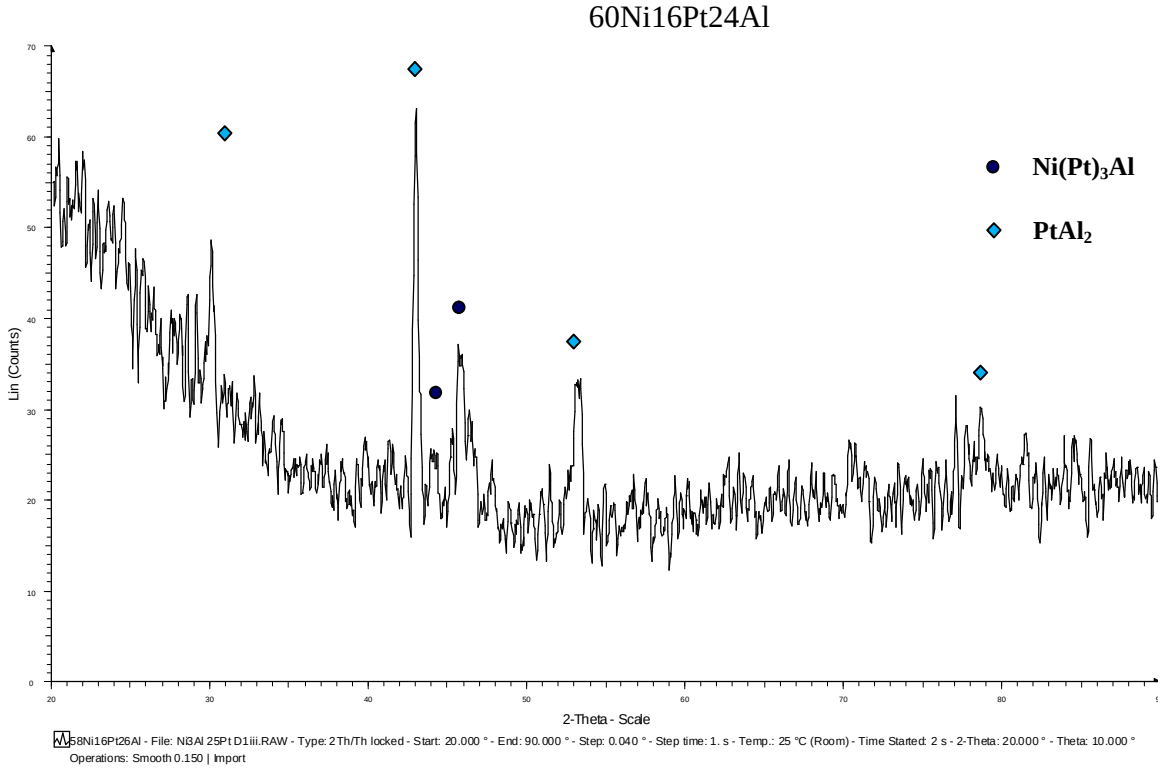

Figure 71 XRD trace for '60Ni16Pt24Al'

Calculated average nominal compositions (at.%)	Compounds detected by XRD
76Ni4Pt20Al	**$Ni(Pt)_3Al$,** Ni
73Ni7Pt20Al	**$Ni(Pt)_3Al$,** Ni
68Ni9Pt23Al	**$Ni(Pt)_3Al$**
67Ni10Pt23Al	**$Ni(Pt)_3Al$,** $PtAl_2$
64Ni12Pt24Al	**$Ni(Pt)_3Al$**
60Ni16Pt24Al	$Ni(Pt)_3Al$, **$PtAl_2$**

Table 43 Compounds detected in γ′-Ni_3Al with Pt additions following DSC reaction

5.4.6 γ′-Ni_3Al with Ru Additions

The XRD traces for samples with nominal compositions of ‘78Ni5Ru17Al’, ‘77Ni5Ru18Al’, 7’4Ni5Ru21Al’ and ‘73Ni6Ru21Al’ can be seen in Figure 72, Figure 73, Figure 74 and Figure 75. A summary of the compounds detected during XRD can be seen in Table 44.

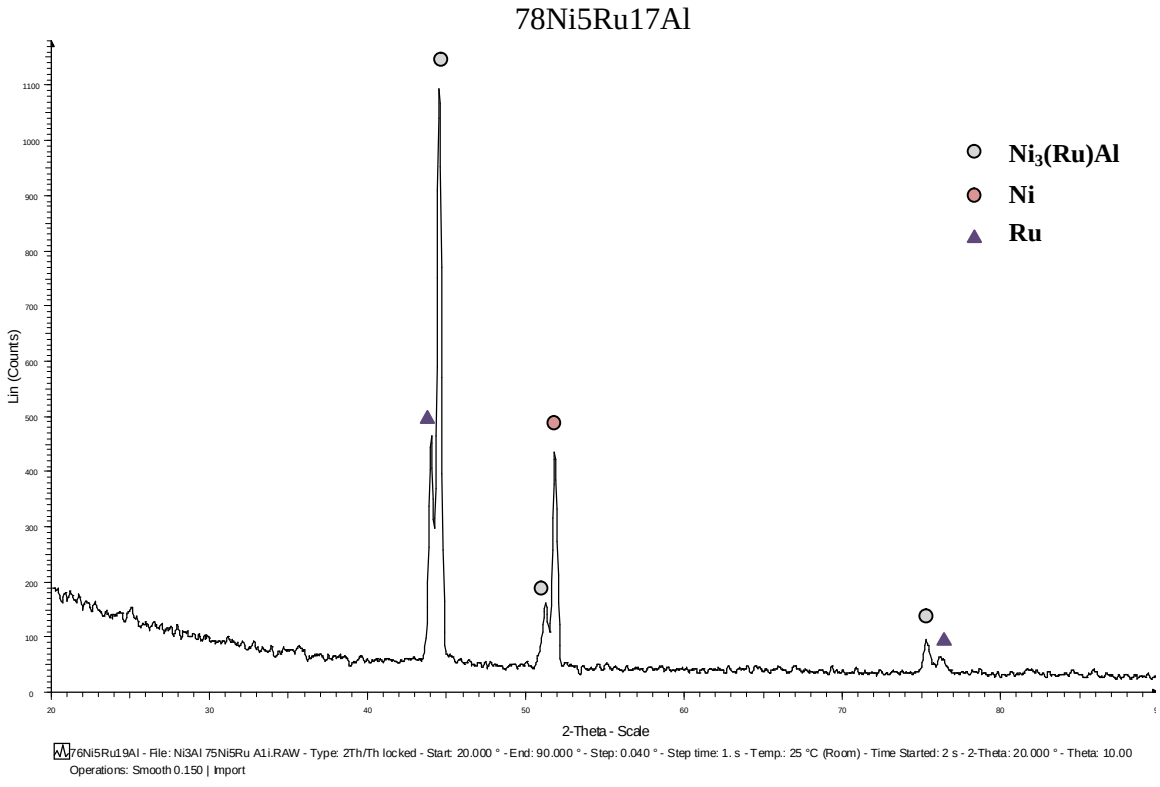

Figure 72 XRD trace for ‘78Ni5Ru17Al’

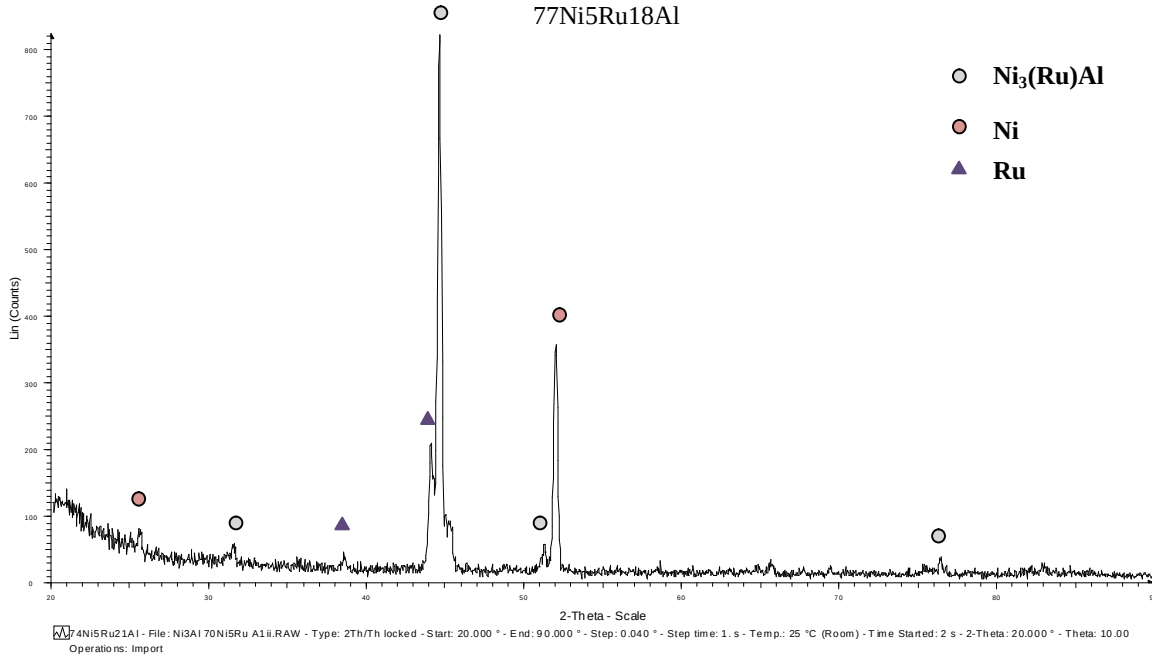

Figure 73 XRD trace for '77Ni5Ru18Al'

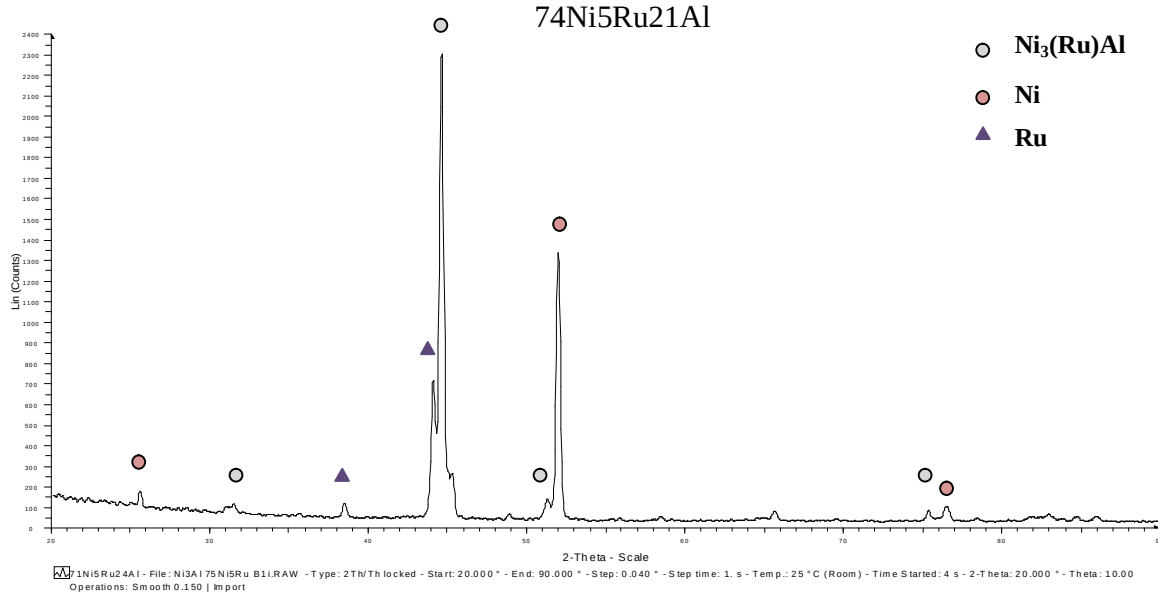

Figure 74 XRD trace for '74Ni5Ru21Al'

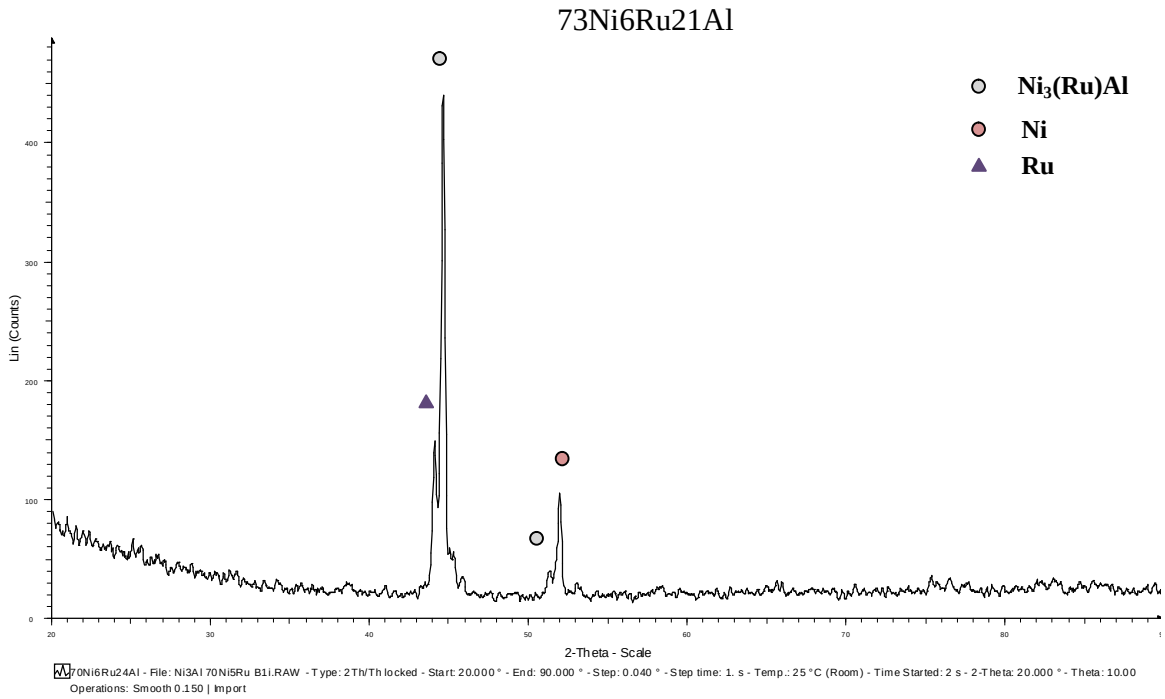

Figure 75 XRD trace for '73Ni6Ru21Al'

Calculated average nominal compositions (at.%)	Compounds detected by XRD
78Ni5Ru17Al	**Ni_3(Ru)Al**, Ru, Ni
77Ni5Ru18Al	**Ni_3(Ru)Al**, Ru, Ni
74Ni5Ru21Al	**Ni_3(Ru)Al**, Ru, Ni
73Ni6Ru21Al	**Ni_3(Ru)Al**, Ru, Ni

Table 44 Compounds detected in γ′-Ni_3Al with Ru additions following DSC reaction

5.5 EDX Results

Following X-ray Diffraction, the reacted samples were analysed using Energy Dispersive X-ray (EDX) analysis on the Scanning Electron Microscope.

5.5.1 β-NiAl

Figure 76 shows the EDX linescan and summary for the sample with a nominal composition of '47Ni53Al'. A summary of the EDX results for NiAl can be seen in Table 45.

47Ni53Al

Spectrum processing :
Peak possibly omitted : 0.259 keV

Processing option : All elements analyzed (Normalised)
Number of iterations = 3

Standard :
Al Al2O3 1-Jun-1999 12:00 AM
Ni Ni 1-Jun-1999 12:00 AM

Element	Weight%	Atomic%
Al K	31.97	50.56
Ni K	68.03	49.44
Totals	100.00	

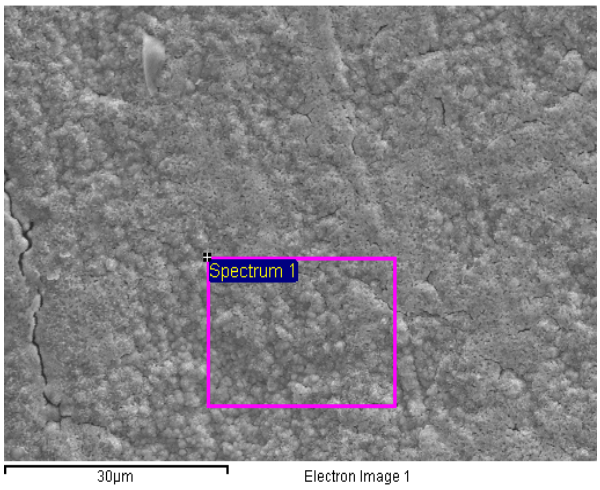

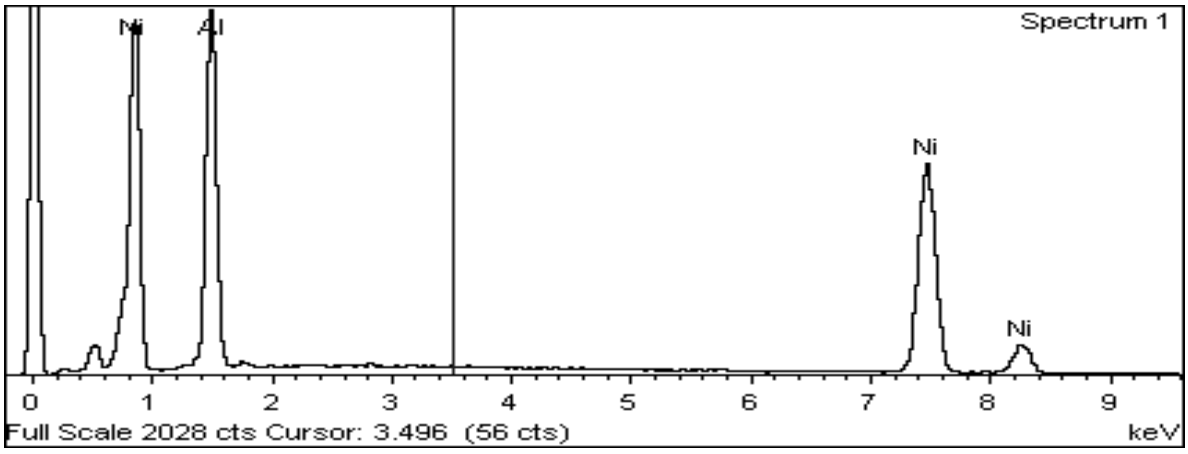

Figure 76 EDX results summary for '47Ni53Al'

Calculated average nominal compositions (at.%)	Element at%	
	Al	Ni
44Ni56Al B3iii	55.9	44.1
45Ni55Al B2iii	32.2	67.8
47Ni53Al C2ii	50.6	49.4
49Ni51Al D1i	14.2	85.8
50Ni50Al C4i	30.4	69.6
54Ni46Al A3ii	4.5	95.5

Table 45 EDX results for NiAl following reaction in the DSC

As can be seen in the table above, two of the samples had Ni and Al values close to the nominal compositions calculated from the as-deposited multilayers. However, four of the samples had high Ni values, which would indicate that interdiffusion between the multilayers was incomplete.

5.5.2 β-NiAl with Pt

Figure 77 shows the EDX linescan and summary for the sample with a nominal composition of '40Ni14.5Pt45.5Al'. A summary of the EDX results for (Ni, Pt)Al can be seen in Table 46.

40Ni14.5Pt45.5Al

Spectrum processing :
Peak possibly omitted : 0.244 keV
Processing option : All elements analyzed (Normalised)
Number of iterations = 4
Standard :
O SiO2 1-Jun-1999 12:00 AM
Al Al2O3 1-Jun-1999 12:00 AM
Ni Ni 1-Jun-1999 12:00 AM
Pt Pt 1-Jun-1999 12:00 AM

Element	Weight%	Atomic%
Al K	20.55	51.77
Ni K	16.41	26.22
Pt M	59.50	22.00
Totals	100.00	

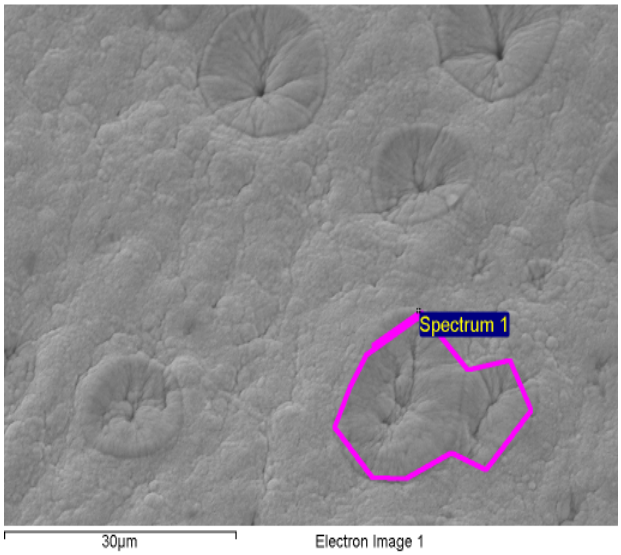

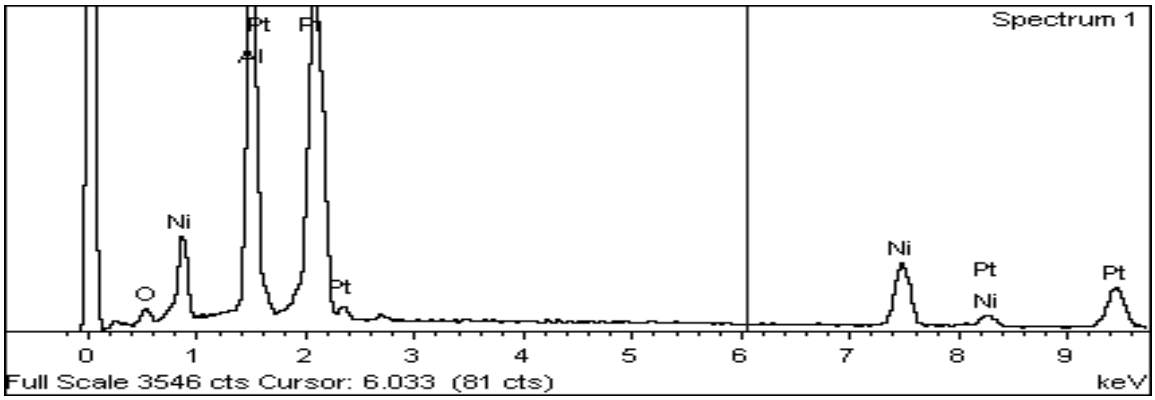

Figure 77 EDX results summary for '40Ni14.5Pt45.5Al' showing 'island' features (spectrum 1)

Calculated average nominal compositions (at.%)	Element at%		
	Al	Ni	Pt
48Ni6Pt46Al C2i	26.3	54.5	19.2
49Ni8Pt43Al C3ii	23.0	55.7	21.2
41Ni13Pt46Al B2iii	38.5	32. 7	28.8
40Ni14.5Pt45Al B3i (islands)	3.6 (51.8)	59.0 (26.2)	37.4 (22.0)
40Ni16Pt44Al C2ii	40.3	33.6	26.1
29Ni22Pt49Al C2ii	20.1 (58.1)	66.1 (3.9)	13.78 (38.0)

Table 46 EDX results for NiPtAl following reaction in the DSC

The percentages of Ni and Pt are high in comparison with the percentage of Al expected from full interdiffusion of the sputtered layers and foil. Since the samples were produced by sputtering Ni and Pt onto Al foil, this would indicate that the outward diffusion of the Al was incomplete during reaction in the DSC, it would have reacted with the Ni first before diffusing out to the Pt layer. In the case of the 14.5% Pt and 22% Pt samples, Al-rich 'islands' have formed, while the bulk outer layer has a low Al concentration.

5.5.3 β-NiAl with Ru

Figure 78 shows the EDX linescan and summary for the sample with a nominal composition of '38Ni14Ru48A'l. A summary of the EDX results for (Ni, Ru)Al can be seen in Table 47.

38Ni14Ru48Al C2ii

Spectrum processing :
No peaks omitted

Processing option : All elements analyzed (Normalised)
Number of iterations = 3

Standard:
Al Al2O3 1-Jun-1999 12:00 AM
Ni Ni 1-Jun-1999 12:00 AM
Ru Ru 1-Jun-1999 12:00 AM

Element	Weight%	Atomic%
Al K	7.36	21.14
Ni K	14.22	18.76
Ru L	78.42	60.10
Totals	100.00	

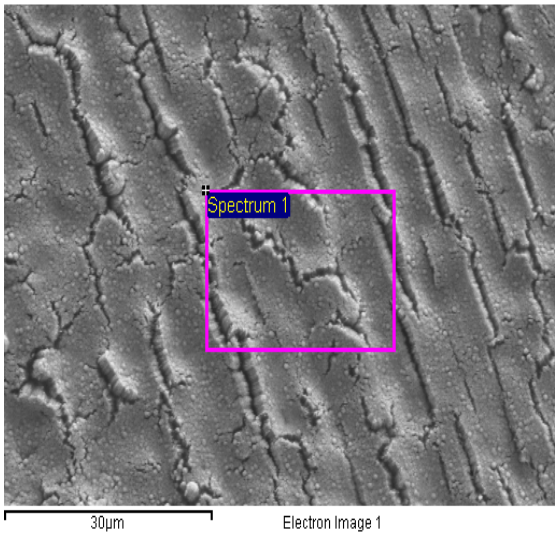

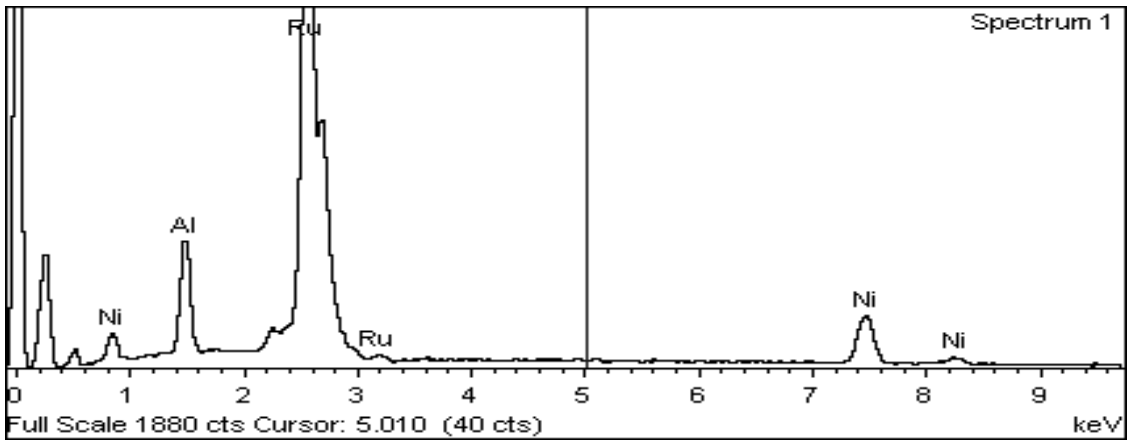

Figure 78 EDX results summary for '38Ni14Ru48Al'

Calculated average nominal compositions (at.%)	Element at%		
	Al	Ni	Ru
50Ni5Ru45Al B2ii	15.7	35.3	48.9
51Ni7Ru42Al B3ii	7.9	37.5	54.6
44Ni11Ru45Al B3iii	60.0	28.6	11.4
36Ni14Ru50Al B2ii	29.1	16.8	54.1
38Ni14Ru48Al C2ii	21.1	18.8	60.1
40Ni18Ru42Al B3iii	8.6	13.4	78.0

Table 47 EDX results for NiRuAl following reaction in the DSC

The percentage of Ru is high in comparison with the expected Al and Ni levels in all of the samples except for the 11% Ru sample. This would indicate that the inward diffusion of the Ru was incomplete during reaction in the DSC. The 11% Ru sample has the amount of Ru expected, with a high percentage of Al and low Ni.

5.5.4 γ′-Ni_3Al

Figure 79 shows the EDX linescan and summary for the sample with a nominal composition of '77.5Ni22.5Al'. A summary of the EDX results for Ni_3Al can be seen in Table 48.

77.5Ni22.5Al B3i (coated side)

Spectrum processing :
Peak possibly omitted : 0.260 keV

Processing option : All elements analyzed (Normalised)
Number of iterations = 4

Standard :
Al Al2O3 1-Jun-1999 12:00 AM
Ni Ni 1-Jun-1999 12:00 AM

Element	Weight%	Atomic%
Al K	56.14	73.58
Ni K	43.86	26.42
Totals	100.00	

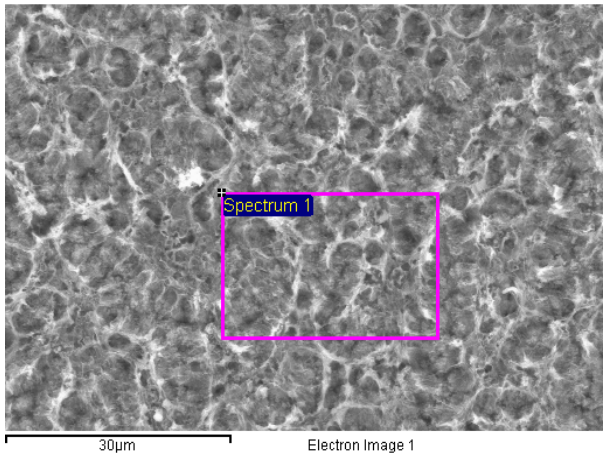

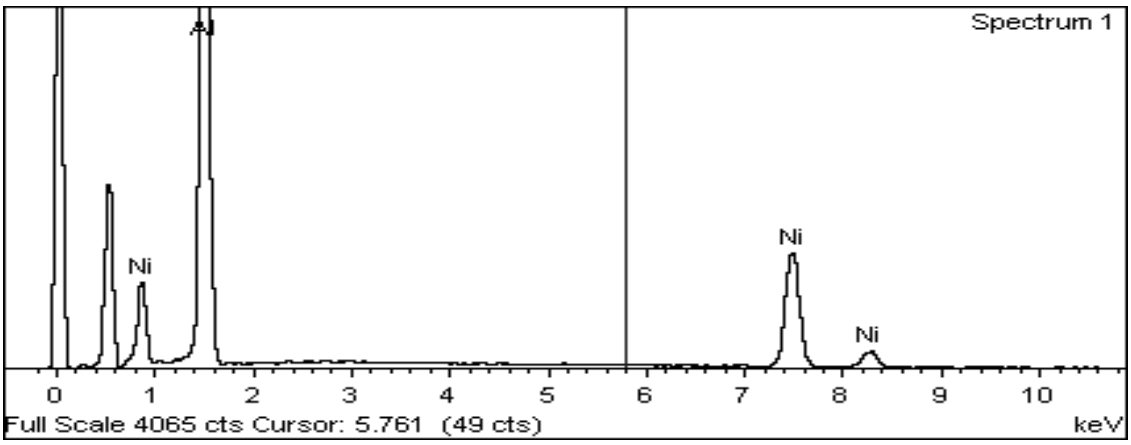

Figure 79 EDX results summary for '77.5Ni22.5Al' (coated side)

Calculated average nominal compositions (at.%)		Element at%	
		Ni	Al
77.5Ni22.5Al B3i	1	99.0	1.0
	2	26.4	73.6
79Ni21Al C2i		67.5	32.5

Table 48 EDX results for Ni_3Al following reaction in the DSC

The results for the Al coated onto only one side of the Ni foil show that the elements did not completely react. The Al had not diffused to the opposite side of the Ni foil, only 1 at% Al, whilst the Ni had diffused through to the other side of the Al (26% Ni). The Ni foil coated on both sides with Al, has a higher percentage of Al at the top layer than expected again indicating incomplete interdiffusion between the Ni and Al.

Diffusion could have been improved by using thinner multilayers and by holding the samples at a higher temperature for longer. The layer thicknesses were 10µm Ni and 5µm Al and the maximum temperature reached was 800°C.

5.5.5 γ′-Ni_3Al with Pt

Figure 80 shows the EDX linescan and summary for the sample with a nominal composition of '60Ni16Pt24Al'. A summary of the EDX results for $(Ni, Pt)_3Al$ can be seen in Table 49.

60Ni16Pt 24Al D1ii (side 1)

Spectrum processing :
Peak possibly omitted : 0.256 keV

Processing option : All elements analyzed (Normalised)
Number of iterations = 3

Standard :
Al Al2O3 1-Jun-1999 12:00 AM
Ni Ni 1-Jun-1999 12:00 AM

Element	Weight%	Atomic%
Al K	35.40	54.39
Ni K	64.60	45.61
Totals	100.00	

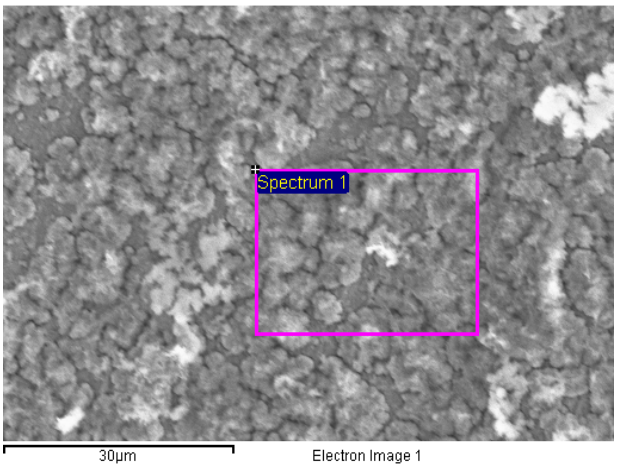

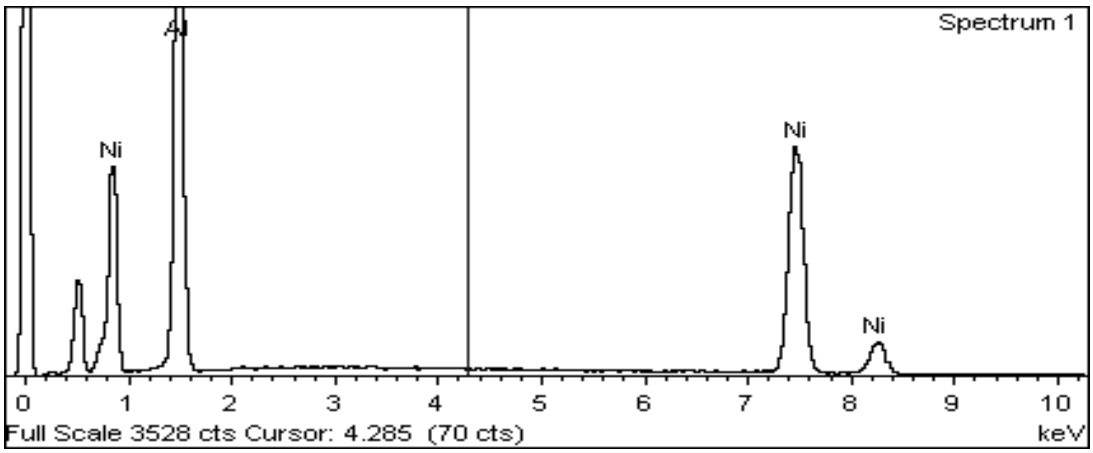

Figure 80 EDX results summary for '60Ni16Pt24Al' side 1

Calculated average nominal compositions (at.%)		Element at%		
		Al	Ni	Pt
73Ni7Pt20Al	side 1	56.4	-	43.6
D1ii	side 2	61.2	16.4	22.4
68Ni9Pt23Al	side 1	87.9	11.5	0.6
D1ii	side 2	15.1	84.9	-
64Ni12Pt24Al	side 1	53.9	-	46.1
A1ii	side 2	55.0	45.0	-
60Ni16Pt 24Al	side 1	54.4	45.6	-
D1ii	side 2	51.5	-	48.5

Table 49 EDX results for $(Ni, Pt)_3Al$ following reaction in the DSC

These samples were produced by sputtering Al and Pt onto Ni foil.

As can be seen in the above tables, all of the samples have distinct layers, Ni-Al on one side and Pt-Al on the other side (12% Pt and 16% Pt) or Ni-Pt-Al on one side and either Pt-Al (7% Pt) or Ni-Al (9% Pt) on the other side. This could have been due to the layers peeling apart.

5.5.6 γ′-Ni_3Al with Ru

Figure 81 shows the EDX linescan and summary for the sample with a nominal composition of '73Ni6Ru21Al'. A summary of the EDX results for $(Ni, Ru)_3Al$ can be seen in Table 50.

73Ni6Ru21Al D1ii (side 2)

Spectrum processing :
No peaks omitted

Processing option : All elements analyzed (Normalised)
Number of iterations = 3

Standard :
Al Al2O3 1-Jun-1999 12:00 AM
Ni Ni 1-Jun-1999 12:00 AM
Ru Ru 1-Jun-1999 12:00 AM

Element	Weight%	Atomic%
Al K	17.26	38.93
Ni K	25.89	26.84
Ru L	56.85	34.23
Totals	100.00	

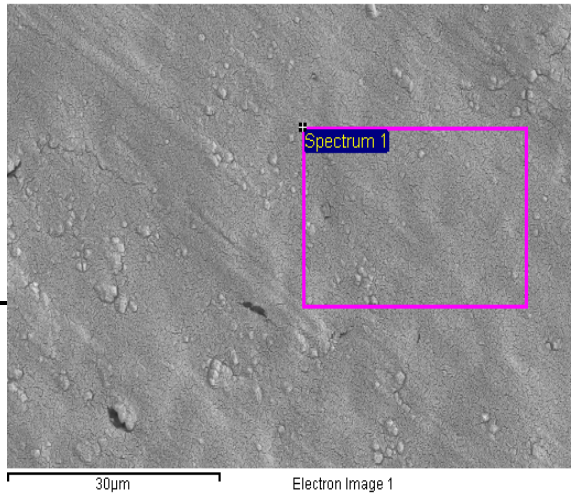

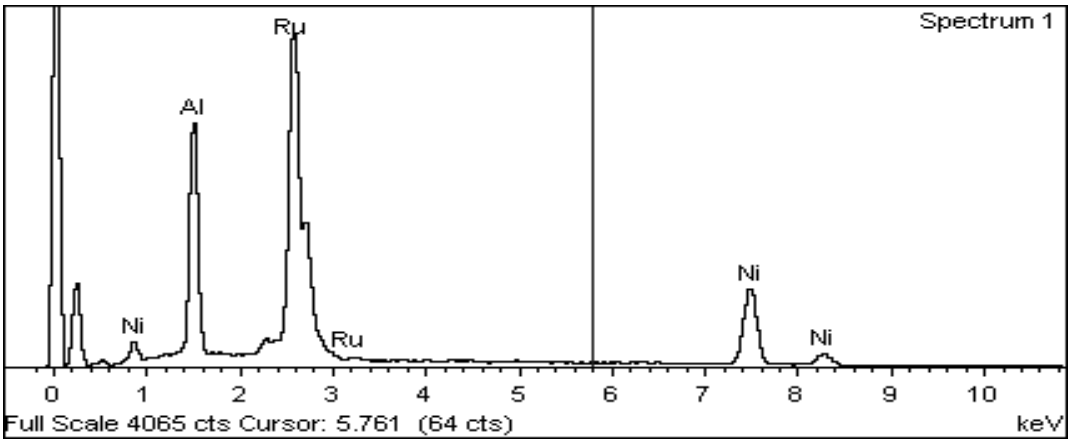

Figure 81 EDX results summary for '73Ni6Ru21Al' side 2

Calculated average nominal compositions (at.%)		Element at%		
		Al	Ni	Ru
74Ni5Ru21Al	side 1	45.5	30.8	23.7
B1iii	side 2	33.1	38.1	28.8
73Ni6Ru21Al	side 1	43.7	36.6	19.7
B1ii	side 2	38.9	26.8	34.2

Table 50 EDX results for $(Ni, Ru)_3Al$ following reaction in the DSC

The $(Ni, Ru)_3Al$ samples did not have the separating effects that the $(Ni, Pt)_3Al$ had. The concentrations of Ru and Al again appear to be high in comparison with the Ni. This is because Ni was the central layer and did not have enough time at temperature to fully interdiffuse.

6.0 Discussion

6.1 DSC Measurements

In this work, DSC measurements were obtained from foil samples manufactured with multiple sputtered layers. The DSC was calibrated using pure metals and the same parameters as the experimental runs, as described in section 4.5.3. The heating rate chosen was 5ºC/min and this was kept consistent for all of the calibration runs and all of the tests. Figure 82 shows the influence of heating rate on the reaction of Al foil during heating in the Cranfield DSC. The enthalpy values were calculated by the DSC computer using the Setaram Setsoft2000 software. When these values were compared to the true peak areas there was a maximum difference of +/- 8kJ/mol in the enthalpy values.

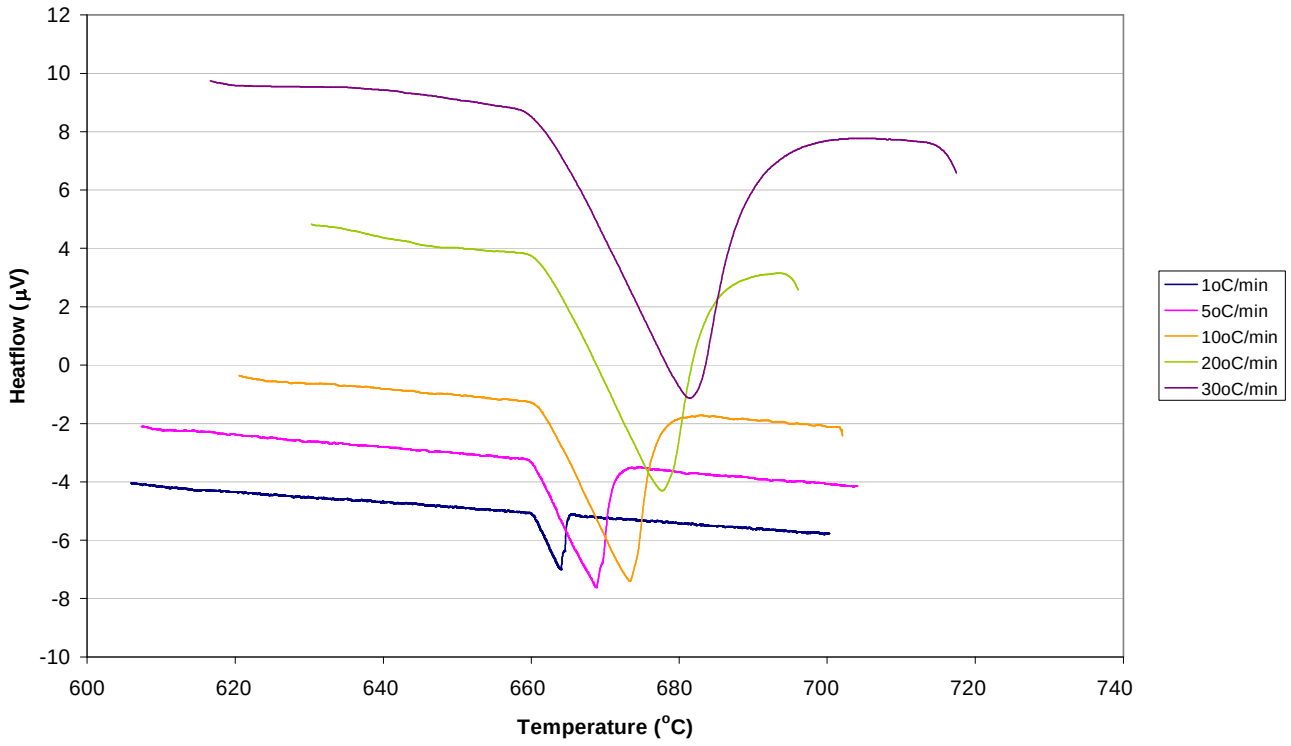

Figure 82 DSC curves for Al at different heating rates in the Cranfield experimental set-up (foil samples heated up to 800°C)

In contrast, different DSC methods have been reported in the literature:

1) Nash et al[142] used powder samples dropped from room temperature into a high temperature reaction calorimeter set at 1200ºC. The samples were produced by mixing elemental powders in the required molar ratio and pressing them into a pellet. The weight of a typical sample was ~100g. The enthalpy of reaction ($\Delta H_{reaction)}$ was obtained by dropping a pellet into the calorimeter from room temperature in an argon atmosphere. The pellet was then removed and again dropped into the calorimeter from room temperature to obtain the heat content of the compound ($\Delta H_{heat\ content).}$ The difference between the two measurements was taken to be the heat of formation at 25°C. This led to a complete reaction to the NiAl compound in the calorimeter at a fast heating rate.

2) Henig et al[143] and Rzyman et al[144] used solution calorimetry to obtain their values for the heats of formation of the Ni-Al system. In solution calorimetry, a sample weighing ~0.5g is placed in a thin-walled rotary container and heated to a temperature between room temperature and 1200K, before being dropped into a liquid bath inside the calorimetric furnace. The temperature change is measured using thermocouples situated directly below the bottom of the bath crucible.[145]

The difference in the heats of formation that have been measured between the current work and data in the literature could be the result of several differences in experimental methods:

1. Rate of heating – fast versus slow.
2. Powder samples versus foil samples.
3. Enthalpy of reaction at 25ºC versus reaction during heating to 800ºC.
4. Results from the Cranfield DSC were converted from J/g into kJ/mol using the number of moles in the average nominal composition of the sample (i.e. the moles that would have been present if the whole of the sample had transformed into the targeted compound). Since interdiffusion between the multiple layers was

incomplete in some samples (from XRD and SEM/EDX results), this led to a significant error in calculating the enthalpy values for these samples in the current work.

6.2 Ni-Al

The compounds that are possible to form from Ni and Al can be seen in the binary phase diagram in Figure 11. The enthalpy of formation and melting point for each compound is listed in Table 51.

Phase	Melting point (°C)	Enthalpy of Formation (kJ/mol)	Composition (atomic % Ni)	Composition (atomic % Al)
Al	660.4	-	0 - 3.3	96.7 – 100
$NiAl_3$	854	-38	25	75
Ni_2Al_3	1133	-56	36.8 – 41.5	58.5 – 62.8
NiAl	1638	-60	41.5 – 65	35 -58.5
Ni_5Al_3	700	-56	63 – 68	32 -37
Ni_3Al	1400	-40.5	73.8 – 76.6	23.4 -26.2
Ni	1455	-	80 - 100	0 - 20

Table 51 Some nickel aluminide characteristics[136]

As can be seen from Table 33, page 101, the enthalpies of formation for the β-phase samples calculated from the DSC measurement ranged from -40kJ/mol to -86kJ/mol. The compounds formed during these reactions were NiAl and Ni_2Al_3. From Table 36, page 110, it can be seen that the enthalpies of formation for the γ′-phase samples ranged from -59kJ/mol to -76kJ/mol. The compounds formed were Ni_3Al and NiAl.

6.2.1 Heats of Formation of Ni-Al Compounds

Pretorius et al[146, 147, 148] proposed a prediction model for the formation of nickel aluminides based on their concentration and heats of formation. According to this effective heat of formation (EHF) model:

> "After first phase formation in metal-metal binary systems the effective concentration moves in the direction of the remaining element and the next phase to form at the growth interface is the next phase richer in the unreacted element."

The effective heat of formation, $\Delta H'$ (kJ/mol), can be defined as:

$$\Delta H' = \Delta H^{\circ} \times \frac{\text{effective concentration limiting element}}{\text{compound concentration limiting element}}$$

where ΔH° = heat of formation in kJ/mol.

Values for the effective heats of formation of Ni-Al compounds are given in Table 52 below:

Phase	Composition	ΔH° (kJ/mol)	$\Delta H'$ (kJ/mol)
$NiAl_3$	$Ni_{0.25}Al_{0.75}$	-38	-5.32
Ni_2Al_3	$Ni_{0.4}Al_{0.6}$	-57	-4.99
NiAl	$Ni_{0.5}Al_{0.5}$	-59	-4.13
Ni_3Al	$Ni_{0.75}Al_{0.25}$	-41	-1.91

Table 52 The effective heats of formation for nickel aluminide phases[146]

The ΔH° values in this table are not exactly the same as those in Table 51 as they are taken from a different reference source.

The phase with the highest value of $\Delta H'$ is $NiAl_3$, so according to the EHF model this would be the first phase to form.

For a thin Al film on thick Ni, the order of phase formation should be:

$$\mathbf{NiAl_3 \Rightarrow Ni_2Al_3 \Rightarrow NiAl \Rightarrow Ni_5Al_3 \Rightarrow Ni_3Al}$$

For thin Ni film on thick Al, $NiAl_3$ will still be the first phase to form. However, once all the Ni has been consumed there are no other Al-rich phases, therefore, no other phases will form.

The results in the current work are for films with a similar order of magnitude to each other. Therefore, they are not quite the same as either of the above cases.

Effective heats of formation diagrams can be constructed by plotting the heats of formation of each compound in the binary system against compositional concentration and triangulating the points. Each triangle represents the energy released as a function of concentration during formation of a particular phase. Figure 83 shows the EHF diagram for the Ni-Al system.

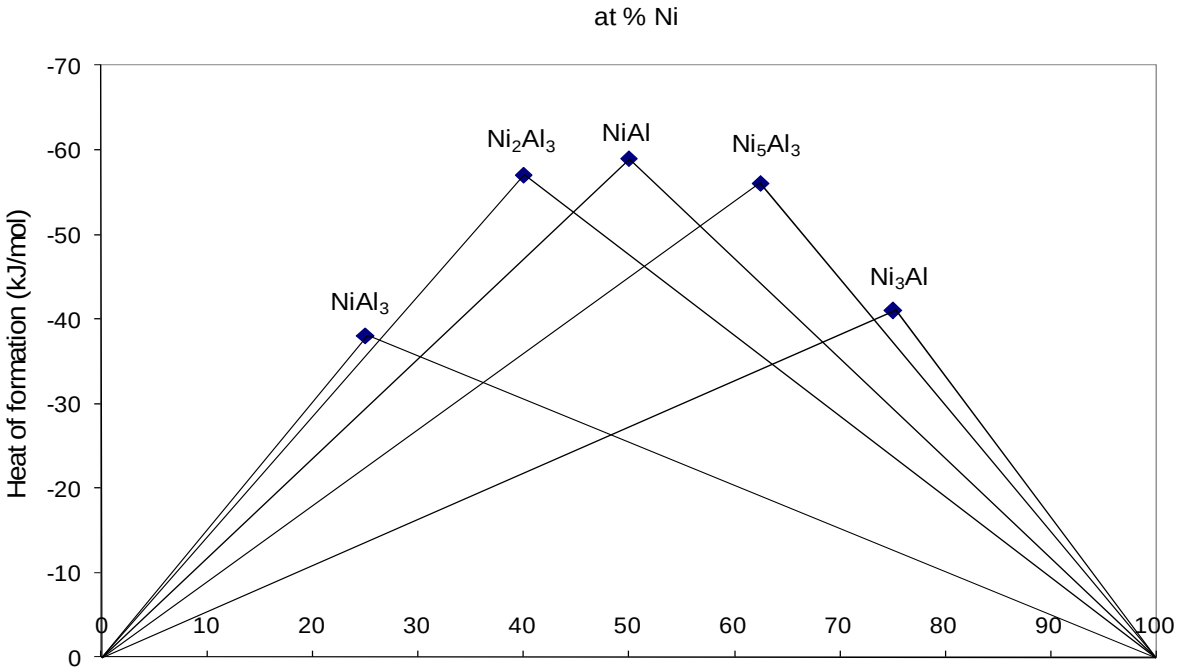

Figure 83 The effective heats of formation diagram for Ni-Al system.

As can be seen in Figure 83, there is very little driver for $NiAl_3$ formation, making Ni_2Al_3 easier to form.

Despite thermodynamic considerations, according to d'Heurle et al[149], Ni_5Al_3 will only form when the correct composition, $Ni_{0.625}Al_{0.375}$ is quenched from high temperature to a metastable state. Hence, in this study, which forms compounds by direct reaction, it is unlikely that this compound will form. They also state that $NiAl_3$ is easier to form than Ni_3Al because Al can diffuse more easily into $NiAl_3$ than Ni atoms can diffuse into Ni_3Al, due to the diffusion characteristics in the two compounds being similar to pure Al and pure Ni respectively.

Figure 84, Figure 85 and Figure 86 show the transformation onset temperature, peak maximum temperature and enthalpy of formation of the Ni-Al compounds with respect to Ni content as measured in this study. The transformation onset temperature for intermetallic Ni-Al compounds is typically 580°C and for the γ′-phase compounds is 710°C. There are no relationships between the average Ni content of the sample and either the 'onset temperature' or 'peak temperature' in the NiAl composition range in Figures 84 and 85 respectively.

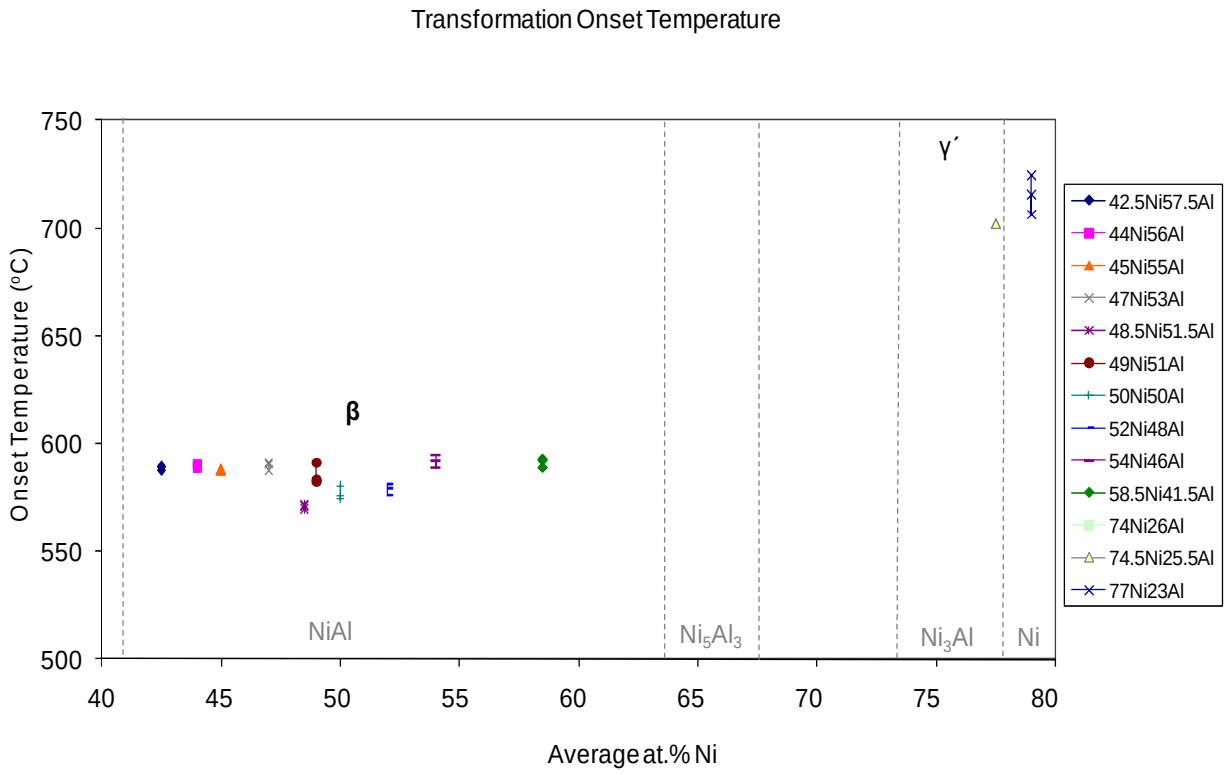

Figure 84 Transformation onset temperatures plotted against average %Ni of the sample

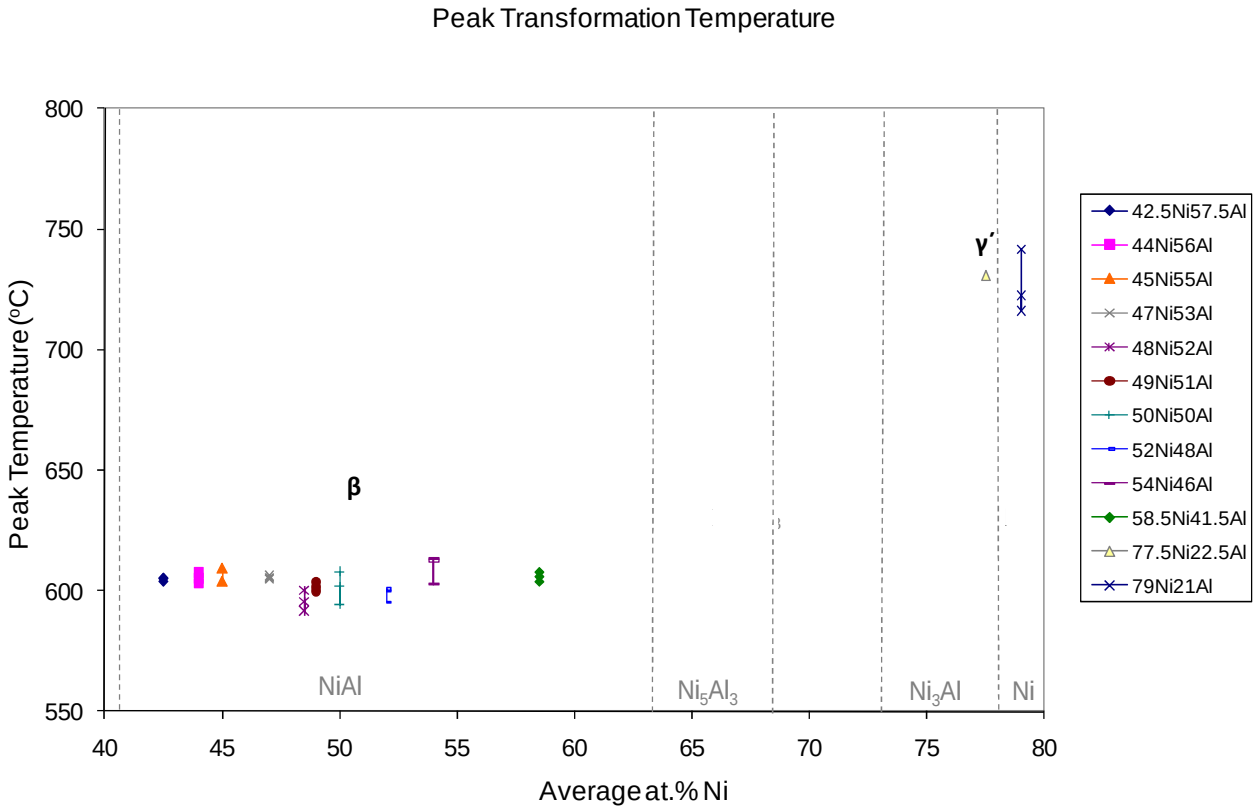

Figure 85 Peak maximum temperatures plotted against average %Ni of the sample

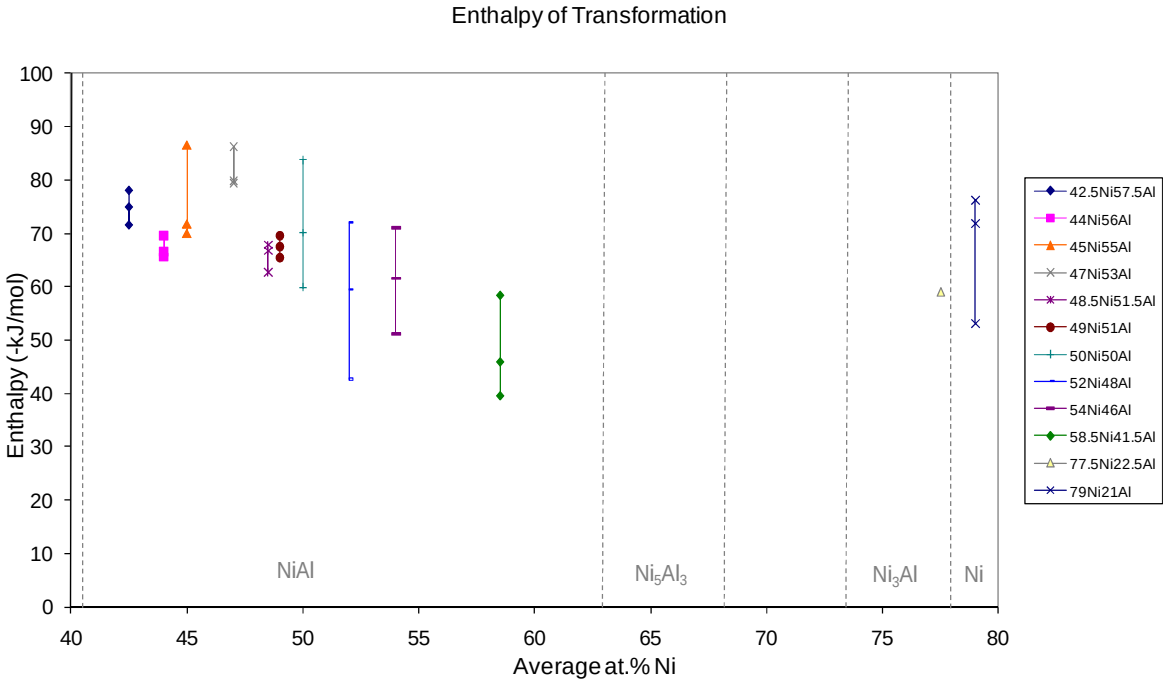

Figure 86 Enthalpy values plotted against average %Ni of the sample

From the enthalpy graph above, it can be seen that samples with average nominal off-stoichiometric compositions '45Ni/55Al' and '47Ni53Al' and the average nominal stoichiometric composition '50Ni50Al' evolve the most heat during reaction, leading to more stable compounds. All of the samples with greater than an average 50% Ni show a large amount of scatter in the measured enthalpy.

If we compare the enthalpy values for the β-phase samples with those in the literature (Figure 86), we can see that the values from the current work are similar to those of Henig et al[143], who used solution calorimetry, but more exothermic than those of Nash et al[142], Saint-Ramond (Table 51) and Pretorius (Table 52) until we reach the higher Ni concentrations (>51% Ni). However, Henig and Nash used X-ray diffraction (XRD) analysis to confirm that their results were for the formation of a single Ni-Al phase, whereas the XRD analysis for the current work shows that Ni_2Al_3 and NiAl were both formed during reaction in the DSC.

If we compare enthalpy values for the γ′-phase samples with those in the literature, we can see that the values from the current work are more exothermic than those of both Rzyman et al[144] and Huang et al[150] who used solution calorimetry and thermodynamic modelling respectively to produce their results. However, XRD analysis showed that the γ′-phase samples formed some NiAl as well as Ni_3Al during reaction in the DSC.

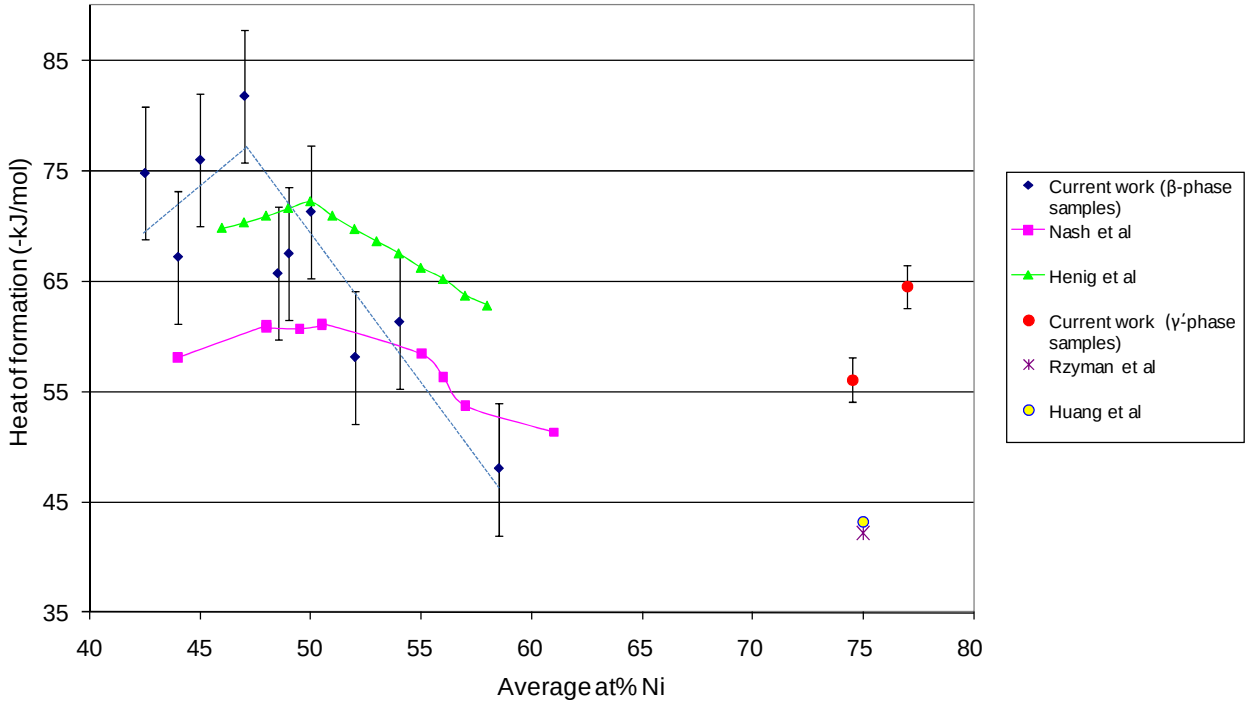

Figure 87 Comparison of enthalpies of formation versus average %Ni of the sample

Nash et al found that 48% Ni, 49.5% Ni and 50.5% Ni gave the highest heats of formation and they were all very similar, whereas the current work found that the sample containing an average of 47% Ni gave the highest heat of formation. However, all three sets of results show that the enthalpy of formation is composition dependent and that it is asymmetrical about the stoichiometric composition, with the Ni-rich side showing a marked decrease. According to Nash, this is due to the fact that there is a change in defect structure. On the Ni-rich side the Ni atoms substitute for Al atoms on the Al sub-lattice, whereas on the Al-

rich side the high Al ratio is accommodated by vacancies on the Ni-rich sub-lattice. This results in a decreasing enthalpy of formation due to a lower number of bonds and more vacancies.

The difference in the heats of formation that has been measured between the current work and Nash's work could be the result of several differences in experimental methods as described in section 6.1.

6.2.2 Stability of Ni-Al Compounds

The relative stability of a compound can be assessed by plotting the energy of formation against melting temperature as in Figure 88 below.

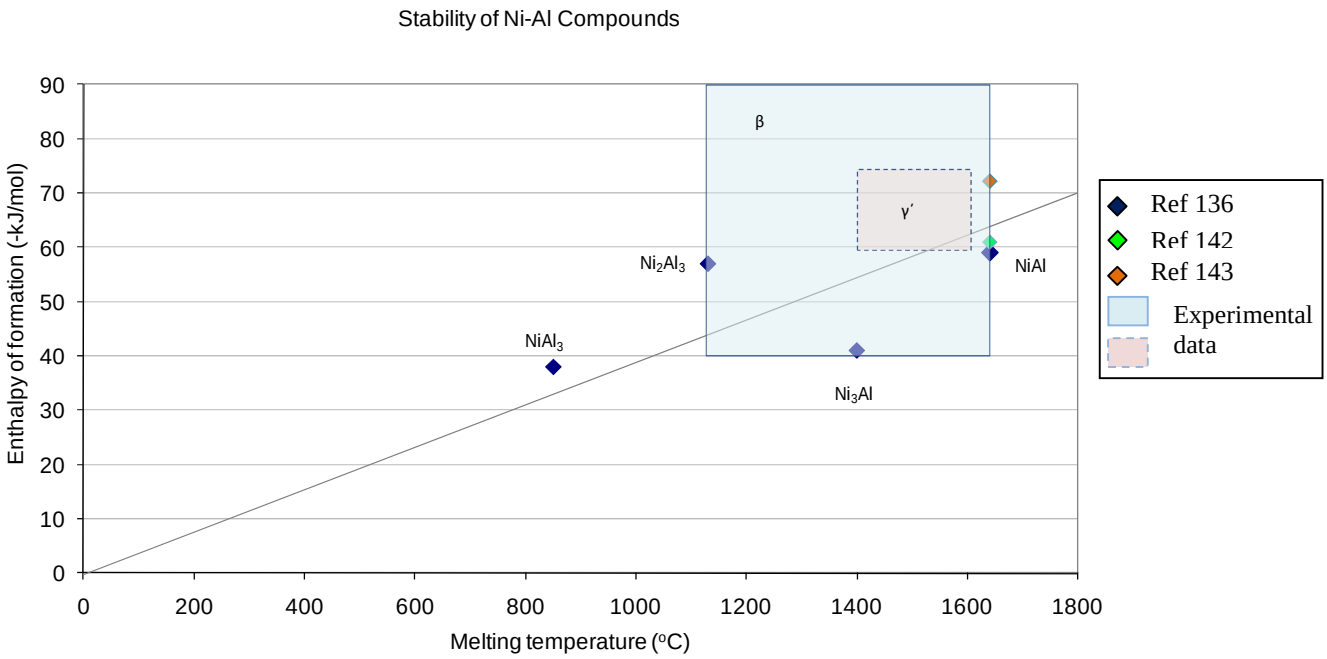

Figure 88 Enthalpy of formation versus melting point of Ni-Al compounds

The most stable compound is the compound with the best balance of high enthalpy of formation and high melting point, NiAl. For samples in the current study, the enthalpy results have been plotted against the melting points of the compounds identified in them by XRD.

Figure 89 shows the enthalpy of formation for the Ni-Al compounds plotted against the reaction trigger temperature.

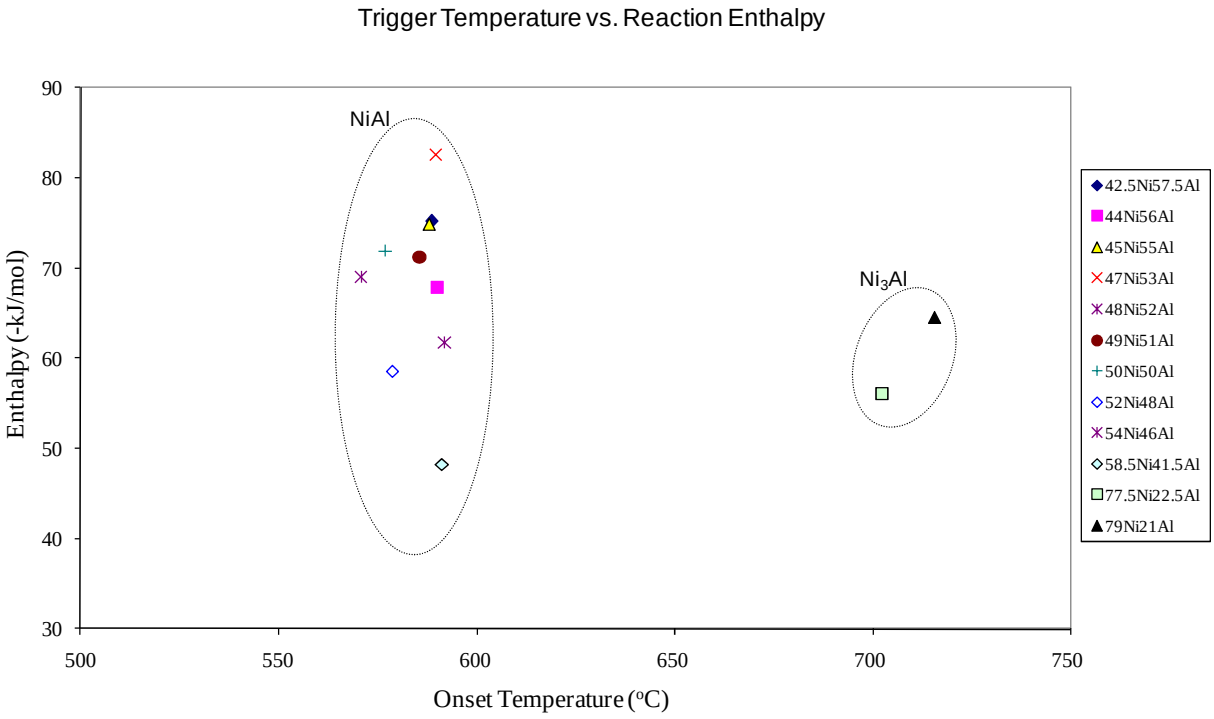

Figure 89 Enthalpy of formation versus reaction trigger temperature of nominal Ni-Al compounds

As we can see from the graph above, there is no relationship between the enthalpy of formation and the trigger temperature (reaction onset temperature.) This lack of a relationship is caused by the enthalpy being a thermodynamic property, whereas the trigger

temperature is affected by both kinetic and thermodynamic factors. Thus, the trigger temperature cannot be used as a substitute for the melting point temperature in any analysis.

The samples intended to produce NiAl and Ni_3Al had mixtures of phases, which could have caused the spread in the enthalpy values.

6.3 Platinum Addition

The compounds that it is possible to form from Pt and Al can be seen in the binary phase diagram in Figure 90. The enthalpy of formation and melting point for each compound is listed in Table 53.

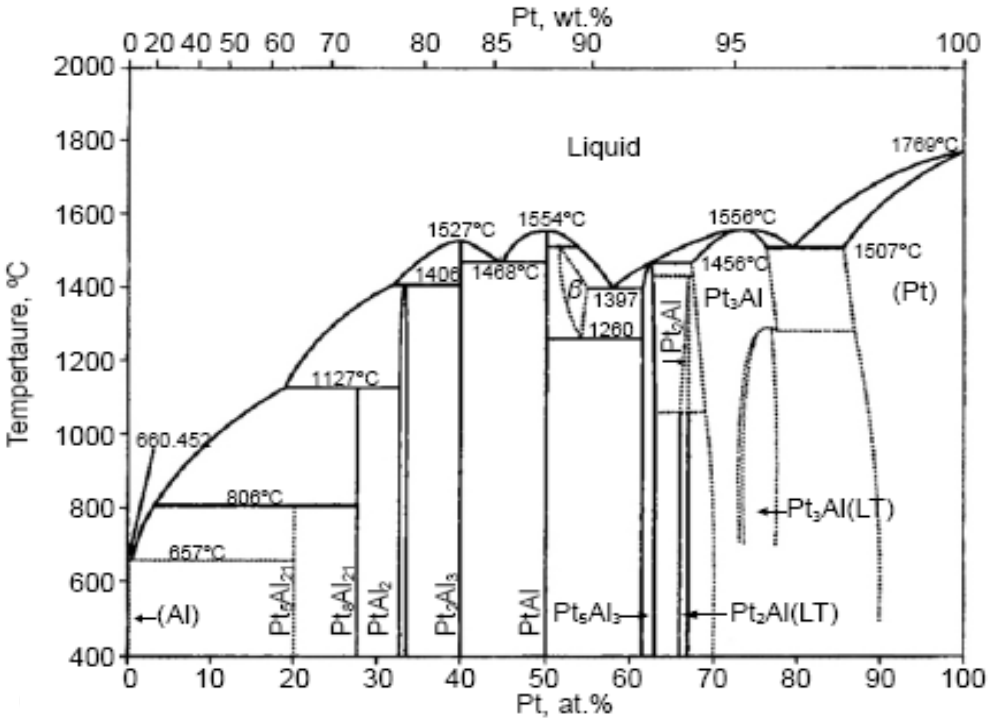

Figure 90 The Pt-Al binary phase diagram[151]

Phase	Melting point (°C)	Enthalpy of Formation (kJ/mol)	Composition (at % Pt)
Al	660.4	-	
Pt_5Al_{21}	806	-55	19.2
Pt_8Al_{21}	1127	-71	27.0
$PtAl_2$	1406	-84	31.5-33.5
Pt_2Al_3	1527	-95	40.0
PtAl	1554	-100	50.0
Pt_5Al_3	1465	-88	61.5-63.0
Pt_2Al	1430	-88	66-67
Pt_3Al	1455 – 1556	-70	67.3-77.7
Pt	1507 - 1769	-	83.8-100

Table 53 Some platinum aluminide characteristics[136]

The compounds that it is possible to form from Ni and Pt can be seen in the binary phase diagram in Figure 91. NiPt and Ni_3Pt may form at lower temperatures, although at the temperatures of interest for coating service, Ni and Pt are in solid solution.

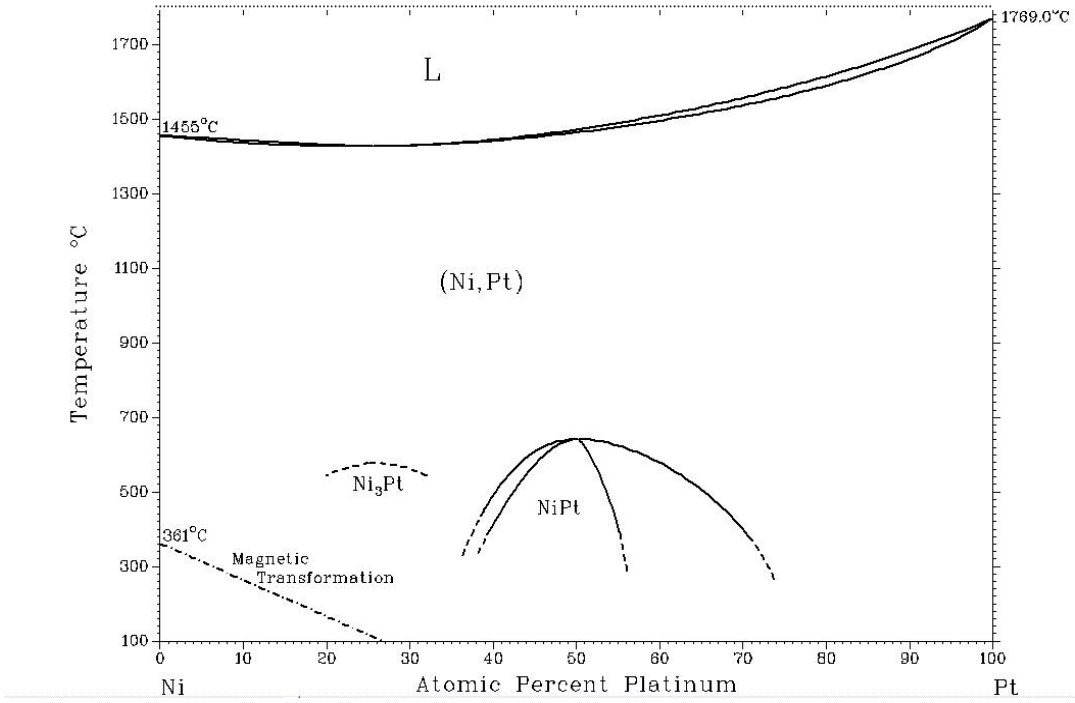

Figure 91 The Ni-Pt binary phase diagram[152]

6.3.1 Heats of Formation of Ni-Pt-Al Compounds

The effective heat of formation model can be applied to the interface between a layer of platinum and a layer of aluminium. Values for the effective heats of formation of Pt-Al compounds are given in Table 54 below:

Phase	Composition	ΔH° (kJ/mol)	$\Delta H'$ (kJ/mol)
Pt_5Al_{21}	$Pt_{0.192}Al_{0.808}$	-57	-5.94
Pt_8Al_{21}	$Pt_{0.276}Al_{0.724}$	-71	-5.14
$PtAl_2$	$Pt_{0.333}Al_{0.667}$	-84	-5.05
Pt_2Al_3	$Pt_{0.400}Al_{0.600}$	-95	-4.75
PtAl	$Pt_{0.500}Al_{0.500}$	-100	-4.00
Pt_5Al_3	$Pt_{0.625}Al_{0.375}$	-88	-2.82
Pt_2Al	$Pt_{0.667}Al_{0.333}$	-88	-2.64
Pt_3Al	$Pt_{0.75}Al_{0.25}$	-70	-1.87

Table 54 The effective heats of formation for platinum aluminide phases[143]

The phase with the highest value of $\Delta H'$ is Pt_5Al_{21}, so according to the EHF model this would be the first phase to form.

For thin Al film on thick Pt, the order of phase formation should be:

$$\mathbf{Pt_5Al_{21} \Rightarrow Pt_8Al_{21} \Rightarrow PtAl_2 \Rightarrow Pt_2Al_3 \Rightarrow PtAl}$$

However, according to Pretorius[142], the Pt_5Al_{21} phase has 416 atoms per unit cell making it extremely difficult to nucleate.

Figure 92 below shows the EHF diagram for the PtAl system.

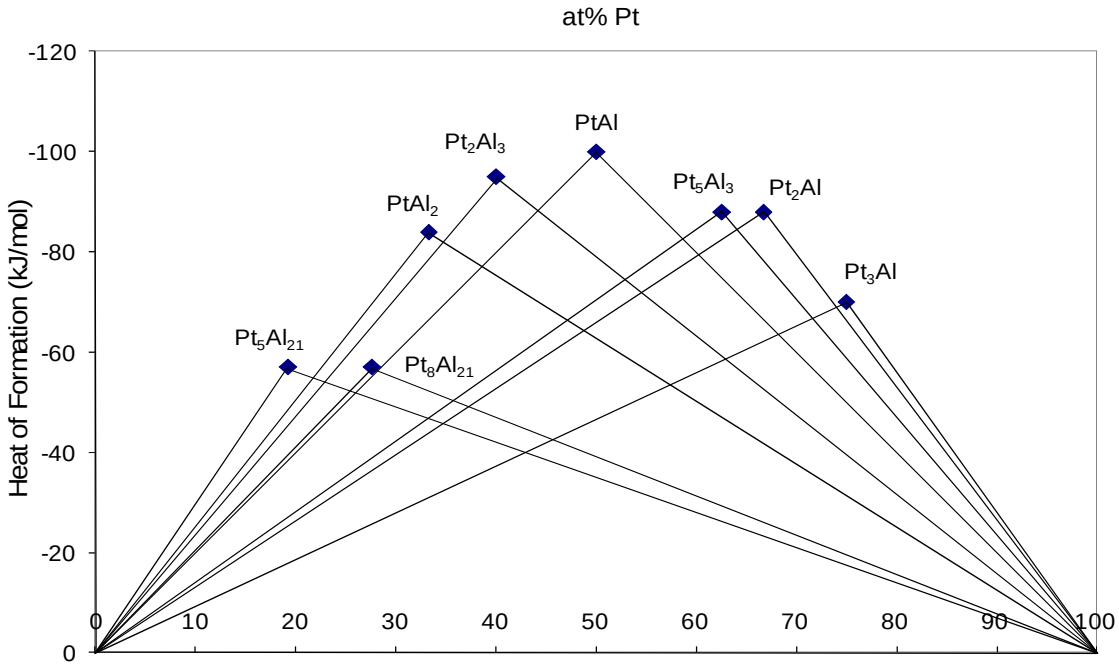

Figure 92 The effective heats of formation diagram for Pt-Al system.

6.3.1.1 NiPtAl

Philip Nash and Hsin-Ning Su carried out reaction synthesis calorimetry, as described in section 6.1, to find the enthalpies of formation for the Al-Ni-Pt system[(152)] and their results can be seen in Table 55 below.

Composition	Pt (at.%)	Enthalpy of Formation (kJ/mol)	Phases found using XRD
$Ni_{0.45}Pt_{0.05}Al_{0.50}$	5	-60.75 +/- 2.59	B2
$Ni_{0.40}Pt_{0.05}Al_{0.55}$	5	-60.99 +/- 1.33	B2 + Ni_2Al_3
$Ni_{0.45}Pt_{0.10}Al_{0.45}$	10	-60.27 +/- 2.38	B2
$Ni_{0.40}Pt_{0.10}Al_{0.50}$	10	-67.91 +/- 1.93	B2
$Ni_{0.40}Pt_{0.15}Al_{0.45}$	15	-61.64 +/- 1.79	B2
$Ni_{0.30}Pt_{0.20}Al_{0.50}$	20	-72.09 +/- 2.38	B2 + ?

Table 55 Nash and Su's enthalpy of formation values for the (Ni, Pt)Al ternary system [(152)]

Figure 93, Figure 94 and Figure 95 show the transformation onset temperature, peak maximum temperature and enthalpy of formation of the samples intended to produce NiPtAl compounds with respect to sample average Pt contents measured in this thesis.

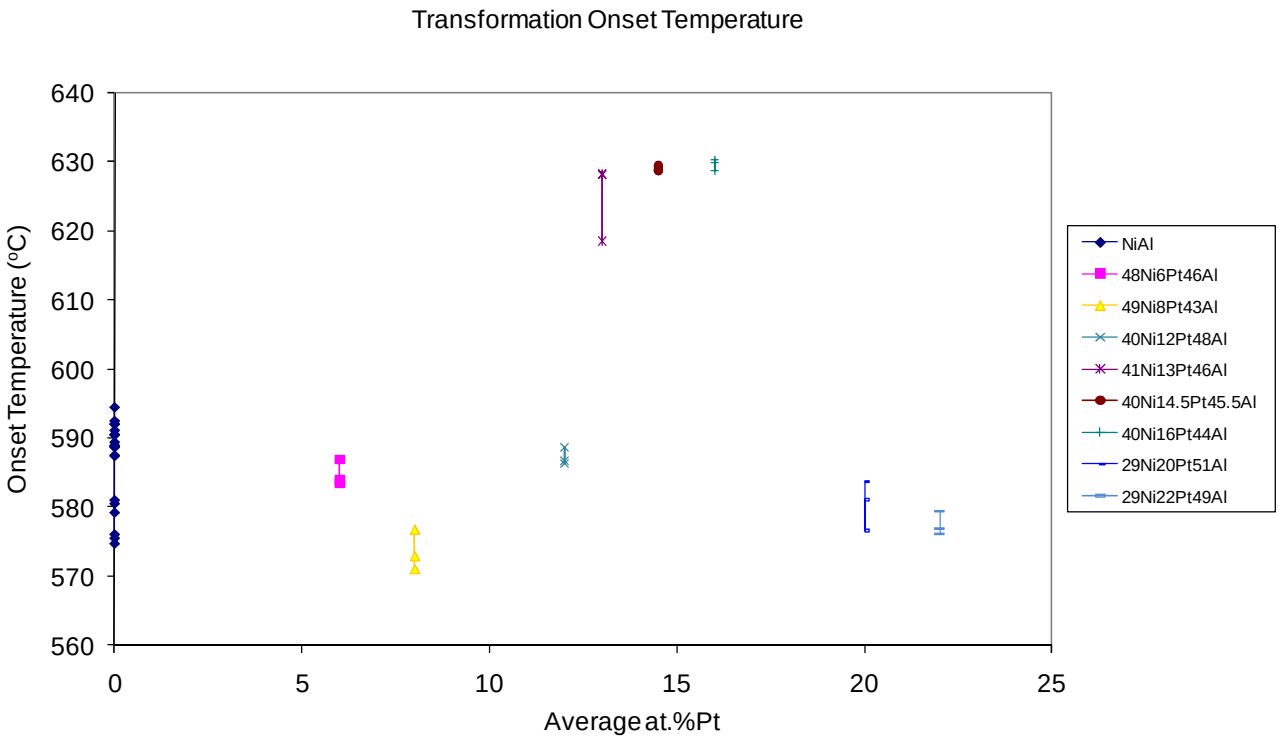

Figure 93 Transformation onset temperatures plotted against nominal %Pt for samples intended to produce NiPtAl

Onset temperatures were in the range 570°C to 630°C. There is no consistent trend with nominal Pt content of the sample but the highest values were found in the 13% - 16% Pt samples.

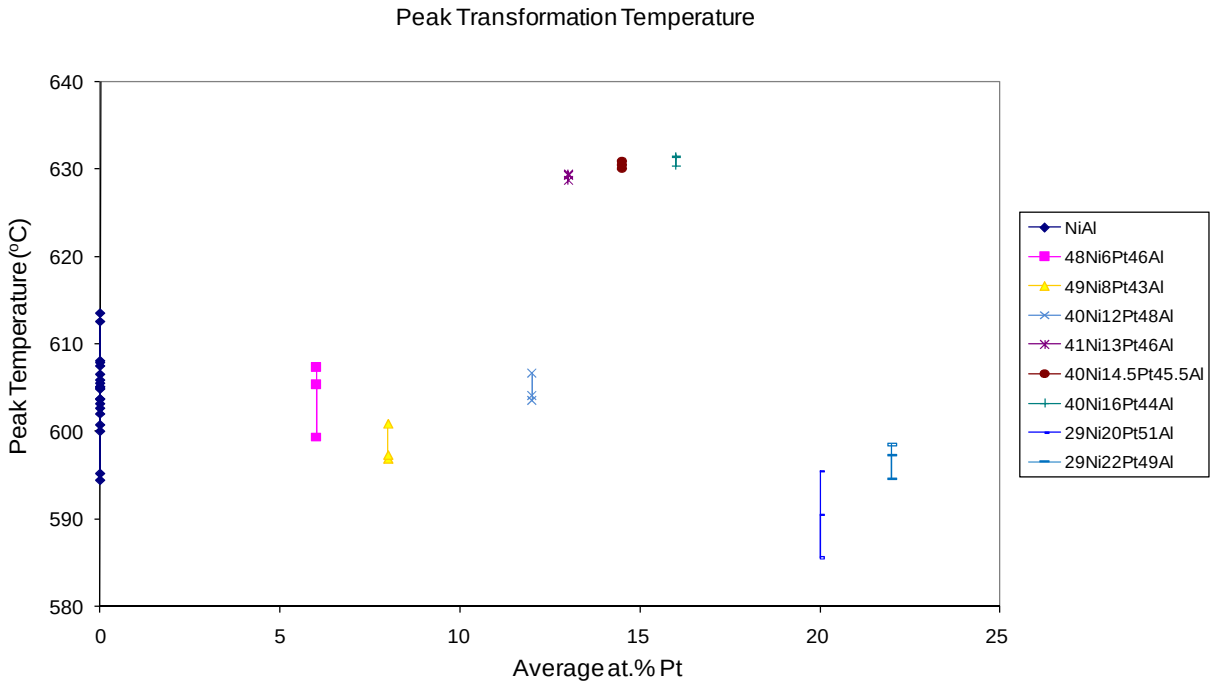

Figure 94 Peak maximum temperatures plotted against nominal %Pt for samples intended to produce NiPtAl

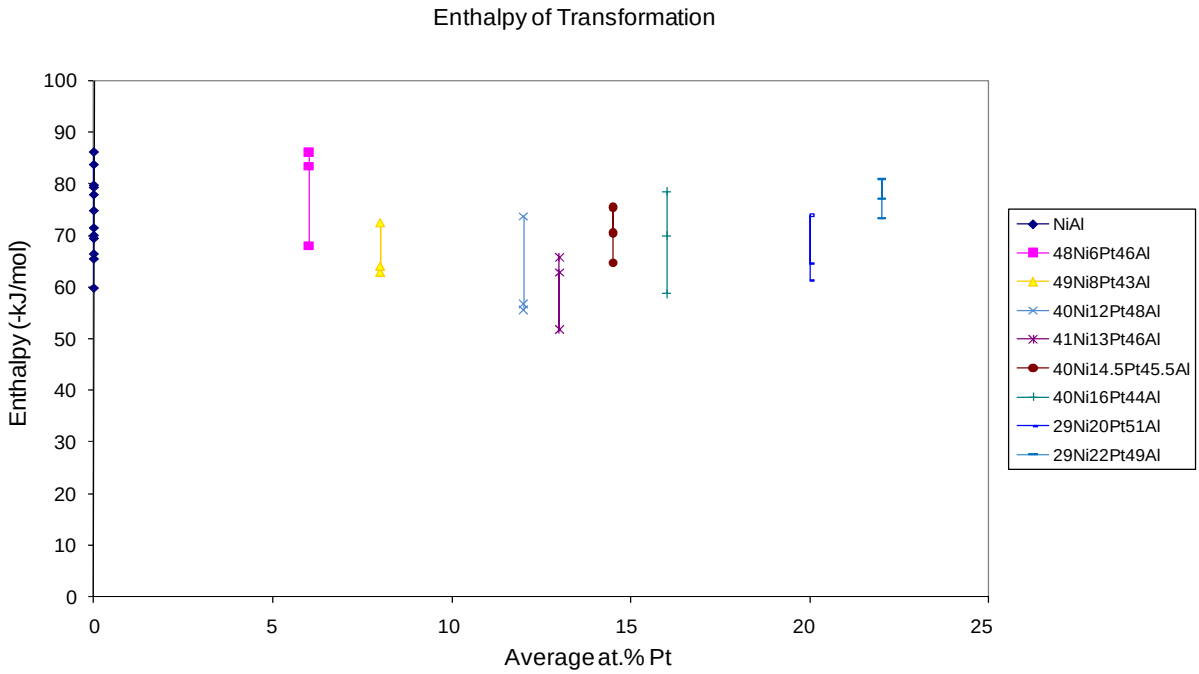

Figure 95 Enthalpy plotted against nominal %Pt for samples intended to produce NiPtAl

Peak temperatures were in the range 585°C to 635°C. There is no consistent trend with nominal Pt content of the sample but the highest temperature values were found in the 13% to 16% Pt samples. Enthalpy values were in the range -50 kJ/mol to -90 kJ/mol. Again, there is no consistent trend with nominal Pt content of the sample but the highest enthalpy values were found in the 6% Pt sample.

If we compare the enthalpy values for NiPtAl with those in the literature (Figure 96), we can see that the values from the current work are similar to those of Nash and Su[152] apart from the sample with a nominal 6%Pt. Their work showed that the enthalpy of formation is not only affected by the % Pt but also by the % Al.

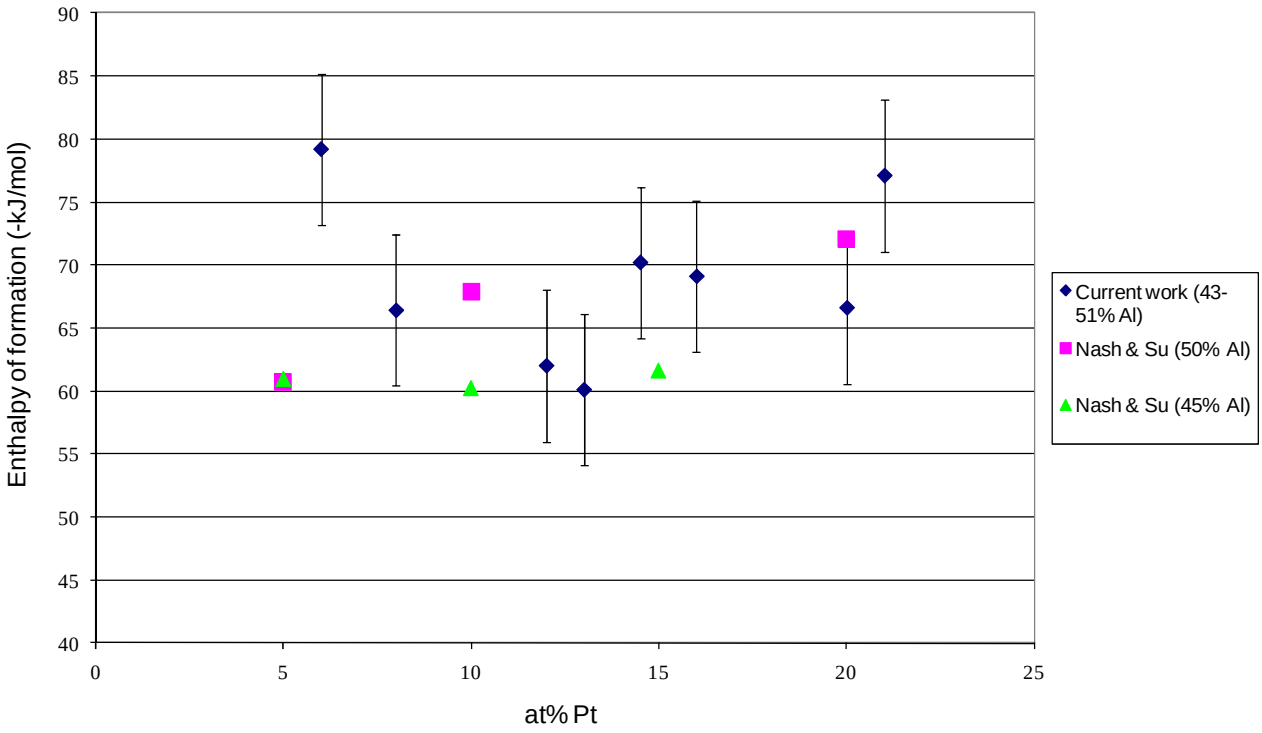

Figure 96 Comparison of enthalpies of formation versus nominal %Pt for samples intended to produce NiPtAl

Average nominal values of Al content in the current work varies between 43% and 51%.

6.3.1.2 $(Ni, Pt)_3Al$

Nash and Su's reaction synthesis calorimetry results for the enthalpies of formation of the $(Ni, Pt)_3Al$ system [152] can be seen in Table 56 below.

Composition	Pt (at.%)	Enthalpy of Formation (kJ/mol)	Phases found using XRD
$Ni_{0.68}Pt_{0.05}Al_{0.27}$	5	-41.85 +/- 1.70	$B2 + L1_2$
$Ni_{0.63}Pt_{0.10}Al_{0.27}$	10	-49.84 +/- 1.79	$B2 + L1_2$

Table 56 Nash and Su's enthalpy of formation values for the $(Ni, Pt)_3Al$ ternary system

Figure 97, Figure 98 and Figure 99 show the transformation onset temperature, peak maximum temperature and enthalpy of formation of the samples intended to produce $(Ni, Pt)_3Al$ compounds with respect to average Pt content based on measurements made in this thesis.

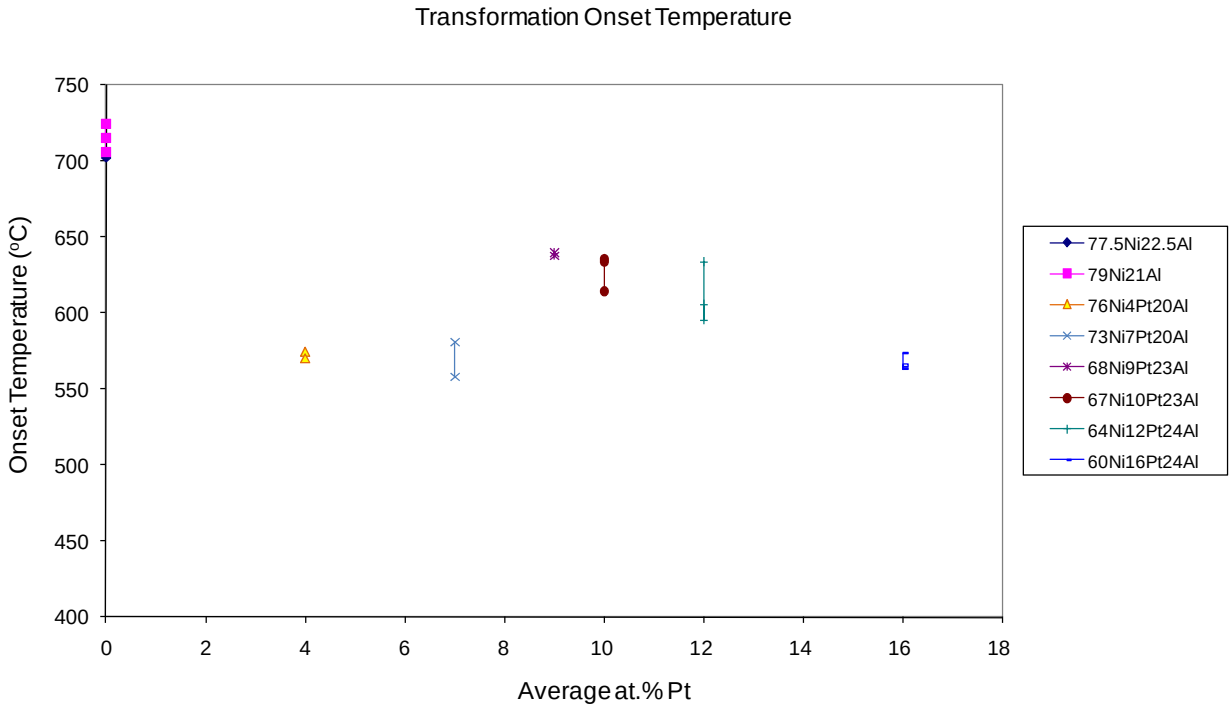

Figure 97 Transformation onset temperatures plotted against nominal %Pt for samples intended to produce $(Ni, Pt)_3Al$

Onset temperatures were in the range 560°C to 640°C. There is no consistent trend with nominal Pt content of the sample.

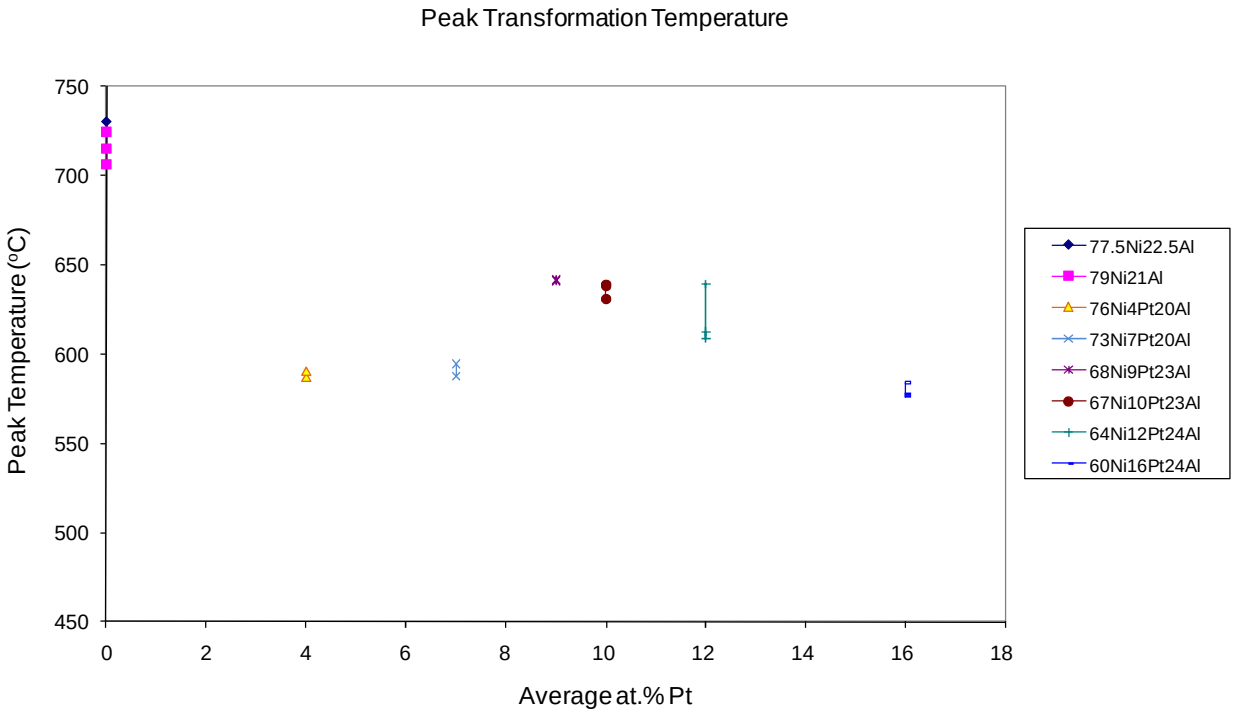

Figure 98 Peak maximum temperatures plotted against nominal %Pt for samples intended to produce $(Ni, Pt)_3Al$

Peak temperatures were in the range 575°C to 645°C. There is no consistent trend with nominal Pt content of the sample.

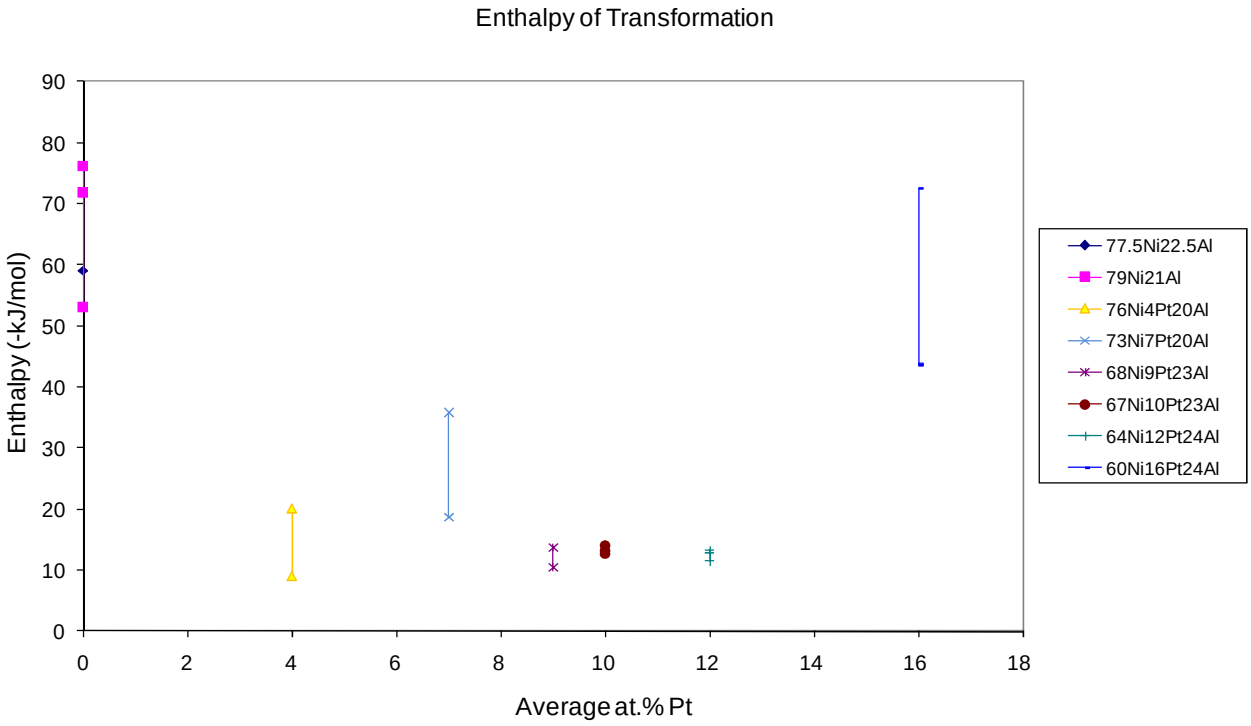

Figure 99 Enthalpy plotted against nominal %Pt for samples intended to produce (Ni, $Pt)_3Al$

Enthalpy values were in the range -9 kJ/mol to -72 kJ/mol. The nominal 16% Pt sample evolved similar amounts of heat during reaction to the samples without any Pt and both show a large amount of scatter.

If we compare the enthalpy values for (Ni, $Pt)_3Al$ with those in the literature (Figure 100), we can see that the value for the sample nominally containing 16% Pt from the current work is similar to those of Nash and Su for 5% Pt and 10% Pt. The rest of the values for the current work are much lower, which could have been due to some of the layers peeling apart.

The samples for the current work contain $PtAl_2$ as well as the $(Ni, Pt)_3Al$ that they were intended to produce. However, from Table 56 it can be seen that Nash and Su also formed two phase samples.

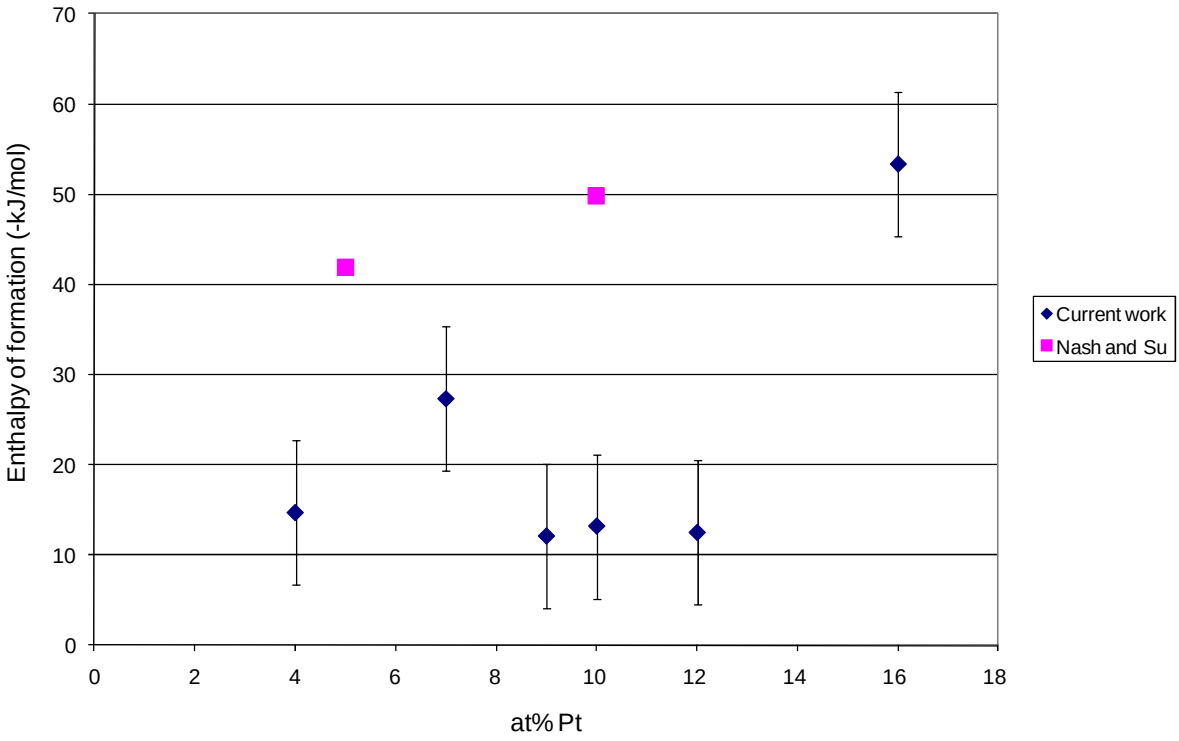

Figure 100 Comparison of enthalpies of formation versus nominal %Pt for samples intended to produce $(Ni, Pt)_3Al$

6.3.2 Stability of Ni-Pt-Al Compounds

The energy of formation against melting temperature for Pt-Al can be seen in Figure 101 below.

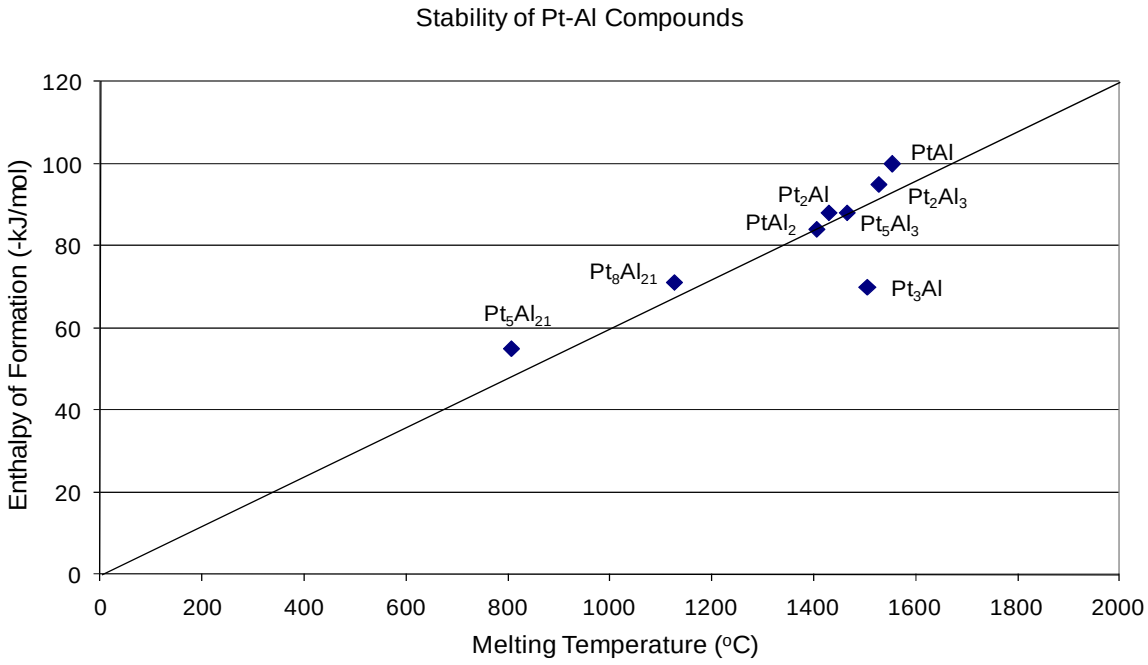

Figure 101 Enthalpy of formation versus melting point of Pt-Al compounds[147]

The most stable compound is the compound with the highest melting point and highest enthalpy value, PtAl.

The Ni-Pt-Al system graph could not be found in the literature, therefore, the experimental data for the current study could not be plotted on the graph above.

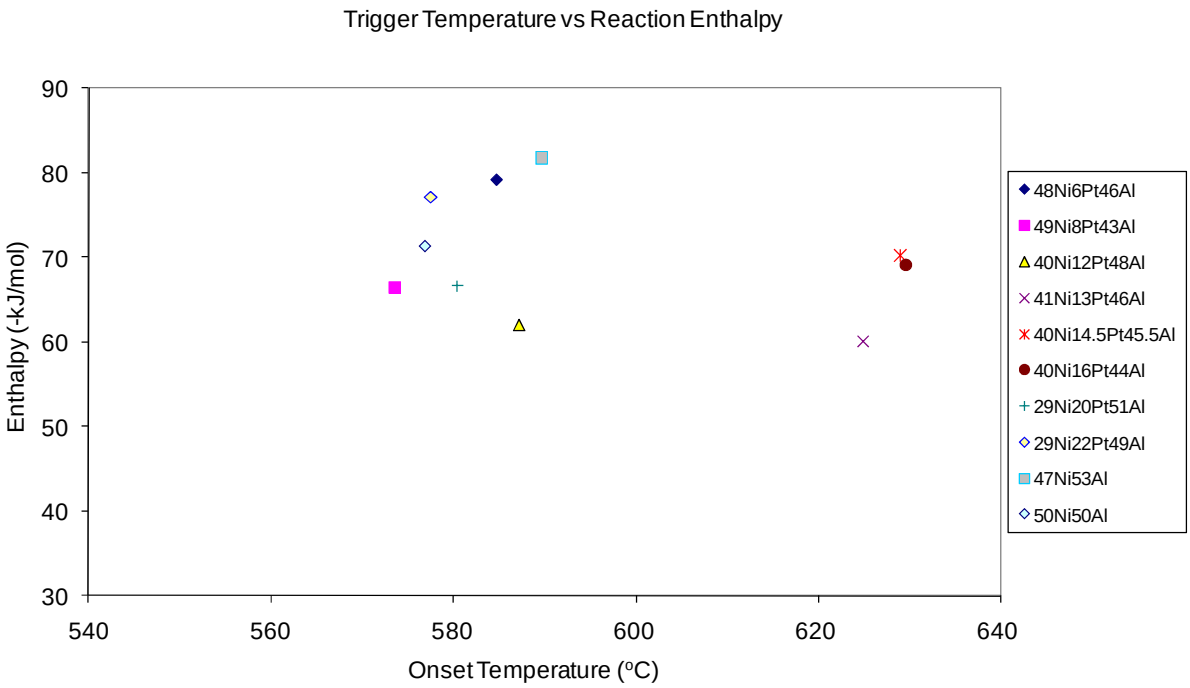

Figure 102 Enthalpy of formation versus reaction trigger temperature of samples intended to produce NiPtAl compounds

As can be seen from the graph above and in Figure 103, there is no relationship between the enthalpy of formation and the trigger temperature (reaction onset temperature). As discussed previously, this is a result of enthalpy being a thermodynamic property, whereas the trigger temperature is affected by both kinetic and thermodynamic factors.

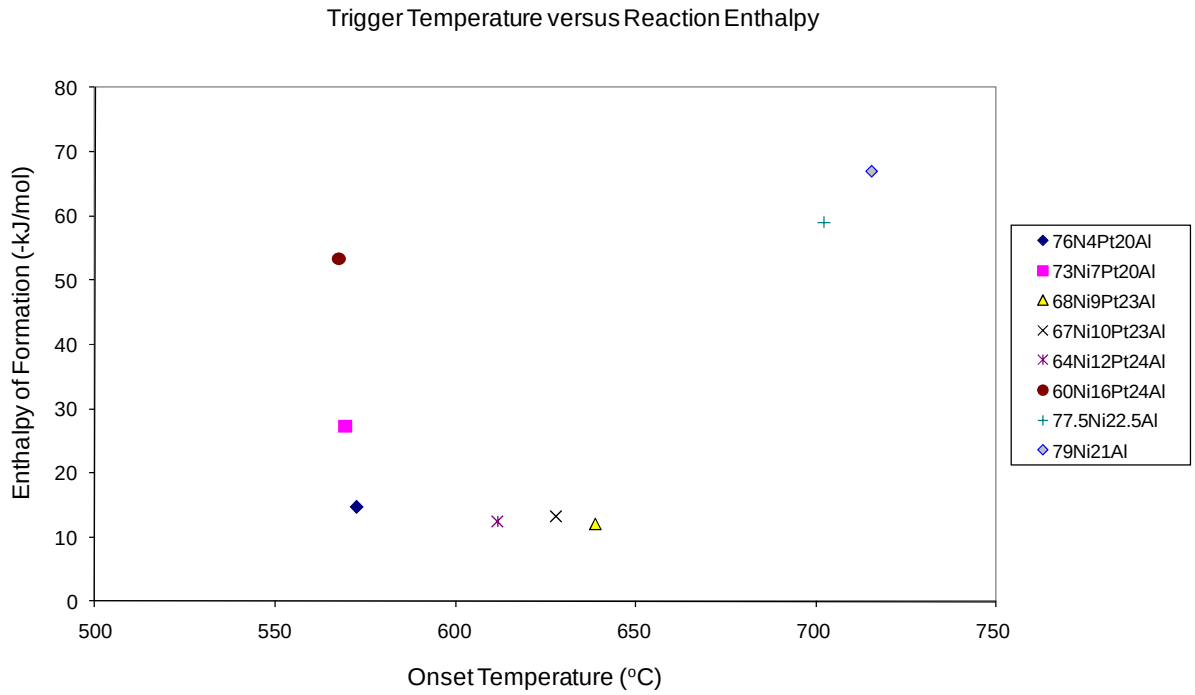

Figure 103 Enthalpy of formation versus reaction trigger temperature of samples intended to produce $(Ni, Pt)_3Al$ compounds

The sample with the highest enthalpy value nominally contains 16% Pt.

6.4 Ruthenium Addition

The compounds that it is possible to form from Ru and Al can be seen in the binary phase diagram in Figure 104. The enthalpy of formation and melting point for each compound is listed in Table 57.

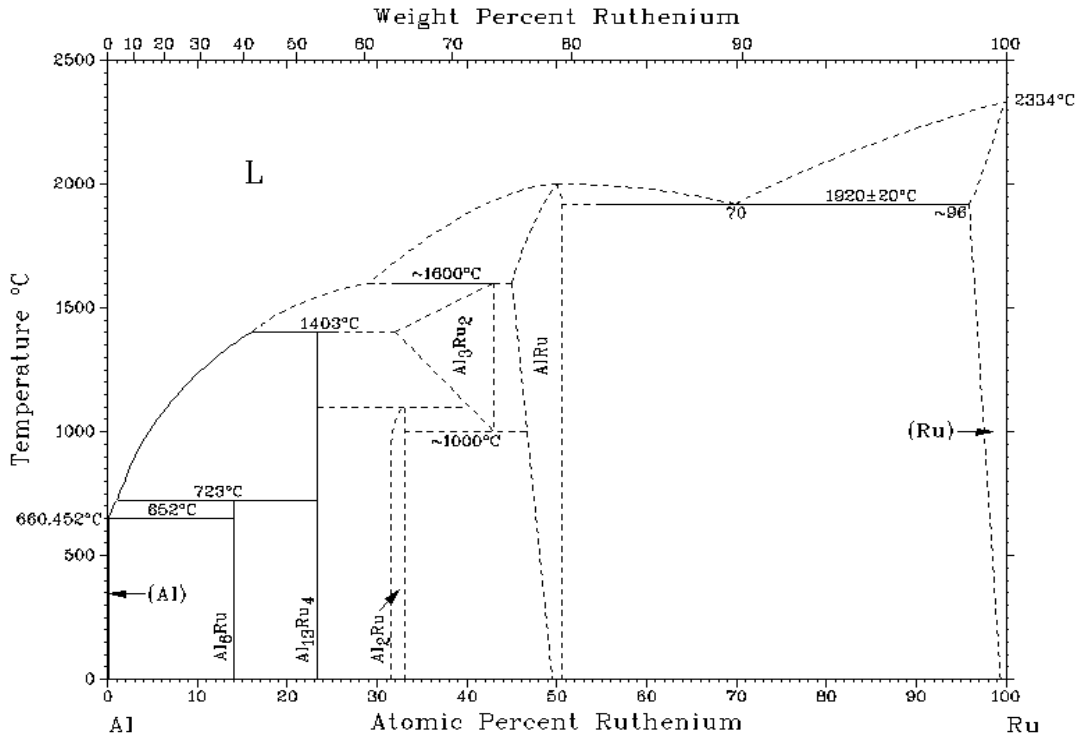

Figure 104 The Ru-Al binary phase diagram[152]

Phase	Melting point (°C)	Enthalpy of Formation (kJ/mol)	Composition (atomic % Ru)
Al	660.4	-	0
$RuAl_6$	723	-22.3	14.3
Ru_4Al_{13}	1403	-38.5	23.5
$RuAl_2$	1460	-45.1	31.5-33.3
Ru_2Al_3	1600	-43.9	32-43
RuAl	2050	-54.5 (-124.5 experimental)	44-50.5
Ru	2334	-	100

Table 57 Some ruthenium aluminide characteristics [152, 153, 154]

No compounds form from Ni and Ru, only limited solid solution as can be seen in the binary phase diagram in Figure 105.

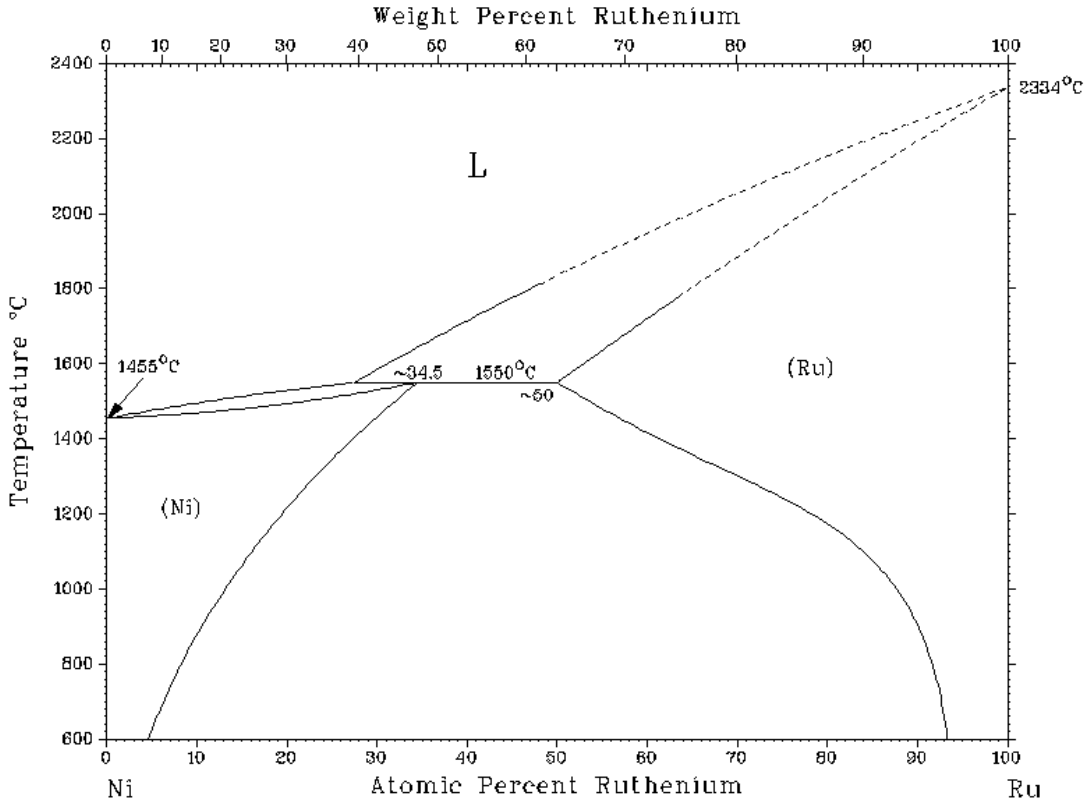

Figure 105 The Ni-Ru binary phase diagram[152]

6.4.1 Heats of Formation of Ni-Ru-Al Compounds

There have not been any effective heats of formation for RuAl published in the open literature. However, using the enthalpy of formation values in Table 57, the EHF diagram can be plotted (Figure 106).

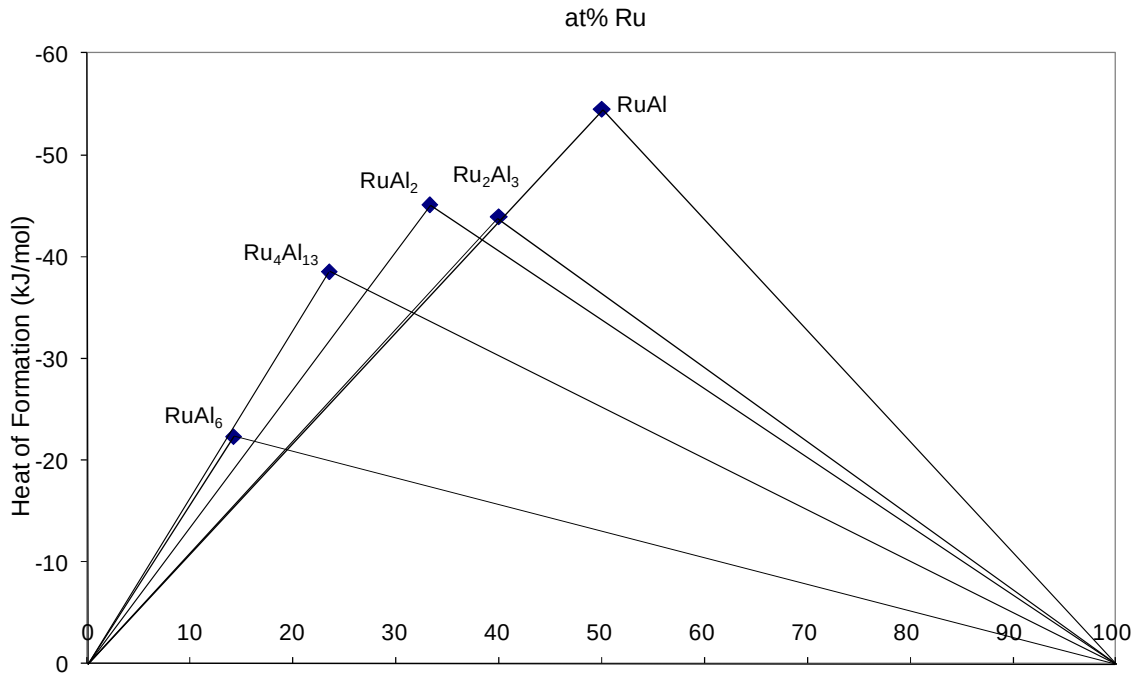

Figure 106 The effective heats of formation diagram for Ru-Al system

For thin Al film on thick Ru, the order of phase formation is likely to be:

$$\mathbf{RuAl_6 \Rightarrow Ru_4Al_{13} \Rightarrow RuAl_2 \Rightarrow Ru_2Al_3 \Rightarrow RuAl}$$

6.4.1.1 NiRuAl

The results of Su's reaction calorimetry experiments [155, 156] to find the enthalpies of formation of the Ni-Ru-Al system can be seen in Table 58 below.

Composition	Ru (at.%)	Enthalpy of Formation (kJ/mol)	Phases found using XRD
$Ni_{0.45}Ru_{0.05}Al_{0.50}$	5	-58.7 +/- 2.4	B2
$Ni_{0.40}Ru_{0.10}Al_{0.50}$	10	-55.9 +/- 2.1	B2
$Ni_{0.45}Ru_{0.10}Al_{0.45}$	10	-55.5 +/- 1.2	B2
$Ni_{0.50}Ru_{0.10}Al_{0.40}$	10	-49.5 +/- 1.4	B2
$Ni_{0.35}Ru_{0.15}Al_{0.50}$	15	-58.2 +/- 2.0	B2
$Ni_{0.30}Ru_{0.20}Al_{0.50}$	20	-61.5 +/- 1.1	B2
$Ni_{0.40}Ru_{0.20}Al_{0.40}$	20	-51.6 +/- 1.0	B2

Table 58 Enthalpy of formation values for the NiRuAl ternary system [155, 156]

Figure 107, Figure 108 and Figure 109 show the transformation onset temperature, peak maximum temperature and enthalpy of formation of the samples intended to produce NiRuAl compounds with respect to average Ru content based on measurements made in this thesis.

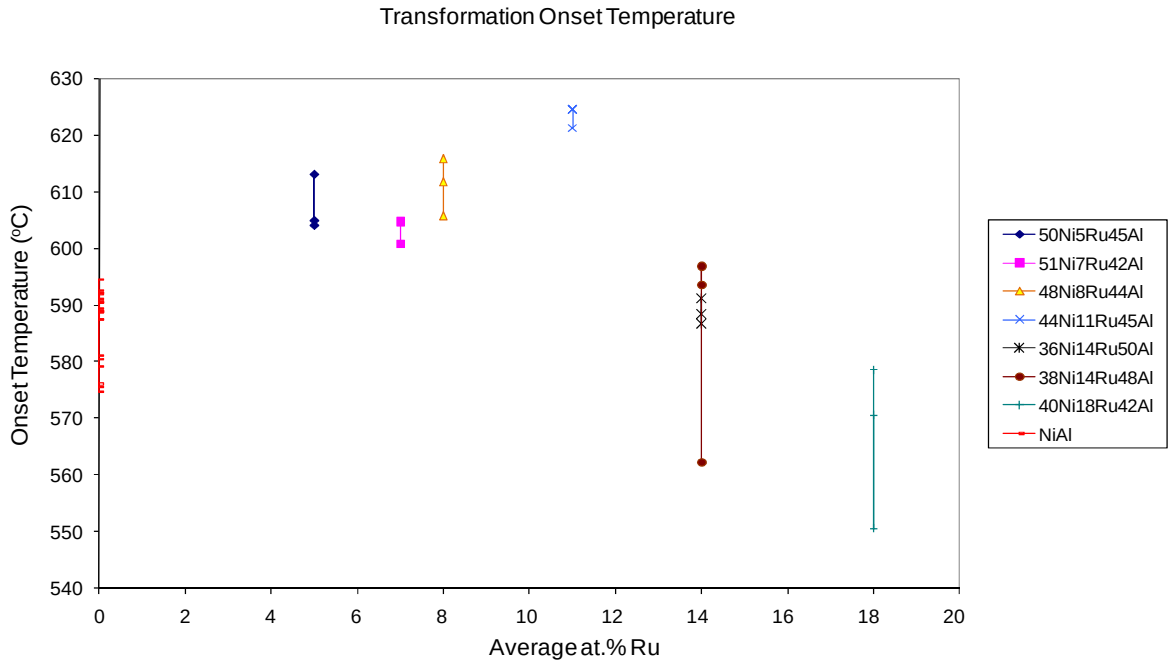

Figure 107 Transformation onset temperatures plotted against nominal %Ru for samples intended to produce NiRuAl

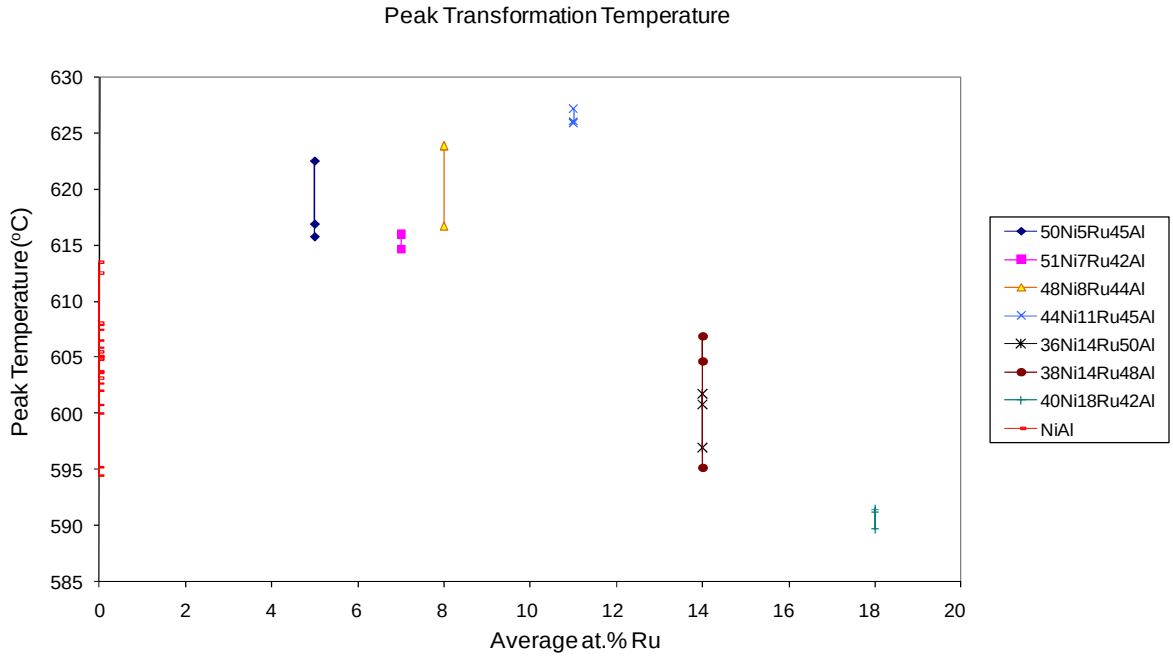

Figure 108 Peak maximum temperatures plotted against nominal %Ru for samples intended to produce NiRuAl

Onset temperatures were in the range 550°C to 625°C and peak temperatures were in the range 590°C to 630°C. There is no consistent trend with nominal Ru content of the sample.

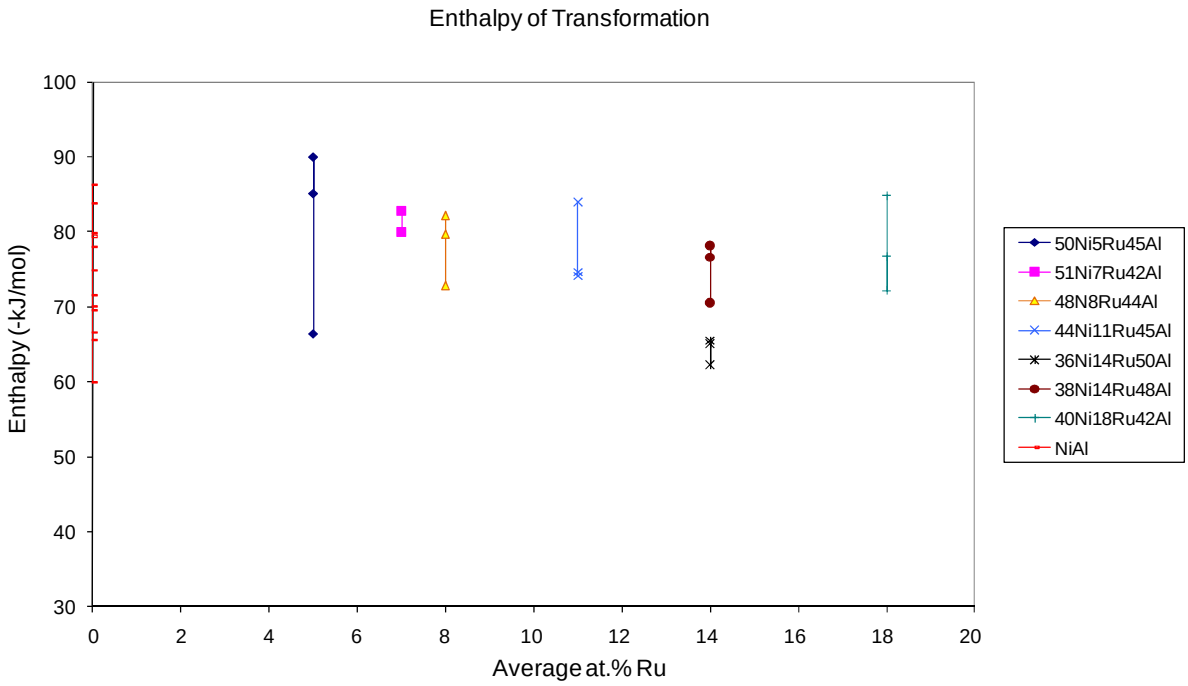

Figure 109 Enthalpy plotted against nominal %Ru for samples intended to produce NiRuAl

Enthalpy values were in the range -60 kJ/mol to -90 kJ/mol. There is no consistent trend with nominal Ru content of the sample.

If we compare the enthalpy values for the samples intended to produce NiRuAl with those in the literature (Figure 110), we can see that the enthalpy values for the current work are more exothermic than those of Su although they follow a similar trend.

The addition of Ru would appear to stabilise the reaction of the β phase as there is only a slight composition dependence over the range 5-18% Ru. There is far more variation of enthalpy with increasing Al content in the Ni-Al phase than in the nominal (Ni, Ru)Al samples.

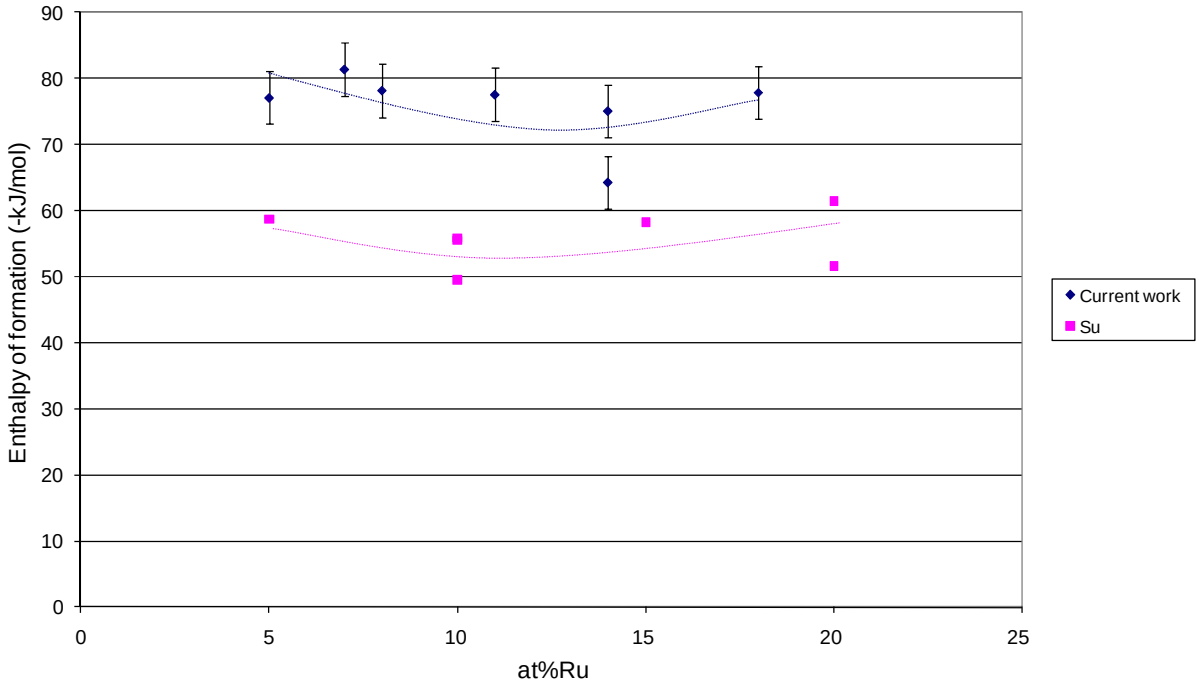

Figure 110 Comparison of enthalpies of formation versus nominal %Ru for samples intended to produce NiRuAl

Su found that 20% Ru gave the highest heat of formation, closely followed by 5% Ru. Similarly, the current work found that 7% Ru and 8% Ru gave the highest heats of formation followed by 18% Ru.

6.4.1.2 (Ni, Ru)$_3$Al

There has not been any heat of formation data for (Ni, Ru)$_3$Al published in the open literature. Figure 111, Figure 112 and Figure 113 show the transformation onset temperature, peak maximum temperature and enthalpy of formation of the samples intended to produce (Ni, Ru)$_3$Al compounds with respect to average Ru content.

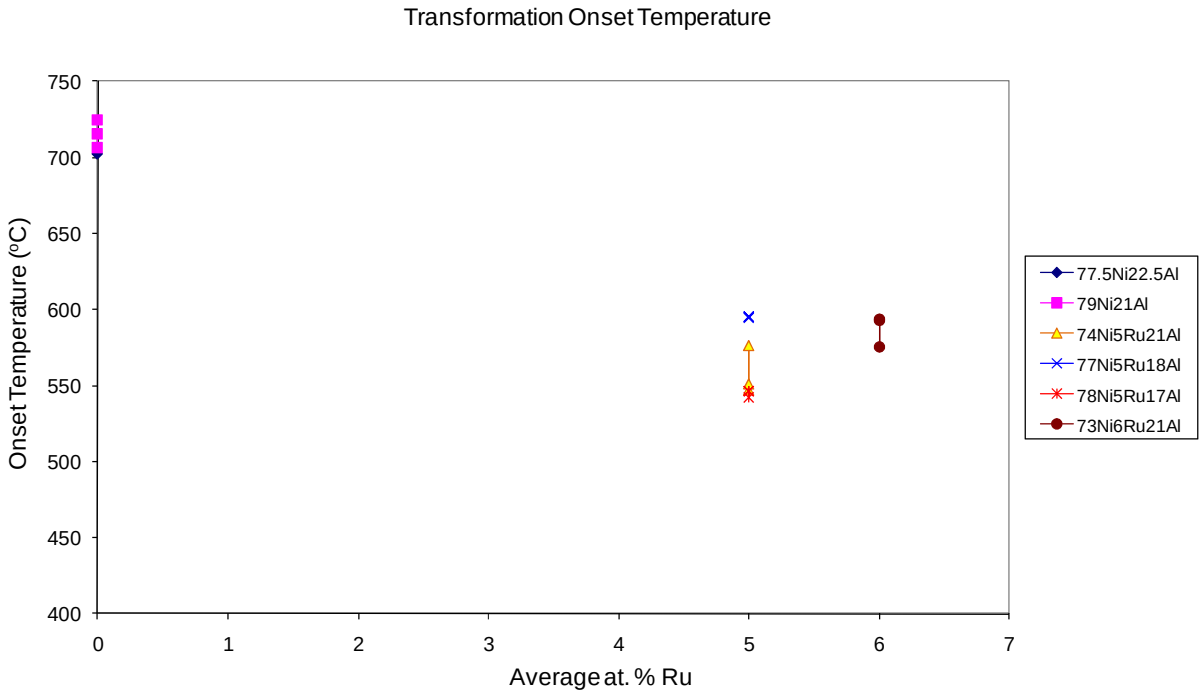

Figure 111 Transformation onset temperatures plotted against nominal %Ru for samples intended to produce (Ni, Ru)$_3$Al

Onset temperatures were in the range 540°C to 595°C and peak temperatures were in the range 560°C to 605°C. Enthalpy values were in the range -60 kJ/mol to-90 kJ/mol.

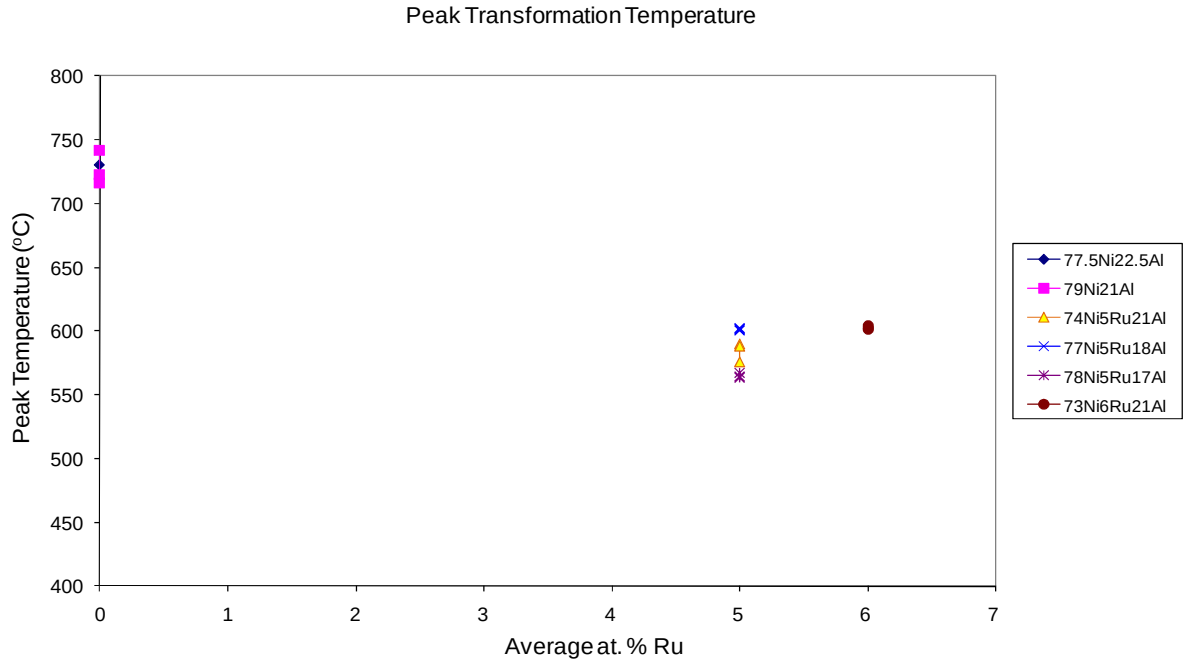

Figure 112 Peak maximum temperatures plotted against nominal %Ru for samples intended to produce $(Ni, Ru)_3Al$

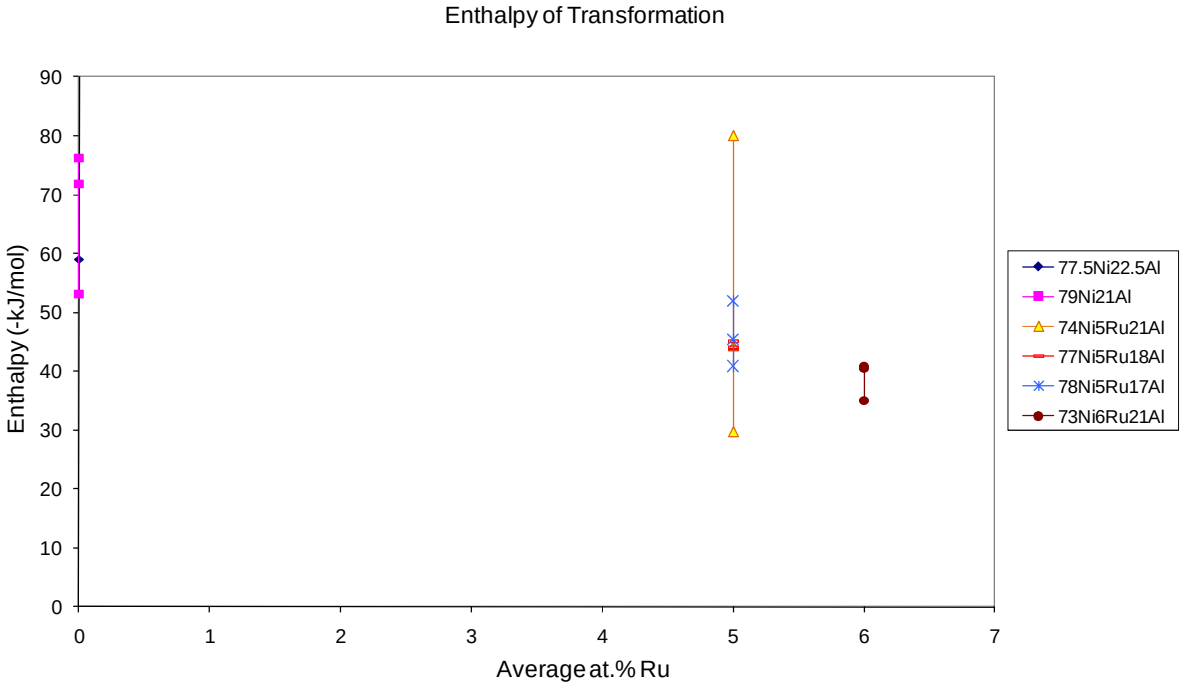

Figure 113 Enthalpy plotted against nominal %Ru for samples intended to produce $(Ni, Ru)_3Al$

6.4.2 Stability of Ni-Ru-Al Compounds

The energy of formation against melting temperature for Ru-Al can be seen in Figure 114 below.

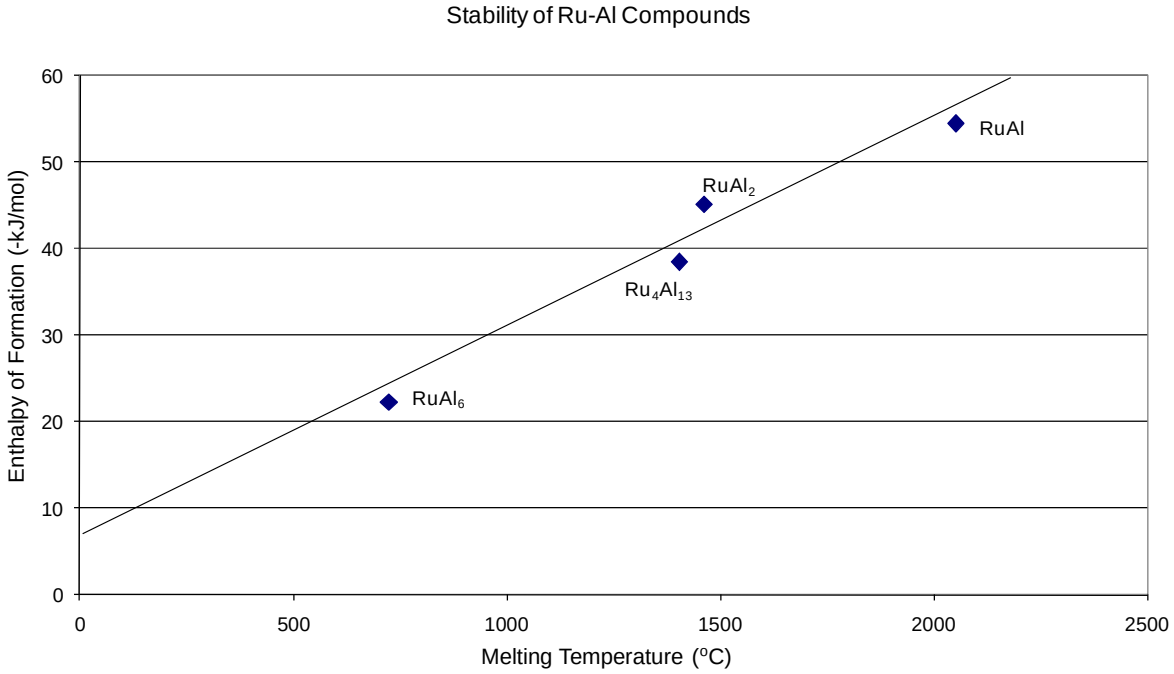

Figure 114 Enthalpy of formation versus melting point of Ru-Al compounds[152, 153, 154]

The most stable compound is the compound with the highest enthalpy combined with the highest melting temperature, RuAl.

The Ni-Ru-Al system graph could not be found in the literature, therefore, the experimental data for the current study could not be plotted on the graph above.

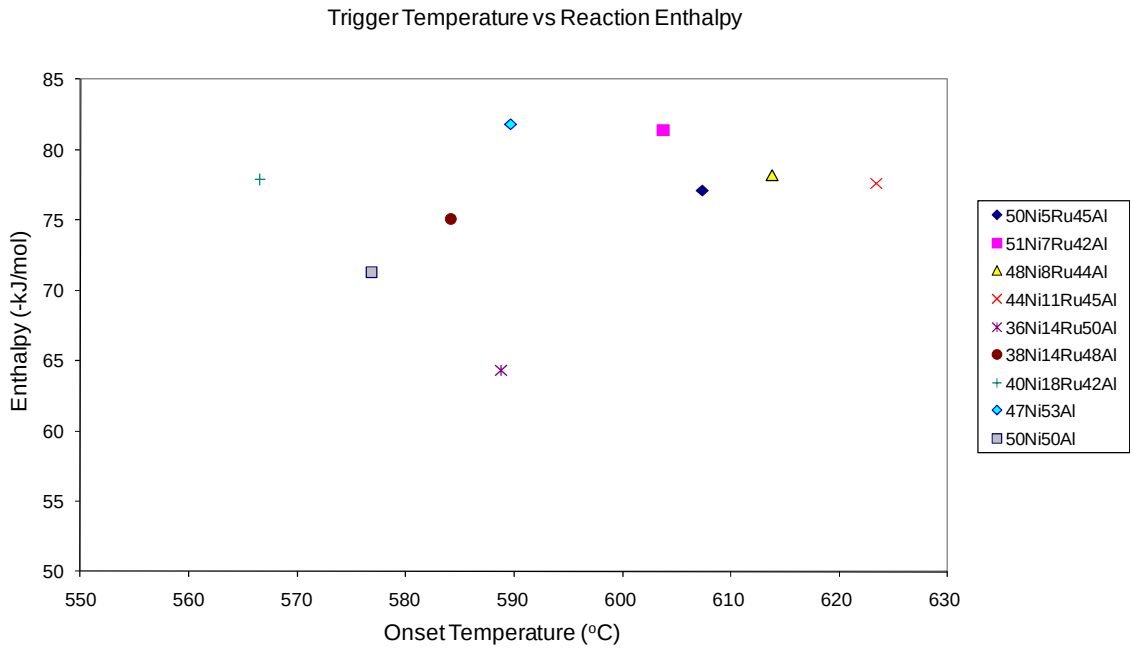

Figure 115 Enthalpy of formation versus reaction trigger temperature of samples intended to produce NiRuAl compounds

As can be seen from the graph above and in Figure 116, there is no relationship between the enthalpy of formation and the trigger temperature (reaction onset temperature). This is consistent with the Ni-Al and Ni-Pt-Al systems presented previously (sections 6.2.2 and 6.3.2) and the kinetic versus thermodynamic explanation.

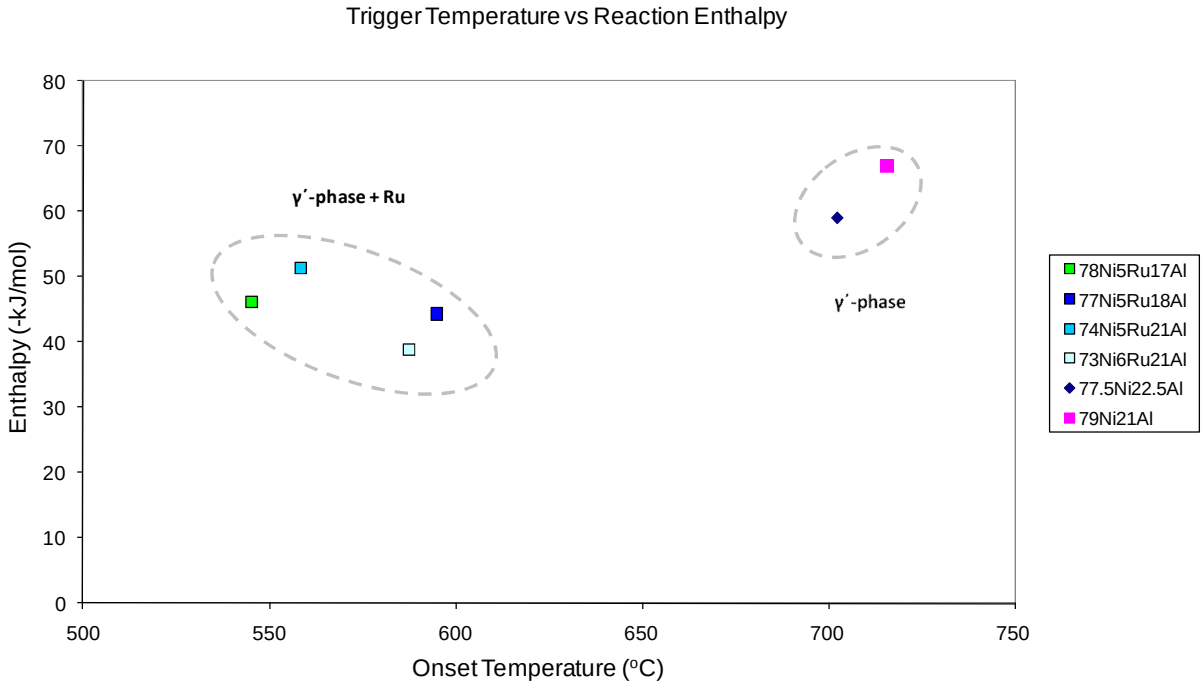

Figure 116 Enthalpy of formation versus reaction trigger temperature of samples intended to produce $(Ni, Ru)_3Al$ compounds

The sample with the highest enthalpy value is the nominal 74Ni5Ru21Al sample.

6.5 Summary

The most stable multilayer coatings from the nominal Ni-Al samples, the nominal Ni-Pt-Al samples and the nominal Ni-Ru-Al samples are plotted together on the graph below.

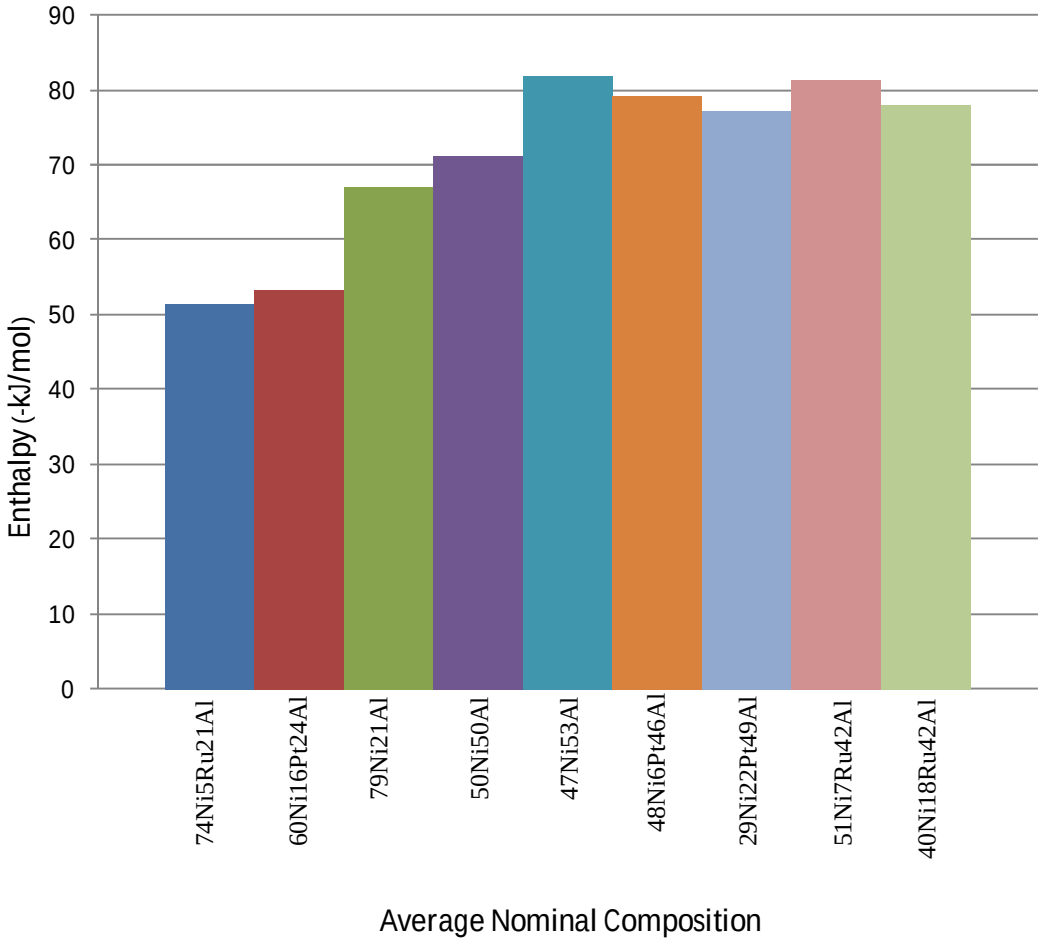

Figure 117 Enthalpy of formation for the most stable multilayers

Platinum and ruthenium additions improve the stability of samples with average compositions within the β-phase region by slightly increasing the enthalpy of formation. Of the systems studied, the as-deposited nominal composition '47Ni53Al' is the most stable

compound, followed by nominal 7% Ru and 6% Pt additions to the β system. The ratio of Ni to Al is also important as it strongly affects the enthalpy values.

The γ′-Ni_3Al region of the Ni-Ru-Al ternary diagram is very small compared to the same region of the Ni-Pt-Al ternary diagram and the samples were affected by peeling of layers. However, the enthalpy values of some of the multilayers were higher than those achieved using powders and very fast heating calorimetry (data from Su [155]). Therefore, it would appear that the samples with average compositions within the γ′-phase region with platinum and ruthenium additions have similar enthalpies to the nominal γ′-Ni_3Al samples. The most stable compounds within this region are those with the as-deposited nominal compositions '74Ni5Ru21Al' and '60Ni16Pt24Al'.

7.0 Conclusions and Further Work

7.1 Conclusions

The aim of this thesis was to research the stability of various intermetallic phases formed by exothermic reaction of multilayer coatings and to select the most stable intermetallics for inclusion in future coating systems.

The conclusions drawn from this study are:

β-Phase:

- Interdiffusion between the layers of the samples was incomplete and the samples produced contained more intermetallic phases than aimed for.
- The phases produced were Ni_2Al_3 and NiAl for the Ni-Al system; Ni(Pt)Al and $PtAl_2$ for the Ni-Pt-Al system and Ni(Ru)Al, RuAl, Ni and Ru for the Ni-Ru-Al system
- Ni-Al samples are stable over a range of off-stoichiometric concentrations ranging from an average 43% Ni to 59% Ni. The highest enthalpy was measured for the sample with a nominal average composition of '47Ni53Al'.
- The most stable of the samples intended to produce β-NiPtAl nominally contained 6% Pt and the most stable of the samples intended to produce β-NiRuAl nominally contained 7% Ru.
- The Ni to Al ratio is important as this strongly affects the stability of the ternary compounds.

γ′-Phase:

- Interdiffusion between the layers of the samples was incomplete and the samples produced contained more intermetallic phases than aimed for.
- The phases produced were Ni_3Al and NiAl for the samples intended to produce Ni_3Al; $(Ni, Pt)_3Al$, Ni and $PtAl_2$ for the samples intended to produce $(Ni,Pt)_3Al$ and $Ni_3(Ru)Al$, Ni and Ru for the samples intended to produce $Ni_3(Ru)Al$.
- The most stable of the samples intended to produce γ′-$Ni(Pt)_3Al$ nominally contained (60% Ni, 16% Pt) 24% Al and the most stable of the samples intended to produce γ′-$Ni_3(Ru)Al$ sample nominally contained 74% Ni, (5% Ru, 21% Al).

General:

- There is no correlation between the onset temperatures of the intermetallic formation reactions and the enthalpy values calculated. It is believed that this is a result of the enthalpies being thermodynamic properties of the intermetallic compounds, whereas the ‘onset temperatures’ are related to interdiffusion (kinetic) factors as well as the thermodynamic driving forces for the reactions. As a result, the reaction onset (or trigger) temperature cannot be used as a substitute for the melting point temperature as a measure of compound stability.

7.2 Further Work

The following research is suggested:

- It is recommended that the Ni_3Al testing could be repeated using aluminium foil as the central layer, in order to prevent the layers from peeling.
- Cross-sections could be prepared to enable the identification of the extent of the different reaction zones within the multi-layered samples.
- A larger number of thinner multilayers could be used and the samples produced could be taken to a higher temperature and held at temperature for a longer time in order for complete diffusion throughout the sample to occur during reaction in the DSC.
- The study could be repeated using other platinum group metals, such as rhodium, rhenium, iridium and palladium.
- The most stable compounds from this study could be coated onto a substrate and cyclic oxidation tests performed.
- The study could be repeated using quaternary compounds such as NiPtRuAl, NiRuHfAl or NiRuAlFe.

8.0 References

1. Meetham, G.W.; *'High-Temperature Materials-a General Review'*, **Journal of Materials Science**, Vol. 26, No. 4, 1991, pp. 853-860

2. Pettit, F.S.; Goward, G.W.*; 'Gas Turbine Applications'*, **Coatings for High Temperature Applications**, ed. E. Lang, Applied Science Publishers, 1983, pp. 341-360

3. Srinivisan, V.; 'High-*Temperature Corrosion and Erosion in Gas Turbine Engines-Where Do We Stand?*', **JoM**, Vol. 46, No. 12, 1994, p. 34

4. www.chevron.com/products/prodserv/fuels/bulletin/aviation fuel/6_at_engines.shtm (9.5.2006)

5. Betteridge, W.; Shaw, S.W.K.; '*Development of Superalloys'***, Materials Science and Technology**, Vol. 3, No. 9, 1987, pp. 682-694

6. Mehta, M.M.; Askew, J.; '*Future Material Needs for low Emissions Gas Turbines'*, Report No. **ASME Paper 97-GT-262**, Int. Gas Turbine and Aeroengine Congress and Exhibition, Orlando, Florida, USA, 2-5 June 1997

7. Shi, C.X.; *'Future of High Temperature Materials for Gas Turbine'*, **Acta Metallurgica Sinica (English Letters)**, Vol. 9, No. 6, 1996, pp. 391-406

8. Driver, D.; Hall, D.W.; Meetham, G.W.; '*The Gas Turbine Engine'*, **The Development of Gas Turbine Materials**, ed. G.W. Meetham, Applied Science Publishers, 1981, pp. 1-30

9. Fritscher, K.; Peters, M.; Rätzer-Scheibe, H-J.; Schulz, U.; '*Superalloys and Coatings'*, **Advanced Aerospace Materials**, Ed. H. Buhl, Springer-Verlag, 1992, pp. 84-107

10. Bradley, E.F.; '***Superalloys; A Technical Guide***', ASM International, 1988

11. Sims, C.T.; Hagel, W.C.; Preface, '***The Superalloys***', John Wiley & Sons, 1972

12. Glover, N.E.; Hicks, M.A.; *'Aeroengine Materials: Past, Present and Future'*, **Experimental Mechanics**, ed. Allison, Balkema, Rotterdam, 1998, pp. 867-877

13. www.tms.org/Meetings/Specialty/Superalloys2000/SuperalloysHistory.html (02.05.2006)

14. Donachie, M.J.; Donachie, S.J.; '***Superalloys; A Technical Guide***', 2nd Edition, ASM International, 2002

15. Meetham, G.W.; '*Steel and Nickel Alloys at High Temperatures*', **Materials and Design**, Vol. 10, No. 2, 1989, pp. 77-92

16. White, C.H.; *'Nickel Base Alloys'*, **The Development of Gas Turbine Materials**, ed. G.W.Meetham, Applied Science Publishers, 1981, pp. 89-120

17. Singer, R.F.; '*New Materials for Industrial Gas Turbines*', **Materials Science and Technology**, Vol. 3, No. 9, 1987, pp. 726-732

18. Pickering, F.E.; '*A Decade of Progress in Turbomachinery Design and Development*', **2nd Cliff Garret Turbomachinery Award Lecture**, October 15, 1985

19. Kablov, E.N.; Toloraiya, V.N.; Orekhov, N.G.; '*Single-Crystal Rhenium-Bearing Nickel Alloys for Turbine Blades of GTE'*, **Metal Science and Heat Treatment,** Vol. 44, Nos. 7-8, 2002, p. 274

20. Kobayashi, T.; Koizumi, Y.; Nakazawa, S.; Yamagata, T.; Harada, H.; '*Design of High Rhenium containing Single Crystal Superalloys with Balanced Intermediate and High Temperature Creep Strengths'*, **Proceedings of the Fourth International Charles Parsons Turbine Conference on "Advances in Turbine Materials, Design and Manufacturing",** Newcastle-upon-Tyne, 4-6 November 1997, pp. 766-773

21. Bhadeshia, H.K.D.H.; '*1st, 2nd and 3rd Generation Single Crystal Nickel Based Superalloys*',www.msm.cam.ac.uk/phase-trans/2003/Superalloys/SX/SX.html (12/02/09)

22. Malik, M.; Morbioli, R.; Huber, P.; *'The Corrosion Resistance of Protective Coatings'*, **High Temperature Alloys for Gas Turbines 1982**, ed. R. Brunetard et al, D. Reidel Publishing Co., 1982, pp. 87-98

23. Felix, P.C.; '*The Role of Corrosion in Modern Gas Turbines*'**, High Temperature Alloys for Gas Turbines 1978**, ed. D Coutsouradis et al, Applied Science Publishers, 1978, pp. 69-80

24. Restall, J.E.; '*Surface Degradation and Protective Treatment*', **The Development of Gas Turbine Materials**, ed. G.W.Meetham, Applied Science Publishers, 1981, pp. 259-290

25. Pomeroy, M.J.; '*Coatings for Gas Turbine Materials and Long Term Stability Issues*', **Materials and Design**, Vol. 26, 2005, pp. 223-231

26. Rhys-Jones, T.N.; '*Coatings for Blade and Vane Applications in Gas Turbines*', **Corrosion Science**, Vol. 29, No. 6, 1989, pp. 623-646

27. Nicholls, J.R.; Stephenson, D.J.; '*High Temperature Coatings for Gas Turbines*', **Intermetallic Compounds: Vol. 2, Practice**, ed. J.H. Westbrook and R.L. Fleischer, John Wiley and Sons, 1995, pp.489-500

28. Nicholls, J.R.; '*Designing Oxidation-Resistant Coatings'*, **JoM**, Vol. 52, No. 1, 2000, pp. 28-35

29. Conner, J.A.; Connor, W.B.; '*Ranking Protective coatings: Laboratory vs. Field Experience*', **JoM**, Vol. 46, No. 12, 1994, pp. 35-46

30. Goward, G.W.; '*Progress in Coatings for Gas Turbine Airfoils*', **Surface and Coatings Technology**, 108-109, 1998, pp. 73-79

31. Duret, C.; Davin, A.; Marijnissen, G.; Pichoir, R.; '*Recent Approaches to the Development of Corrosion Resistant Coatings*', **High Temperature Alloys for Gas Turbines 1982**, ed. R. Brunetard et al, D.Reidel Publishing Company, 1982, pp. 53-86

32. Smith, A.B.; Kempster, A.; '*Utilization of Aluminide Diffusion Coatings to Improve High Temperature Performance*', **Corrosion 2005**, Houston, Texas, pp.5407-5421

33. Wing, G.R.; McGill, I.R.; '*The Protection of Gas Turbine Blades*', **Platinum Metals Review,** No. 25, 1981, pp. 94-105

34. Nicholls, J.R.; Stephenson, D.J.; '*High Temperature Coatings for Gas Turbines*', **Metals and Materials**, Vol. 7, No. 3, 1991, pp. 156-163

35. Stringer, J.; '*Role of Coatings in Energy-producing Systems: an Overview*', **Materials Science and Engineering**, Vol. 87, 1987, pp. 1-10

36. Fairbanks, J.W.; Hecht, R.J.; '*The Durability and Performance of Coatings in Gas Turbine and Diesel Engines*', **Materials Science and Engineering**, Vol. 88, 1987, pp. 321-330

37. Wood, J.H.; Goldman, E.H.; '*Protective Coatings***'**, **Superalloys II**, ed. C.T.Sims, N.S. Stoloff, W.C. Hagel, John Wiley and Sons, 1987, pp.359-384

38. Simonov, V.N.; Khasyanov, M.A.; '*Mathematical Modeling of the Formation of Diffusion Coatings with Periodic Structure'*, **Metal Science and Heat Treatment,** Vol. 36, N0. 6, 1994, pp. 287-291

39. Bartlett, E.S.; Beale, H.A.; '*Oxidation Protective Coatings for Superalloys and Refractory Metals*', **Metals Handbook**, Vol. 5, 9th Edition, ASM, 1982, pp. 375-386

40. TWI Ltd; www.twi.co.uk/content/tfhvofts.html (13.02.09)

41. Deloro Stellite; www.stellite.com/ProductsServices/Equipment/HVOF/tabid/347/Default.aspx (13.02.09)

42. Nicholl, A.R.; '*The Production and Performance Evaluation of High Temperature Coatings'*, **Coatings and Surface Treatment for Corrosion and Wear Resistance**, ed. K.N. Stafford, P.M. Datta, C.G. Coogan, Ellis Horwood Ltd., 1984, pp. 180-212

43. Movchan, B.A.; Demchishin, A.V.; '*Study of the Structure and Properties of Thick Vacuum Condensates of Nickel, Titanium, Tungsten, Aluminium Oxide and Zirconium Dioxide*', **Physics of Metals and Metallography**, Vol. 28, No. 4, 1969, pp. 653-660

44. Thornton, J.A.; '*Influence of Apparatus Geometry and Deposition Conditions on the Structure and Topography of Thick Sputtered Coatings*', **Journal of Vacuum Science and Technology**, Vol. 11, No. 4, 1974, pp. 666-670

45. Teer, D.G.; Delcea, B.L.; '*Grain Structure of Ion-Plated Coatings*', **Thin Solid Films**, Vol. 54, 1978, pp. 295-301

46. Monteiro, O.R.;Vizir, A.; Brown, I.G.; '*Multilayer Thin Films With Chevron-Like Microstructure*', **Journal of Applied Physics**, Vol. 31, 1998, pp. 3188-3196

47. Tryon, B.; Murphy, K.S.; Cao, F.; Levi, C.G.; '*Ruthenium-Containing Bond Coats for Thermal Barrier Coating Systems*', **JoM**, Vol. 58, No.1, 2006, pp. 53-59

48. Haynes, J.A.; Zhang, Y.; Lee, W.Y.; Pint, B.A.; Wright, I.G.; Cooley, K.M.; '*Effects of Platinum Additions and Sulfur Impurities on the Microstructure and Scale Adhesion Behavior of Single Phase CVD Aluminide Bond Coatings'* **Elevated Temperature Coatings: Science and Technology III**, ed. J.M.Hampikian and N.B. Dahotre, The Minerals, Metals and Materials Society, 1999, pp. 185-196

49. Terry, S.G.; Litty, J.R.; Levi, C.G.; '*Evolution of Porosity and Texture in Thermal Barrier Coatings Grown by EB-PVD'*, **Elevated Temperature Coatings: Science and Technology III**, ed. J.M.Hampikian and N.B. Dahotre, The Minerals, Metals and Materials Society, 1999, pp. 13-25

50. Stiger, M.J.; Yanar, N.M.; Pettit, F.S.; Meier, G.H.; '*Mechanisms for the Failure of Electron Beam Physical Vapor Deposited Thermal Barrier Coatings Induced by High Temperature Oxidation'* **Elevated Temperature Coatings: Science and Technology III**, ed. J.M.Hampikian and N.B. Dahotre, The Minerals, Metals and Materials Society, 1999, pp. 51-65

51. Herman, H.; Shankar, N.R.; '*Survivability of Thermal Barrier Coatings'*, **Materials Science and Engineering**, Vol. 88, 1987, pp. 69-74

52. Brindley, W.J.; Miller, R.A.; '*TBCs for Better Engine Efficiency*', **Advanced Materials and Processes**, Vol. 136, Issue 2, August 1989, pp. 29-33

53. Beele, W.; Marijnissen, G.; van Lieshout, A.; '*The Evolution of Thermal Barrier Coatings-Status and Upcoming Solutions for Today's Key Issues*', **Surface and Coatings Technology**, Vol. 120-121, 1999, pp. 61-67

54. Gell, M.; Liangde, X.; Ma, X.; Jordan, E.H.; Padture, N.P.; '*Highly Durable Thermal Barrier Coatings Made by the Solution Precursor Plasma Spray Process*', **Surface and Coatings Technology**, Vol. 177-178, 2004, pp. 97-102

55. Sourmail, T.; '*Coatings for Turbine Blades*', **Cambridge University**, 2003 (www.msm.cam.ac.uk/phase-trans/2003/superalloys/coatings)

56. Du, Y.; Jin, Z.; Huang, P.J.; '*Thermodynamic Assessment of the ZrO_2-$YO_{1.5}$ System*', **Journal of the American Ceramic Society**, Vol. 74, 1991, pp. 1569-1577

57. Rickerby, D.S.; White, D.K.; Bell, S.R.; '*Thermal Barrier Coating for a Superalloy Article'*, **US Patent 5763107**, 1998

58. Rickerby, D.S.; Wing, R.G.; '*Thermal Barrier Coating for a Superalloy Article and a Method of Application Thereof*', **US Patent 5942337**, 1999

59. Rickerby, D.S.; Bell, S.R.; Wing, R.G.; '*Article Including Thermal Barrier Coated Superalloy Substrate'*, **US Patent 5981091**, 1999

60. Kaden, U.; Layens, C.; Peters, M.; Kaysser, W.A.; '*Thermal Stability of an EB-PVD Thermal Barrier Coating System on a Single Crystal Nickel-Base Superalloy*', **Elevated Temperature Coatings: Science and Technology III**, ed. J.M.Hampikian and N.B. Dahotre, The Minerals, Metals and Materials Society, 1999, pp. 27-38

61. Movchan, M.; Rudoy, Y.; '*Composition, Structure and Properties of Gradient Thermal Barrier Coatings Produced by Electron Beam Physical Vapor Deposition'*, **Materials and Design**, Vol. 19, Nos. 5/6, 1998, pp. 253-258

62. Sauthoff, G.; '***Intermetallics***', VCH Publishers, 1995

63. Perepezko, J.H.; '*Microstructural Stability'*, **Intermetallic Compounds: Vol. 1, Principles**, ed. J.H. Westbrook and R.L. Fleischer, John Wiley and Sons Ltd, 1994, pp. 849-870

64. Doychak, J.; '*Oxidation Behavior of High Temperature Intermetallics'*, **Intermetallic Compounds: Vol. 1, Principles**, ed. J.H. Westbrook and R.L. Fleischer, John Wiley and Sons Ltd, 1994, pp. 977-1016

65. Miracle, D.B.; Darolia, R.; *' NiAl and its Alloys'*, **Intermetallic Compounds: Vol. 2, Practice**, ed. J.H. Westbrook and R.L. Fleischer, John Wiley and Sons Ltd, 1994, pp. 53-72

66. Kogachi, M. ; Takeda, Y.; Kim, S. ; *' Observation of High Temperature Al Vacancies and Al Antistructure Atoms in B2 NiAl Superalloys'*, **Scripta Materiala,** Vol. 34, No. 12, 1996, pp. 1845-1850

67. Liu, C.T.; Pope, D.P.; '*Ni_3Al and its Alloys'*, **Intermetallic Compounds: Vol. 2, Practice**, ed. J.H. Westbrook and R.L. Fleischer, John Wiley and Sons Ltd, 1994, pp. 17-51

68. Jackson, M.R.; Rairden, J.R.; '*Protective Coatings for Superalloys and the Use of Phase Diagrams*', **National Bureau of Standards SP-496**, Applications of Phase Diagrams in Metallurgy and Ceramics, Proceedings of Wokshop, Gaithersburg, 1997, pp. 425-439

69. Chakravorty, S.; West, D.R.F.; '*The Constitution of the Ni-Al-Ru System'*, **Journal of Materials Science**, Vol. 21, 1986, pp. 2721-2730

70. Cornish, L.A.; Whitcomb, M.J.; *' A Metallographic Study of the Al-Ni-Re Phase Diagram*', **Journal of Alloys and Compounds**, Vol. 291, Nos. 1-2, Sept. 1999, pp. 145-166

71. Gleeson, B; Sordelet, D; Wang, W; '*Portion of 1100℃ Ni-Al-Pt Phase Diagram*', Iowa State University, unpublished

72. Meier, G.H.; Pettit, F.S.; '*High-Temperature Corrosion of Alumina-Forming Coatings for Superalloys'*, **Surface and Coatings Technology**, Vol. 39/40, 1989, pp. 1-17

73. Angenete, J.; Stiller, K.; '*Comparison of Inward and Outward Grown Pt Modified Aluminide Diffusion Coatings on a Ni Based Single Crystal Superalloy'*, **Surface and Coatings Technology**, Vol. 150, 2002, pp. 107-118

74. Tatlock, G.J.; Hurd, T.J.; Punni, J.S.; '*High Temperature Degradation of Nickel Based Alloys – A Consideration of the Role of Platinum'*, **Platinum Metals Review**, Vol. 31, No. 1, 1987, pp. 26-31

75. Fisher, G.A.; '*The Optimisation of Bondcoat Oxides for Improved Thermal Barrier Coating Adhesion'*, **PhD Thesis 1998**, Cranfield University

76. Tawancy, H.M.; Abbas, N.M.; Rhys-Jones, T.N.; '*Effect of Substrate Composition on the Oxidation Behavior of Platinum-Aluminized Nickel-Base Superalloys'*, **Surface and Coatings Technology**, Vol. 54/55, 1992, pp. 1-7

77. Tawancy, H.M.; Abbas, N.M.; Rhys-Jones, T.N.; 'Role *of Platinum in Aluminide Coatings'*, **Surface and Coatings Technology**, Vol. 49, 1991, pp. 1-7

78. Streiff, R.; Cerclier, O.; Boone, D.H.; 'Structure *and Hot Corrosion Behavior of Platinum-Modified Aluminide Coatings'*, **Surface and Coatings Technology**, Vol. 32, 1987, pp. 111-126

79. Moretto, P.; Bressers, J.; Arrell, D.J.; '*Evolution of a $PtAl_2$ Coating on the Nickel-Base Alloy CMSX-6 Subjected to Thermo-Mechanical Fatigue '*, **Materials Science and Engineering**, Vol. A272, No. 2, 1999, pp. 310-320

80. Haynes, J.A.; Pint, B.A.; Zhang, Y.; Wright, I.G.; '*Comparison of the Cyclic Oxidation Behavior of β-NiAl, β-NiPtAl and γ-γ′ NiPtAl Coatings on Various Superalloys*', **Surface and Coatings Technology**, Vol. 202, 2007, pp. 730-734

81. Haynes, J.A.; Pint, B.A.; Zhang, Y.; Wright, I.G.; '*The Effect of Platinum Content on γ-γ′ NiPtAl Coatings*', **Surface and Coatings Technology**, Vol. 203, 2008, pp. 413-416

82. Gleeson, B.; Wang, W.; Hayash, S.; Sordelet, D.; '*Effects of Platinum on the Interdiffusion and Oxidation Behavior of Ni-Al Based Alloys*', **Materials Science Forum**, Vols. 461-464, 2004, pp. 213-222

83. Izumi, T.; Mu, N.; Zhang, L.; Gleeson, B.; '*Effects of Targeted γ-Ni + γ′-Ni3Al-Based Coating Compositions on Oxidation Behavior*', **Surface and Coatings Technology**, Vol. 202, 2007, pp. 628-631

84. Zhang, Y.; Ballard, D.A.; Stacy, J.P.; Pint, B.A.; Haynes, J.A.; '*Synthesis and Oxidation Behavior of Platinum-Enriched γ + γ′ Bond Coating on Ni-Based Superalloy*', **Surface and Coatings Technology**, Vol. 201, 2006, pp. 3857-3861

85. Bose, S.; '***High temperature coatings***', Butterworth-Heinemann, 2007

86. Zhao, X.; Xiao, P.; '*Effect of Platinum on the Durability of Thermal Barrier Systems with a γ + γ′ Bond Coat*', **Thin Solid Films**, Vol. 517, 2008, pp. 828-834

87. Zhao, X.; Shapiro, I.P.; Xiao, P.; '*Spinel Formation in Thermal Barrier Systems with a Pt-Enriched γ-Ni + γ′-Ni_3Al Bond Coat*', **Surface and Coatings Technology**, Vol. 202, 2008, pp. 2905-2916

88. Caron, P.; '*High γ' Solvus New Generation Nickel-Based Superalloys for Single Crystal Turbine Blade Applications'*, **Superalloys 2000**, ed. T. M. Pollock et al, TMS (the Minerals, Metals and Materials Society), 2000, pp. 737-746

89. Murakami, H.; Honma, T.; Koizumi, Y.; Harada, H.; '*Distribution of Platinum Group Metals in Ni-Base Single-Crystal Alloys'*, **Superalloys 2000**, ed. T. M. Pollock et al, TMS (the Minerals, Metals and Materials Society), 2000, pp. 747-756

90. Zheng, Y.; Wang, X.; Dong, J.; Han, Y.; Murakami, H.; Harada, H.; '*Effect of Ru Addition on Cast Nickel Base Superalloy with Low Content of Cr and High Content of W '*, **Superalloys 2000**, ed. T. M. Pollock et al, TMS (the Minerals, Metals and Materials Society), 2000, pp. 305-311

91. Tryon, B.; Feng, Q.; Pollock T.; '*Intermetallic Phases Formed by Ruthenium-Nickel Alloy Interdiffusion*', **Intermetallics**, Vol. 12, Iss. 7-9, 2004, pp. 957-962

92. Tryon, B.; Pollock, T.M.; Gigliotti, M.F.X.; Hemker, K.; '*Thermal Expansion Behavior of Ruthenium Aluminides'*, **Scripta Materiala**, Vol. 50, 2004, pp. 845-848

93. Bellina, P.; Catanoiu Soare, A.; Morales, F.M.; Vlad, A.; Rühle, M.; '*Oxidation of Ru-containing Alloys'*, Presentation at the **2003 HIPERCOAT TBC Workshop**, Paris

94. Bellina, P.; Catanoiu Soare, A.; Morales, F.M.; Rühle, M.; *'The Formation of Discontinuous Al2O3 Layers during High Temperature Oxidation of RuAl Alloys,'* **Journal of Materials Research,** 2005

95. Cao, F.; Nandy, C.K.; Stobbe, D.; Pollock, T.M.; '*Oxidation of Ruthenium Aluminide-Based Alloys: The Role of Microstructure and Platinum Additions*', **Intermetallics**, Vol. 15, 2007, pp.34-43

96. Wolff, I.M.; '*Toward a Better Understanding of Ruthenium Aluminide'*, **JOM**, Vol. 49, No. 1, 1997, pp. 34-39

97. Tawancy, A.M.; Abbas, N.M.; *'Performance of Selected Thermal Barrier Coating Systems with Various Combinations of Pt-Group Metals'*, **King Fahd University** technical report for Rolls-Royce plc, September 2000

98. Tawancy, A.M.; Abbas, N.M.; '*Comparative Behavior of Low-cost Pt, CN122 + Pt and Pt/REJ2 Bond Coats Deposited on Alloy CMSX-4'*, **King Fahd University** technical report for Rolls-Royce plc, March 2001

99. Fleischer, R.L.; McKee, D.W.; '*Mechanical and Oxidation Properties of AlRu-based High Temperature Alloys*', **Metallurgical Transactions A,** Vol. 24A, No. 3, 1993, pp.759 - 763

100. Alperine, S.; Steinmetz, P.; Friant-Costantini, A.; Josso, P.; '*Structure and High Temperature Performance of Various Palladium-Modified Aluminide Coatings; A Low Cost Alternative to Platinum Aluminides'*, **Surface and Coatings Technology**, Vol. 43/44, 1990, pp. 347-358

101. Fisher, G.; Chan, W.Y.; Datta, P.K.; Burnell-Gray, J.S.; '*Noble Metal Aluminide Coatings for Gas Turbines'*, **Platinum Metals Review**, Vol. 43, No. 2, 1999, pp. 59-61

102. Birks, N.; Meier, G.H.; '***Introduction to the High Temperature Oxidation of Metals***', Edward Arnold Publishers Ltd, 1983

103. Birks, N.; Meier, G.H.; Pettit, F.S.; '***Introduction to the High Temperature Oxidation of Metals***', 2nd Edition, Cambridge University Press, 2006

104. Scully, J.C.; '*Oxidation*', **The Fundamentals of Corrosion**, 3rd edition, Pergamon Press, 1990

105. Cambridge University; 'www.doitpoms.ac.uk/tlplib/Ellingham_diagrams/Ellingham.php' (1.7.09)

106. Lai, G.Y.; '***High Temperature Corrosion and Materials Applications',*** ASM International, 2007

107. Tryon, B.; '*Multi-Layered Ruthenium-Containing Bond Coats for Thermal Barrier Coatings*', **PhD Thesis 2005**, University of Michigan, USA

108. Khanna, A.S.; '***Introduction to High Temperature Oxidation and Corrosion***', ASM International, OH, 2002

109. Wagner, C.; '*Beitrag zur Theorie des Anlaufvorgangs'*, **Z. Physikalische Chemie**, Vol 21, 1933

110. Angenete, J.; '*Aluminide Diffusion Coatings for Ni Based Superalloys*', **PhD Thesis 2002**, Göteburg University, Sweden

111. Wortman, D.J.; Duderstadt, E.C.; Nelson, W.A.; '*Bond Coat Development for Thermal Barrier Coatings*', **Journal of Engineering for Gas Turbines and Power**, Vol. 112, No. 4, 1990, pp. 527-530

112. Evans, A.G.; Mumm, D.R.; Hutchinson, J.W.; Meier, G.H.; Pettit, F.S.; '*Mechanisms Controlling the Durability of Thermal Barrier Coatings'*, **Progress in Materials Science**, Vol. 46, 2001, pp. 505-553

113. Clarke, D.R.; Sergo, V.; He, M-Y.; '*Precursor to TBC Failure caused by Constrained Phase Transformation in the Thermally Grown Oxide*', **Elevated Temperature Coatings: Science and Technology III**, ed. J.M.Hampikian and N.B. Dahotre, The Minerals, Metals and Materials Society, 1999, pp. 67-78

114. Banks, J.P.; Saunders, S.R.J.; Chunnilall, C.J.; '*Adhesion of Thermal Barrier Coatings – the Development of Metastable Alumina*', **Materials at High Temperatures**, Vol. 17, No. 2, 2000, pp.225-230

115. Quadakkers, W.J.; Tyagi, A.K.; Clemens, D.; Anton, R.; 'The *Significance of Bond Coat Oxidation for the Life of TBC Coatings*', **Elevated Temperature Coatings: Science and Technology III**, ed. J.M.Hampikian and N.B. Dahotre, The Minerals, Metals and Materials Society, 1999, pp. 119-130

116. Li, M.H.; Sun, X.F.; Gong, S.K.; Zhang, Z.Y.; Guan, H.R.; Hu, Z.Q.; '*Phase Transformation and Bond Coat Oxidation Behavior of EB-PVD Thermal Barrier Coating*', **Surface and Coatings Technology**, Vol. 176, 2004, pp. 209-214

117. Padture, N.P.; Gell, M.; Jordan, E.H.; '*Thermal Barrier Coatings for Gas-Turbine Engine Applications*', **Science**, Vol 296, 2002, pp. 280-284

118. Tolpygo, V.K.; Clarke, D.R.; '*Morphological Evolution of Thermal Barrier Coatings Induced by Cyclic Oxidation*', **Surface and Coatings Technology**, Vol. 163-164, 2003, pp. 81-86

119. Tolpygo, V.K.; Clarke, D.R.; Murphy, K.S.; '*Oxidation-Induced Failure of EB-PVD Thermal Barrier Coatings*', **Surface and Coatings Technology**, Vol. 146-147, 2001, pp. 124-131

120. Hebsur, M.G.; Nesbitt, J.A.; Barrett, C.A.; '*High Temperature Oxidation Resistant and Low Coefficient of Thermal Expansion NiAl-Base Bond Coat Developed for a Turbine Blade Application*', **Research and Technology**, NASA, TM-2003-211990, pp. 15-16

121. Mumm, D.R.; Evans, A.G.; Spitsberg, I.T.; '*Characterization of a Cyclic Displacement Instability for a Thermally Grown Oxide in a Thermal Barrier Coating*', **Acta Materialia**, Vol 49, 2001, pp. 2329-2340

122. Balint, D.S.; Hutchinson, J.W.; '*Mode II Edge Delamination of Compressed Thin Films*', **Journal of Applied Mechanics**, Vol. 68, 2001, pp. 725-730

123. Balint, D.S.; Xu, T.; Hutchinson, J.W.; Evans, A.G.; '*Influence of Bond Coat Thickness on the Cyclic Rumpling of Thermally Grown Oxides*', **Acta Materialia**, Vol. 54, 2006, pp. 1815-1820

124. Evans, A.G.; Clarke, D.R.; Levi, C.G.; '*The Influence of Oxides on the Performance of Advanced Gas Turbines*', **Journal of the European Ceramic Society**, Vol. 28, 2008, pp. 1405-1419

125. He, M.Y.; Evans, A.G.; Hutchinson, J.W.; '*The Ratcheting of Compressed Thermally Grown Thin Films on Ductile Substrates'*, **Acta Materiala**, Vol. 48, iss. 10, 2000, pp. 2593-2601

126. Ibegazene-Ouali, F.; Mevrel, R.; Rio, C.; Renollet, Y.; '*Microstructural Evolution and Degradation Modes in Cyclic and Isothermal Oxidation of an EB-PVD Thermal Barrier Coating*', **Materials at High Temperatures**, Vol. 17, No. 2, 2000, pp. 205-218

127. Rapp, R.A.; Zhang, Y.S.; '*Hot Corrosion of Materials: Fundamental Studies*', **JOM,** Vol. 46, No. 12, 1994, pp. 47-55

128. Tabakoff, W.; '*Erosion Resistance of Superalloys and Different Coatings Exposed to Particulate Flows at High Temperature*', **Surface and Coatings Technology**, Vol. 120-121, 1999, pp. 542-547

129. Hamed, A.; Tabakoff, W.; Wenglarz, R.; '*Erosion and Deposition in Turbomachinery*', **Journal of Propulsion and Power**, Vol. 22, No. 2, 2006, pp. 350-360

130 Stephenson, D.J.; Nicholls, J.R.; '*Modelling the Influence of Surface Oxidation on High Temperature Erosion*', **Wear**, Vol. 186-187, 1995, pp. 284-290

131. Restall, J.E.; Stephenson, D.J.; '*High Temperature Erosion of Coated Superalloys for Gas Turbines*', **Materials Science and Engineering**, Vol. 88, 1987, pp. 273-282

132. Tabakoff, W.; Shanov, V.; '*Erosion Rate Testing at High Temperature for Turbomachinery Use*', **Surface Coatings and Technology**, Vol. 76-77, 1995, pp. 75-80

133. Wellman, R.G.; Deakin, M.J.; Nicholls, J.R.; *'The Effect of TBC Morphology on the Erosion Rate of EB PVD TBCs'*, **Wear,** Vol. 258, 2005, pp. 349-356

134. Silva Cruz, R.; '*TiB_2 Ceramic and DLC Multilayered PVD Coatings*', **PhD Thesis 2007**, Cranfield University

135. http//dsa.dimes.tudelft.nl/usage/technology/FIB (20.11.07)

136. Saint-Ramond, B.; '*Low Mass Platinum Aluminide Bondcoat for Thermal Barrier Coating*', **MPhil Thesis 2001**, Cranfield University

137. Erdös, E.; '*X-Ray Diffraction*', **Analysis of High Temperature Materials**, ed. O. Van Der Biest, Applied Science Publishers, 1983, pp. 189-203

138. Chen, J.H.; Little, J.A.; '*Degradation of the Platinum Aluminide Coating on CMSX-4 at 1100°C*', **Surface and Coatings Technology**, Vol. 92, 1997, pp. 69-77

139. Impey, S.A.; '*Surface Analysis of Materials'*, Lecture Notes, Advanced Materials MSc Course, Cranfield University, 2007

140. Gleeson, B.; Sordelet, D.; Wang, W.; Hayashi, S.; '*Nickel-platinum-aluminium Ternary Phase Diagram 1150*°C', Iowa State University

141. Villars, P.; Prince, A.; Okamoto, H.; '*Ni-Al-Ru 1000*°C *Ternary Phase Diagram'*, **The Handbook of Ternary Phase Diagrams**, ASM International, 1995

142. Nash, P.; Kleppa, O.; '*Composition Dependence of the Enthalpies of Formation of NiAl'*, **Journal of Metals and Compounds**, Vol. 321, 2001, pp. 228-231

143. Henig, T.H.; Lukas, H.L.; '*Calorimetric Determination of the Enthalpy of Formation and Description of the Defect Structure of the Ordered β-Phase (Ni, Cu)$_{1-x}$Al$_x$*, **Zeitschrift fur Metallkunde**, Vol 66, 1975, pp. 98-106

144. Rzyman, K.; Moser, Z.; Watson, R.E.; Weinert, M.; '*Enthalpies of Formation of Ni_3Al: Experiment versus Theory*', **Journal of Phase Equilibria**, Vol. 17, No. 3, 1996, pp. 173-178

145. Rzyman, K.; Moser, Z.; '*Calorimetric Studies on the Enthalpies of Formation of Al_3Ni_2, AlNi and $AlNi_3$*', **Progress in Materials Science**, Vol. 49, Issue 3-4, 2004, pp. 581-606

146. Pretorius, R.; '*Phase Sequence of Silicide Formation at Metal-Silicon Interfaces'*, **Vacuum**, Vol. 41, No. 4-6, 1990, pp. 1038-1042

147. Pretorius, R.;Marais, T.K.; Theron, C.C.; *'Thin Film Compound Phase Formation Sequence: an Effective Heat of Formation Model'*, **Materials Science and Engineering**, Vol. 10, 1993, pp. 1-83

148. Pretorius, R.; De Reus, R.; Vredenberg, A.M.; Saris, F.W.; *'Use of the Effective Heat of Formation Rule for Predicting Phase Formation Sequence in Al-Ni Systems'*, **Materials Letters**, Vol. 9, No. 12, 1990, pp. 494-499

149. d'Heurle, F.M.; Ghez, R.; *'Reactive Diffusion in a Prototype System: Nickel-Aluminium II: The Ordered Cu_3Au Rule and the Sequence of Phase Formation, Nucleation'*, **Thin Solid Films**, Vol. 215, 1992, pp.26-34

150. Huang, W.; Chang, Y.A.; *'A Thermodynamic Analysis of the Ni-Al System'*, **Intermetallics**, Vol. 6, 1998, pp. 487-498

151. Cornish, L.A.; Süss, R.; Watson, A.; Prins, S.N.; *'Building a Thermodynamic Database for Platinum-Based Superalloys:Part I'*, **Platinum Metals Review**, Vol. 51, Issue 3, 2007, pp. 104-115

152. Illinois Institute of Technology; http://tptc.iit.edu/Center/research/PhaseDiagram/Content/results.htm (14.11.07)

153. Prins, S.N.; Cornish, L.A.; Stumpf, W.E.; Sundman, B.; *'Thermodynamic Assessment of the Al-Ru System'*, **Calphad**, Vol. 27, No. 1, 2003, pp.79-90

154. Jung, W.G.; Kleppa, O.J.; *'Standard Molar Enthalpies of Formation of Metal Aluminide MeAl (Me = Ru, Rh, Os, Ir)'*, **Metallurgical Transactions B**, Vol. 23B, 1992, pp. 53-56

155. Su, H-N.; *'Thermodynamic Modeling of Al and Ni Based Ternary Alloy'*, **PhD Thesis 2004**, Illinois Institute of Technology

156. Su, H-N.; Nash, P.; *'Enthalpies of Formation in the Al-Ni-Ru System by Direct Reaction Synthesis Calorimetry'*, **Journal of Alloys and Compounds**, Vol. 403, 2005, pp. 217-222

APPENDIX 1

DSC Data

Ni-Al

NiAl

Calculated average nominal compositions (at.%)	Calculated at.% Ni	Onset temp(°C) calculated by DSC	Peak (°C) calculated by DSC	Integration (kJ/mol) calculated by DSC
42.5Ni57.5Al A3i	42.5	587.52	605.1	-78.0
42.5Ni57.5Al A3ii	42.5	589.43	604.93	-71.5
42.5Ni57.5Al A3iii	42.5	588.95	603.72	-74.9
44Ni56Al B3i	44	590.47	603.14	-65.5
44Ni56Al B3ii	44	588.68	607.46	-69.5
44Ni56Al B3iii	44	590.47	605.07	-66.5
45Ni55Al B2i	45	588.05	609.29	-89.3
45Ni55Al B2ii	45	588.1	603.88	-71.7
45Ni55Al B2iii	45	587.75	603.82	-69.9
47Ni53Al C2i	47	591.12	606.5	-79.8
47Ni53Al C2ii	47	587.4	604.82	-86.2
47Ni53Al C2iii	47	590.53	605.49	-79.4
48.5Ni51.5Al A3i	48.5	571.58	595.55	-67.8
48.5Ni51.5Al A3ii	48.5	569.81	591.67	-62.7
48.5Ni51.5Al A3iii	48.5	570.93	600.09	-66.7
49Ni51Al D1i	49	591.13	601.74	-69.5
49Ni51Al D1ii	49	582.12	603.76	-67.5
49Ni51Al D1iii	49	583.23	600.02	-65.5
50Ni50Al C4i	50	580.49	602	-83.8
50Ni50Al C4ii	50	575.47	594.44	-70.1
50Ni50Al C4iii	50	574.67	608.05	-59.9
52Ni48Al D2i	52	576.02	595.19	-42.7
52Ni48Al D2ii	52	579.17	600.74	-59.5
52Ni48Al D2iii	52	581	600.02	-72.0
54Ni46Al A3i	54	592.07	613.47	-71.1
54Ni46Al A3ii	54	588.86	602.64	-51.1
54Ni46Al A3iii	54	594.47	612.51	-61.6
58.5Ni41.5Al C3i	58.5	592	607.84	-58.4
58.5Ni41.5Al C3ii	58.5	592.51	605.85	-45.9
58.5Ni41.5Al C3iii	58.5	588.8	603.67	-39.6

NiAl + Pt

Calculated average nominal compositions (at.%)	Calculated at.% Pt	Onset temp(°C) calculated by DSC	Peak (°C) calculated by DSC	Integration (kJ/mol) calculated by DSC
48Ni/6Pt/46Al	6	586.9	607.36	-86.1
	6	583.84	599.34	-83.4
	6	583.4	605.37	-71.34
49Ni/8Pt/43Al	8	571.01	596.88	-62.8
	8	576.71	597.34	-72.5
	8	572.87	600.86	-64.0
40Ni/12Pt/48Al	12	586.71	603.53	-73.7
	12	588.65	606.62	-56.7
	12	586.28	604.11	-55.5
41Ni/13Pt/46Al	13	628.06	629.24	-65.7
	13	618.46	628.65	-51.8
	13	628.15	629.37	-62.8
40Ni/14.5Pt/45.5Al	14.5	629.4	630.9	-70.5
	14.5	628.65	630.01	-75.5
	14.5	628.81	630.46	-64.7
40Ni/16Pt/44Al	16	629.74	631.3	-58.7
	16	628.76	630.37	-70.0
	16	630.23	631.45	-78.5
29Ni/20Pt/51Al	20	581.07	590.5	-61.3
	20	576.62	585.55	-73.9
	20	583.63	595.45	-64.5
29Ni/22Pt/49Al	22	576.1	598.51	-73.3
	22	576.94	594.62	-80.9
	22	579.38	597.25	-77.1

NiAl + Ru

Calculated average nominal compositions (at.%)	Calculated at.% Ru	Onset temp(°C) calculated by DSC	Peak (°C) calculated by DSC	Integration (kJ/mol) calculated by DSC
50Ni/5Ru/45Al	5	604.1	616.87	-66.3
	5	613.07	622.51	-90.0
	5	604.95	615.74	-85.1
51Ni/7Ru/42Al	7	604.73	615.98	-80.0
	7	600.77	614.62	-82.8
48Ni/8Ru/44Al	8	605.78	616.72	-82.2
	8	611.75	623.79	-79.7
	8	615.8	623.82	-72.8
44Ni/11Ru/45Al	11	621.19	627.16	-84.0
	11	624.46	625.87	-74.1
	11	624.53	626.05	-74.6
36Ni/14Ru/50Al	14	586.76	596.97	-65.5
	14	591.17	601.79	-62.3
	14	588.45	600.75	-65.1
38Ni/14Ru/48Al	14	593.55	604.62	-70.5
	14	596.79	606.86	-78.2
	14	562.2	595.15	-76.6
40Ni/18Ru/42Al	18	578.56	591.45	-84.8
	18	550.56	589.67	-72.2
	18	570.57	591.24	-76.7

APPENDIX 2

DSC Data

Ni_3Al

Ni_3Al

Calculated average nominal compositions (at.%)	Calculated at.% Ni	Onset temp(°C) calculated by DSC	Peak (°C) calculated by DSC	Integration (kJ/mol) calculated by DSC
77.5Ni22.5Al (1 side) B3i	77.5	702.13	730.56	-59.0
79Ni21Al C2i	79	724.6	741.64	-53.1
79Ni21Al C2ii	79	706.21	716.16	-71.8
79Ni21Al C2iii	79	715.34	722.37	-76.2

Ni_3Al + Pt

Calculated average nominal compositions (at.%)	Calculated at.% Pt	Onset temp(°C) calculated by DSC	Peak (°C) calculated by DSC	Integration (kJ/mol) calculated by DSC
76Ni4Pt20Al	4	574.67	586.83	-9.1
	4	570.48	590.59	-20.2
73Ni7Pt20Al	7	558.01	587.55	-18.7
	7	580.83	594.46	-35.8
68Ni9Pt23Al	9	637.71	641.8	-10.5
	9	639.75	640.9	-13.7
67Ni10Pt23Al	10	614.25	631.07	-12.6
	10	635.38	638.26	-14.0
	10	633.67	639.34	-13.1
64Ni12Pt24Al	12	633.7	639.34	-13.2
	12	595.67	608.94	-12.8
	12	605.71	612.62	-11.5
60Ni16Pt24Al	16	565.8	577.93	-43.6
	16	563.5	576.19	-43.7
	16	573.62	584.04	-72.5

Ni_3Al + Ru

Calculated average nominal compositions (at.%)	Calculated at.% Ru	Onset temp(°C) calculated by DSC	Peak (°C) calculated by DSC	Integration (kJ/mol) calculated by DSC
78Ni5Ru17Al A1i	5	546.43	567.57	-40.9
	5	546.66	563.06	-45.4
	5	542.3	564.38	-52.0
74Ni5Ru21Al B1i	5	547.07	589.82	-80.1
	5	576.64	588.03	-44.3
	5	551.07	575.68	-29.7
77Ni5Ru18Al A1i	5	594.38	600.23	-44.0
	5	595.04	602.75	-43.7
	5	594.97	601.04	-45.1
73Ni6Ru21Al B1i	6	592.93	601.56	-40.8
	6	575.58	604.61	-40.5
	6	593.61	602.7	-35.0